On the Role of Allosteric Cooperativity in the Regulation of Protein Kinase A and its Implications in Disease

A Dissertation
SUBMITTED TO THE FACULTY OF THE
UNIVERSITY OF MINNESOTA
BY

Caitlin Elizabeth Walker

IN PARTIAL FULFILLMENT OF THE REQUIREMENTS
FOR THE DEGREE OF
DOCTOR OF PHILOSOPHY

Dr. David A. Bernlohr

May 2021

Abstract

First articulated half a century ago, allostery has remained a universal phenomenon and is essential in understanding processes beyond the molecular level, such as cellular signaling and disease. Allostery, also referred to as allosteric regulation, is a process by which biological macromolecules transmit the effect of binding at one site to an often distal, functional site, allowing for regulation. To facilitate the modulation of function between sites, allosteric signal is propagated through conserved amino acid residues, often comprising various structural elements of a protein. In general, allosteric communication is of fundamental interest and potentially of high relevance for drug design and protein engineering. Furthermore, the dysfunction of allosteric networks has been implicated in the etiology of human diseases. However, defining these networks of residues that mediate crosstalk between distal sites remains experimentally challenging and thus, poorly characterized. Since allosteric signal propagation relies on subtle conformational rearrangements, nuclear magnetic resonance (NMR) has emerged as an instrumental tool in investigating allosteric communication. This thesis aims to map allosteric networks at atomic resolution to understand how mutations in protein kinase A (PKA) influence allosteric communication to elicit the progression of various disease states. In this work we demonstrate how disease mutations associated with Cushing's Syndrome and Fibrolamellar Hepatocellular Carcinoma attenuate the allosteric network of PKA, thereby disrupting the finely tuned regulation, specificity, and activation of PKA to generate dysfunctional signaling. The findings of this thesis provide critical insights into the importance of intramolecular allostery in facilitating functional signaling, directly showing how changes in allosteric networks of proteins lead to dysfunction.

Table of Contents

Abstract ..... **i**
Table of Contents ..... **ii**
List of Tables ..... **v**
List of Figures ..... **vi**
List of Abbreviations ..... **viii**
Preface **1**
Chapter 1 Overview of cAMP-dependent Protein Kinase A **5**
1.1 Protein Phosphorylation and Protein Kinases 5
1.2 Architecture of PKA-C 6
1.3 Regulation of PKA 10
1.3.1 The Regulatory Subunits and A-kinase Anchoring Proteins 10
1.3.2 PKA Activation and Inactivation 12
1.4 Conformational States and Dynamics of PKA 14
1.5 Chemical Mechanism of PKA-C 16
1.6 Relevance of PKA in Human Diseases 18
1.6.1 Cushing's Syndrome (CS) 18
1.6.2 Fibrolamellar Hepatocellular Carcinoma (FL-HCC) 19
1.6.3 Cardiac Myxomas (CM) 20
Chapter 2 An NMR Perspective on Intramolecular Allosteric Communication in PKA. **22**
2.1 Introduction 22
2.2 PKA as a Model Allosteric Enzyme 23
2.3 H/D Exchange 24
2.4 Chemical Shift Perturbation 27
2.5 Slow Timescale Motions (μs-ms) 31
2.6 Fast Timescale Motions 34
2.7 Concluding Remarks 36
Chapter 3 Probing Protein-Protein Interactions Using Asymmetric Labeling and Carbonyl-Carbon Selective Heteronuclear NMR Spectroscopy. **38**
3.1 Synopsis 39
3.2 Introduction 40
3.3 Results 40
3.3.1 Mapping two binding partners fingerprints simultaneously. 40

3.3.2 Fingerprinting three binding partners using one sample. 43
3.3.3 Measuring Residual Dipolar Coupling (RDC) of complexes using one sample. 45
3.3.4 Measuring long-range distances and transient complexes using CCLS for Paramagnetic Relaxation Enhancements (PRE). 47
3.3.5 Improving sensitivity with the G5 pulse. 49
3.4 Conclusion and Perspectives 49
3.5 Acknowledgements 50
Chapter 4 Cushing's Syndrome Driver Mutation Disrupts Protein Kinase A Allosteric Network, Altering Both Regulation and Substrate Specificity 51
4.1 Synopsis 52
4.2 Introduction 53
4.3 Results 55
4.4 Discussion 65
4.5 Materials and Methods 69
4.6 Acknowledgements 75
4.7 Author Contributions 75
4.8 Supplementary Figures 76
4.9 Supplementary Tables 82
Chapter 5 Defective Internal Allosteric Network Imparts Dysfunctional ATP/Substrate Binding Cooperativity in Oncogenic Chimera of Protein Kinase A 86
5.1 Synopsis 87
5.2 Introduction 88
5.3 Results 89
5.4 Discussion 99
5.5 Materials and Methods 101
5.6 Acknowledgements 107
5.7 Author Contributions 107
5.8 Supplementary Figures 108
5.9 Supplementary Tables 116
Chapter 6 Is Disrupted Nucleotide-Substrate Cooperativity a Common Trait for Cushing's Syndrome Driving Mutations of Protein Kinase A? 120
6.1 Synopsis 121
6.2 Introduction 122
6.3 Results 124

6.4 Discussion 131
6.5 Materials and Methods 133
6.6 Acknowledgements 137
6.7 Author Contributions 138
6.8 Supplementary Figures 139
6.9 Supplementary Tables 145
Perspectives 150
List of Publications 152
References 153

List of Tables

Table 4.1. Changes in enthalpy, entropy, free energy, and dissociation constant of binding ATPγN, PKI_{5-24} and VPS36 for PKA-C^{WT} and PKA-C^{L205R}. 82
Table 4.2. Kinetic parameters of Kemptide and VPS36 phosphorylation by PKA-C^{WT} and PKA-C^{L205R}. 83
Table 4.3. PCA and standard deviation of the CONCISE analysis of the structural states analyzed. 84
Table 4.4. Melting temperatures (T_m) as determined using circular dichroism. 85
Table 5.1. Changes in enthalpy, entropy, free energy, and dissociation constant of binding ATPγN for PKA-C^{WT} and PKA-C^{DNAJB1} derived from ITC experiments. 116
Table 5.2. Changes in enthalpy, entropy, free energy, and dissociation constant for the binding of PKI_{5-24} to the apo and nucleotide-saturated forms of PKA-C^{WT} and PKA-C^{DNAJB1} derived from ITC experiments. 117
Table 5.3. Kinetic parameters of Kemptide, CREB, and KSR1 phosphorylation for PKA-C^{WT} and PKA-C^{DNAJB1}. 118
Table 5.4. CONCISE analysis of PKA-C^{WT} and PKA-C^{DNAJB1}. 119
Table 6.1. Changes in enthalpy, entropy, free energy, and dissociation constant for the binding of nucleotide to PKA-C^{E31V}. 145
Table 6.2. Changes in enthalpy, entropy, free energy, and dissociation constant for the binding of PKI_{5-24} to apo and nucleotide-saturated PKA-C^{E31V}. 146
Table 6.3. Kinetic parameters of Kemptide phosphorylation by PKA-C^{WT} and PKA-C^{E31V}. 147
Table 6.4. Changes in relative binding free energy, ΔΔG, and cooperativity from PKA-C^{WT} to PKA-C^{E31V} for the binding of PKI_{5-24} and the binding of ATP in the apo and binary states. 148
Table 6.5. Changes in enthalpy, entropy, free energy, and dissociation constant for the binding of PKI_{5-24} to apo and nucleotide-saturated PKA-C^{W196R}. 149

List of Figures

Figure 1.1. Architecture of PKA-C. 7
Figure 1.2. Important conserved motifs in eukaryotic protein kinases. 9
Figure 1.3. Architecture of PKA R-subunits. 12
Figure 1.4. General cAMP signaling pathway. 13
Figure 1.5. Structural transitions and energy landscape of PKA-C. 15
Figure 2.1. Timescales of protein motions and their corresponding NMR techniques. 23
Figure 2.2. Distribution of amide fractionation factors for apo, ADP-bound and ADP/PKI-bound PKA-C. 26
Figure 2.3. Chemical shift perturbations upon ligand binding for PKA-C^{WT} and PKA-C^{Y204A}. 28
Figure 2.4. Cushing's syndrome somatic mutation disrupts the allosteric network of PKA-C to elicit dysfunction. 30
Figure 2.5. Slow timescale backbone dynamics of PKA-C in different ternary complexes. 32
Figure 2.6. Allosteric changes in conformational dynamics of PKA-C^{WT} upon binding PLN (top) or PLN^{R14del} (bottom). 33
Figure 2.7. Changes in the conformational entropy of PKA-C during the enzymatic cycle. 36
Figure 3.1. CCLS pulse sequence. 42
Figure 3.2. DCLS pulse sequence. 44
Figure 3.3. CCLS/DCLS RDC. 46
Figure 3.4. CCLS-PRE. 48
Figure 3.5. CCLS G5-pulse implementation. 49
Figure 4.1. Architecture of PKA-C and locations of the Cushing's syndrome mutations. 55
Figure 4.2. Allosteric network of interactions observed upon pseudo-substrate binding. 58
Figure 4.3. Rewiring of allosteric network of PKA-C^{L205R} upon binding VPS36. 61
Figure 4.4. Conformational dynamics of the activation loop of PKA-C^{WT} and PKA-C^{L205R} upon binding substrate. 62
Figure 4.5. Cushing's mutations are located in allosteric nodes identified via CHESCA. 66
Figure 4.6. Schematic of the energy landscape for PKA-C^{WT} and PKA-C^{L205R}, combining thermodynamics and MD simulations data. 68
Figure 4.7. [^{1}H, ^{15}N]-TROSY-HSQC spectra for PKA-C^{WT} and PKA-C^{L205R} in apo, ATPγN, ATPγN /PKI-bound and ATPγN/VPS36-bound forms. 76
Figure 4.8. Chemical shift perturbations (CSP) observed upon ligand binding for PKA-C^{WT} and PKA-C^{L205R}. 77
Figure 4.9. Intensity plot for the binding of VPS36 to ATPγN-saturated PKA-C^{L205R}. 78
Figure 4.10. Principal component analysis (PCA) of the catalytic lobes in PKA-C^{WT} and PKA-C^{L205R}. 79
Figure 4.11. Probability of the formation of inter-residue contact and ΔRMSF of PKA-C upon forming ternary complexes with PKI_{5-24} or VPS36. 80
Figure 4.12. Allosteric changes upon peptide binding revealed by MD simulation and mutual information (Mutinf) analysis. 81

Figure 5.1. Multiple conformations adopted by the dynamic J-domain alters allosteric binding cooperativity of PKA-C. 90
Figure 5.2. Attenuation in binding cooperativity does not influence phosphoryl transfer. 92
Figure 5.3. Defective internal allosteric network of PKA-C^{DNAJB1} 93
Figure 5.4. Reduced crosstalk amongst structural communities of chimeric PKA-C^{DNAJB1} relative to PKA-C^{WT}. 94
Figure 5.5. Global coordinated response of PKA-C^{WT} and PKA-C^{DNAJB1} to ligand binding. 96
Figure 5.6. Community-specific responses of PKA-C^{WT} and PKA-C^{DNAJB1} upon ATPγN and PKI_{5-24} binding. 98
Figure 5.7. SAXS profiles for PKA-C^{WT}. 108
Figure 5.8. Thermodynamics of PKA-C^{DNAJB1} binding nucleotide and pseudo-substrate. 109
Figure 5.9. Steady state kinetics of phosphoryl transfer. 110
Figure 5.10. NMR amide fingerprints of PKA-C^{DNAJB1} and PKA-C^{WT}. 111
Figure 5.11. NMR backbone assignment of $DNAJB1_{1-69}$. 112
Figure 5.12. Chemical shift perturbations (CSP) observed upon ligand binding for PKA-C^{WT} and PKA-C^{DNAJB1}. 113
Figure 5.13. CONCISE scores of each individual community mapped onto the surface of a PKA-C^{WT} and b PKA-C^{DNAJB1}. 114
Figure 5.14. Isolation and purification of PKA-C^{DNAJB1} and $DNAJB1_{1-69}$. 115
Figure 6.1. Structural and kinetic characterization of PKA-C^{E31V}. 123
Figure 6.2. Chemical shift perturbation of PKA-C^{E31V}. 125
Figure 6.3. The reduction in binding cooperativity corresponds to a decrease in intramolecular allosteric connectivities. 126
Figure 6.4. Community analysis of PKA-C^{E31V} 128
Figure 6.5. Altered dynamics of PKA-C^{E31V} reveled by MD simulations. 129
Figure 6.6. Relationship between coordinated structural changes identified by CHESCA and the nucleotide-substrate binding cooperativity (σ) determined by ITC measurements. 131
Figure 6.7. [^{1}H, ^{15}N]-TROSY-HSQC spectra for PKA-C^{WT} and PKA-C^{E31V} in the apo, ATPγN-, ADP-, and ATPγN/PKI-bound forms. 139
Figure 6.8. Change in chemical shift perturbation between PKA-C^{WT} and PKA-C^{E31V}. 140
Figure 6.9. Attenuated allostery of PKA-C^{E31V} revealed by MD simulations. 141
Figure 6.10. Distinct interaction profile of PKI_{5-24} in the ternary complex with PKA-C^{WT} and PKA-C^{E31V}. 142
Figure 6.11. Thermodynamic cycle linking the free energy perturbation (FEP) calculation to ratio of K_d and σ. 143
Figure 6.12. Correlation score analysis of PKA-C^{L205R} and PKA-C^{W196R}. 144

List of Abbreviations

ADP: Adenosine Diphosphate

AKAP: A-kinase-anchoring Protein

AKIP: A-kinase-interacting Protein

ATP: Adenosine Triphosphate

ATPγN: Adenylyl-imidodiphosphate

cAMP: Cyclic Adenosine Monophosphate

CCS: Combined Chemical Shift

CHESCA: CHEmical Shift Covariance Analysis

CM: Cardiac Myxomas

CONCISE: Coordinated Chemical Shifts Behavior

CREB: cAMP Response Element-binding Protein

CS: Cushing's Syndrome

CSP: Chemical Shift Perturbation

DNAJB1: DnaJ Heat Shock Protein Family (Hsp40) Member B1

FL-HCC: Fibrolamellar Hepatocellular Carcinoma

HMQC: Heteronuclear Multiple Quantum Coherence

HSQC: Heteronuclear Single Quantum Coherence

INEPT: Insensitive Nuclei Enhanced by Polarization Transfer

ITC: Isothermal Titration Calorimetry

MD: Molecular Dynamics

NMR: Nuclear Magnetic Resonance

PKA: Protein Kinase A

PKA-C: Protein Kinase A Catalytic Subunit

PKI: Protein Kinase Inhibitor

PKI_{5-24}: Protein Kinase Inhibitor residues 5-24

PLN: Phospholamban

PPI: Protein-Protein Interactions

RMSD: Root Mean Square Deviation

RMSF: Root Mean Square Fluctuation

SAXS: Small Angle X-ray Scattering

TROSY: Transverse Relaxation Optimized Spectroscopy

Preface

Allostery, also referred to as allosteric regulation, is a process by which biological macromolecules transmit the effect of binding at one site to an often distal, functional site, allowing for regulation. First articulated half a century ago, allostery has remained a universal phenomenon and is essential in understanding processes beyond the molecular level, such as cellular signaling and disease[1-3]. Despite its importance, allosteric mechanisms have remained an enigma, eluding a general, quantifiable and predictive atomic description.

Allostery has evolved over time as experimental techniques have improved. The first allosteric protein studied, hemoglobin, was highly amenable to high-resolution x-ray crystallography. Thus, classical models of allostery, including the Monod-Wyman-Changeux (MWC)[4] and the Koshland-Nemethy-Filmer (KNF) models[5], evolved from static structural images and led to the paradigm that allostery involves conformational change. Indeed, further studies involving hemoglobin by Parsegian and colleagues[6], and later Nussinov[7, 8], deduced that allosteric transitions involved multiple pre-existing dynamic and conformational states, whose relative populations were tunable over a range of physiological conditions. As experimental structural, dynamic, and thermodynamic approaches have been developed, modern descriptions of allostery have become more complex, with the static-centric view of allostery being replaced by more quantitative, dynamic views. Regardless of the view, allostery offers a highly specific way to modulate protein function and control nearly all biological processes.

To facilitate the modulation of function between sites, allosteric signal is propagated through conserved amino acid residues, comprising various structural elements, defined as an allosteric network or pathway. In general, allosteric communication is of fundamental interest and potentially of high relevance for drug design and protein engineering. Furthermore, the dysfunction of allosteric networks has been significantly associated with the etiology of human diseases[9-12]. However, defining these networks of residues that mediate crosstalk between distal sites remains experimentally challenging and thus, poorly characterized. Computational approaches have provided insights into some of the underpinnings of allostery, but have their shortcomings[13-15]. Since allosteric signal propagation relies on subtle, but critical conformation and side-chain packing rearrangements, nuclear magnetic resonance

(NMR) has emerged as an instrumental tool in investigating allosteric communication[16-18].

Regulating nearly all cellular processes, protein kinases comprise one of the largest and most diverse families of enzymes. Protein kinases act as molecular switches by phosphorylating Ser/Thr/Tyr groups to modulate the activity of protein substrates. It has been estimated that nearly one-third of all cellular proteins are phosphorylated at some stage. Given their role in dictating cellular signaling outcomes, the catalytic activity of kinases is stringently regulated. Indeed, abnormal phosphorylation patterns are observed in various pathological conditions including endocrine disorders[19, 20], cancers[21], immunodeficiencies[22], and cardiovascular disease[23].

For the past few decades, mutations in kinase genes have been found to underlie many human diseases, and the knowledge of these diseases is of great clinical interest[24, 25]. Mutations can either be activating or inactivating, although activating mutations are much more commonly associated with disease as they often cause constitutive activation leading to pronounced phenotypes. A mechanistic understanding of the molecular mechanisms underlying mutations involvement in various disease states is likely to revolutionize treatment.

Cyclic AMP-dependent protein kinase A (PKA) has served as the prototype for the eukaryotic kinase superfamily, modulating most of the physiological response to cAMP in the cell. Recently, genetic alterations in PKA have been associated with a variety of metabolic and tumorigenic disease states, most recently, Cushing's syndrome (CS)[26-30] and Fibrolamellar Hepatocellular Carcinoma (FL-HCC)[31, 32]. While an enormous amount of information about the structure and function of PKA is available, the mechanisms underlying these disease states are largely unknown. The overall goal of this work is to map allosteric networks based on the covariance analysis of chemical shifts to elucidate, at atomic resolution, how mutations in PKA-C influence allostery and elicit the progression of various disease states.

Specifically, this thesis aims to address the following questions: How do mutations in PKA-C influence allostery and cooperativity to elicit the progression of various metabolic and tumorigenic disease states? What role do alterations in intramolecular allostery and cooperativity play in PKA-C regulation, activity, and substrate specificity? Is there a relationship between binding cooperativity and intramolecular allostery? These questions

were addressed using a combination of NMR spectroscopy, isothermal titration calorimetry (ITC), activity assays, and molecular dynamic (MD) simulations.

Chapter 1 reviews background on PKA structure, regulation, and catalysis, and introduces the involvement of PKA in various human diseases. **Chapter 2** discusses some of the major advances in solution-state NMR methods that have facilitated the characterization of allostery as applied to cAMP-dependent protein kinase A. The following chapters consist of re-prints with permission from peer reviewed articles. A cumulative list of publications published or in preparation are located at the end of this thesis, including works that address topics outside the scope of this thesis.

Protein-protein interactions (PPIs) regulate nearly all cellular processes, though the study of them by NMR spectroscopy is usually complicated by the necessity to prepare multiple samples to 'visualize' all components. Chapter 3 reviews a method that is applicable for the study of PPIs using a combination of asymmetric labeling and a selective pulse sequence.

Chapter 3: "Probing Protein-Protein Interactions Using Asymmetric Labeling and Carbonyl-Carbon Selective Heteronuclear NMR Spectroscopy." Larsen, E.K.; Olivieri, C.; **Walker, C.;** V.S., M.; Gao, J.; Bernlohr, D.A.; Tonelli, M.; Markley, J.L.; Veglia, G. (2018) *Molecules.* 23, 1937. PMCID: PMC6205158.

Recent literature has identified mutations in PKA-C that are linked to the development of cortisol-secreting adrenocortical adenomas resulting in Cushing's syndrome, but the aberrant mechanism of these mutations is unknown. Motivated by this, Chapter 4 details how the most common Cushing's syndrome mutation disrupts the intramolecular allosteric network eliciting changes in cooperativity, substrate specificity, and regulation.

Chapter 4: "Cushing's Syndrome Driver Mutation Disrupts Protein Kinase A Allosteric Network Altering Both Regulation and Substrate Specificity." **Walker, C.;** Wang, Y.; Olivieri, C.; Karamafrooz, A.; Casby, J.; Bathon, K.; Calebiro, D.; Gao, J.; Bernlohr, D.A.; Taylor, S.S.; Veglia, G. (2019) *Science Advances*. 5, eaaw9298. PMCID: PMC6713507.

An aberrant fusion of the *DNAJB1* and *PRKACA* genes generates a chimeric protein kinase that is the oncogene responsible for the pathogenesis of Fibrolamellar

Hepatocellular Carcinoma (FL-HCC). Chapter 5 probes the contribution of dysfunctional allosteric cooperativity of this chimeric protein kinase in eliciting FL-HCC.

Chapter 5: “Defective Internal Allosteric Network Imparts Dysfunctional ATP/Substrate Binding Cooperativity in Oncogenic Chimera of Protein Kinase A.” Olivieri, C.*; **Walker, C.*;** Karamafrooz, A.*; Wang, Y.; V.S., M.; Porcelli, F.; Blumenthal, D.K.; Thomas, D.D.; Bernlohr, D.A.; Sandford, S.M.; Taylor, S.S.; Veglia, G. (2021) *Communications Biology*. 4(321). PMCID: PMC7946884. *authors contributed equally

Multiple mutations are associated with Cushing’s syndrome, all lying on the R-subunit interface with the exception of one. Chapter 6 investigates an allosteric Cushing’s syndrome mutation, showing that losses in binding cooperativity are proportional to attenuations in intramolecular allostery and further suggesting a common mechanism underlies all Cushing’s syndrome mutations.

Chapter 6: “Is Disrupted Nucleotide-Substrate Cooperativity a Common Trait for Cushing’s Syndrome Driving Mutations of Protein Kinase A?” **Walker, C.;** Wang, Y.; Olivieri, C.; V.S., Manu; Gao, J.; Bernlohr, D.A.; Calebiro, D.; Taylor, S.S.; Veglia, G. (2021) *Submitted.*

The findings of these works provide critical insights into the importance of intramolecular allostery in facilitating functional signaling, while at the same time directly show how changes in allosteric networks of a protein lead to disease. Furthermore, the work presented here shows the intricacy of allosteric information transfer and demonstrates how small perturbations to protein or ligand architectures can disrupt catalytic function through alterations of these networks and conformational ensembles. These studies provide a foundation for future studies on the allosteric mechanisms of proteins and their disease-associated variations with a particular emphasis on how mutations and ligands exert control over allosteric networks to manifest (dys)function.

Chapter 1 Overview of cAMP-dependent Protein Kinase A

1.1 Protein Phosphorylation and Protein Kinases

Protein phosphorylation is one of the most common and most important post-translational modifications, responsible for regulating every basic cellular process including metabolism, cell growth, cell division, muscle contraction, immunity, and memory. Protein kinases are responsible for catalyzing the transfer of the γ-phosphate from adenosine triphosphate (ATP) to specific amino acids in proteins – in eukaryotes, these are usually Ser, Thr, and Tyr residues. Indeed protein kinases themselves are in turn regulated by phosphorylation, along with inhibitory and activation protein partners, cellular localization, protein degradation and gene transcription. Considering the broad importance of phosphorylation in signal transduction, it is not surprising that over 500 kinases have been discovered and that they comprise ~2% of the human genome[33]. Furthermore, it is estimated that 30% of all cellular proteins are phosphorylated on at least one residue.

Despite their diversity in sequence and regulation, all kinases share a highly conserved catalytic domain fold that was first observed following the crystallization of cAMP-dependent protein kinase A (PKA) in 1991[34-36]. This crystal structure not only provided the canonical domain organization of a kinase but also revealed how kinases recognize peptide/protein substrates[37]. Classical protein kinases have catalytic domains of 250-300 amino acids in length. The catalytic domains adopt a bilobal fold, consisting of two structurally and functionally distinct lobes that contribute to catalysis and regulation. Details regarding specific structural features of kinases within each catalytic domain will be discussed further in section 1.2 in the context of PKA. Briefly, the smaller N-lobe is composed of 5 β-sheets and 1 helical subdomain called the αC-helix, while the larger C-lobe is composed of α-helices plus a β-sheet. Between the N- and C-lobe is the binding cleft (commonly known as the active site) responsible for binding adenosine triphosphate (ATP), with the adenosine moiety buried in a hydrophobic pocket and the phosphate backbone oriented outward towards solution, and one or two divalent cations: magnesium or manganese. These cations provide coordination within the active site. The C-lobe on the other hand serves as a tethering surface for substrates, positioning them appropriately

for phosphoryl transfer. In addition to a conserved domain layout, all catalytic domains contain a conserved set of non-consecutive hydrophobic residues referred to as “spines” that anchor all elements important for catalysis to the αF-helix, located within the C-lobe. The regulatory spine (R-spine) is the hallmark of an active kinase and is assembled as part of regulation. In contrast, the catalytic spine (C-spine) is completed upon the binding of the adenine ring of ATP[38, 39].

While their core domain fold is conserved, most kinases are flanked by other domains or are a part of a multi-subunit complex that is in part responsible for the regulation of the catalytic domain. The toggle between active and inactive states is often complex and highly regulated. In the case of PKA, N- and C-terminal extensions flank the catalytic (C) subunit to assist in maintaining PKA-C in an active conformation, while relying on regulatory subunits to regulate activity. Whereas for cyclin dependent kinase 2 (Cdk2), activation is dependent on the association with a cyclin subunit. Along with phosphorylation on the activation loop, these domains or subunits are ultimately responsible for properly positioning subdomains (αC-helix, activation loop, DFG motif) or motifs within the catalytic domain.

1.2 Architecture of PKA-C

The sequence homology of kinases was first described in a monumental paper by Hanks and Hunter in which they described, from 65 known sequence available at the time, conserved residues and twelve ‘subdomains’ that are conserved throughout the kinome[40, 41]. From these comparisons, twelve residues: Gly50 and Gly52 in subdomain I, Lys72 in subdomain II, Gly91 in subdomain III, Asp166 and Asn171 in subdomain VIB, Asp184 and Gly186 in subdomain VII, Glu208 in subdomain VIII, Asp220 and Gly225 in subdomain IX, and Arg280 in subdomain XI, were recognized at being invariant or nearly invariant, thus implicating them as playing essential roles in enzyme function. The results of these comparisons also indicated that kinases all fold into a topologically similar 3-dimensional structure and perform phosphoryl transfer with a common mechanism. Despite all kinases sharing a similar 3-dimensional structure, Hanks and Hunter devised a classification scheme based on each kinases structural and functional properties and grouped corresponding kinase’s together in families (**Figure 1.1**) [40, 41]. This classification is still in use today, although updated.

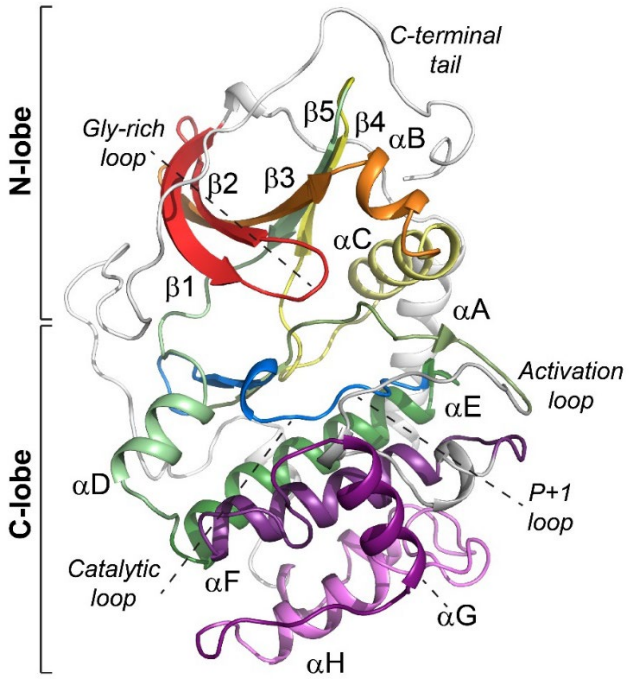

Figure 1.1. Architecture of PKA-C.
The subdomains of PKA-C colored as defined by Hanks and Hunter [41]. PKA-C is composed of a N-lobe that binds and orients ATP for catalysis and a C-lobe that serves as a docking site for substrate or regulatory subunit. PDB: 1ATP

Since its crystallization in 1991, PKA-C has served as the prototypical kinase and has been used as a model kinase where basic questions widely applicable for the EPK superfamily can be addressed. PKA-C adopts the characteristic bilobal kinase fold with a smaller N-lobe composed of β-sheets and a larger C-lobe filled with α-helices (**Figure 1.1**). Both lobes are flanked by a helical motif in the N-terminus (αA) and a loosely structured tail in the C-terminus (C-tail). Consistent with all kinases, the N-lobe is responsible for binding and orienting the phosphates of ATP for efficient phosphoryl transfer, while the C-lobe provides a scaffold for substrate binding and regulatory sites. Within the small lobe and between β1 and β2 is the glycine-rich loop which contains a conserved GxGxxG motif and is responsible for folding over the nucleotide and positioning the γ-phosphate of adenosine triphosphate (ATP) (**Figure 1.2 panel A**)[42]. Indeed, mutation of either Gly50 or Gly52 in this motif within PKA-C results in a decrease in affinity for ATP accompanied by a decrease in K_M and K_d for Kemptide. Linking the β-strands to the αC-helix is a conserved salt bridge occurring between Lys72 in β3 and Glu91 in the αC-helix. This interaction directly depends on the conformation of the mobile αC-helix. The importance of Lys72 is highlighted in pseudo-kinases where loss of this residue

results in a loss in catalytic activity. The αC-helix is another highly conserved, key element within the N-lobe responsible for bringing together different elements of the kinase and whose orientation determines kinase activation (**Figure 1.2 panel B**). For PKA, the αC-helix is highly ordered, adopting an αC-*in* conformation permitting activity. Whereas, in the inactive conformation the αC-helix is either disordered or adopts an αC-*out* conformation that results in Glu91 facing outward toward solvent[43, 44]. In addition to controlling activation, the αC-helix's electrostatic interactions with the activation loop (pThr197), cation-π interactions with the αA-helix (Trp30), and ion pair interactions with the C-tail (Phe350) serve to stabilize the orientation of the αC-helix in a catalytically competent state[42].

The C-lobe of PKA-C contains various loops each with conserved residues positioned in the active site cleft that play pivotal roles in catalysis. Amongst these loops in the catalytic loop (residues 166-171) which contains Asp166 that functions as a catalytic based, Lys168 which interacts with the γ-phosphate of ATP, and Asn171 that interacts with the secondary Mg^{2+} ion that bridges the β- and γ-phosphates of ATP. Following the catalytic loop is the conserved DFG motif (residues 184-187) which contributes to ATP binding in addition to regulating catalysis. The activation loop begins following the DFG motif and extending up to the APE motif, including the P+1 loop. This 20-30 residue segment is responsible for binding substrates, although it lies outside the active-site cleft (**Figure 1.2 panel C**). The activation loop contains the phosphorylation site Thr197 that upon phosphorylation, becomes ordered and adopts an active conformation. Within this loop is the P+1 loop or peptide positioning loop (residues 198-208) that tethers the P+1 residue of substrates into a hydrophobic pocket composed of Leu198, Pro202 and Leu205. Overall, the activation loop is the most variable part of the kinase core – both in length and sequence – and its highly dynamic regulation is one of two elements that distinguish eukaryotic protein kinases (EPKs) from eukaryotic-like kinases in prokaryotes[45, 46]. The conserved APE motif (Ala206-Pro207-Glu208) ends the activation loop segment of the kinase providing integration between various structures within the C-lobe. Glu208 forms a salt bridge with Arg280 of the αH-αI loop, stabilizing the position of the activation segment relative to the GHI-domain (αG-, αH-, αI-helices). Within the interior of the C-lobe is a series of stable, hydrophobic α-helices (αE, αF, and αH),

with the large αF-helix serving as a scaffold for the assembly of two hydrophobic spines (discussed later)[39].

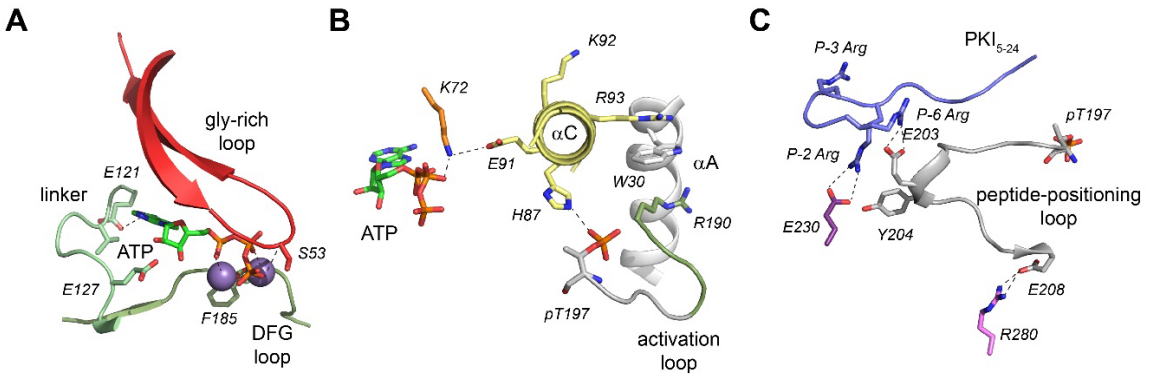

Figure 1.2. Important conserved motifs in eukaryotic protein kinases.
(**A**) Interactions occurring between ATP and residues in the active site cleft. (**B**) Interactions between the αC-helix, activation loop, αA-helix, and ATP-binding groove. All interactions are critical to elicit activity. (**C**) Interactions between the peptide position loop and the pseudosubstrate, PKI_{5-24}. PDB ID: 1ATP

On either side of the two lobes in PKA-C are two critical segments that have been shown to optimize the catalytic efficiency and increase stability of the kinase. Preceding the N-lobe is the N-terminal segment consisting of a myristoylation motif (GNAAAAK) followed by an amphipathic helix (αA-helix). Upon myristoylation of the N-terminal Gly, the myristoyl group interconverts between a “myr-in” and “myr-out” conformation, where the myr-out conformation is able to bind to the membrane. Additional post-translational modifications occur in this portion of PKA-C including deamidation of Asn2 and phosphorylation at Ser10. Indeed, phosphorylation at Ser10 stabilizes a helix-turn-helix conformation of the N-terminal αA-helix, which in turn increases the correlated motions between the N-terminus and glycine-rich loop[47]. The αA-helix tethers the αC-helix in the αC-*in* position through cation-π interactions between Trp30 and the sidechains of Arg93 (αC-helix) and Arg190 (β9)[47, 48]. Wrapping around both lobes with ends firmly anchored to each lobe is the C-terminal tail. The C-terminal tail consists of three major segments: N-lobe tether, active site tether, and C-lobe tether[49]. The N-lobe tether, the most terminal portion of the C-terminal tail, contains a FxxF motif (recognition site of PDK1) that docks into the PDK1 interacting fragment (PIF) pocket in the N-lobe, contributing to the stability of the αC-helix[50]. The active site tether has two main functions. This portion of the C-terminal tail controls the entry and exit of ATP (residues 320-327), while residues 328-

334, which contains a cluster of acidic residues, helps attract basic substrates to the active site[51]. An additional phosphorylation site is present in the C-terminal tail at Ser338 and has been shown to be critical for a fully functional kinase[52].

Despite the extensive work done to understand conserved features of kinases through a structure-function perspective, many conserved residues were unexplained by primary sequence alone. Using Local Spatial Patterns (LSP) alignment, Kornev and coworkers identified a series of hydrophobic residues within the core of the kinase that had previously not been recognized in playing an important role in regulation[39]. These hydrophobic motifs, termed 'spines,' traversed the kinase core, integrating catalytic and regulatory elements of the kinase and finally anchoring to the αF-helix[38]. The first hydrophobic motif, termed regulatory or R-spine, is composed of Leu95 from the αC-helix, Leu106 from β4, Tyr164 from the HRD motif of the catalytic loop and Phe185 from the DFG loop. In the active state, kinases contain an assembled R-spine and in the inactive state the R-spine is disassembled. Most often, disassembly of the R-spine results from the flipping of the phenylalanine in the DFG motif (commonly termed 'DFG-out') or displacement of the αC-helix. The second hydrophobic motif, termed catalytic or C-spine, is composed of Val57 and Ala70 which contact the adenine ring of ATP, Met128 from the αD-helix, Leu172, L173 and Ile174 from β7, and Leu227 and Met231 from the αF-helix. This spine is fully assembled by the adenine ring upon ATP binding thereby linking the two lobes together and committing the kinase to catalysis. Both R- and C-spines are docked into the αF-helix. More recently, hydrophobic residues surrounding the spine, termed 'shell' residues, were shown to contribute to the activity of the kinase via stabilization of the R-spine residues. In PKA-C, these residues include Val104, Met118, and Met120[43].

1.3 Regulation of PKA

1.3.1 The Regulatory Subunits and A-kinase Anchoring Proteins

In its inactive state, PKA exists as a hetero-tetramer composed of two catalytic (C) subunits that bind to a dimer of regulatory (R) subunits[53]. Upon increases in intracellular cyclic-adenosine monophosphate (cAMP), two cAMP molecules bind each R-subunit resulting in a conformational change and thereby releasing PKA-C. Multiple genes code for R and C subunits. A total of three genes code for the C-subunit, referred to as Cα, Cβ, and Cγ each with a host of other splice variants. Four regulatory subunit genes have been

identified and are subdivided into two classes: RI isoforms (α and β) and RII isoforms (α and β). All four subunits are functionally non-redundant. While RIα and RIIα are ubiquitously expressed, RIβ and RIIβ are tissue specific. All R-subunits differ in their amino acid sequences (75% identity), molecular weight, isoelectric point, and cAMP binding affinity. RII subunits contain an auto-phosphorylation site within their inhibitory sequence (IS) affecting RII:C interactions and signal amplification. Moreover, RI subunits require ATP and two magnesium ions, while RII subunits have no dependence on nucleotide or magnesium to form high-affinity complexes.

R-subunits all have a conserved domain structure composed of an N-terminal dimerization and docking domain (D/D), which is responsible for the assembly of the R-subunit dimer and interactions between R-subunits and A-kinase anchoring proteins (AKAPs) (**Figure 1.3 panel A**) [54]. Structurally, the D/D domain is ~50 residue segment that forms an anti-parallel X-type helical bundle, creating a hydrophobic surface for AKAP docking. Connecting the D/D to cyclic-nucleotide binding domain (CNB) A is a flexible linker region that includes the IS. The IS contains PKA's substrate recognition sequence, acting as a substrate (in the case of RII subunits) or a pseudo-substrate (in the case of RI subunits) by binding the active site of PKA-C. The two CNB domains (CNB-A, CNB-B) are located c-terminally from the linker region. Each CNB domain consists of an eight β-strand sandwich with a Phosphate Binding Cassette (PBC) at the core of the sandwich. Both CNB-A and CNB-B undergo large conformational changes upon binding cAMP, with CNB-A forming the most extensive contact with PKA-C in the absence of cAMP (**Figure 1.3 panel B**).

Tethering the kinase to distinct subcellular compartments, AKAPs mediate second messenger responsiveness acting as scaffold[54, 55]. Originally it was proposed that AKAPs were specific towards RII subunits, while RI subunits were primarily cytosolic. However, more recently RI-specific AKAP's have been discovered, challenging this assumption. To date, more than 50 AKAPs have been discovered all sharing a characteristic motif for R-subunit binding but differ largely in their remaining sequence. All contain a targeting domain that is responsible for localizing AKAPs to specific subcellular locations (i.e. cytoskeleton, golgi, ER, nucleus, mitochondria). In addition, AKAPs contain modular interaction motifs for interactions with other signaling molecules including kinase substrates, phosphodiesterase (PDE), phosphatases, additional kinases, and channels.

By functioning as scaffolds that assemble and tether distinct signaling molecules to subcellular compartments, AKAPs ensure precise PKA-centered regulation and signal transduction[55].

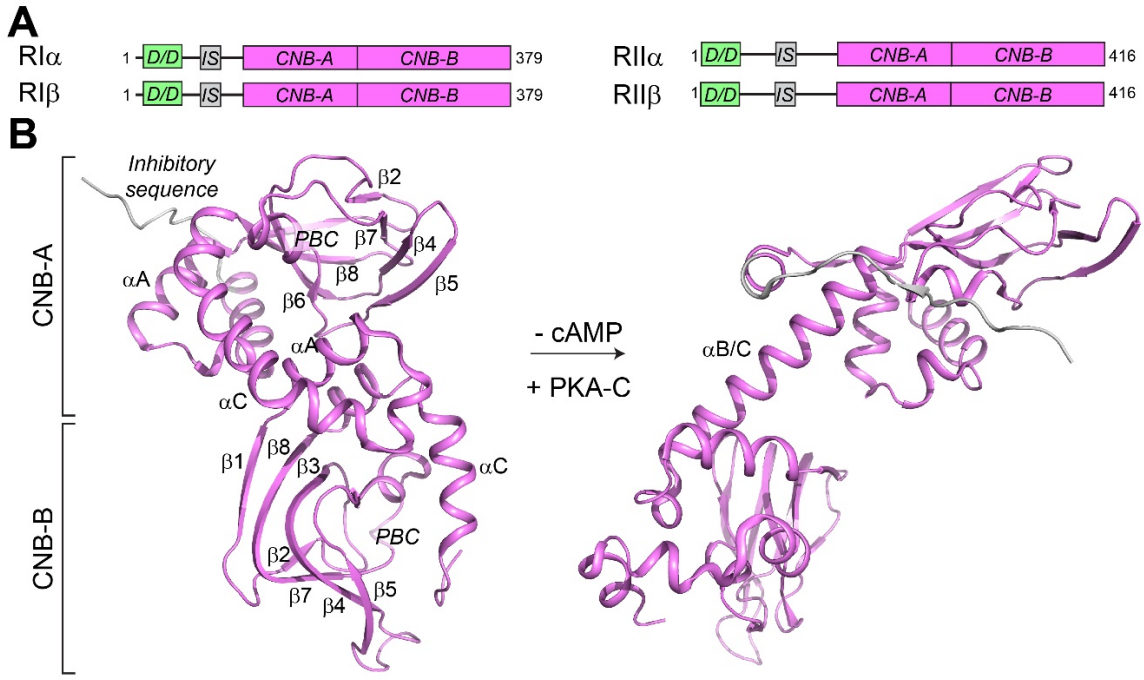

Figure 1.3. Architecture of PKA R-subunits.
(**A**) Domain architecture of RI and RII subunits. D/D refers to the dimerization/docking domain, IS refers to the inhibitory sequence, and CNB refers to cyclic-nucleotide binding domains. (**B**) Structural transition from cAMP-bound RIα (compact) to PKA-C-bound RIα (extended) highlighting the secondary structural elements of RI subunits. PDB ID: 1RL3 (+cAMP structure); 6NO7 (-cAMP, +PKA-C structure)

1.3.2 PKA Activation and Inactivation

Cellular signal transmission requires spatiotemporally controlled molecular interactions that begin at the cell surface[56]. At the cell surface information is received by receptor complexes often in the form of hormones or neurotransmitters, as is the case for PKA signaling. Signaling via hormones or neurotransmitters often involves second messenger molecules which relay the effects of receptor input to cytoplasmic and nuclear targets. The largest family of receptors are G protein-coupled receptors (GPCRs), with cAMP being the best-studied second messenger downstream of GPCRs.

Following activation of GPCRs, stimulatory or inhibitory G alpha proteins control adenylyl cyclase (AC), thereby regulating the conversion of ATP to cAMP. Once

synthesized, cAMP diffusion is restricted through molecular machinery responsible for coordinating localized cAMP signaling events. The coordinated effort of ACs and PDEs compartmentalize cAMP near AKAPs. This compartmentalization ensures information flow between supramolecular signaling complexes. Upon cAMP-mediated activation of PKA-C, substrates co-localized, either via AKAPs or via other scaffolds, are phosphorylated. Independent of cAMP, PKA is hypothesized to be activated by mechanisms involving the nuclear factor κB (NF-κB), the Ubiquitin Proteasome System (UPS), and the transforming growth factor-beta (TGF-β). All mechanisms involve either other proteins interacting with PKA-C to block activity and target distinct cellular targets, or binding to the R:C holoenzyme thereby activating PKA-C.

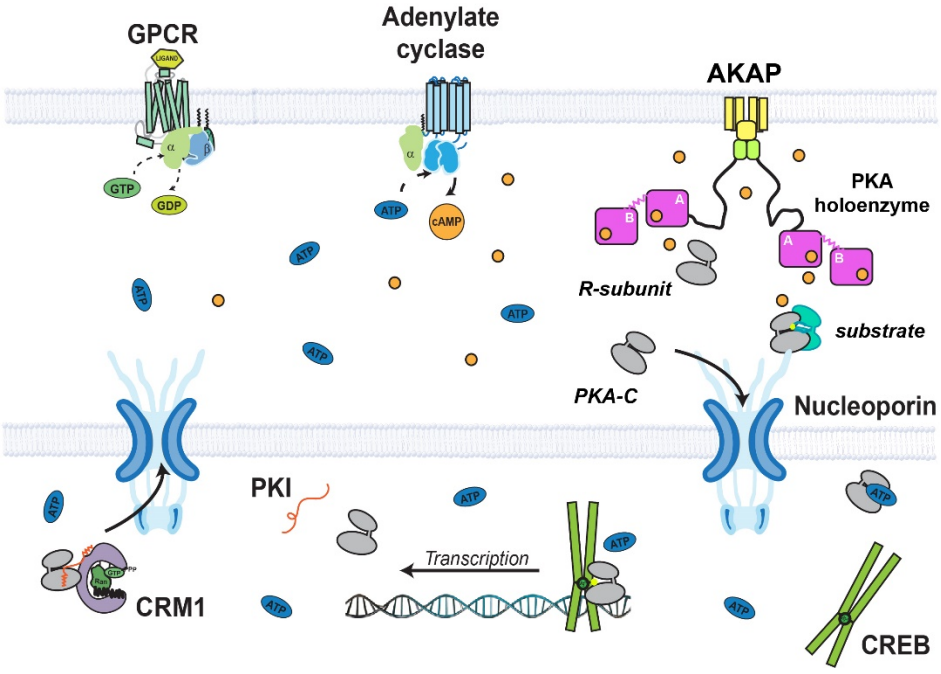

Figure 1.4. General cAMP signaling pathway.
Upon binding an extracellular ligand, a GPCR converts GTP to GDP triggering the intracellular increase in [cAMP] by adenylate cyclase. At high [cAMP], cAMP can bind to the regulatory subunits of PKA resulting in a conformational change and thereby releasing PKA-C to phosphorylate substrates. PKA-C is also able to translocate to the nucleus via a nucleoporin to phosphorylate transcription factors, such as CREB, to upregulate lipid metabolism and cell proliferation.

PKA inhibition and the restriction of cAMP fluxes occurs via several control points within the cAMP signaling pathway outlined above and through direct inhibition of PKA-C activity. Upstream of PKA, regulation occurs in the form of GPCR localization and desensitization, GTP hydrolysis, and cAMP hydrolysis by PDE, many mechanisms themselves involving feedback thanks to the concerted response of kinases,

phosphatases, and the UPS system within seconds to minutes. The resulting lower cAMP levels lead to a reformation of the PKA holoenzyme. On the other hand, direct inhibition of PKA-C activity can be achieved through interaction with the PKA inhibitor peptide (PKI)[57]. PKI is a heat stable endogenous peptide that is responsible both for inhibiting activity of PKA-C and exporting PKA-C from the nucleus. Two functional domains allow for these processes to occur including a pseudo-substrate recognition sequence and a nuclear export signal (NES)[58]. Importantly, this NES domain is masked prior to binding PKA-C and only upon interaction with PKA-C becomes visible[59]. Following binding to PKA-C, PKI undergoes an increase in helicity of the NES motif that is preparatory for nuclear export by the CRM1/RanGTP complex[60]. Another interacting partner responsible for restricting PKA-C activity is A-kinase interacting protein (AKIP1)[61]. Conserved amongst mammals, little is known about AKIP1 outside of its ability to retain and inhibit PKA-C in the nucleus via a nuclear localization sequence (NLS).

1.4 Conformational States and Dynamics of PKA

It is well established that proteins kinases are very flexible, undergoing significant conformational changes upon activation and throughout the catalytic cycle. Indeed, the flexibility of any protein has been shown to be critical for their functionality. X-ray crystallography has been used extensively to study a variety of kinases, while NMR has been used to study only a few including: PKA-C [47, 60, 62-71], extracellular receptor kinase 2 (ERK2)[72], cyclin-dependent protein kinase 2 (Cdk2)[73], p38 kinase[74-76], and Abl-kinase[77]. Perhaps the most studied of these though is PKA-C.

Extensive x-ray crystallographic studies of PKA-C have identified three major conformational states: open (apo-form), intermediate (binary, or nucleotide-bound form), and closed (ternary, or substrate/pseudo-substrate-bound form) (**Figure 1.5 panel A**) [34-36, 63, 78, 79]. These studies indicate that PKA-C, like other kinases, undergoes a closing motion upon binding nucleotide and pseudosubstrate/substrate and an opening motion following phosphorylation and release of substrate and nucleotide. While x-ray studies have identified discrete conformational states of PKA-C, NMR studies have allowed the conformational dynamics of PKA-C to be mapped. The μs-ms conformational dynamics of PKA-C were first mapped using the TROSY Hahn-Echo experiment[80]. These studies revealed that the kinase in the absence of nucleotide or pseudosubstrate/substrate is dynamic, but uncommitted to catalysis (**Figure 1.5 panel B**). Upon nucleotide binding the

kinase becomes more dynamic, undergoing significant conformational exchange in the μs to ms timescale in catalytically critical regions such as the glycine-rich, activation, DFG, and peptide positioning loop. Since nucleotide-bound enzyme is the preamble to substrate binding, the dynamic nature of this state is critical to substrate recognition. While the subsequent binding of substrate shifts the conformational equilibrium towards a closed state with persistent dynamics that correlate with the rate of catalytic turnover, the binding of pseudosubstrate, PKI_{5-24}, dramatically attenuates the dynamics of the enzyme, shifting the kinase to a dynamically quenched state. These results were later corroborated by thermocalorimetric data revealing that the binding of substrate is entropically-driven, while the binding of pseudosubstrate is enthalpically-driven.

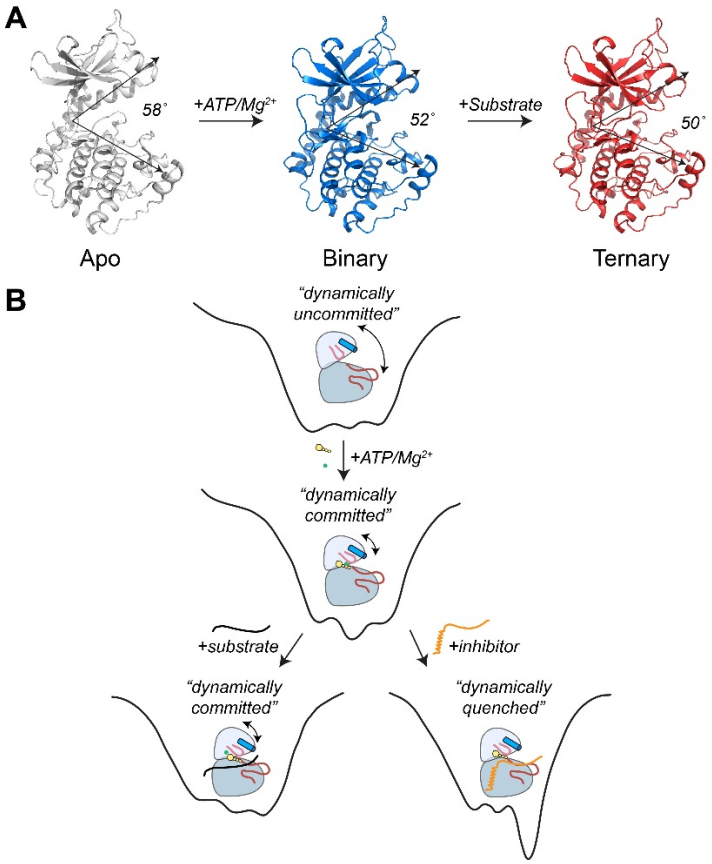

Figure 1.5. Structural transitions and energy landscape of PKA-C.
(**A**) The structural transitions of PKA-C upon binding nucleotide and (pseudo)substrate as depicted by their crystal structures. PDB ID: 1J3H (apo), 1BKX (binary), and 1ATP (ternary). (**B**) The conformational energy landscape of PKA-C upon effector binding. The apo enzyme is dynamically uncommitted sampling a large range of conformations in solution, while upon binding ATP the dynamics become synchronous ("dynamically committed"). Following the binding of substrate such as PLN, dynamics persist but are redistributed. Binding of inhibitor or pseudosubstrate such as PKI_{5-24}, the dynamics are quenched. Adapted from [80].

The importance of synchronous dynamics in catalysis was further underscored in the case of PKA-C mutant Y204A[70, 81, 82]. Y204A, distal to the active site, has been shown to be structurally indistinguishable from the wild-type kinase but exhibits substantial reductions in k_{cat}/K_M and k_{cat}. Indeed, μs to ms spin relaxation measurements indicate that Y204A obliterates synchronous motions present in the wild-type enzyme, motions essential for catalytic efficiency. Furthermore, in a follow-up study the dependence of synchronous dynamics was evaluated in the context of substrate binding[68]. Upon binding a cardiac substrate of PKA-C, phospholamban (PLN), catalytically critical elements of PKA-C remain dynamic, while the dynamics of other elements of PKA-C are attenuated. In contrast, when binding a mutant of PLN, R14del, PKA-C displays enhanced conformational dynamics in regions important for catalysis. More recent studies of PKA-C have focused on the role of conformational dynamics in the context of the catalytic cycle[83]. Using relaxation dispersion measurements, Wang and coworkers discovered that synchronous breathing motions of the kinase in the μs-ms timescale accompany positive binding cooperativity between ATP and substrate, meanwhile asynchronous dynamics drive the negative cooperativity between ADP and phosphorylated substrate. These studies and others have demonstrated that the conformational landscape of the kinase is modulated by changes in the dynamics of PKA-C which themselves are induced by ligand binding.

1.5 Chemical Mechanism of PKA-C

By far the best understood protein kinase from a mechanistic standpoint is PKA-C[84]. Reactions catalyzed by protein kinases require both ATP and substrate and are thus viewed as a bi-substrate kinetic mechanism. The first mechanistic study of PKA-C was performed by Cook *et al*. in 1982 in which a series of initial velocity measurements were performed using ATP and the standard substrate Kemptide with ADP and pKemptide acting as competitive inhibitors[85]. This study concluded that reactants bound in a random bi-bi mechanism, meaning the binding of either ATP or Kemptide does not occlude the binding of the other. Despite this, PKA-C still preferentially binds ATP first prior to substrate[86]. This has been substantiated by Whitehouse and Walsh[87] and more recently, NMR spectroscopic and thermodynamic methods which showed ATP has an order of magnitude higher affinity for apo PKA-C compared to Kemptide[82]. While the

majority of kinases undergo random kinetic mechanisms, there are numerous examples of kinases where ordered processes are observed.

As is a requirement for all protein kinases to perform catalysis, PKA-C contains two Mg^{2+} binding sites. In PKA-C the first Mg^{2+} is chelated between the β- and γ-phosphates and Asp184 in the activation loop. This is the primary Mg^{2+} binding site and binds under low concentration conditions. The second Mg^{2+} ion is located between the α- and γ-phosphates and Asp184 and Asp171, but binds only under high [Mg^{2+}] conditions. The involvement of Mg^{2+} during the catalytic cycle were recently elucidated using the high-affinity substrate derived from PKI_{5-24}, PKS_{5-24}. Recent crystal structures of PKA-C's Michaelis complex, partial phosphorylation complex and product complex have provided insights into the chemical steps of turnover by PKA-C[88]. While Mg^{2+} is present in both binding sites in the Michaelis complex and partial phosphorylation complex, Mg^{2+} was absent in the first site in the product complex. This suggests that the removal of Mg^{2+} is required prior to the release of ADP[89]. Overall, metal ions play a critical role in phosphoryl transfer and turnover, but the exact mechanism of involvement of metal ions is not conserved amongst protein kinases.

Further work on PKA-C dissected the rates associated with each step within the catalytic cycle. Using pre-steady-state quenched flow techniques at high [Mg^{2+}] revealed the that chemical step of PKA-C has a rate of k_{chem} = 500 ± 60 s^{-1}, while k_{cat} = 21 ± 1 s^{-1}[90]. These studies revealed that for low affinity substrates, as most are assumed to be, the phosphoryl transfer step is very rapid, while ADP release is the rate-limiting step. For high affinity substrates, such as PKS_{5-24}, ADP release was only partially the rate-limiting step[91]. At physiological [Mg^{2+}] and upon initiation of catalysis with ATP, studies have shown the chemical step is slightly attenuated in part due to a conformational change upon ATP binding that precedes phosphoryl transfer[92]. These same studies have shown a similar behavior during ADP release as a result of low [Mg^{2+}], highlighting the subtle role Mg^{2+} plays in catalysis. It is likely that the conformational changes observed under low [Mg^{2+}] are present under high [Mg^{2+}], but happen too fast to be observed. Moreover, NMR studies under high and low [Mg^{2+}] have shown changes in the conformational dynamics of PKA-C[80].

1.6 Relevance of PKA in Human Diseases

1.6.1 Cushing's Syndrome (CS)

A number of genetic defects have been associated with adrenal diseases including McCune-Albright syndrome[93], Carney complex[94-96], and more recently, Cushing's syndrome (CS)[26-29]. CS results from overproduction of cortisol either via endogenous (i.e. adrenocortical adenomas, bilateral adrenocortical hyperplasia, and cancer) or exogenous (i.e. steroids) means[97, 98]. The clinical picture of patients with CS is characterized by severe comorbidities including central obesity, hypertension, and metabolic abnormalities. Moreover, for CS patients prolonged hypercortisolism ultimately leads to increased morbidity and mortality due to cardiovascular, infectious, and other complications. While the molecular pathogenesis of other adrenal diseases has been thoroughly investigated, the underpinnings of CS was not well established until recently.

Indeed, in endocrine tissues, activation of the cAMP signaling pathway leads to increased function and replication of endocrine cells[99]. In normal physiology, adrenocortical cells are under tight regulation of cortisol secretion via the hypothalamic-pituitary-adrenal axis. Secretion of corticotropin-releasing hormone (CRH) stimulates the release of adrenocorticotropic hormone (ACTH) from the pituitary gland, in turn binding to the melanocortin-2 receptor (MCR2) and leading to the activation of adenylate cyclase. Following increases in intracellular cAMP, PKA activation stimulates glucocorticoid production thereby leading to increases in cortisol production via transcriptional induction of steroidogenic enzyme genes.

With the aim of identifying genetic alterations in patients with sporadic cortisol-secreting adrenocortical adenomas that produce Cushing's syndrome, whole exome sequencing was conducted by several groups. Beuschlein *et al.* discovered two mutations in the gene encoding the C-subunit of PKA (*PRKACA*) in nearly 30% of adrenocortical adenomas associated with overt Cushing's syndrome[28]. The most common mutation identified resulted in the substitution of a leucine residue at position 205 with arginine (L205R). The second mutation identified resulted in the insertion of a tryptophan residues between Leu198 and Cys199 (L198_C199insW). In vitro studies showed impaired inhibition of both mutants by R-subunits, causing constitutive activation independent of cAMP. Importantly, these mutations fall on residues that are highly conserved across species suggesting their key role in protein function.

The findings from this initial study were confirmed by various other independent studies[26, 27, 29]. Following these studies, additional papers in the proceeding years identified additional mutations including: C199_G200insV, S212R+insIILR, W196R, E31V, and d243-247+E248Q. Although less mutated than the common L205R mutation, all mutations involve amino acids that are located on the surface of PKA-C and at the interface with R-subunits. From analysis of the x-ray structure of the PKA-C:RIIβ holoenzyme, it was inferred that it was likely these mutations would interfere with the association with the R-subunits rendering PKA-C constitutively active.

Altogether these results demonstrate that *PRKACA* mutations are a main contributor to adrenocortical tumorigenesis, but *PRKACA* is not the only gene mutated in cortisol-producing adenomas. Activating mutations have been identified in the genes encoding G protein subunit α[26, 27, 29], phosphodiesterase 8B[100], and the regulatory subunit of PKA 1α[96], and catenin beta 1[101, 102], though at a lower frequency than PKA-C. In totality, the cAMP signaling pathway is highly mutated in CS, along with other metabolic disorders.

1.6.2 Fibrolamellar Hepatocellular Carcinoma (FL-HCC)

Fibrolamellar hepatocellular carcinoma (FL-HCC) is a rare and aggressive liver cancer that predominantly occurs in teenagers without a history of chronic liver disease[103, 104]. FL-HCC accounts for 1-9% of hepatocellular carcinoma (HCC) cases and is histologically characterized by large eosinophilic cells, prominent nucleloli, and intratumoral fibrosis. Symptoms of FL-HCC are often vague with patients presenting with no symptoms during the early-stage. As FL-HCC progresses, patients often have abdominal pain, malaise, nausea, weight loss, and present with a palpable mass in the abdomen. Formal diagnosis of FL-HCC requires histological confirmation along with immunohistochemical detection of anterior gradient-2, a highly specific protein for FL-HCC. Treatment for FL-HCC includes surgical resection, followed by transplantation. Common treatments for other cancers such as chemotherapy or radiation, are not successful. For patients who undergo resection the 5-year survival ranges from 50-70%, but when disease presents at a stage too advanced for resection, the 5-year survival rate is 0%.

PKA overexpression is associated with colon cancer, invasive breast carcinoma, and rectal adenocarcinoma, but more recently was linked to FL-HCC. In 2014, Honeyman

et al. identified a chimeric transcript expressed in FL-HCC and not in normal liver tissue that arises because of a ~400 kB deletion on chromosome 19[31]. The chimeric RNA codes for a protein that contains the amino-terminal domain of *DNAJB1*, which encodes a member of the heat shock 40 protein family, fused in frame to exons 2-10 of *PRKACA*. The chimeric fusion, *DNAJB1-PRKACA*, was detected in 15/15 FL-HCC samples, and had not previously been reported in the literature although was confirmed in Graham *et al*[32]. Indeed, these studies confirmed the RNA transcript was translated into a chimeric protein, from hereon referred to as PKA-C^{DNAJB1}, and retains full kinase activity when compared to wild-type PKA-C (PKA-C^{WT}). In patients with FL-HCC, the *DNAJB1-PRKACA* transcript is up-regulated. Further studies involving mice models have gone on to show that *DNAJB1-PRKACA* alone drives tumorigenesis in FL-HCC, and is not a result from enhanced *PRKACA* expression alone[105]. In addition to confirming *DNAJB1-PRKACA* is an oncogene, the authors show that the catalytic activity of the kinase domain is necessary and required for tumorigenesis.

Structurally, the kinase domain of PKA-C^{DNAJB1} adopts a near identical structure to the wild-type kinase upon binding nucleotide and PKI_{5-24}[106]. Superposition of PKA-C^{DNAJB1} and PKA-C^{WT} reveals that the N-terminal helix of the kinase is extended in PKA-C^{DNAJB1} with the DNAJB1 appendix adopting its canonical fold beneath the large lobe of the kinase core. Despite the additional appendix on the kinase, PKA-C^{DNAJB1} retains its ability to bind to both RI and RII regulatory subunits. Subsequent studies of PKA-C^{DNAJB1} have shown that the DNAJB1 appendix is quite dynamic adopting a variety of conformations in solution[64, 107]. Indeed, some studies have suggested that this domain alone is responsible for the recruitment of β-catenin[105] and Hsp70[108] and that this scaffolding function is involved in the oncogenic action of PKA-C^{DNAJB1}. Regardless, the exact molecular mechanisms of FL-HCC and the involvement of PKA-C^{DNAJB1} are still under debate and investigation.

1.6.3 Cardiac Myxomas (CM)

Tumors of the heart are rare with an incidence between 0.0017 and 0.19 percent although three quarters are benign[109]. Although rare, nearly half of the benign heart tumors are classified as cardiac myxomas (CM). CM occur in all age groups, but are most frequent between the third and sixth decades of life. Most CM occur sporadically, but are sometimes classified as ‘complex’ in the case that they are familial and in combination

with two or more of the following conditions: skin myxomas, myxoid fibroadenomas of the breast, pituitary adenomas, primary adrenocortical micronodular dysplasia with Cushing's syndrome, Carney complex, and testicular tumors. Derived from multipotent mesenchymal cells, CM usually develop in the atria, with a majority originating in the left atrium and to a lesser extent, the right atrium. Patients with CM exhibit symptoms including shortness of breath, dizziness, fainting, palpitations, and chest pain or tightness. Treatment of CM involves surgical removal and sometimes repair of patients' mitral valve. Although myxoma are not at risk for metastasis, complications are common. If left untreated CM can lead to embolisms, arrhythmias, and heart failure.

Multiple studies have investigated the pathogenesis of CM. Indeed, two-thirds of Carney complex-associated CM exhibit mutations in *PRKAR1A*, the gene encoding the protein kinase A type 1α regulatory subunit[110]. With the exception of a recent study, these mutations are only associated with familial CM, therefore leaving the pathogenesis of sporadic CM unknown. Recently one study by Tseng ***et al***. identified mutations, specifically insertions, in PKA-C associated with sporadic CM[111]. From Sanger sequencing of 41 CM specimens, mutations were identified in four (9.7%). In contrast to CS mutations, all CM associated mutations were in-frame microinsertions of 18-33 bp from exons 7 and 8. These in-frame microinsertions resulted in the following mutations: S212insTEYLAPEIILS, S212SLAPEIILS, S212insTVIILS, and L224insGYNKAVDWWAL. All mutations were located near the peptide positioning loop and adjacent to where substrate would bind. Biochemical characterization confirmed that all mutations enhanced the phosphorylation of substrates such as cAMP-response element binding protein (CREB) indicating each mutation elicited higher activity in comparison to the wild-type kinase. The authors of this study suggested that this was because the mutations interfered with the binding of PKA-C to the regulatory subunits. Since the initial publication identifying the in-frame microinsertions associated with CM, no studies have confirmed the existence or addressed the biochemical consequences of these mutations leaving many questions unanswered. Future studies will need to focus on the contribution of the cAMP signaling pathway in the pathogenesis of CM.

Chapter 2 An NMR Perspective on Intramolecular Allosteric Communication in PKA.

2.1 Introduction

Allostery is a fundamental biological regulatory mechanism characterized by the long-range coupling of remote sites within a molecular system, whereby allosteric effectors such as small molecules (*i.e.* inhibitors, activator) or binding partners (*i.e.* proteins, DNA, RNA) and post-translational modifications work to modulate protein function (Reviews on allostery: [1, 2, 112-115]). Despite the importance of allosteric regulation in most biological processes the molecular mechanisms underpinning allostery continue to be revised and remain largely uncharacterized. Classical biochemistry postulates that proteins exist in two states, commonly referred to as an active (R) state and inactive (T) state, and that interconversion between these states is modulated by allosteric effectors. Many models have been developed to explain allosteric effects including induced fit or conformational selection (population shift), sequential or concerted mechanism and evidence supports all[116-121]. Regardless, in their simplest view all models postulate that effectors modulate substrate binding affinity and/or enzymatic activity by inducing or stabilizing specific conformational states.

While early studies of allostery relied on crystallographic work providing a purely mechanical view based on structural changes induced upon binding allosteric effectors have been invaluable, more recent studies have highlighted the role of protein motions in mediating these long-range, structural changes. Indeed, the intimate link between these internal motions over a wide range of timescales and structure underlies a protein's function. In particular, NMR spectroscopy has been instrumental in exploring the different ways protein motions contribute to allosteric interactions (**Figure 2.1**) [17, 18]. In addition to providing structural information of biological systems in solution, NMR is highly sensitive to subtle changes in protein structure and dynamics providing unique information on the amplitude of motions taking place on a wide range of timescales and residue specific information.

In the following sections, I will discuss some of the major advances in solution-state NMR methods that have facilitated the characterization of allostery as applied to cAMP-dependent protein kinase A (PKA), as well as the role of several complementary techniques in elucidating allosteric networks. Furthermore, this review of NMR methods

to characterize allostery will showcase powerful experimental techniques used to elucidate the allosteric mechanisms of PKA-C.

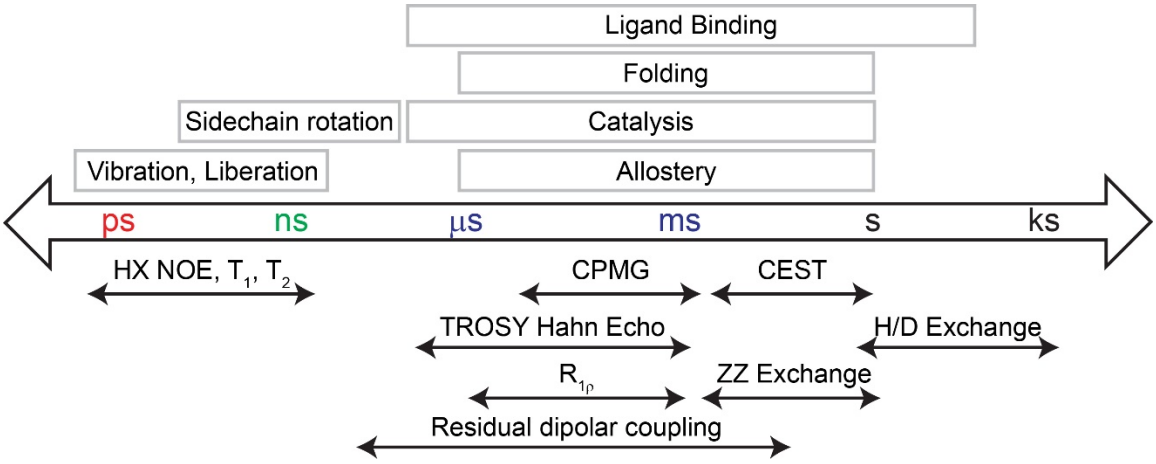

Figure 2.1. Timescales of protein motions and their corresponding NMR techniques. Schematic of the timescale for various protein motions (above) and the corresponding NMR experiments (below) to characterize them. Adapted from [18].

2.2 PKA as a Model Allosteric Enzyme

Regulation of protein function is critical in the careful control of virtually all cellular processes. Regulation can be exerted at various stages of a biomolecule's lifetime, including: regulation of gene transcription and translation, control of protein activation and degradation. Allosteric regulation is one of the many controls exerted to control the activity level of biomolecules, including enzymes.

PKA is one of the most well studied members of the AGC kinase family and has been a standard for years of research on kinase catalysis and allostery. In its resting state, PKA consists of two catalytic subunits (PKA-C) and two regulatory subunits. Upon binding cAMP, the regulatory subunits undergo a conformational change thereby releasing catalytically competent PKA-C. To date, groups have studied both the regulatory subunits and catalytic subunits in isolation. The catalytic subunit of PKA contains a small lobe composed of β-sheets and a large lobe composed of α-helices. The binding of nucleotide occurs within the small lobe, docking near the glycine-rich loop in the crevice between the small and large lobe, while the large lobe is responsible for binding substrate and regulatory subunits. Pioneering structural studies by Taylor and coworkers provided snapshots of major conformational states associated with PKA-C allostery using

nucleotide analogues, pseudosubstrates and inhibitors. On the basis of this data, Taylor and coworkers revealed a hinge-like conformational change associated with the binding of substrate and nucleotide and proposed an extensive allosteric network involved in substrate recognition and conversion. Indeed, the driving force of allostery in PKA-C relies on its intrinsic flexibility, as significant conformational changes within the kinase are observed locally and globally upon effector binding. Indeed, the interplay between structure and dynamics underlies the functions of proteins.

Along with conformational changes, extensive studies have shown how fast and slow conformational dynamics, conformational entropy, and intramolecular interactions contribute to allostery in the catalytic subunit of protein kinase A. Together these studies have shown PKA-C to be an elegant example of how classical (structure based) and modern (dynamic based) views of allosteric signaling merge. The following sections describe the studies undertaken to map the conformational dynamics and allosteric signaling of PKA-C using NMR in an effort to understand their role in enzymatic turnover and function.

2.3 H/D Exchange

The transitions of the kinase between different states involves both conformational and dynamic changes that propagate from the ligand binding sites to remote parts of the molecule. Indeed, a complete understanding of allosteric signaling required for this propagation necessitates the analysis of intra- and intermolecular interactions that hold a protein together such as hydrophobic packing, ionic interactions, hydrogen bonds, and Van der Waals forces. Among those interactions, hydrogen bonds have recently been shown to be critical in catalysis and inhibition. Traditionally, hydrogen/deuterium exchange mass spectrometry (DXMS) has been used extensively to analyze hydrogen bond networks of proteins to identify domains that might be involved in allosteric transitions, however, it lacks site-specific information[122]. Unlike DXMS, solution NMR spectroscopy monitors hydrogen/deuterium (H/D) exchange in a site-specific manner allowing for hydrogen bonds throughout the protein to be tracked at the atomic level.

To obtain residue-specific information about the hydrogen bond strengths and therefore insights into protein conformational dynamics and allow for the identification of long-range allosteric changes upon effector binding or mutations, Li and coworkers measured the H/D fractionation factors of PKA-C using solution NMR spectroscopy[69].

While H/D exchange traditionally requires the lyophilization of the protein under examination, equilibrium fractionation factors (φ) report directly on hydrogen bond strength and can be measured by incubating proteins in H_2O/D_2O solutions without lyophilization[123, 124]. Briefly, backbone amide fractionation factors of PKA-C were measured by incubating the kinase in aqueous solutions with D_2O concentrations ranging from 5% to 60% in three different forms: apo, ADP-, and ADP/PKI-bound. H/D equilibrium fractionation factors are defined as the equilibrium constant of following reaction:

$$NH:B + \frac{1}{2}D_2O \Leftrightarrow ND:B + \frac{1}{2}H_2O$$

where NH represents a weak acid and B a weak base. Following acquisition of a series of ^{1}H-^{15}N TROSY-HSQC's[125] on the three different forms of the kinase for all D_2O concentrations, fractionation factors were obtained by the linear least-squares analysis of the following:

$$\frac{1}{I} = C(\varphi\frac{1-x}{x} + 1)$$

where *I* is the peak intensity, *x* is the mole fraction of water, and *C* is the normalization parameter, which is the inverse peak intensity at 100% H_2O. Once measured and fit with the equation above, φ values report on the preference of each amide site in exchanging deuterium over protium. For amide sites that are involved in strong hydrogen bonds φ values are <1, whereas amide sites that are involved in weak hydrogen bonds φ values are >1[126].

Globally, upon binding nucleotide and pseudosubstrate and undergoing the transition from the open to closed conformation, the average φ values decrease (**Figure 2.2**). This decrease suggests a strengthening of the intramolecular hydrogen bonds and are consistent with X-ray crystallography[42], NMR spectroscopy[82], fluorescence[127, 128], thermodynamic and DXMS analyses[122] which have previously shown the structure of PKA-C becoming more compact and closed upon nucleotide and pseudosubstrate binding. Furthermore, the changes in hydrogen bond strength upon the binding of effectors are not localized to the binding site, rather they are pervasive throughout the entire protein. Upon binding ADP, hydrogen bonds are strengthened both in the N-lobe and C-lobe, while subsequent binding of pseudosubstrate strengthens hydrogen bonds located primarily in the large lobe. Moreover, these studies revealed that the hydrophobic core is more

resistant to deuterium exchange upon effector binding, consistent with the rigidification of the core.

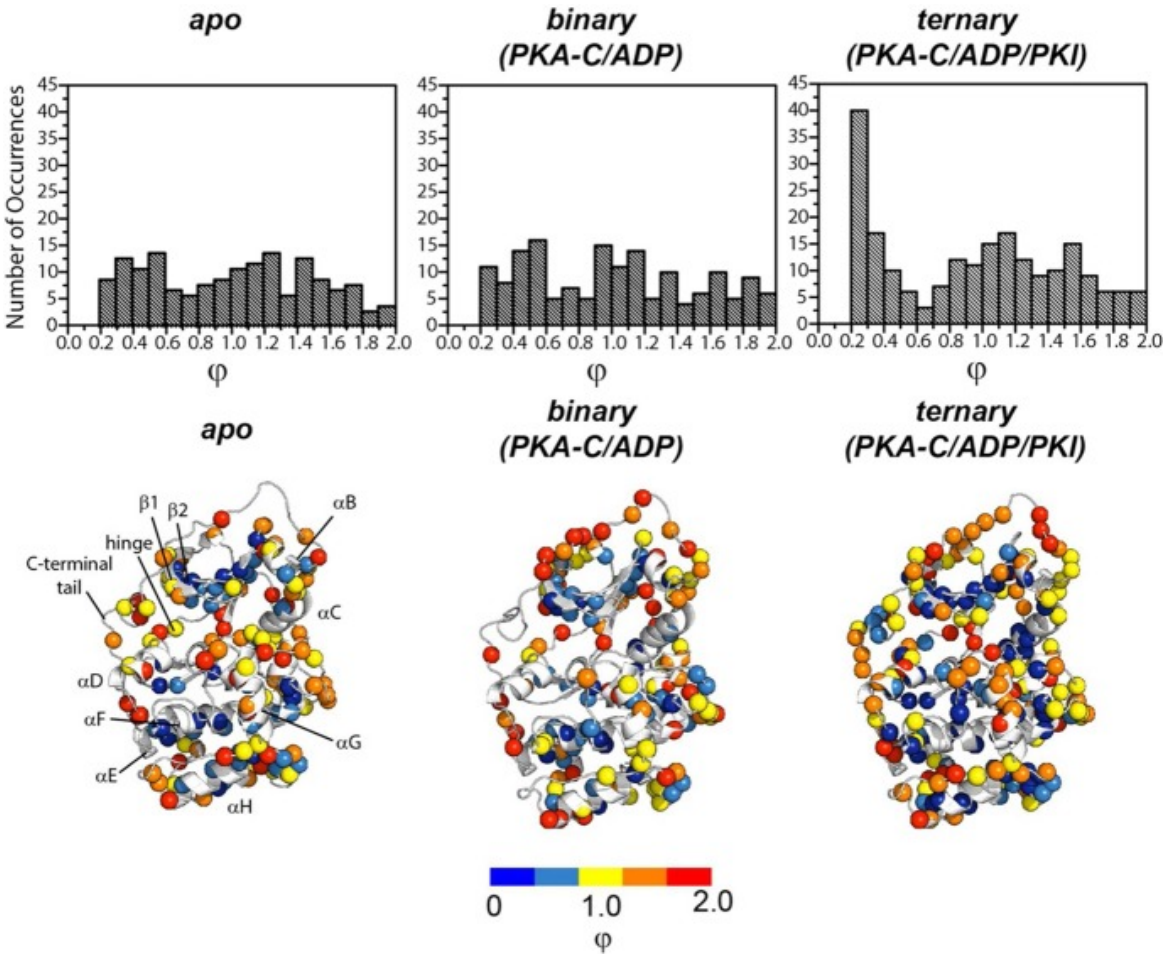

Figure 2.2. Distribution of amide fractionation factors for apo, ADP-bound and ADP/PKI-bound PKA-C.
The distribution of amide fractionation factors for apo, ADP-bound, and ADP/PKI-bound PKA-C. Histogram displays the number of occurrences vs fractionation factor values for each state, while fractionation factors are mapped onto the structure of PKA-C. Blue spheres correspond to strong hydrogen bonds and high φ values, while red spheres correspond to weak hydrogen bonds and low φ values. Figure reprinted with permission from [69] and can be found at the following link: https://pubs.acs.org/doi/10.1021/acs.biochem.5b00387. Copyright 2015 Biochemistry.

Overall these studies on PKA-C revealed that changes in the allosteric network of the kinase are manifested through variations in hydrogen bond strengths. While these changes are not uni-directional, they provide a residue specific view of allosteric communication within proteins and enzymes. H/D fractionation factors emerge as an important complement to other NMR parameters to characterize protein conformational dynamics and to identify long range allosteric changes upon ligand binding or mutations.

2.4 Chemical Shift Perturbation

Of the NMR methods for monitoring changes in an allosteric system, perturbation of chemical shifts is the most straight-forward. NMR-active nuclei are highly sensitive to alterations in local chemical and structural environment and thus provide invaluable information regarding conformational changes and interactions with effectors. Chemical shifts are especially useful for measuring populations of states in the fast chemical exchange timescale. The simplest case involves an enzyme that interconverts between two states referred to as T- and R-states (nomenclature used from hereon). The expression representing this interconversion is given by the following equation:

$$\delta_{obs} = p_R\delta_R + p_T\delta_T$$

Where the observed chemical shift (δ_{obs}) is a population weighted average of the T- and R-states, $p_{R/T}$ are the equilibrium populations of each state, and $\delta_{R/T}$ are the chemical shifts of each state. Importantly, this expression is only valid for fast exchange between the two states. Thus, changes in chemical shift in any allosteric system can be representative of the equilibrium shift between conformations. Powerful methods to decode the allosteric information embedded in chemical shift changes have been introduced by Melacini and coworkers[129-132], McDermott and coworkers[133], and more recently, Dokholyan and coworkers[134].

Studies on the allostery of PKA-C began with atomic-resolution mapping of the backbone of PKA-C by Masterson and coworkers[82]. This study represented the first picture of the changes occurring during the transition from apo to intermediate and from intermediate to closed conformations. From chemical shift perturbation (CSP) measurements, it was apparent that PKA-C is dynamic, interconverting between multiple dynamic or conformational states as evidenced by exchange broadening of highly conserved residues. Moreover, the characterization of PKA-C by NMR revealed that the kinase exhibits positive cooperativity for ligand binding, such that the binding of nucleotide increases the affinity of subsequent (pseudo)substrate binding. To test the existence of an allosteric network that facilitates the positive cooperativity of ligand binding, Masterson and coworkers mutated Tyr204 to Ala (Y204A). Indeed, this single point mutation caused disruptions of the allosteric network as evidenced by CSP and the reduction in binding cooperativity (**Figure 2.3**). Specifically, Y204A caused an overall rearrangement of the allosteric communication between the two lobes of the kinase upon nucleotide binding and

an interruption of this communication upon substrate binding as deduced from CSP measurements. Additional MD studies and dynamics studies on PKA-C^{Y204A} have further highlighted the altered allosteric communication and will be discussed further in the following sections 2.5 and 2.6.

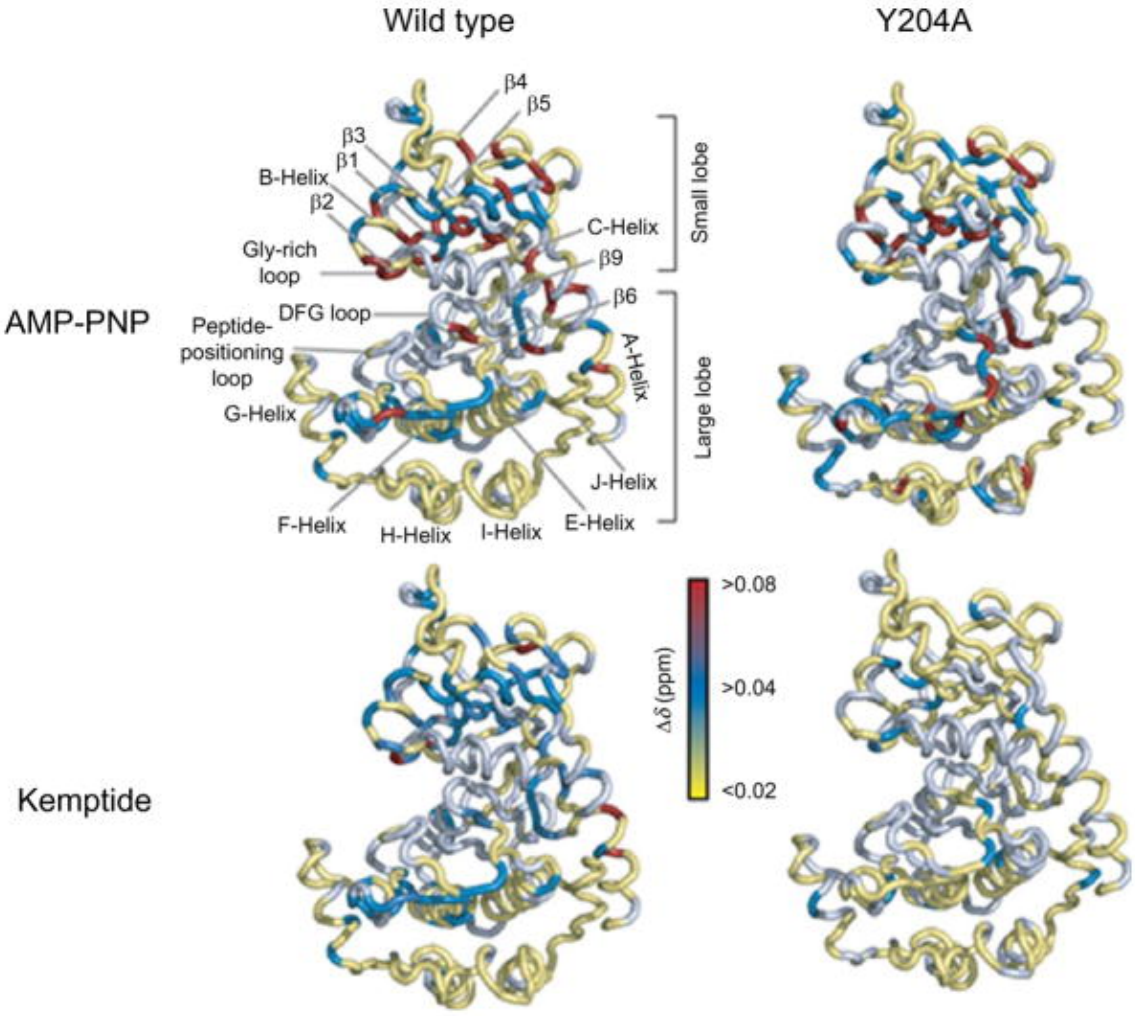

Figure 2.3. Chemical shift perturbations upon ligand binding for PKA-C^{WT} and PKA-C^{Y204A}. Upon binding both nucleotide and substrate, Kemptide, PKA-C^{Y204A} experiences attenuated local and allosteric perturbations. Reprinted with permission from [135]. Copyright 2012 Elsevier.

Following the initial characterization of chemical shift perturbations upon nucleotide and (pseudo)substrate binding[82], recent studies of PKA-C have focused on mapping the allosteric network of PKA-C[83] and its associated mutations[65, 107]. In a powerful method introduced by Melacini and coworkers, CHEmical Shift Covariance Analysis (CHESCA) uses statistical comparative analyses of NMR chemical shifts elicited

by selected effectors to identify patterns of chemical shift perturbations[129]. This method is governed by two assumptions: first, subtle but functionally relevant structural changes that underlie allosteric modulations of dynamics are effectively probed by measuring NMR chemical shift variations; and second, when a system is subjected to a set of perturbations, residues that belong to the same allosteric network exhibit concerted responses in response to the effector set. Perturbations to the collective response of residues or the allosteric network may arise from mutations, modifications of the effector, and binding partner. Briefly, after assigning the spectra for each state from the perturbation library, a combined chemical shift (CCS) is computed for each residue which represents the weighted contributions from the ppm values of the amide proton and nitrogen. Next, a correlation matrix is generated containing residue numbers and a Pearson's correlation coefficient between every two residues contained in the matrix. Generally, Pearson's correlation coefficients greater than 0.98 will be used to map onto a 2D matrix of residue number vs residue number for visual evaluation of allosteric networks. In addition to generating a correlation matrix, CHESCA allows for agglomerative clustering in order to define functional clusters of coupled residues using dendrograms. Nonetheless, this method has been successfully applied to various systems including exchange protein activated by cAMP (EPAC)[129, 136], α-subunit of tryptophan synthase[137, 138], cystic fibrosis transmembrane conductance regulator[139], and PKA-C[65, 83].

To map the site-specific allosteric changes during the catalytic cycle of PKA-C, Wang and coworkers used CHESCA on the methyl groups of the kinase[83]. Indeed, mapping the allosteric network of PKA-C over the reaction coordinate suggested that both nucleotide and substrate binding bring together important catalytic motifs and organize the active site for catalysis in a cooperative manner. These studies further emphasized the concerted structural changes necessary for ligand binding and release as first captured by x-ray crystallography.

Since perturbations to the allosteric network of a protein often arise from mutations, additional studies of PKA-C focused on the impact of point and in-frame fusion mutations in PKA-C[65, 107]. In a first-of-its-kind study, our group used solution NMR to map the allosteric network of a point mutation associated with Cushing's syndrome in order to gain mechanistic insights into the mutation's multifarious effects[65]. Previous studies of this particular point mutation, L205R, suggested that regulation was disrupted on the basis of

an inability of PKA-C^{L205R} to bind to regulatory subunits. Additionally, phosphoproteomic studies revealed dramatic changes in the phosphorylation profile of the kinase. Using CHESCA, we found that L205R disrupts the internal allosteric communication of the kinase, preventing the kinase from reaching a fully closed state, reducing the enzymes affinity for both nucleotide and (pseudo)substrates and thus hindering endogenous regulation (see Chapter 4). Notably, these studies showed that while this was true for canonical substrates, non-canonical substrates identified by phosphoproteomic analyses exhibited the opposite. Indeed, for non-canonical substrates, PKA-C^{L205R} exhibited a higher catalytic efficiency and a rearrangement of the internal allosteric network. Together, these results indicated that a rewiring of the internal allosteric network and global changes in dynamics contribute to the complex dysfunction of the signaling network of PKA-C^{L205R} (**Figure 2.4**).

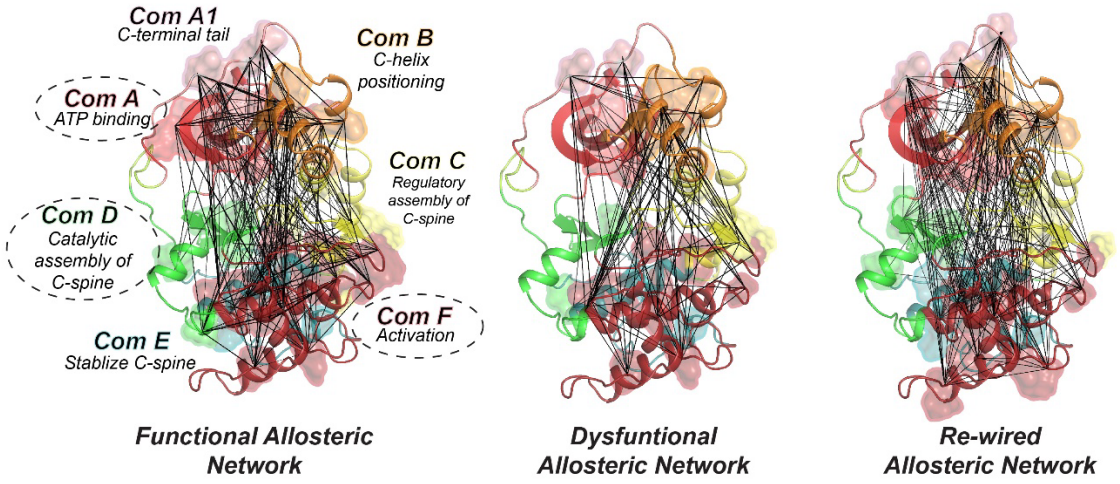

Figure 2.4. Cushing's syndrome somatic mutation disrupts the allosteric network of PKA-C to elicit dysfunction.
CHESCA correlation matrices for PKA-C^{WT} + PKI, PKA-C^{L205R} + PKI, and PKA-C^{L205R} + VPS36, respectively, plotted on the structure of PKA-C with colors to match previous community map analyses [140]. Adapted from [65]. Copyright 2019 American Association for the Advancement of Science.

Further studies on how mutations disrupt the allosteric network of PKA-C have followed this initial study as pertaining to fibrolamellar hepatocellular carcinoma (FL-HCC)[107]. It is well established that FL-HCC is driven by the gene fusion between heat shock protein 40 (*DNAJB1*) and *PRKACA*. Structurally this fusion protein (hereon referred to as PKA-C^{DNAJB1}) results in an extended αA-helix with the J-domain of *DNAJB1* tucked under the large lobe of the kinase, while the kinase core is virtually identical to the wild-

type enzyme[106]. Despite the little differences in structure, it has remained unclear how this kinase contributes to the progression of FL-HCC. Using CHESCA analyses coupled with thermodynamic experiments, Olivieri and coworkers found that similar to PKA-C^{L205R}, the dynamic J-domain of PKA-C^{DNAJB1} re-wires the intramolecular allostery of the kinase[107]. Concomitant with the disruption in allosteric network, PKA-C^{DNAJB1} attenuates the canonical positive cooperativity between nucleotide and (pseudo)substrate. Indeed, reductions in both intramolecular allostery and binding cooperativity have been exhibited for other Cushing's syndrome, further solidifying the link between allostery and cooperativity[141].

2.5 Slow Timescale Motions (μs-ms)

Any type of long-distance signaling, otherwise termed allostery requires signal transmission; however, mechanisms can vary widely. In general, transmission of signal can occur in two different manners: 1) a sequential set of events propagated from the allosteric site to the active site or by 2) modification of the dynamics of the protein. Originally, both models assumed large conformational changes, but that has since been challenged by Cooper and Dryden[142] and confirmed in studies of calmodulin[143], PDZ domains[144], and the catabolite activator protein[145]. Several of the most critical functions of biomolecules occur in the μs-ms timescale, including but not limited to allostery, catalysis, folding, and ligand binding. The experiments used to probe protein dynamics over this timescale are often referred to as relaxation dispersion NMR and include: TROSY Hahn-echo, Carr-Purcell-Meiboom-Gill (CPMG), Chemical exchange saturation transfer (CEST). Indeed, when used in conjunction with one another, these experiments provide a near complete picture of the processes governing enzyme function having been successfully applied to systems to examine ligand binding, protein motions, enzymatic catalysis, and protein folding.

Veglia and coworkers have used NMR extensively to characterize the role of μs-ms conformational motions in substrate recognition and the binding of inhibitors or pseudosubstrates. Indeed, the methods of characterization mentioned in the preceding paragraph have been successfully applied to various systems[146-150]. First characterizing the role of slow timescale motions in substrate recognition, Masterson and coworkers measured the transverse relaxation (R_{ex}) rate of the backbone of PKA-C using the TROSY Hahn-Echo experiment[67]. The authors observed very little conformational

exchange in the absence of nucleotide and substrate, while synchronous motions specifically in the residues surrounding the active site are promoted upon nucleotide binding (**Figure 2.5**). Subsequently, upon binding of a substrate of PKA-C, phospholamban (PLN), the dynamics of PKA-C are redistributed, but persist around the active site of the kinase. Importantly, these dynamics occur on the same timescale as the rate-determining step of enzyme turnover. Together these μs-ms conformational dynamics proceed through continuous paths throughout the active site, while simultaneously occurring in remote regions of the enzyme, underscoring the complexity of the allosteric network of PKA-C. Furthermore, these initial studies highlighted the importance of well-tuned dynamic interplay between enzyme and substrate to maintain optimal catalysis. In a follow-up study, Masterson and coworkers looked at these slow timescale motions upon binding inhibitors[80] and compared them to what was observed for the binding of substrate. Using the TROSY Hahn-Echo experiment, the authors observed that pseudosubstrate PKI_{5-24} and excess Mg^{2+}, which acts as a noncompetitive inhibitor to PKA-C[151], restrict the slow timescale conformational dynamics of the kinase. These studies led to the finding that inhibitor binding modifies the energy landscape of the kinase in a manner different from substrate by restricting the motions of the enzyme backbone. Uniquely, these studies together highlight the role of dynamics in modulating active vs inactive sites, as oppose to the structural motifs alone.

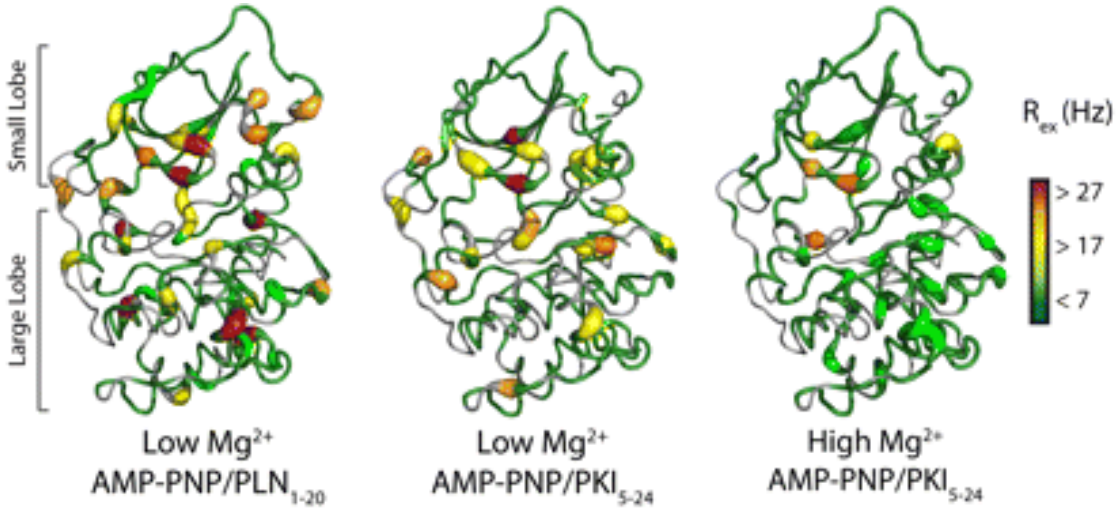

Figure 2.5. Slow timescale backbone dynamics of PKA-C in different ternary complexes. Adapted from [80]. Copyright 2011 National Academy of Sciences, U.S.A.

In a follow up study, Kim and coworkers sought to determine how substrates alter the conformational dynamics of the kinase[68]. For these studies, authors compared canonical substrate, PLN, to a lethal variant R14del (PLN^{R14del}) linked to familial dilated cardiomyopathy. Measuring the R_{ex} values from the TROSY Hahn-Echo experiment, authors found striking differences in the conformational dynamics between wild-type PLN and PLN^{R14del}. Upon binding PLN, PKA-C experiences attenuated dynamics when compared to the binding of nucleotide; whereas, for the binding of PLN^{R14del} PKA-C experiences enhanced conformational dynamics particularly in regions essential for catalysis (**Figure 2.6**). Importantly, these enhanced conformational dynamics contribute to a reduction in binding affinity, cooperativity, and turnover towards PLN^{R14del}. Ultimately the deletion of R14 disrupts the intermolecular interactions between the enzyme and substrate, augmenting the conformational dynamics involved in the opening and closing of the active site and enzyme turnover. These monumental studies introduced the concept that dysfunctional conformational dynamics of biomolecules may result in pathological phenotypes via alterations in dynamic allostery.

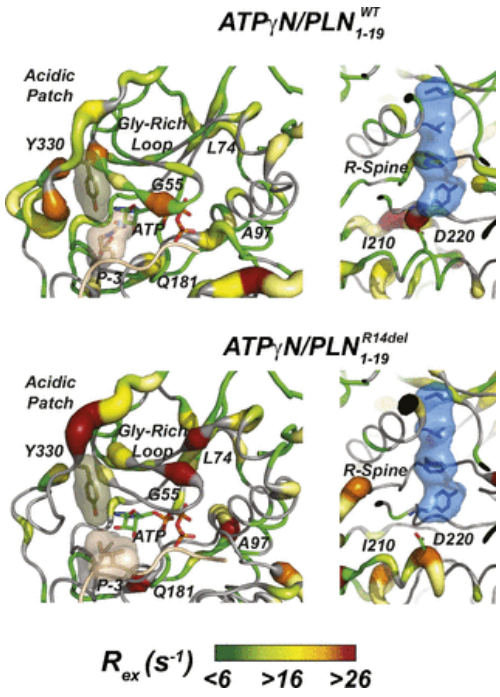

Figure 2.6. Allosteric changes in conformational dynamics of PKA-C^{WT} upon binding PLN (top) or PLN^{R14del} (bottom).
Slow conformational dynamics plotted on the X-ray crystal structure of PKA-C. Upon binding PLN^{R14del}, PKA-C experiences an increase in conformational dynamics. Reprinted with permission from [68]. Copyright 2015 National Academy of Sciences, U.S.A.

It has been postulated that the switch between active and inactive states depends on the structural architecture of the conserved hydrophobic spines. The assembly of both the C- and R-spine are highly regulated, with the assembly of the R-spine requiring phosphorylation of the activation loop (T197) and the C-spine requiring ATP binding. Once assembled, the kinase can bind substrate cooperatively. How the C- and R- spine orchestrate the transition between active and inactive states was investigated by Kim and coworkers[66]. To assess the contribution of slow timescale conformational dynamics to catalysis, authors probed the structural fluctuations of the methyl sidechains of PKA-C using CPMG experiments. From CPMG relaxation dispersion curves, one is able to determine the transverse relaxation rate (R_{ex}), the kinetics of exchange (k_{ex}), and the populations of the conformational equilibrium. In the absence of nucleotide or (pseudo)substrate, the kinase shows significant R_{ex} values for several residues located in the hydrophobic core, the C-spine (V57 and L172), the R-spine (L95), the R-spine shell (V104), along with residues bridging the two spines (L167, I180 and I150). Dispersion curves are unable to be globally fit, suggesting the motions of the apo enzyme core are asynchronous. Nucleotide binding attenuates R_{ex} values throughout the enzyme and can be fit globally to extract an exchange rate constant (k_{ex}) of 2500 ± 300 s^{-1} suggesting the motions of the nucleotide-bound kinase become synchronous. In agreement with previous studies[67, 80], upon binding substrate slow timescale dynamics persist, while pseudosubstrate binding abrogates most of the conformational exchange. To verify the importance of the residues in conformational exchange in the allosteric network, authors mutated two highly conserved residues (V104 and I150) that experience large R_{ex} values. Upon mutation, that kinase no longer is auto-phosphorylated at T197 and retains no activity confirming their importance in intramolecular allosteric signaling. These studies underscore the importance of assembled R- and C- spines with PKA-C displaying uncorrelated motions when either is disassembled, as is the case for apo PKA-C.

2.6 Fast Timescale Motions

As allostery is thermodynamic by nature, a manner in which protein motions can modulate allostery is through conformational entropy. Recent advances in NMR have allowed the fast timescale motions of various systems to be characterized to reveal how changes in these motions can alter allosteric signal via changes in binding affinity. Although multiple NMR methods including HX NOE, T_1, and T_2 experiments probe fast timescale dynamics, this section will place a particular emphasis on the role of protein

motions in modulating allostery via conformational entropy using relaxation violated coherence transfer cross-correlation experiments.

Recently, Veglia and coworkers have used NMR to extensively characterize the role of fast timescale motions in catalytic turnover. The method used in the proceeding paragraphs to characterize ps-ns motions have been successfully applied to various systems including the proteasome[152], metalloproteins[153], and calmodulin[143, 154]. It is well established that both experimentally and computationally allosteric cooperativity can be modulated by changes in conformational motion. Wang and coworkers sought to understand the role of conformational entropy in the kinases enzymatic cycle, particularly in relation to the allosteric cooperativity of PKA-C that is well established[83]. The conformational entropy was determined by measuring the ps-ns dynamics of methyl groups using relaxation violated coherence transfer cross-correlation experiments.

Using rotational correlation times obtained by dynamic light scattering, methyl group order parameters methyl-bearing side chains were measured. Similar to slow timescale dynamics measurements, authors observed an overall rigidification upon nucleotide binding. Upon binding the substrate PKS_{5-24} (shares the sequence of PKI_{5-24} with a serine at the p-site), the conformational dynamics throughout the entire kinase increase (**Figure 2.7**). For the portion of the catalytic cycle following phosphorylation, a reverse, correlated trend is observed. Taken together, the conformational dynamics data indicate the nucleotide binding to PKA-C synchronizes the motions, while asynchronous motions in the second portion of the enzymatic cycle are critical in destabilizing the intramolecular dynamic network to enable product release. This study and others suggest that if the motions of groups of two allosteric sites are coupled, the binding of one site would change the distribution of competent or non-competent states on the other site, thereby modulating positive and negative cooperativity, respectively. Moreover, these and other studies suggest that by altering the conformational dynamics of a protein or disrupting the allosteric coupling of the motions, a kinases function can be manipulated to affect signaling.

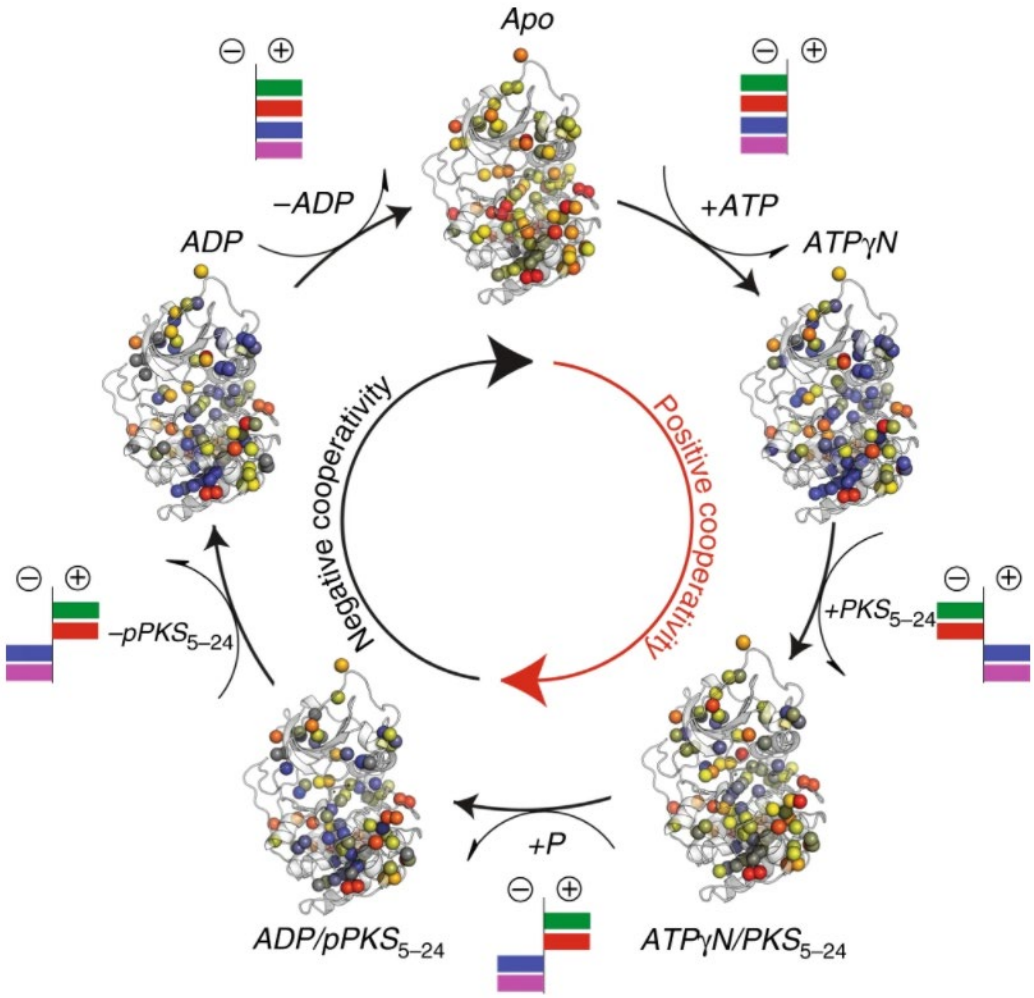

Figure 2.7. Changes in the conformational entropy of PKA-C during the enzymatic cycle. Methyl group O^2 values obtained for the different ligated forms of PKA-C. Values are plotted with a color gradient from the most rigid (blue) to the most mobile (red). Additionally, total free energy (green), enthalpy (red), entropy (blue) values as obtained from ITC measurements are indicated for each transition. Reprinted with permission from [83]. Copyright 2019 Springer Nature.

2.7 Concluding Remarks

Allostery has been intensely studied since it was originally described decades ago, though few systems have been studied as extensively as protein kinase A. The detailed mechanistic studies provided here showcase powerful experimental techniques used to elucidate intramolecular allostery, while at the same time offering monumental insights into the role allostery plays in enzymatic function. Indeed, insight gained from NMR can be especially helpful when combined with other experimental techniques. Additional methods including modern computational methods, although not described here in detail,

can provide another perspective on enzyme allostery. Despite decades of research, experimental and computational tools continue to challenge the notions we have of enzyme allostery and to provide novel perspectives.

Chapter 3 Probing Protein-Protein Interactions Using Asymmetric Labeling and Carbonyl-Carbon Selective Heteronuclear NMR Spectroscopy.

Erik K. Larsen[1], Cristina Olivieri[2], Caitlin Walker[2], Manu V.S.[2], Jiali Gao[1], David A. Bernlohr[2], Marco Tonelli[3], John L. Markley[4], and Gianluigi Veglia[1,2a]

[1]*Department of Chemistry, University of Minnesota, Minneapolis, MN 55455, USA.*

[2]*Department of Biochemistry, Molecular Biology, and Biophysics, University of Minnesota, Minneapolis, MN 55455, USA*

[3]*National Magnetic Resonance Facility at Madison, Madison, WI 53706, USA.*

[4]*Department of Biochemistry, University of Wisconsin-Madison, Madison, WI, 53706, USA.*

Reprinted from *Molecules* 23(8).

3.1 Synopsis

Protein-protein interactions (PPIs) regulate a plethora of cellular processes and NMR spectroscopy has been a leading technique to characterize them at the atomic resolution. Technically, however, PPIs characterization has been challenging due to multiple samples required to characterize the hot spots at the protein interface. Here, we review our recently developed methods that greatly simplify PPI studies, minimizing the number of samples required to fully characterize residues involved in the protein-protein binding interface. This original strategy combines asymmetric labeling of two binding partners and the carbonyl-carbon label selective (CCLS) pulse sequence element implemented into heteronuclear single quantum correlation (^{1}H-^{15}N HSQC) spectra. The CCLS scheme removes signals of the J-coupled ^{15}N-^{13}C resonances, recording simultaneously two individual amide fingerprints for each binding partner. We show the application to the measurements of chemical shift correlations, residual dipolar couplings (RDCs) as well as paramagnetic relaxation enhancements (PRE). These experiments open an avenue for further modifications of existing experiments facilitating the NMR analysis of PPIs.

3.2 Introduction

Biological processes rely primarily on protein-protein interactions (PPIs) to mediate cellular function [155]. Historically biochemical techniques (co-immunoprecipitation, yeast-two hybrid, pull-down assays, etc.) measuring parameters intrinsic to the whole complex have been used to characterize these PPIs [156, 157]. Recently, advances in nuclear magnetic resonance (NMR) spectroscopy have provided the means to characterize PPIs at atomic resolution, offering fine details of individual macromolecules participating within the complex [158-160]. In addition to allowing the characterization of these complexes at atomic resolution, NMR is well suited for studying dynamic, transient (~100 μM K_D), and lowly populated states of complexes [161-163].

The mapping of PPIs using several observables such as chemical shift perturbation (CSP), residual dipolar couplings (RDC), intra- and inter-molecular as well as solvent paramagnetic relaxation enhancement (PRE) [164-166], cross-saturation (CS), and nuclear Overhauser effects (NOEs) has been well established [159]. These methods nevertheless fall short when studying large complexes due to the inherent attenuation of transverse relaxation times (T_2) resulting in a reduction of both signal intensity and resolution. Despite methods such as TROSY [167], deuteration [168, 169], and selective labeling [170, 171] addressing these concerns, multiple samples are still required to distinguish one species from another. Recently, several new NMR experiments based on simultaneous, interleaved detection of up to three NMR active species with distinct isotopic labeling have provided the opportunity to map the effect of PPIs on individual components within a macromolecular complex. While there are outstanding reviews on protein-protein interactions [172-178], here we focus on our recently developed method that exploits spin-echo filtering-based experiments with strategic protein labeling schemes to characterize protein-protein complexes.

3.3 Results

3.3.1 Mapping two binding partners fingerprints simultaneously.

Traditional approaches to map PPIs at an atomic level involve repeat experiments with reverse labeling patterns such that the interaction is probed from both binding partners. Prior to the introduction of the spin-echo filtering experiment by Bax *et al.* [179], three-bond homonuclear ^{1}H-^{1}H *J* couplings had been used to derive backbone and side-

chain conformational restraints [180-185]. This new experiment relied on measuring the magnetization loss due to unresolved *J* coupling and utilized an interleaved detection method, where two spectra are recorded simultaneously, but differ by 180° pulse positions on the ^{15}N channel. The spin-echo filtered experiment introduced by Bax is the building block for the Carbonyl Carbon Label Selective (CCLS) ^{1}H-^{15}N HSQC pulse sequence [186], which requires specific isotopic labeling to simultaneously map the chemical shift perturbations from two binding partners. The CCLS ^{1}H-^{15}N HSQC pulse sequence utilizes spin-echo filtering with a short magnetization transfer period between ^{15}N and $^{13}C'$ in order to detect ^{1}H-^{15}N correlations adjacent to the NMR inactive ($^{12}C'$) carbonyl groups (**Figure 3.1 panel A**). Building on the constant time (CT) HSQC, the CCLS ^{1}H-^{15}N HSQC necessitates the acquisition of two spectra, a reference spectrum and a suppression spectrum, in an interleaved manner. The reference spectrum is acquired using the pulse sequence reported in **Figure 3.1 panel A**, with the 180° pulse on $^{13}C'$ during the ^{15}N CT evolution period applied at position *a* as proposed by Vuister *et.al*. [179], allowing for the removal of $^{13}C'$-^{15}N coupling. The suppression spectrum is acquired with the 180° $^{13}C'$ pulse at position *b*, leaving ^{13}C-^{15}N *J* coupling active and converting the transverse in-phase magnetization of ^{15}N spins linked to $^{13}C'$ to antiphase magnetization. This antiphase magnetization contains components in both the *x*- and *y*-direction. The π ^{1}H and ^{13}C pulses appliedat the end of the ^{15}N evolution convert the *y*-component, $4H_zN_yC'_z$, to an unobservable multiple quantum coherence, $4H_yN_zC'_y$, while the *x*-component, $4H_yN_zC'_y$, is dephased by the G2 gradient (**Figure 3.1 panel A**). As a result, signals from ^{1}H-^{15}N groups coupled to $^{13}C'$ are suppressed, while signals from ^{1}H-^{15}N groups coupled to $^{12}C'$ are unaffected. The suppression spectrum can then be subtracted from the reference spectrum leaving the U-^{15}N, ^{13}C species observable (**Figure 3.1 panel B**).

We tested the sensitivity of the CCLS method by comparing a reference CCLS-HSQC spectrum and a conventional HNCO spectrum of the 20-kDa protein U-^{13}C, ^{15}N-Ubiquitin at 10, 20, 30, and 40°C corresponding to average T_2 values of 27, 33, 40, and 47 ms, respectively [186]. The slower tumbling rates at lower temperatures lead to longer rotational correlation times (τ_C) and faster relaxation resulting in broader linewidths. We found the reference CCLS-HSQC experiment was more sensitive compared to the HNCO experiment for lower temperatures, demonstrating that the shorter time delay (T_{NC}) allows for increased sensitivity for large proteins or protein-protein complexes. The sensitivity

enhancement gained from optimal T_{NC} values compensates for the decrease in S/N observed upon subtraction of the suppression spectrum from the reference spectrum.

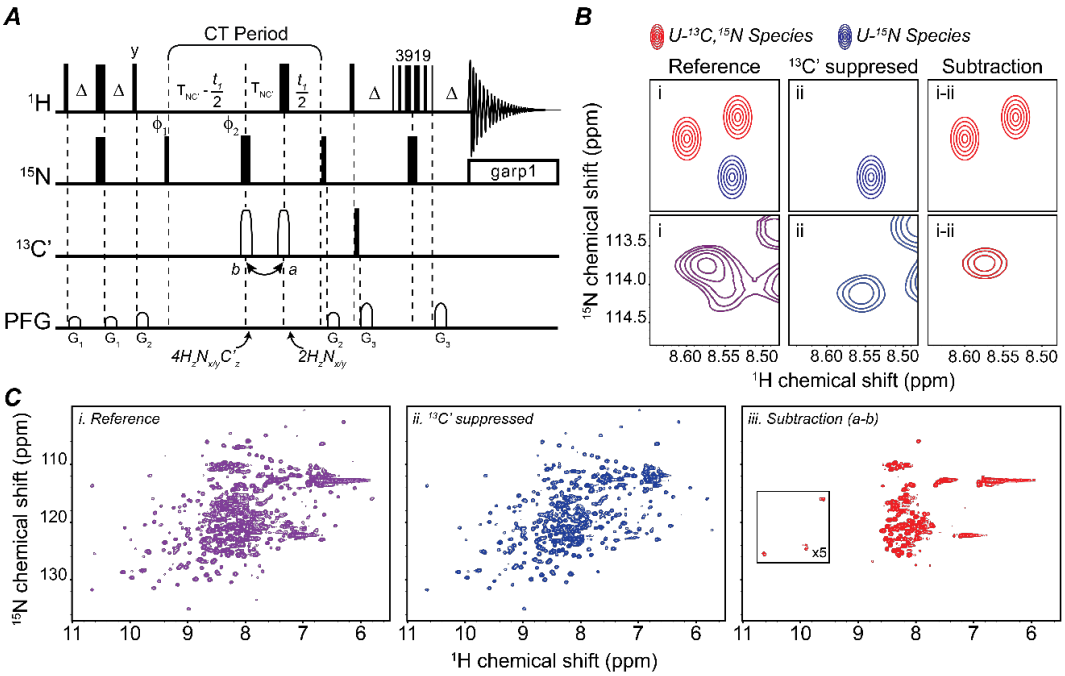

Figure 3.1. CCLS pulse sequence.
(**A**) Schematic of the CCLS-HSQC pulse sequence. It can be assumed unless otherwise indicated that all rectangular pulses are applied along the x-axis. 90° and 180° flip angles are represented by narrow bars and wide bars, respectively. The carrier frequency for ^{1}H is set on resonance with water at 4.77 ppm; the carrier frequency for ^{15}N is set in the center of the amide region at 121.8 ppm; the ^{13}C offset is set to 174.8 for the C' region. The reference spectrum is recorded with the shaped pulse for ^{13}C' (open rectangle) at position *a* while the suppression spectrum is recorded with this pulse in position *b*. A 3-9-19 watergate pulse scheme is used in the reverse INEPT transfer. GARP1 decoupling with a field strength of 1kHz is used during acquisition of ^{15}N. Delay durations: Δ = 2.4 ms; δ = 0.11 ms; $T_{NC'}$ = 16.5 ms. Phase cycling: φ_1 = x,-x, φ_2 = x,x,-x,-x, φ_{rec} = x,-x. A second FID is acquired for each increment by changing the φ_1 phase to y,-y in order to accomplish States quadrature detection for the ^{15}N indirect dimension. The φ_1 and φ_{rec} phases are also incremented by 180° every other ^{15}N increment for States-TPPI acquisition. The gradients use the Wurst shaped z-axis gradients of 1 ms. Gradient strengths (G/cm): G1: 5, G2: 7, G3: 17. The CCLS-HSQC pulse sequence is based on the fast HSQC experiment [187] to preserve water magnetization. (**B**) Example spectra representing the reference spectrum, the suppression spectrum, and the resulting subtraction spectrum followed by insets from the PKA-C/PKIα complex displaying the separation of resonances from each species. The blue and red species are present in the reference CCLS-HSQC, while the suppression spectrum contains only red species. Subtraction of the suppression from the reference spectrum results in a third spectrum containing only the blue species. (**C**) CCLS-HSQC experiment on the 50 kDa PKA-C/PKIα complex. The reference spectrum (left, purple) displays resonances from both U-^{15}N labeled PKA-C as well as U-^{15}N, ^{13}C labeled PKIα (S/N = 40). The suppression spectrum (middle, blue) suppresses signal from the ^{13}C' labeled PKIα showing only peaks from ^{12}C' labeled PKA-C (S/N = 50). Upon subtraction of the suppression spectrum from the reference spectrum, a sub-spectrum is obtained containing only peaks from PKIα (right, red) (S/N = 15).

Furthermore, we applied this technique to resolve assignment ambiguities on the 41 kDa catalytic subunit of cAMP-dependent protein kinase A (PKA-C) [53, 188]. PKA-C is the prototypical Ser/Thr kinase and, until relatively recently, had remained unexplored by NMR due to its size and presence of conformational exchange effects on the µs-ms timescale [75, 76, 189, 190]. Advances in pulse sequence design and sample preparation have since made it possible to investigate this system using NMR [62, 66, 70, 80]. We successfully implemented the CCLS-HSQC pulse sequence to assist in the assignment of multiple catalytically relevant residues of PKA-C. Furthermore, recent work from our group demonstrates the ability of this pulse sequence to simultaneously detect PKA-C in complex with an endogenous inhibitor, the heat-stable protein kinase A inhibitor (PKIα) [53, 191], giving the possibility to detect the mutual effect of PKA-C and PKIα interaction (**Figure 3.1 panel C -** unpublished data). Together these applications underscore the ability of CCLS to simultaneously detect PPIs and emphasizes the performance of this pulse sequence with high molecular weight systems.

3.3.2 Fingerprinting three binding partners using one sample.

Masterson *et. al.* applied the CCLS pulse sequence element to deconvolute PPIs in a ternary mixture simultaneously [192].The dual carbon label selective (DCLS) ^{1}H-^{15}N HSQC experiment requires three labeled binding partners, with the first species U-^{15}N labeled, the second ^{15}N, ^{13}C' labeled, and the third U-^{13}C, ^{15}N labeled. The deconvolution of these spectra follows the same spin-echo filtering theory as CCLS, with additional filtering of Cα coupled spins (**Figure 3.2 panel A**). Cα suppression requires a longer $T_{NC\alpha}$ delay due to both inter- and intra-residue ^{1}H-^{13}Cα J coupling [193]. Increasing the $T_{NC\alpha}$ delay nullifies protein backbone conformation dependency of $^{1}J_{NC\alpha}$ and $^{2}J_{NC\alpha}$ as it completely suppresses signal from $^{1}J_{NC\alpha}$ while inverting the residual signal intensities of $^{2}J_{NC\alpha}$.

This and the previously introduced pulse sequence rely on selective labeling of individual binding partners. Asymmetric selective labeling schemes to study PPIs in a multiple component sample are increasing in popularity [194-197] both for solution and solid-state NMR spectroscopy. For instance, Anglister and coworkers have demonstrated the application of asymmetric deuteration in combination with transferred nuclear Overhauser spectroscopy to study intermolecular nuclear Overhauser effects (NOEs) of large, fast exchanging protein complexes [198-200]. With respect to CCLS and DCLS,

selective labeling of ^{13}C' can be accomplished in recombinant proteins using either ^{15}N- and ^{13}C'-labeled amino acids or 1-^{13}C pyruvate and ^{13}C-labeled $NaHCO_3$ as the sole carbon sources [201-205]. Selective $^{13}C\alpha$ labeling is achieved by using 2-^{13}C glucose as the sole carbon source [202].

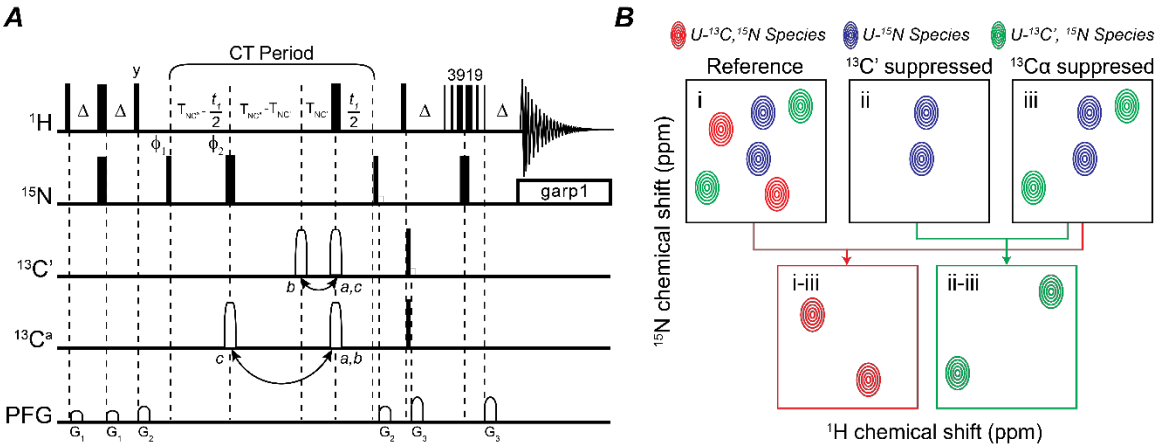

Figure 3.2. DCLS pulse sequence.
(**A**) Schematic of the DCLS-HSQC pulse sequence. It can be assumed unless otherwise indicated that all pulses are applied along the x-axis. 90° and 180° flip angles are represented by narrow bars and wide bars, respectively. The reference spectrum is recorded with the shaped pulse for ^{13}C (open rectangle) at position *a* while the ^{13}C' suppression spectrum is recorded with this pulse in position *b* and the $^{13}C\alpha$ suppression spectrum is recorded with the $^{13}C\alpha$ shaped pulse in position *c*. A 3-9-19 watergate pulse scheme is used in the reverse INEPT transfer. GARP1 decoupling with a field strength of 1kHz is used during acquisition of ^{15}N. The carrier frequency for ^{1}H is set on resonance with water at 4.7 ppm; the carrier frequency for ^{15}N is set in the center of the amide region at 120 ppm; the ^{13}C offset is set to 56 ppm. Selective ^{13}C' ($^{13}C\alpha$) sine shaped pulses are centered at 174 (56 ppm) and a null 113 ppm away. Delay durations: Δ = 2.4 ms; δ = 0.11 ms; $T_{NC'}$ = 16.4 ms; $T_{NC\alpha}$ = 24.5 ms. Phase cycling: φ_1 = x,-x, φ_2 = x,x,-x,-x, φ_{rec} = x,-x. A second FID is acquired for each increment by changing the φ_1 phase to y,-y in order to accomplish States quadrature detection for the ^{15}N indirect dimension. The φ_1 and φ_{rec} phases are also incremented by 180° every other ^{15}N increment for States-TPPI acquisition. The gradients use the Wurst shaped z-axis gradients of 1 ms. Gradient strengths (G/cm): G1: 5, G2: 7, G3: 17. (**B**) Example spectra representing the reference spectrum, the two suppression spectra, and the resulting subtraction spectra. The red, green and blue species are present in the reference DCLS-HSQC (a), while the first suppression spectrum (b) contains resonances from the red species and the second suppression spectrum (c) contains resonances from the red and green species. Subtracting spectrum c from a results in only resonances from the blue species and subtracting spectrum c from b yields only resonances from the green species. This linear subtraction scheme results in spectra with each component in the mixture isolated.

The DCLS experiment requires the acquisition of three interleaved experiments in parallel (**Figure 3.2 panel B**). A reference data set is collected observing all three species simultaneously, followed by the first suppression data set where amide resonances adjacent to ^{13}C' are undetected, identical to the CCLS suppression spectrum. Lastly, a

second suppression data set is collected where amide resonances coupled to $^{13}C\alpha$ are not detected. Deconvolution of the spectra is obtained by a linear combination of the data set. Subtraction of the second suppression spectrum from the reference spectrum provides a subspectrum containing only resonances from the U-^{13}C, ^{15}N labeled species. The subtraction of the first suppression spectrum from the second suppression spectrum provides an additional subspectrum containing only resonances from the U-^{15}N, $^{13}C'$ labeled species. In this manner, subspectra are obtained from a single sample for each individual component of the ternary mixture and all resonances can be resolved. As a proof of concept Masterson *et. al.* applied this labeling scheme and pulse sequence to three non-interacting proteins, maltose binding protein (MBP), Kemptide, and ubiquitin. By applying DCLS, the authors obtained subspectra corresponding to each individual component of the ternary mixture displaying the potential of this approach to study protein-protein interactions with a single sample.

3.3.3 Measuring Residual Dipolar Coupling (RDC) of complexes using one sample.

Residual dipolar coupling (RDC) allows orientation specific data to be derived via dipole-dipole interactions. The orientation restraints provided by RDC have proven useful in protein structure determination, nucleic acid structure, domain orientation, and more recently PPIs [206, 207]. We implemented CCLS and DCLS to sensitivity-enhanced TROSY or anti-TROSY spin-state selection to record the simultaneous measurement of RDCs [206, 208-211] for the relative orientations of multiple proteins within a single sample (**Figure 3.3 panels A-B**). RDC measurements are susceptible to experimental condition variations, which alter alignment tensors making difficult the direct correlations of orientational constraints obtained from different samples. Our approach, together with specific isotopic labeling, eliminates the need for multiple samples thus removing errors associated with sample inconsistencies [206].

Similar to DCLS (**Figure 3.3 panel C**), we applied this pulse sequence to a non-interacting mixture of U-^{2}H, ^{15}N MBP, ^{15}N-Ser^{5}, $^{13}C'$-Ala^{4} Kemptide, and, U-^{13}C, ^{15}N ubiquitin [212]. Following the same linear subtraction scheme reported for DCLS, we were able to measure RDCs for each individual component in a ternary mixture. Importantly, these RDC values were in agreement with back calculated values determined from already solved crystal structures of MBP [213] and ubiquitin [214], confirming that the

backbone conformational space of these proteins, along with their relative alignment tensors, were sufficiently defined.

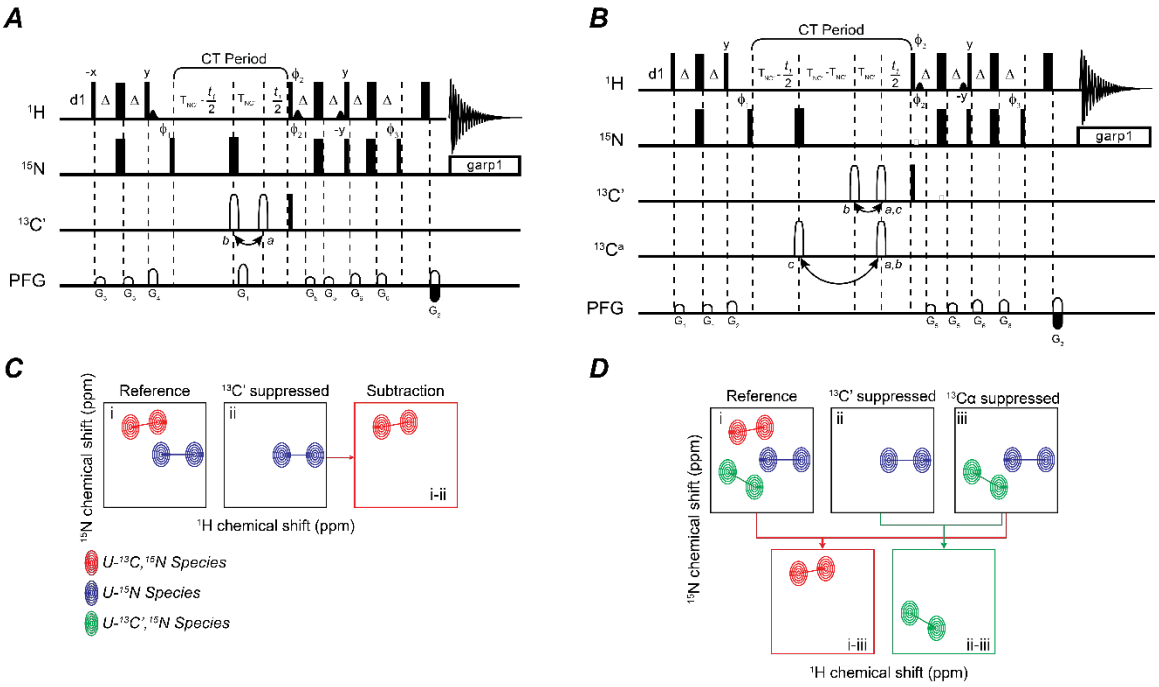

Figure 3.3. CCLS/DCLS RDC.
Schematic of the gradient-selected TROSY-based pulse sequence for binary (**A**) or ternary (**B**) mixtures of proteins. It can be assumed unless otherwise indicated that all pulses are applied along the x-axis. 90° and 180° flip angles are represented by narrow bars and wide bars respectfully. The reference spectrum is recorded with the shaped pulse for ^{13}C (open rectangle) at position *a* while the $^{13}C'$ suppression spectrum is recorded with this pulse in position *b* and the $^{13}C\alpha$ suppression spectrum is recorded with the $^{13}C\alpha$ shaped pulse in position *c*. The carrier frequency for ^{1}H is set on resonance with water at 4.77 ppm; the carrier frequency for ^{15}N is set in the center of the amide region at 121.8 ppm; the ^{13}C offset is set to 56 ppm. Selective $^{13}C'$ ($^{13}C\alpha$) sine shaped pulses are centered at 174.8 ppm (56 ppm). Delay durations: Δ = 2.4 ms; δ_1 = 1.5 s; $T_{NC'}$ = 16.5 ms; $T_{NC\alpha}$ = 23.5 ms. Phase cycling: φ_1 = x,-x, φ_2 = -x, φ_3 = -y, φ_{rec} = x,-x. Gradient strengths must be adjusted following the relationship $G_2 = G_1 \cdot (\gamma_N/\gamma_H)$, where γ_N and γ_H are the gyromagnetic ratios of ^{15}N and ^{1}H, respectively. A second FID is collected for each increment by changing the φ_2 and φ_3 to x and y respectively and by inverting the sign of the G_2 gradient in order to accomplish States quadrature detection for the ^{15}N indirect dimension. The φ_1 and φ_{rec} phases are also incremented by 180° every other ^{15}N increment for States-TPPI acquisition. The gradients use the Wurst shaped z-axis gradients of 1 ms. Gradient strengths (G/cm): G_3: 3, G_4: 13, G_5: 4, G_6: 5. To measure $^{1}J_{HN}$ coupling and NH RDC (in aligned media), a second spectrum, featuring the anti-TROSY component, is acquired by changing the φ_3 phase to y. (**C**) Example spectra representing the reference spectrum, the suppression spectrum, and the resulting subtraction spectrum. The blue and red species are present in the reference CCLS-HSQC, while the suppression spectrum contains only red species. Subtraction of the suppression from the reference spectrum results in a third spectrum containing only the blue species. (**D**) Example spectra representing the reference spectrum, the two suppression spectra, and the resulting subtraction spectra. The red, green and blue species are present in the reference DCLS-HSQC (a), while the first suppression spectrum (b) contains resonances from the red species and the second suppression spectrum (c) contains resonances

from the red and green species. Subtracting spectrum c from a results in only resonances from the blue species and subtracting spectrum c from b yields only resonances from the green species. This linear subtraction scheme results in spectra with each component in the mixture isolated.

3.3.4 Measuring long-range distances and transient complexes using CCLS for Paramagnetic Relaxation Enhancements (PRE).

Paramagnetic relaxation enhancements (PRE) have been used extensively to obtain long-distance restraints for structure calculation and to study PPIs for both stable and transient complexes [215-220]. In the standard PRE experiment that involves two interacting proteins, the intra- or inter-molecular effects of a paramagnetic center are detected for only one of the binding partners in each independent NMR experiment (**Figure 3.4 panel Ai**). To accurately probe these interactions, a minimum of four samples with differing spin label positions as well as reversed labeling schemes are required. Recently, we incorporated the CCLS pulse sequence in the traditional $^{1}H_{N}$-Γ_2 ($^{1}H_{N}$-Γ_2-CCLS) [217] that, together with an asymmetric labeling scheme, enables the detection of both intra- and inter-molecular paramagnetic relaxation enhancements (PREs) simultaneously using only one sample [164] (**Figure 3.4 panel B**). In this newly proposed strategy, one of the two binding partners must be U-^{15}N labeled and the second U-^{15}N, ^{13}C labeled (**Figure 3.4 panel Aii**). We also tested the proposed pulse sequence on the non-covalent, transient dimerization of ubiquitin. Specifically, we studied the complex formed between U-^{15}N, ^{13}C wild-type ubiquitin and the U-^{15}N-spin labeled K48C mutant. We were able to discriminate intra- and inter-molecular interactions detecting the structural and dynamics changes intrinsic to ubiquitin upon dimerization (**Figure 3.4 panel C**). The Γ_2 rates obtained with the new pulse sequence were confirmed to be identical to standard experiments. This work demonstrates that the Γ_2-CCLS PRE experiment is suitable for identifying structural changes occurring in both binding partners upon formation of transient and permanent interactions using a reduced number of samples.

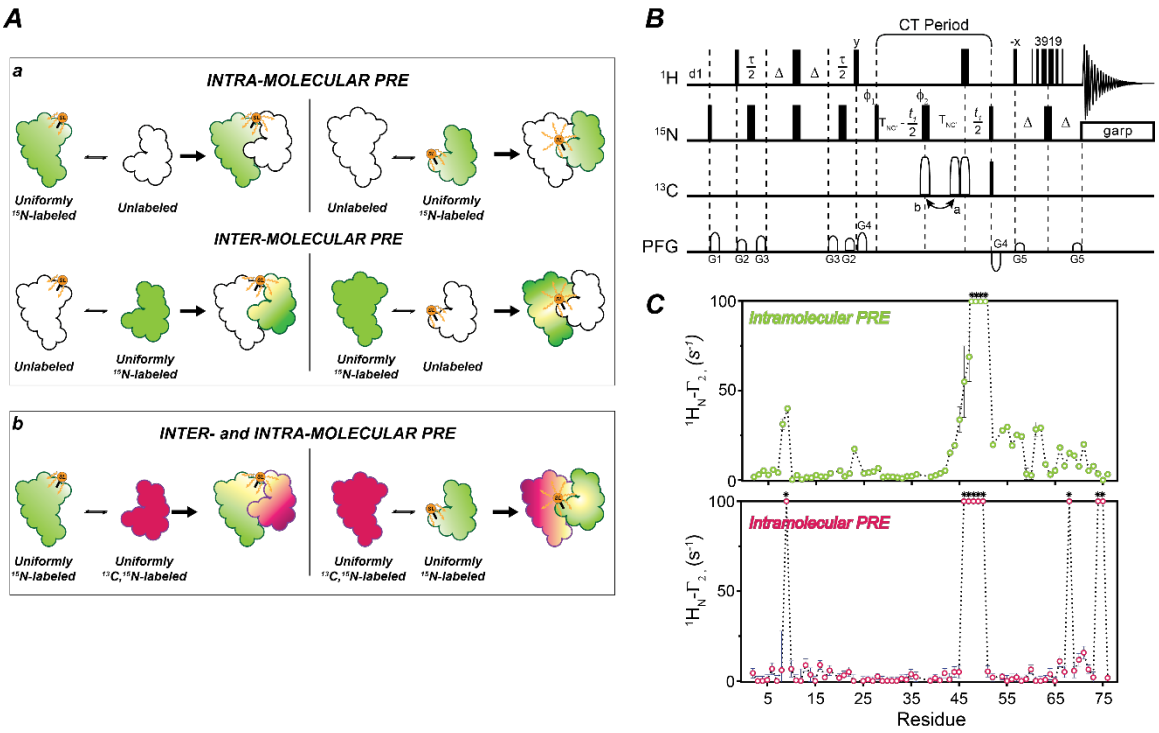

Figure 3.4. CCLS-PRE.

(**A**) Schematic of the standard experiment for the detection of intra- and inter-molecular PRE. In this case four different samples are needed. The first sample for the intra-molecular PRE is prepared with an asymmetric labeling scheme using the first binding partner uniformly ^{15}N labeled with a conjugated spin label (SL) and the second is NMR silent (unlabeled). A sample with a reversed labeling scheme is necessary to detect the intra-molecular PRE for the second binding partner (top panel A). For the inter-molecular PRE, two additional samples are required: one NMR silent with the conjugated SL and a second NMR active (e.g., ^{15}N or ^{13}C labeled) (lower panel A). Simultaneous detection of inter- and intra-molecular PRE using $^{1}H_N$-Γ_2-CCLS experiment. One species is uniformly ^{15}N labeled while the other is ^{13}C and ^{15}N labeled (b) and this allows the simultaneous detection of intra- and inter-molecular PREs. As reported before, reverse positioning of the SL is required for obtaining a complete characterization of the complex. (**B**) The ^{1}H-Γ_2-CCLS pulse sequence for PRE Γ_2 measurements. The narrow and wide bars represent 90° and 180° hard pulses, respectively. The three ^{13}C 180° shaped pulses are 256 μs long Q3 pulse, the first two and the last one shaped pulses are applied to ^{13}C′ and ^{13}CA, respectively. The ^{13}C′ 180° shaped pulse may be at either position a or b. When it is at position a, the $^{1}J_{NC'}$ is decoupled and reference spectra are acquired. When it is at position b, the $^{1}J_{NC'}$ is present and ^{13}C′-suppressed spectra are acquired. The flipping angles and phases of the pulses in 3919 are 20.8°$_x$, 62.2°$_x$, 131.6°$_x$, 131.6°$_{-x}$, 62.2°$_{-x}$, and 20.8°$_{-x}$, respectively, and the interval between pulses is 188 μs (= 1/d, d is the distance in Hz between center and next null). T = 16.5 ms, Δ = 2.6 ms. G1=(1 ms, 25.0 G/cm), G2=(0.3 ms, 5.0 G/cm), G3=(0.3 ms, 8.0 G/cm), G4=(1 ms, 15.0 G/cm), G5=(1 ms, 10.0 G/cm). Phase cycling scheme is φ1= (x, -x), φ2=(x, x, -x, -x), φ3=4(x), 4(-x), φ_{rec}=(x, -x, x, -x, -x, x, -x, x). The quadrature detections in t_1 dimension are acquired via States-TPPI of φ1. Constant time mode is used to measure Γ_2, that is $\Gamma_2 = ln(S_1/S_2)/(\tau_2 - \tau_1)$, where S_1 and S_2 are signal intensities of a peak measured with $\tau = \tau_1$ and $\tau = \tau_2$, respectively. 2×2 spectra are acquired in an interleave mode via changing relaxation delay τ (minimum 2 ms) and changing the ^{13}C′ 180° shaped pulse from position a to b, respectively. (**C**) Intra- and inter-molecular PRE measurements of ^{15}N-Ubi^{K48C} obtained with

the $^{1}H_N$-Γ_2-CCLS experiment. $^{1}H_N$-Γ_2 rate plot calculated for K48C mutant conjugate with MTSL in presence of Ubi^{WT} (upper panel C). $^{1}H_N$-Γ_2 rate plot calculated for WT ubiquitin in presence of Ubi^{K48C}-MTSL (lower panel C).

3.3.5 Improving sensitivity with the G5 pulse.

Advances in NMR methodology (TROSY, deuteration, selective labeling) have allowed for studies of protein-protein complexes approaching 1 MDa [221, 222]; however, these studies lack the ability to distinguish one species from another without the preparation of multiple samples. A recent technological advance that can improve nearly any pulse sequence is the universal triply compensated π pulses for high field spectrometers [223, 224], which we have incorporated into the CCLS pulse sequence (**Figure 3.5**). All inversion and refocusing pulses in the ^{1}H and ^{15}N channel were replaced with G5 pulses except the ^{15}N refocusing pulse in middle of 3-9-19 water suppression. We were able to improve the signal intensity from 6% to 23% compared to the regular CCLS version. These experiments were performed on the Bruker 900 MHz AVIII spectrometer at 298K, and this enhancement will only be more significant in GHz spectrometers.

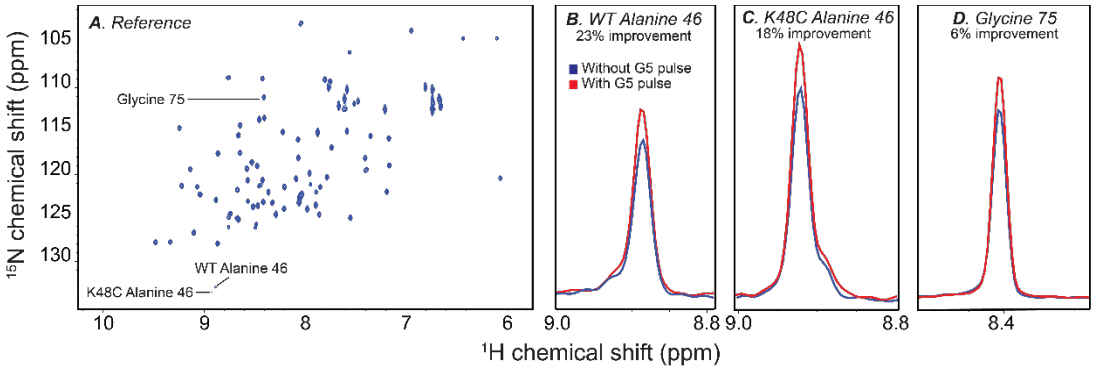

Figure 3.5. CCLS G5-pulse implementation.
(**A**) CCLS ^{1}H-^{15}N HSQC reference spectrum of ^{15}N, ^{13}C Ubi^{WT} and U-^{15}N Ubi^{K48C} mutant. (**B**) Overlay spectra of the Ubi^{WT} alanine 46 peak demonstrating a 23% signal intensity improvement with the G5 pulse. (**C**) Overlay spectra of the Ubi^{K48C} alanine 46 peak demonstrating an 18% signal intensity improvement with the G5 pulse. (**D**) Overlay spectra of the glycine 75 peak demonstrating a 6% improvement with the G5 pulse.

3.4 Conclusion and Perspectives

Here, we demonstrate the CCLS/DCLS pulse sequences enable the study of PPIs through simultaneous inter-leaved detection of all components in a single sample. As we

have illustrated, the CCLS and DCLS pulse sequence blocks can be applied to a multitude of well-established experiments (RDC and PRE). Extrapolating from this integration into existing NMR experiments, could NOESY be the next step? The possibility of observing multiple species in a single sample for NOESY experimentation is viable as Anglister *et. al*.[198] has reviewed difference spectroscopy and its application to 2D NOESY experiments. However, the pulse sequences are long thereby limiting sensitivity which the CCLS/DCLS pulse blocks show promise toward combating. Thus, reflecting upon the versatility of the CCLS/DCLS pulse block and the associated advantages afforded, we envisage the insertion into other existing NMR experiments to study a wide range of multicomponent systems.

3.5 Acknowledgements

This work is supported by the NIH (GM100310 to GV and P41 GM103399 to JLM). NMR experiments were carried out at the National Magnetic Resonance Facility at Madison and the Minnesota Nuclear Magnetic Resonance Center.

Chapter 4 Cushing's Syndrome Driver Mutation Disrupts Protein Kinase A Allosteric Network, Altering Both Regulation and Substrate Specificity

Caitlin Walker[1], Yingjie Wang[1,2], Cristina Olivieri[1], Adak Karmafrooz[1], Jordan Casby[1], Kerstin Bathon[3], Davide Calebiro[4,5], Jiali Gao[2,6], David A. Bernlohr[1], Susan S. Taylor[7], and Gianluigi Veglia[1,2*]

[1]Department of Biochemistry, Molecular Biology, and Biophysics, University of Minnesota, Minneapolis, MN 55455, USA.

[2]Department of Chemistry, University of Minnesota, Minneapolis, MN 55455, USA.

[3]Institute for Pharmacology and Toxicology, University of Würzburg, 97078 Würzburg, Germany.

[4]Institute of Metabolism and Systems Research, University of Birmingham, Birmingham B15 2TT, UK.

[5]Centre of Membrane Proteins and Receptors, University of Birmingham, Birmingham B15 2TT, UK.

[6]Shenzhen Bay Laboratory and Laboratory of Computational Chemistry and Drug Design, Peking University Graduate School, Shenzhen 518055, China.

[7] Departments of Chemistry and Biochemistry and Pharmacology, University of California San Diego, La Jolla, CA 92093, USA.

Reprinted from *Science Advances* 5(8).

4.1 Synopsis

Genetic alterations in the *PRKACA* gene coding for the catalytic α subunit of the cAMP-dependent protein kinase A (PKA-C) are linked to cortisol-secreting adrenocortical adenomas resulting in Cushing's syndrome. Among those, a single mutation (L205R) located in the P+1 loop of the kinase's active site has been found in up to 67% of patients. The X-ray structures of the wild-type and mutant kinases are essentially identical and the aberrant mechanism of function of this mutant remains under active debate. Using NMR spectroscopy, thermodynamics, kinetic assays, and molecular dynamics simulations, we found that this single mutation causes global changes in the enzyme, disrupting the intramolecular allosteric network and structural coupling between the small and large lobes. The altered intramolecular allosteric interactions and loss of nucleotide/pseudo-substrate binding cooperativity explain the impaired regulation of the kinase by regulatory subunits and the endogenous protein kinase inhibitor. Remarkably, by rewiring its internal allosteric network, PKA-C^{L205R} is able to bind and phosphorylate non-canonical substrates, explaining the changes in substrate specificity detected by phosphoproteomic analyses. Both the lack of regulation and change in substrate specificity reveal the complex role of this mutated kinase in the formation of cortisol-secreting adrenocortical adenomas.

4.2 Introduction

The cAMP-dependent protein kinase A (PKA) plays a fundamental role in the function and replication of endocrine cells [225] and aberrant cAMP signaling has been linked to several endocrine diseases [226]. The first mutations in PKA have been found in the regulatory (R) subunits, which have been associated with Carney complex, a multiple neoplasia syndrome manifesting via adrenocortical adenomas, cutaneous and neuronal tumors, cardiac myxomas and pigmented lesions of the skin and mucosae [226]. Only recently, somatic mutations have been identified in the *PRKACA* gene coding for the catalytic α subunit of PKA (PKA-C) and discovered in cortisol-secreting adrenocortical adenomas responsible for Cushing's syndrome [227] (**Figure 4.1 panel A**). Nearly all identified mutations lie adjacent to the active site cleft and the regulatory/catalytic subunit interface (**Figure 4.1 panel B,C**). Among these mutations, the most frequently found (PKA-C^{L205R}) is a point mutation leading to substitution of Leu at position 205 (or 206, depending on the convention used for numbering) with Arg and has been found in up to 67% of Cushing's syndrome patients [27-29, 102, 228].

Inactive PKA exists as an inactive holoenzyme (R_2C_2) containing a regulatory (R) subunit dimer bound to two catalytic (C) subunits. The inhibitory sequence of the R-subunit occupies the active site of the enzyme (**Figure 4.1 panel D**). Upon stimulation of membrane receptors coupled to the stimulatory G_s protein, produced cAMP binds to the R-subunits unleashing active C-subunits [229]. The spatiotemporal regulation of the kinase is provided by ancillary proteins such as A-kinase anchoring proteins (AKAPs) that, via interactions with R-subunits, localize PKA-C in close proximity to its substrates [55]. In addition, PKA-C is regulated by an endogenous inhibitor (PKI), whose function is to block access to substrates and recruit PKA-C to the nuclear export complex (CRM1 and RanGTP) [229]. When this spatiotemporal regulation fails, PKA-C hyper-phosphorylates its targets, leading to disease.

Structurally, PKA-C consists of two lobes. The N-lobe, smaller and more dynamic, comprises mostly β-strands as well as the αC-helix and harbors the ATP binding site [35]. The C-lobe, larger and made up by α-helices, is more rigid and harbors the substrate binding groove. PKA-C toggles between three major conformational states: open (apo), intermediate (nucleotide-bound), and closed (ternary complex with nucleotide/substrate-

bound) [42]. The L205R mutation is located at the interface of the N- and C- lobes of PKA-C in the P+1 loop, a highly conserved region of the enzyme that creates a hydrophobic pocket for substrate docking. Based on its positioning, the L205R mutation has been proposed and shown by independent laboratories to disrupt the binding of R-subunits and render the enzyme constitutively active [230, 231]. *In vivo* studies revealed that the catalytic activity of PKA-C^{L205R} is comparable to that of wild-type [230]. However, recent phosphoproteomic mapping showed a drastic change in the phosphorylation profile, suggesting that the mutation preserves the ability to phosphorylate downstream substrates, although with a different selectivity [20, 232]. Based on these data, it has been proposed that disruption of the signaling network leading to the phosphorylation of novel substrates may contribute to tumorigenesis. Notably, the X-ray crystal structures of the wild-type and mutant kinase in complex with nucleotide and pseudo-substrate, PKI_{5-24}, are nearly superimposable (RMSD = 0.49 Å) [106] and do not thoroughly explain the weaker binding for R-subunit, the lack of regulation by PKI as well as the changes in the phosphoproteomic profile.

To gain mechanistic insights on the multifarious effects of this single mutation, we carried out solution NMR spectroscopy in concert with binding thermodynamics, kinetic assays, and molecular dynamics (MD) simulations. We found that this single mutation, in addition to changing the protein-protein interface for substrate recognition, causes a disruption of the internal allosteric communication, reducing its affinity for nucleotide. The partial ablation of the intramolecular allosteric communication prevents the kinase from reaching a completely closed state, reducing the binding affinity for canonical substrates and pseudo-substrates, thus hindering endogenous regulation. Notably, kinetic assays using a substrate identified by phosphoproteomic analyses as a preferred substrate of PKA-C^{L205R} [20] show a higher catalytic efficiency and a rearrangement of the internal structural dynamics and allosteric communication. Taken together, our results indicate that rewiring of the internal allosteric network and global changes in dynamics contribute to the complex dysregulation of the signaling network of PKA-C^{L205R} within tumor cells.

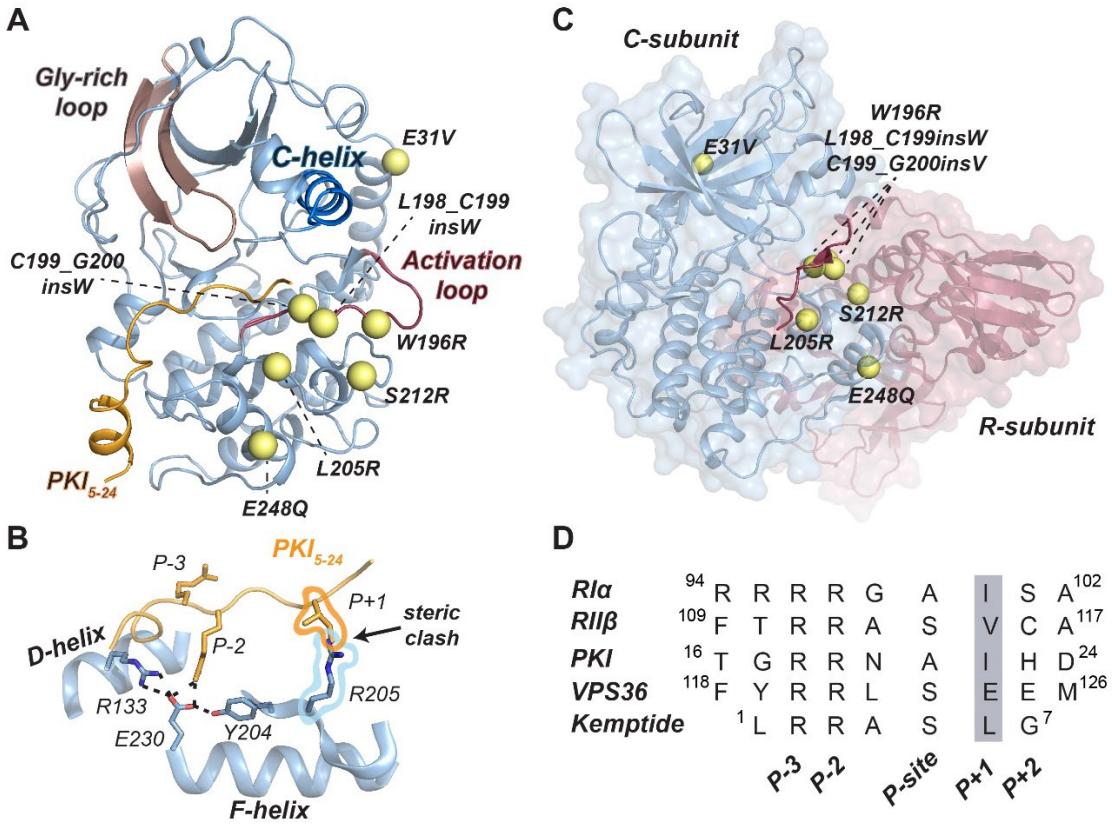

Figure 4.1. Architecture of PKA-C and locations of the Cushing's syndrome mutations. (**A**) Structure of PKA-C (PDB ID: 1ATP) in complex with pseudo-substrate PKI depicting the location of Cushing's syndrome mutations (yellow spheres) in relation to structural elements of the kinase. The E248Q mutations includes an additional deletion (del243-247) and the S212R mutation includes an insertion (insIILR) not depicted. (**B**) X-ray structure of PKA-C^{L205R} (PDB: 4WB6) with the overlay of PKI$_{5-24}$ (PKI^{WT} from PDB: 1ATP) describing the architecture of the peptide binding site and steric clash between kinase PKA-C^{L205R} and pseudo-substrate. (**C**) Structure of R/C complex (PDB ID: 2QCS) depicting locations of Cushing's mutations in relation to the pseudo-substrate inhibitory sequence of the R-subunit. (**D**) Primary sequence comparison of common regulators (RIα, RIIβ, PKI) and peptide substrates of the catalytic subunit (Kemptide and VPS36).

4.3 Results

PKA-C^{L205R} shows a marked loss of binding cooperativity between ATP and PKI. To determine the thermodynamics of nucleotide binding (ATPγN) to both PKA-C^{WT} and PKA-C^{L205R}, we used isothermal titration calorimetry (ITC). We found that PKA-C^{L205R} exhibits a 3-fold lower binding affinity compared to PKA-C^{WT} (K_d of 215 ± 15 versus 83 ± 8 μM). Fitting of the titration curves shows the binding of ATPγN to PKA-C^{L205R} is enthalpically favorable and entropically unfavorable; whereas both contributions are favorable for

ATPγN binding to PKA-C^{WT}. To evaluate the binding cooperativity between nucleotide and substrate [71, 82], we analyzed the binding thermodynamics of the pseudo-substrate peptide inhibitor, PKI_{5-24}, to both PKA-C^{WT} and PKA-C^{L205R} in the presence and absence of nucleotide. ΔH, $-T\Delta S$, ΔG and K_d as well as the cooperativity coefficients (σ) derived from ITC titrations are summarized in **Table 4.1**. The binding thermodynamics of PKI_{5-24} to the apo forms of the two kinases is comparable, with similar enthalpy changes (favorable). When saturated with ATPγN, PKA-C^{WT} binds PKI_{5-24} with higher affinity (K_d = 0.16 ± 0.02 μM) [71]. In contrast, PKA-C^{L205R} displays a 62-fold reduction in binding affinity (K_d = 10 ± 3 μM), with a net decrease in both ΔH and ΔS. Importantly, the binding of PKI_{5-24} to the PKA-C^{WT}/ATPγN complex is highly cooperative (σ = 106 ± 18), whereas its binding cooperativity to the PKA-C^{L205R}/ATPγN complex decreases 18-fold (σ = 6 ± 2). Therefore, this single mutation affects both the affinity for ligands as well as the binding cooperativity between nucleotide and pseudo-substrate.

L205R mutation causes a reduction in phosphorylation kinetics. To evaluate the catalytic efficiency of PKA-C^{L205R}, we carried out steady-state coupled assays using the standard substrate, Kemptide. As expected from the binding thermodynamics and previous kinetic assays, the Leu to Arg substitution at the P+1 loop increases the K_M 11-fold (**Table 4.2**). Interestingly, the k_{cat} for the mutant increases from 19 s^{-1} to 41 s^{-1}, which results in an overall decrease in catalytic efficiency (k_{cat}/K_M) by over 5-fold compared to PKA-C^{WT}. These results are in quantitative agreement with experiments carried out by two other independent groups [106, 233].

PKI binding to PKA-C^{L205R} falls short in shifting the enzyme to a fully closed state. To analyze the structural changes of PKA-C upon binding PKI and the effects of the L205R mutation, we mapped the amide backbone fingerprint of the enzyme using [^{1}H, ^{15}N]-TROSY-HSQC experiments [234]. The amide signatures of the kinases in different ligated forms are displayed in **Figure 4.7**. The binding of ATPγN to both PKA-C^{WT} and PKA-C^{L205R} gives rise to similar chemical shift perturbations (CSPs), with the exception of the residues in the Gly-rich, catalytic, and Mg^{2+} positioning loops that show larger chemical shift changes for PKA-C^{WT} (**Figure 4.8**). To evaluate the global response to ligand binding for the kinase and its mutant, we used CONCISE (COordiNated ChemIcal Shifts bEhavior), which performs a statistical analysis on linear chemical shift trajectories of each amide resonance to identify the position of each state along the conformational equilibrium [235].

Following ligand binding, the amide resonances of PKA-C display linear chemical shifts trajectories, with the amide resonances corresponding to the apo enzyme populating one extreme and those of the closed state (ternary complex with PKI) populating the opposite extreme of the linear correlations. This behavior exemplifies a conformational equilibrium along the three major conformational states of the kinase (open, intermediate, and closed), whose relative populations are modulated by ligand binding. A total of 55 residues exhibit linear chemical shift trajectories for both PKA-C^{WT} and PKA-C^{L205R} indicating a fast exchange limit in the NMR chemical shift timescale. These residues are distributed throughout the kinase. We found the binding of ATPγN and PKI shifts the conformational equilibrium of PKA-C^{WT} towards a fully closed state. In contrast, these ligands drive the mutant to a partially closed state, which is located between the intermediate and the closed conformation (**Table 4.3**). This is supported by thermostability data obtained by circular dichroism (CD) measurements (**Table 4.4**). In fact, CD melting curves show that the PKA-C^{WT}/ATPγN/PKI complex has a higher melting temperature (T_m) than the corresponding complex with PKA-C^{L205R}, further suggesting that this complex may adopt a more open and unstable conformation. Since the extent of the closed state is correlated with binding affinity and cooperativity [71], these results are consistent with the loss in allosteric cooperativity revealed by thermocalorimetric data.

L205R disrupts the allosteric network of the kinase upon PKI binding. To determine a possible correlation between the binding cooperativity and the intramolecular allosteric network, we analyzed the correlated chemical shift perturbations for both PKA-C^{WT} and PKA-C^{L205R} using CHEmical Shift Covariance Analysis (CHESCA) [129]. This method identifies the allosteric networks of residues that are involved in concerted responses to ligand binding [130, 132]. The [^{1}H, ^{15}N]-TROSY-HSQC spectra of the three forms of PKA-C (apo, ATPγN-bound, and ATPγN/PKI-bound) were used for the CHESCA analyses. This method relies on the presumption that when subjected to ligand binding, residues belonging to the same allosteric network elicit a correlated linear response, *i.e.*, the chemical shifts show high covariance. The identification of inter-residue covariation by CHESCA relies on agglomerative clustering and singular value decomposition [130, 132]. Pairwise correlations between chemical shift variations experienced by different residues are analyzed to identify networks of coupled residues and are plotted on a correlation matrix. A disruption of the allosteric network is diagnosed by a decrease in the density and extent of the inter-residue correlations.

The CHESCA matrices for PKA-C^{WT} and PKA-C^{L205R} reported in **Figure 4.2 panel A,C** reveal dramatic differences in their allosteric networks. In fact, there is an overall reduction in the number of correlations throughout PKA-C^{L205R} (**Figure 4.2 panel B,D**), with specific domains of the enzyme more impacted by this single mutation. In particular, residues belonging to the Gly-rich, activation loop, and peptide-positioning loop experience the most dramatic reductions in both number and extent of chemical shift covariation. Additionally, correlations within the activation loop (W196), αF- (K217, V219, D220, G225, V226, A233), and αG-helices (Q245) are also ablated. The loss of correlations for the αF-helix is especially important as this motif spans the hydrophobic core of the C-lobe and is conserved throughout the AGC kinase family. The function of the αF-helix is to anchor all the hydrophobic motifs within the kinase core and orchestrate catalysis [39, 66]. As highlighted before, all Cushing's driver mutations, with the exception of E31V, are located near L205R and are likely to affect the enzyme in a similar manner, disrupting these important allosteric nodes.

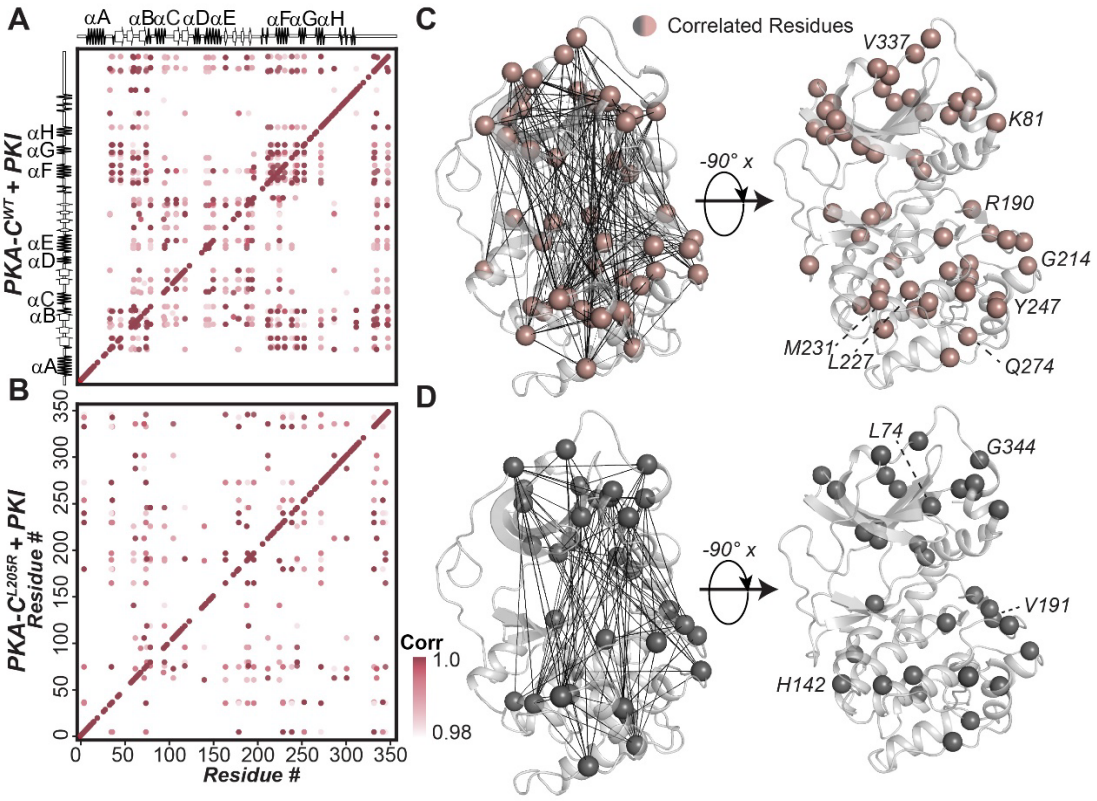

Figure 4.2. Allosteric network of interactions observed upon pseudo-substrate binding. The CHESCA correlation matrix for (**A**) PKA-C^{WT} upon binding PKI, and (**B**) PKA-C^{L205R} upon binding PKI. (**C**) Correlations corresponding to the binding of PKI to PKA-C^{WT} plotted on the

structure of PKA-C. Residues that are commonly correlated for both PKA-C^{WT} and PKA-C^{L205R} are highlighted. (**D**) Correlations corresponding to the binding of PKI to PKA-C^{L205R} plotted on the structure of PKA-C. Specific residues that are correlated for only PKA-C^{L205R} are highlighted. Only correlations with r_{ij} > 0.98 are shown throughout.

L205R disrupts the allosteric network of the kinase upon PKI binding. To determine a possible correlation between the binding cooperativity and the intramolecular allosteric network, we analyzed the correlated chemical shift perturbations for both PKA-C^{WT} and PKA-C^{L205R} using CHEmical Shift Covariance Analysis (CHESCA) [129]. This method identifies the allosteric networks of residues that are involved in concerted responses to ligand binding [132]. The [^{1}H, ^{15}N]-TROSY-HSQC spectra of the three forms of wild-type and PKA-C mutant (apo, ATPγN-bound, and ATPγN/PKI-bound) were used for the analysis. The CHESCA matrices for PKA-C^{WT} and PKA-C^{L205R} reported in **Figure 4.2 panel A,B** reveal dramatic differences in their allosteric networks. In fact, there is an overall reduction in the number of correlations throughout PKA-C^{L205R} (**Figure 4.2 panel C,D**), with specific domains of the enzyme more impacted by this single mutation. In particular, residues belonging to the Gly-rich, activation loop, and peptide-positioning loop experience the most significant reductions in both number and extent of chemical shift covariation. Additionally, several interresidue correlations within the activation loop (W196), αF- (K217, V219, D220, G225, V226, A233), and αG-helices (Q245) are also ablated. The loss of interresidue correlations for the αF-helix is especially important as this motif spans the hydrophobic core of the C-lobe and is conserved throughout the AGC kinase family. The function of the αF-helix is to anchor all the hydrophobic motifs within the kinase core and to orchestrate catalysis [39, 66]. As highlighted before, all Cushing's driver mutations, with the exception of E31V, are located near L205R and are likely to affect the enzyme in a similar manner, disrupting these important allosteric nodes.

Binding of VPS36 substrate to PKA-C^{L205R} rewires the intramolecular allosteric network and re-establishes binding cooperativity. In addition to affecting the regulation of PKA-C by the R-subunits, L205R changes the kinase's downstream substrate specificity [20, 232]. Specifically, it was found that in *E. coli* PKA-C^{L205R} favors non-canonical substrates with negatively charged residues (Glu or Asp) at positions P+1, P+2, and P+3. From our own phosphoproteomic studies on endogenous substrates in human cells [20], we identified several substrates that are preferentially phosphorylated by the mutated kinase. Among those substrates, we selected the top target hyper-

phosphorylated by PKA-C^{L205R}: the vacuolar protein-sorting-associated protein 36 (VPS36), a protein that plays a role in endosomal sorting of ubiquinated cargo proteins by the endosomal sorting complex. The recognition sequence of VPS36 (RRL**S**EEM) for PKA-C has two Glu residues in the P+1 and P+2 positions. Using steady-state coupled enzyme assays with Kemptide and a VPS36-derived peptide (residues 115-130 encompassing the PKA-C recognition sequence and denoted VPS36 from hereon), we found that PKA-C^{L205R} reduces the kinases catalytic efficiency for Kemptide, which contains a hydrophobic residue at the P+1 position. In contrast, the mutation causes an increase in k_{cat} (from 5 to ~18 s^{-1}) for VPS36, leading to a 3-fold increase in catalytic efficiency (**Figure 4.3 panel A** and **Table 4.2**). Additionally, the ITC analysis carried out with VPS36 indicates that PKA-C^{L205R}/ATPγN has an affinity typical of other substrates (K_d = 3.5 ± 0.1 μM), while the binding to wild-type cannot be detected reliably, suggesting a significantly lower binding affinity (**Table 4.1**). A possible explanation is that the acidic residues in positions P+1 and P+2 of VPS36 hamper the intermolecular interactions between the peptide and the residues lining the binding pocket of PKA-C^{WT}, while they might favor the interactions with PKA-C^{L205R}. These results support the proposed altered substrate specificity for PKA-C^{L205R} detected in intact cells.

To further investigate the underlying mechanism for the change in substrate specificity of PKA-C^{L205R}, we analyzed the trajectories of the amide resonances for the wild-type and the mutated kinase upon binding VPS36. Although VPS36 binding causes linear chemical shift changes similar to PKI binding, the number of residues involved in the binding response is significantly higher for PKA-C^{L205R}. In addition, VPS36 binding causes an overall attenuation of the peak intensities throughout the entire fingerprint of the enzyme, with some resonances broadened beyond detection (**Figure 4.9**). For instance, resonances associated with the αF-helix and Gly-rich loop are noticeably broadened suggesting an increase in protein dynamics in the μs-ms timescale. The CONCISE analysis shows that the conformation of the PKA-C^{WT}/ATPγN/VPS36 complex only reaches the intermediate state. In contrast, the PKA-C^{L205R}/ATPγN/VPS36 complex reaches a state lying between the intermediate and closed state (**Figure 4.3 panel B**). This position in-between the intermediate and closed state was also observed in the crystal structure of PKA-C^{WT} bound to a substrate peptide [67], suggesting that the ternary complex of PKA-C^{L205R} with VPS36 adopts a catalytically committed state.

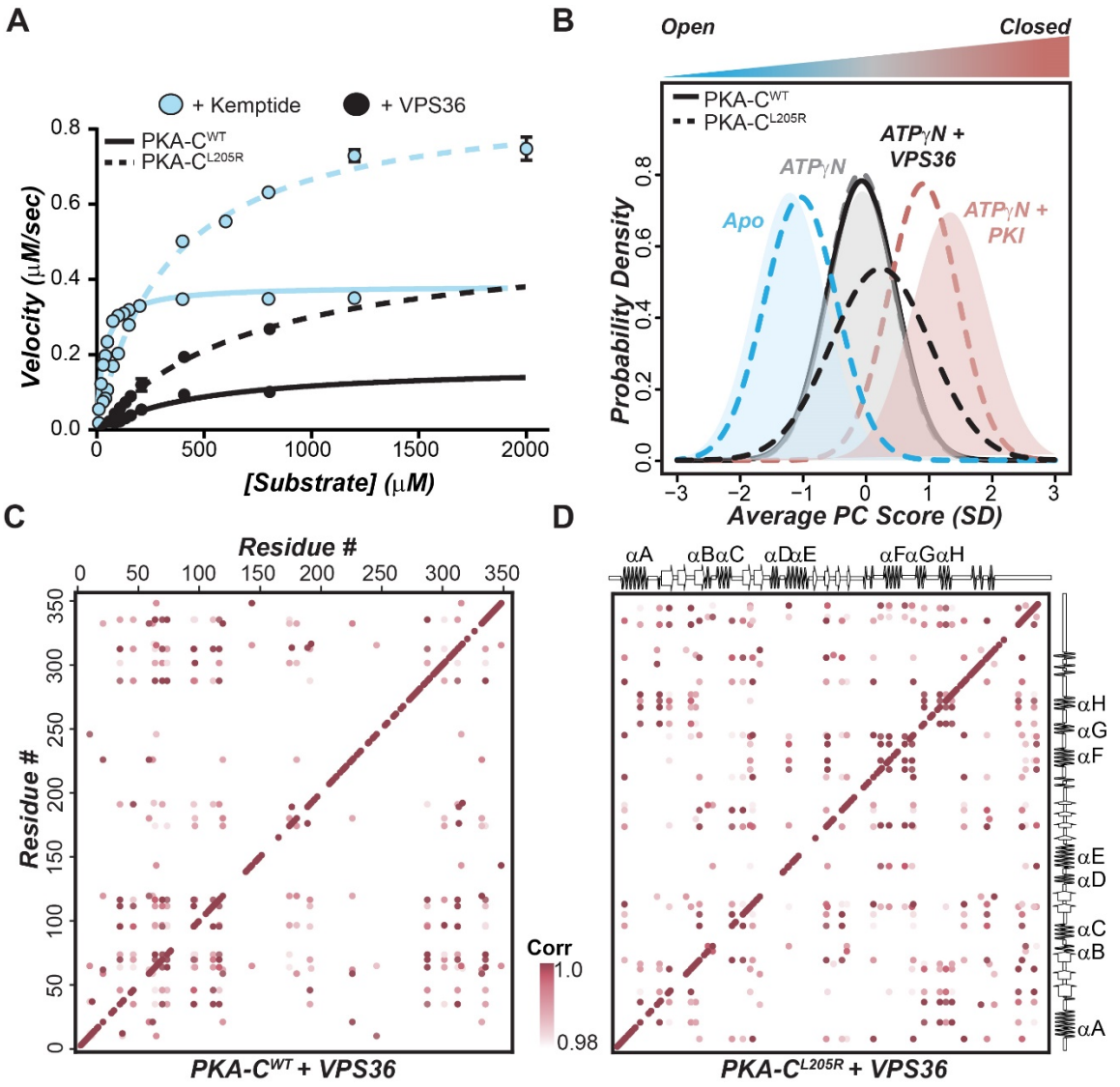

Figure 4.3. Rewiring of allosteric network of PKA-C^{L205R} upon binding VPS36.
(**A**) Steady-state phosphorylation kinetics of Kemptide and VPS36 peptides for PKA-C^{WT} and PKA-C^{L205R}. Corresponding values can be found in **Table 4.2**. (**B**) CONCISE analysis on the apo, ATPγN, ATPγN/PKI, and ATPγN/VPS36 states of PKA-C^{WT} and PKA-C^{L205R}. (**C**) The CHESCA correlation matrix for PKA-C^{WT} upon binding VPS36. (**D**) The CHESCA correlation matrix for PKA-C^{L205R} upon binding VPS36.

The CHESCA maps for VPS36 binding to PKA-C^{WT} and PKA-C^{L205R} are radically different (**Figure 4.3 panel C,D**). While the PKA-C^{WT}/ATPγN/PKI complex shows an intense cross-talk between the small and large lobe, the corresponding map for PKA-C^{WT}/ATPγN/VPS36 reveals a complete loss of allosteric interactions. Notably, correlations between the nucleotide binding site and the substrate binding hub are completely missing.

In particular, the interresidue correlations for the activation loop, peptide-positioning loop, and the αF- and αG- helices are either reduced in their number or completely missing. In contrast, a number of correlations between the N- and C- lobes for PKA-C^{L205R}, which are absent for the complex with PKI, are regained upon VPS36 binding. Note that ten of the resonances corresponding to residues located in and around the Gly-rich loop are broadened beyond detection and could not be included in the CHESCA analysis; therefore, the extent of coordinated changes in chemical shifts is largely underestimated. Nonetheless, the higher density of correlations found in the PKA-C^{L205R}/ATPγN/VPS36 complex underscores an extensive rewiring of the internal allosteric network, supporting the re-established binding cooperativity.

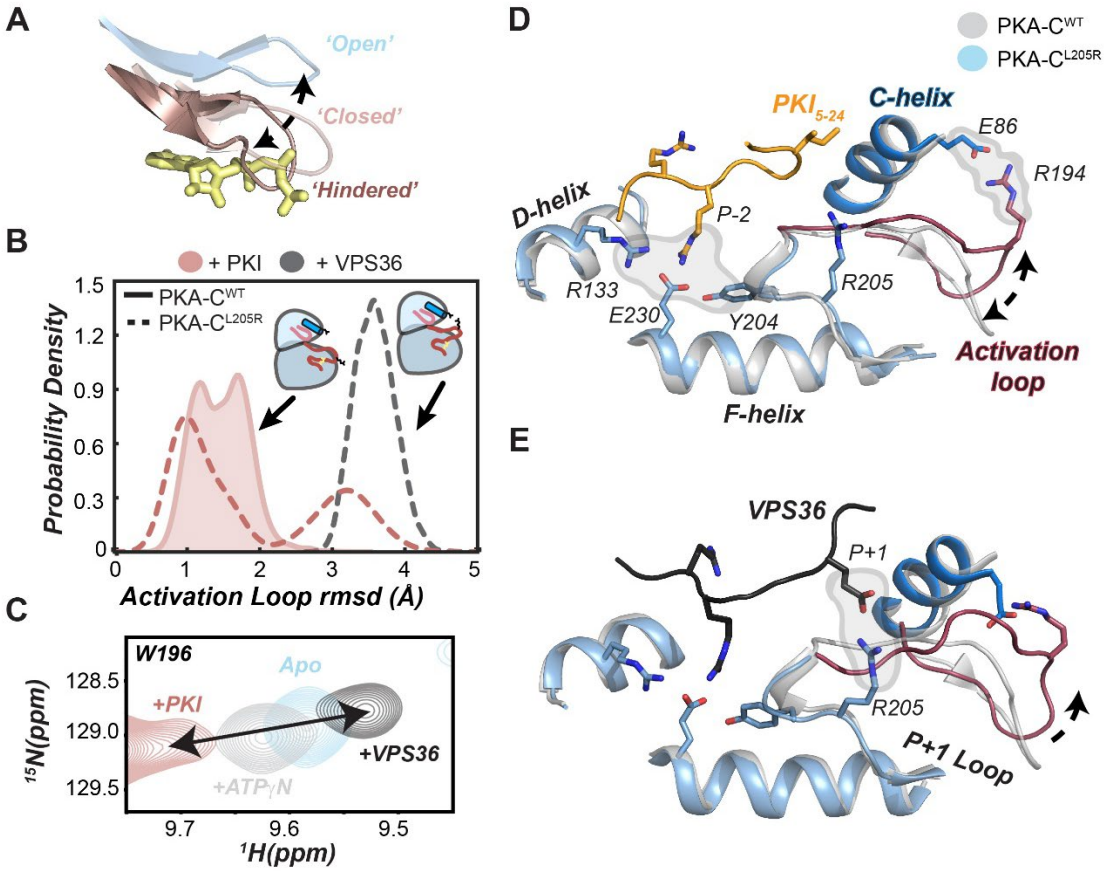

Figure 4.4. Conformational dynamics of the activation loop of PKA-C^{WT} and PKA-C^{L205R} upon binding substrate.
(**A**) Distinct opening-closing motions of the Gly-rich loop highlighting the hindered conformation that occludes the entering of ATP in PKA-C^{L205R}. (**B**) Probability density describing the conformation of the activation loop in response to different substrates and pseudo-substrates. (**C**) [^{1}H, ^{15}N]-TROSY-HSQC spectra showing the backbone amide chemical shift changes of the W196 indole amide (located on the activation loop) in response to binding PKI or VPS36. (**D**) X-ray structure of PKA-

C^{WT} (gray) (PDB ID: 1ATP) with the overlay PKA-C^{L205R} in complex with PKI (light blue) (PDB ID: 4WB6) describing the architecture of the peptide binding site and activation loop flip. (**E**) X-ray structure of PKA-C^{WT} (gray) (PDB ID: 1ATP) with the overlay PKA-C^{L205R} in complex with VPS36 (light blue) (MD simulations) describing the architecture of the peptide binding site and activation loop flip.

PKA-C^{WT} and PKA-C^{L205R} explore different conformational states. To determine the effects of the L205R mutation on the conformational energy landscape of PKA-C, we carried out parallel MD simulations of the ternary complexes in explicit water environments starting from their respective X-ray coordinates (PDB IDs: 4WB6 and 1ATP) [106]. The dominant motion of the kinase core was imaged using principal component analysis (PCA) of the C^{α} atoms encompassing residues 50 to 300. PC1 depicts the global opening-closing motion of the small and large lobes (**Figure 4.10 panel A**), while PC2 describes the shearing motion of the two lobes that can be envisioned as an 'asymmetric bite'. To describe the opening-closing motion of the active site, we monitored the time dependence of the distance between the C^{α} atoms of S53 in the Gly-rich loop and G186 (**Figures 4.10 panel B,C**). The binary and ternary complexes of PKA-C^{WT} and PKA-C^{L205R} sample similar conformational energy basins; however, the apo form of PKA-C^{L205R} explores a considerably broader basin than the wild-type. The Gly-rich loop of PKA-C^{WT} toggles between the open and closed conformations, featuring a transient hydrogen bond between S53 and the γ-phosphate of ATP; whereas the Gly-rich loop of PKA-C^{L205R} exhibits larger motions with the S53-G186 distance ranging from 5 to 18 Å, and more frequently sampling a conformation that hinders nucleotide binding, which might explain its weaker binding affinity (**Figure 4.4 panel A**). The Arg 205 causes steric hindrance with the C-terminal tail of PKI, disrupting the hydrophobic pocket required to anchor the Ile residue in the P+1 position, which likely contributes to the loss of PKI binding affinity.

To visualize the alterations of the protein-protein interaction interface that may influence binding cooperativity, we analyzed the probability distribution of the inter-residue contacts between the substrate and the kinase binding pocket. Overall, PKA-C^{L205R} shows a contact map with PKI similar to the wild-type enzyme (**Figure 4.11 panel A,B**). The high affinity binding region (HAR) and the consensus binding sequences remain bound throughout the entire MD trajectories with a probability of contact greater than 0.8. However, the L205R mutation reduces the probability of interactions between the Ile (at position P+1 in PKI) and the P+1 loop from 0.5 to 0.2. In contrast, VPS36 shows stable

interactions with the P+1 loop with a probability greater than 0.8 for Glu at the P+1 position and R205 (**Figure 4.11 panel C**). Moreover, the N-terminus of VPS36 forms transient interactions with the C-terminal tail located in the small lobe of PKA-C^{L205R}, which are absent in the corresponding complex with PKI. As a result, the peptide is more dynamic, a feature that might explain the dramatic exchange-broadening in the NMR spectrum of PKA-C^{L205R}/ATPγN/VPS36 complex.

As observed previously [80], the backbone of the tertiary complex PKA-C^{WT}/ATP/PKI is mostly rigid (**Figure 4.11 panel D,E,F**). The activation loop adopts a stable conformation as in the X-ray structure (PDB ID: 1ATP) [79] throughout the entire MD simulations with a RMSD of ~1.5 Å. In contrast, the activation loop and the adjacent loop that is anchored to the αF-helix (residues 210-220) in the corresponding PKA-C^{L205R}/ATP/PKI complex are more flexible, adopting two distinct conformations in which the most populated is similar to the X-ray structure (PDB ID: 1ATP), and a second minor flipped conformation (**Figure 4.4 panel B**). In this conformation, the activation loop no longer interacts with the C-lobe and forms a salt bridge with E86 of the αC-helix (**Figure 4.4 panel D,E**). For the PKA-C^{L205R}/ATP/VPS36 complex, the activation loop becomes more ordered and the flipped configuration becomes dominant. The existence of these two conformations is corroborated by chemical shift trajectories observed for the indole resonance of W196 in the activation loop (**Figure 4.4 panel C**). In fact, upon ligand binding the indole resonance of W196 follows a linear chemical shift trajectory from apo to the ternary form. This conformational change is highly correlated with the other major allosteric nodes (CHESCA plots), indicating it follows the cooperative structural changes of the enzyme. In contrast, the CHESCA plots for PKA-C^{L205R} show no correlations for these loops/residues, suggesting that the L205R mutation disrupts the internal allosteric network and may dislodge the activation loop from the large lobe.

The disruption of the allosteric network is mirrored by the pairwise mutual information plots [236] obtained from the analysis of the MD trajectories. For the wild-type enzyme, there are strong inter-residue correlations throughout the entire core of the kinase, especially among key catalytic motifs such as the Gly-rich loop (S53), the activation loop (R194, W196), αF- (Y215), αG- (D241), αH- (N283) helices as well as the PIF motif at the C-terminal tail (F347) (**Figure 4.12 panel A**). In contrast, PKA-C^{L205R} lacks of a number of allosteric interactions within the N-lobe, with only a few correlations

between the activation loop and the C-lobe (**Figure 4.12 panel B**). As for the CHESCA correlation maps, the mutual information plots reveal that the allosteric network between N-lobe and C-terminal tail of PKA-C^{L205R} is partially recovered upon VPS36 binding (**Figure 4.12 panel C**) with the engagement of E91 in the αC-helix and S53 of the Gly-rich loop.

4.4 Discussion

The L205R mutation was discovered independently in our and other laboratories as the dominant genetic alteration in cortisol-producing adrenocortical adenomas responsible for Cushing's syndrome [26-30]. Although it has a direct link with changes in cAMP/PKA signaling, adrenal Cushing's syndrome has different molecular etiologies [226]. Initially, rare germline mutations were found in the *PRKAR1A* gene encoding the regulatory Iα subunit of PKA in patients with Carney complex [96]. Most of these mutations occur at the interface between the R- and C- subunits or near the cAMP-binding site in CNB-A and are thought to cause aberrant regulation of the kinase [237]. Only recently, the focus has shifted toward somatic mutations occurring in the C-subunit of the enzyme. Even in this case, most mutated residues reside at the interface of the R/C complex. However, the molecular mechanisms for the aberrant regulation of cAMP signaling by these mutations have been a matter of debate. Specifically, two independent studies suggested that the L205R mutation interferes with the formation of the holoenzyme, rendering the C-subunit constitutively active [28, 29]. Sato *et al.*, on the other hand, proposed that this mutation does not interfere with the R-subunit regulation and that the development of the pathology is linked to intrinsic higher phosphoryl transfer activity of the mutant kinase [27]. Recent studies both *in vitro* and in intact cells have put forward a possible new mechanism, suggesting that the mutated enzyme has altered substrate specificity [20, 232, 233]. Notably, this arginine preceding the APE motif is characteristic in the CMGC kinase family, and assumes a key role in substrate recognition and kinase activation [238]. Perhaps PKA-C^{L205R} might lead to promiscuity towards substrates of CMGC kinases.

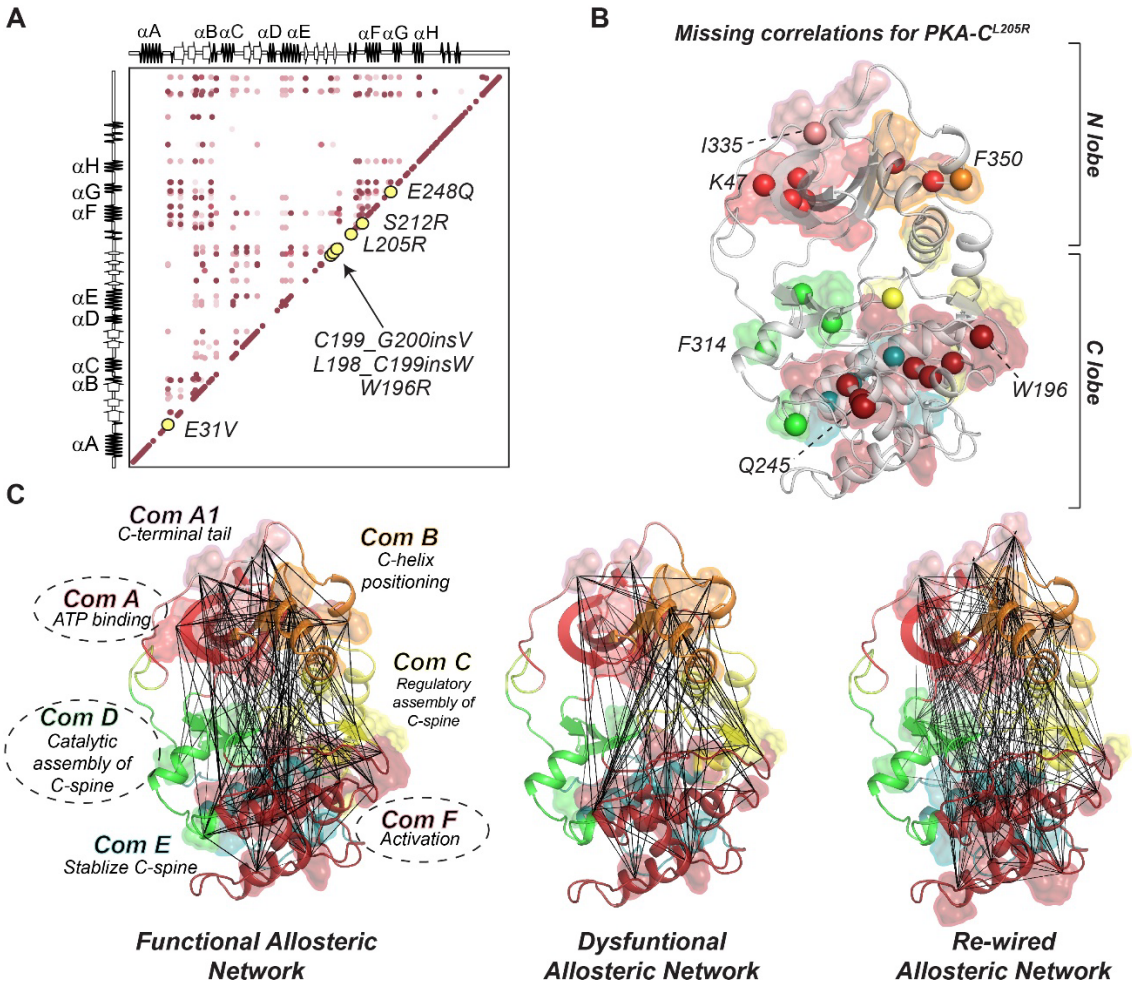

Figure 4.5. Cushing's mutations are located in allosteric nodes identified via CHESCA. (**A**) Correlation matrix of PKA-C^{WT} when bound to PKI emphasizing locations of Cushing's mutation in relation to allosteric nodes. (**B**) Missing correlations for PKA-C^{L205R} upon binding PKI colored according to community map of PKA-C^{WT}. (**C**) CHESCA correlation matrices for PKA-C^{WT} + PKI, PKA-C^{L205R} + PKI, and PKA-C^{L205R} + VPS36, respectively, plotted on the structure of PKA-C with colors specific to the community map analyses completed previously for PKA-C^{WT}[140]. Specific communities are emphasized to highlight elements that experience the most dramatic changes in the number and extent of chemical shift covariance for PKA-C^{L205R} upon binding PKI and VPS36.

Our studies reveal that the dysfunction of PKA-C^{L205R} is multifaceted, whereby allosteric cooperativity is reduced, substrate specificity is altered, and canonical regulation is ablated. The L205R mutation disrupts the hydrophobic interactions between the enzyme and substrate, causing a dramatic decrease in PKI binding affinity. This is in line with the impaired binding of the R-subunits found in our previous study [230] as PKI and R-subunits share similar consensus sequences. Our CHESCA analyses reveal that L205R perturbs the allosteric network of PKA-C and disrupts specific allosteric nodes that connect the

small and the large lobes. The allosteric nodes are defined as the hot spots in the network with the highest number of CHESCA correlations [239]. In particular, the allosteric communication between the node including L205 and encompassing the activation loop, αF-, and αG-helices and the node surrounding the Gly-rich loop, β2, and β3 is ablated. Interestingly, closer analysis of the CHESCA map of PKA-C^{WT} reveals that each allosteric node harbors Cushing's mutations located in the activation/αF/αG node except E31V, where the latter resides at the N-terminal αA-helix, a unique regulatory motif in PKA-C (**Figure 4.5 panel A**) [48]. Although spatially distinct, these allosteric nodes are highly correlated and coupled to one another to facilitate intramolecular communication and control binding cooperativity. Perturbation to one node, such as the case of L205R, has long range effects on the other node. The latter suggests that Cushing's mutations including E31V may disrupt the allosteric communication eliciting similar global responses in terms of binding cooperativity and regulation.

The CHESCA analyses of the chemical shifts parallel the predictions obtained from MD simulations using the community analysis. McClendon *et al.* analyzing the different forms of the kinase identified allosterically linked communities within PKA-C, each associated with a particular function or regulatory mechanism [140]. Plotting correlated residues on PKA-C's community maps reveals that the mutation reduces dramatically the allosteric communication between community A, D, and F with respect to the wild-type enzyme (**Figure 4.5 panel B,C**). In contrast, binding of VPS36 to PKA-C^{L205R} re-establishes the inter-community communication and the allosteric network.

The lack of regulation only partially explains the aberrant function of PKA-C^{L205R}. In fact, our thermodynamic and kinetic analyses reveal that this mutation shifts the specificity of PKA-C^{L205R} toward substrates containing acidic residues in the P+1 and P+2 positions, with a dramatic effect on binding cooperativity. While with the classical consensus sequence the cooperativity is greatly abolished, the mutated enzyme regains cooperativity with complementary substrates such as VPS36, among others. The reason for this behavior is apparent from the atomic mapping of the cooperative global response of the enzyme to ligand binding. While with the classical consensus sequence the allosteric communication between the N-lobe, harboring the ATP binding site, and the C-lobe, with the substrate binding site, is abolished, the binding of the complementary substrate (VPS36) coincides with an extensive rewiring of the allosteric network of

communication between the two lobes altering substrate specificity. It should be noted that VPS36 lacks the HAR region, which might affect its binding kinetics and thermodynamics. As with previous studies [82], VPS36 does not drive the enzyme to a completely closed state, perhaps facilitating product release. It is also worth noting that the reduction of the binding affinity for the nucleotide we observed under our experimental conditions was also detected by Luzi *et al.* [233]. Taken with our NMR and thermodynamic studies, MD simulations suggest that the mutation changes the energy landscape of the kinase (**Figure 4.6**). First, the mutation causes a reduction in binding affinity for nucleotide, which may be due to an increase in the population of the enzyme with the Gly-loop partially occluded. This conformation has been detected in other crystal structures and might prevent the nucleotide to intercalate in the C-spine of the enzyme [240]. Moreover, a significant population of the enzyme spans a conformational space featuring a flipped conformation of the activation loop and a salt bridge formed between R194 and E86 in the αC-helix. Notably, an increased plasticity of the activation loop, highlighted by W196, contributes to disruptions in the docking surface with the R-subunit [241]. At the same time, the R194-E86 salt bridge suggests a different dynamic coupling between the activation loop and the αC-helix. It is possible that this specific conformational state might dictate the selectivity of the substrate binding and the aberrant profile observed in phosphoproteomic assays.

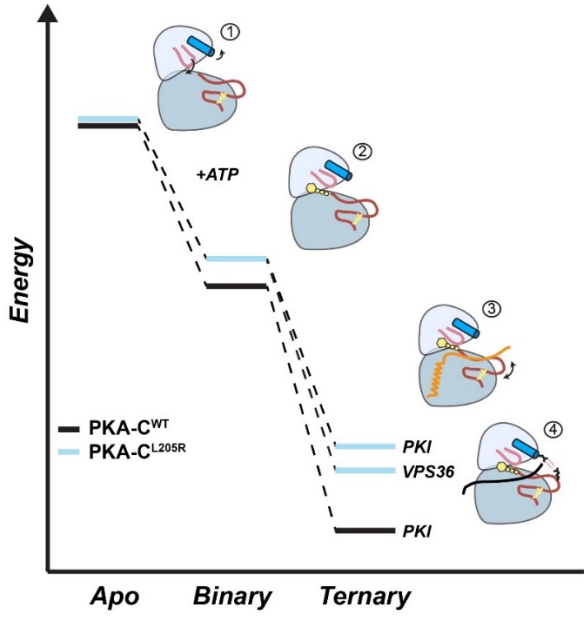

Figure 4.6. Schematic of the energy landscape for PKA-C^{WT} and PKA-C^{L205R}, combining thermodynamics and MD simulations data.

Relative free energy for the binding of ATPγN, PKI, and VPS36 to PKA-C^{WT} and PKA-C^{L205R} derived from ITC data. (1) Apo PKA-C^{L205R} samples mostly uncommitted states, with the Gly-rich loop partially occluded and the αC-helix turned outward. (2) Binary PKA-C^{L205R} features a wired the allosteric network for substrate binding, *i.e.*, committed state (3) Ternary PKA-C^{L205R} complex with lower affinity for PKI (*i.e.*, higher free energy relative to PKA-C^{WT}). The conformation of the activation loop of PKA-C^{L205R} is in equilibrium between an un-flipped and a sparsely populated *flipped* conformation. (4) PKA-C^{L205R}/ATPγN/VPS36 ternary complex features a flipped conformation of the activation loop with the electrostatic interactions between E86 and R194.

Given the ubiquitous nature of PKA and its involvement in numerous cell signaling events, its implication in specific diseases has been overlooked. Only recently, the attention of researchers has been directed to the *PRKACA* gene and its role in pathological lesions. A few years ago, Simon and co-workers discovered the presence of a chimeric construct of the PKA-C subunit that is the main driver of fibrolamellar hepatocellular carcinoma (FLHCC) [31]. Later on, our group and others discovered single mutations or insertions at the R/C interface that are linked to adrenal Cushing's syndrome [26-30]. More recently, Tseng *et al.* reported the discovery of a new insertion in a similar region that is involved in the development of myxoma, a sporadic form of tumor in the atrium of the heart [111]. It is possible that other defects in the *PRKACA* gene might be found to be implicated in the development of other tumors.

The analysis of the allosteric network carried out in this work reveals highly coupled allosteric nodes that harbor all Cushing's mutations found in patients and may help to explain why mutations located in two spatially distinct regions of the enzyme result in the same phenotype. Our findings suggest that analysis of allosteric networks using CHESCA may prove useful in predicting mutations that perturb catalytic function for enzymes beyond PKA-C. Furthermore, our work reveals that rewiring of the intra- and inter-molecular interactions leads to changes in cooperativity and selectivity. This suggests the opportunity to exploit small molecules or peptides able to change the internal communication and modulate the activity of this aberrant mutant selectively, *i.e.*, without affecting the function of the wild-type.

4.5 Materials and Methods

Sample Preparation. Recombinant human Cα subunit of cAMP-dependent protein kinase A cDNA (PKA-C^{WT} and PKA-C^{L205R}) was cloned into a pET-28a vector. A tobacco etch virus (TEV) cleavage site was incorporated via mutagenesis into the vector between the cDNA coding for the kinase and a thrombin cleavage site. The kinase was expressed

in *Escherichia coli* BL21 (DE3) pLysS cells in M9 minimal media supplemented with $^{15}NH_4Cl$. Protein overexpression was induced with 0.4 mM isopropyl β-D-thiogalactopyranoside (IPTG) and carried out overnight at 20°C. PKA-C purification was carried out using Ni^{2+} affinity chromatography. Cells were lysed using French press in 50 mM Tris-HCl, 30 mM KH_2PO_4, 200 mM NaCl, 200 μM ATP, 5 mM 2-mercaptoethanol, and lysozyme (15 mg/ 100 mL lysis buffer) (pH 8.0). After removing cell debris by centrifugation at 18,000 rpm for 45 minutes, supernatant was incubated with Ni^{2+} nitrilotriacetic acid resin (Thermo Scientific) at 4°C overnight. The resin was washed with 50 mM Tris-HCl, 30 mM KH_2PO_4, 200 mM NaCl, 10 mM Imidazole, and 5 mM 2-mercaptoethanol (pH 8.0) and eluted with 50 mM Tris-HCl, 30 mM KH_2PO_4, 200 mM NaCl, 250 mM Imidazole, and 5 mM 2-mercaptoethanol (pH 8.0). Fractions containing PKA-C were cleaved overnight at 4°C with a sufficient amount of recombinant TEV while being dialyzed into 20 mM KH_2PO_4, 25 mM KCl, 0.1 mM PMSF, and 5 mM 2-mercaptoethanol (pH 6.5). The three isoforms of PKA-C (corresponding to the three phosphorylation states with identical catalytic parameters) were separated by chromatography on a HiTrap SP column (GE Healthcare Life Sciences) using a linear gradient from buffer A [20 mM KH_2PO_4 pH 6.5] to 30% buffer B [20 mM KH_2PO_4, 1 M KCl pH 6.5] at a flow rate of 2 mL/min. Isoform II with $pThr^{197}$, $pSer^{338}$, and $pSer^{10}$ was used for all NMR experiments. Peptides (Kemptide/PKI_{5-24}/VPS36) were synthesized using standard Fmoc chemistry on a CEM Liberty Blue microwave synthesizer, cleaved with Reagent K (82.5% TFA, 5% phenol, 5% thioanisole, 2.5% ethanedithiol, and 5% water) for 3 h and purified using a semipreparative Supelco C18 reverse-phase HPLC column at 3 mL/min. The VPS36 peptide sequence used for all studies is as follows: QIEFYRRLSEEMTQR. Molecular weight and the quantity of the peptides were verified by LC-MS and/or amino acid analysis (Texas Tech Protein Chemistry Laboratory).

ITC Measurements. ITC measurements were performed with a low-volume NanoITC (TA Instruments). PKA-C^{WT} and PKA-C^{L205R} were dialyzed into 20 mM MOPS, 90 mM KCl, 10 mM DTT, 10 mM $MgCl_2$, and 1 mM NaN_3 (pH 6.5). PKA-C concentrations for ITC measurements were between 100-130 μM as confirmed by A_{280} = 53860 M^{-1} cm^{-1}. All measurements with ATPγN saturated PKA-C^{WT} and PKA-C^{L205R} were performed at 2 mM ATPγN, and 4 mM ATPγN, respectively. ITC measurements were performed in triplicates with a TA low-volume NanoITC instrument at 300K. For each experiment, 50 μL of 2-4 mM ATPγN, 0.6-4 mM PKI, or 2 mM VPS36 were titrated into ~300 μL of PKA-C. The heat

of dilution was subtracted from each titration curve. Binding was assumed to be 1:1 and the resulting curves were analyzed with the NanoAnalyze software (TA Instruments) using the Wiseman Isotherm [242]:

$$\frac{d[MX]}{d[X_{tot}]} = \Delta H° V_0 \left[\frac{1}{2} + \frac{1-\frac{1-r}{2}-R_m/2}{(R_m^2-2R_m(1-r)+(1+r)^2)^{1/2}}\right] \qquad (1)$$

where *d[MX]* is the change in total complex with respect to change in total protein concentration, $d[X_{tot}]$ is dependent on *r*, the ratio of K_d with respect to the total protein concentration, and R_M, the ratio between total ligand and total protein concentration. The free energy of binding was determined using the following:

$$\Delta G = RT \ln K_d$$

where R is the universal gas constant and T is the temperature at measurement (300K). The entropic contribution to binding was calculated using the following:

$$T\Delta S = \Delta H - \Delta G.$$

Calculations for the cooperativity constant (σ) were calculated as follows:

$$\sigma = \frac{K_{d\ Apo}}{K_{d\ Nucleotide}}$$

where $K_{d\ Apo}$ is the K_d of PKI_{5-24} binding to the apoenzyme and $K_{d\ Nucleotide}$ is the K_d of PKI_{5-24} binding to the nucleotide-bound enzyme.

Enzyme Assays. Steady-state activity assays with Kemptide and VPS36 were performed under saturating ATP concentrations and spectrophotometrically at 298K as described by Cook et al [85]. The values of V_{max} and K_M were obtained from a nonlinear fit of the initial velocities to the Michaelis-Menten equation.

Circular Dichroism. A change in ellipticity was measured at 220 nm on a Jasco J-815 spectrometer. A temperature scan between 20°C and 70°C at a rate of 1 °C/min with an equilibration time of 15 s was performed to unfold the protein. Spectra Manager Pro software was used to fit a two-state sigmoidal function. The inflection point was taken as the T_m(°C), the point at which 50% of the protein is folded.

NMR Spectroscopy. Uniformly ^{15}N-labeled PKA-C^{WT} and PKA-C^{L205R} were overexpressed and purified as described above. NMR experiments were performed in 90

mM KCl, 20 mM KH_2PO_4, 10 mM dithiothreitol (DTT), 10 mM $MgCl_2$, and 1 mM NaN_3 at pH 6.5. Standard TROSY-HSQC experiments were carried out for PKA-C^{L205R} and PKA-C^{WT} on 600-MHz and 900-MHz Bruker Advance III spectrometers equipped with TCI cryoprobes, respectively. Concentrations for samples were 0.2-0.3 mM as determined by A_{280} measurements, 12 mM ATPγN was added for the nucleotide-bound form, and 0.2-1.2 mM PKI or 0.4-1.8 mM VPS36 for the ternary complex. Full-length PKI was used for all NMR experiments and subsequent analyses. Spectra were collected at 300K, processed using NMRPipe [243], and visualized using Sparky [244].

All [^{1}H-^{15}N]-TROSY-HSQC experiments were acquired with 2048 (proton) and 256 (nitrogen) complex points. Spectra acquired in complex with VPS36 were acquired with substantially more scans (NS = 96) compared to other spectra (NS = 32-64). Combined chemical shift perturbations were calculated using ^{1}H and ^{15}N chemical shifts according to the following:

$$\Delta\delta = \sqrt{(\Delta\delta H)^2 + 0.154(\Delta\delta N)^2} \qquad (1)$$

Change in chemical shift perturbations were calculated according to the following for both nucleotide binding and pseudo-substrate binding:

$$\Delta CSP = \Delta\delta_{WT} - \Delta\delta_{L205R}$$

Chemical Shift Analyses.

COordiNated ChemIcal Shift bEhavior (CONCISE). CONCISE was used to monitor chemical shift trajectories and measure the change in equilibrium position using each PKA-C construct (apo, ATPγN, ATPγN/PKI, ATPγN/VPS36). Using principal component analysis (PCA), this method identifies sets of residues whose chemical shifts respond linearly to the conformational transition. Each residue provides a measure of the equilibrium position for every PKA-C construct in the form of scores along the first principal component (PC1). The equilibrium position for a given construct is given by the average of all PC scores over all linear residues. To identify the residues whose chemical shift's follow a linear trajectory, a threshold of 3.0 for the ratio of the standard deviations of PC1 over PC2 was used, and residues not exhibiting a significant chemical shift were excluded based on linewidth. After this threshold was applied, a total of 55 residues formed the

subset that was used to trace the equilibrium position of each state for PKA-C^{WT} and PKA-C^{L205R}.

CHEmical Shift Covariance Analysis (CHESCA). CHESCA was used to identify and functionally characterize allosteric networks of residues eliciting concerted responses to nucleotide, pseudo-substrate, and substrate. A total of three states were used to identify inter-residue correlations: apo, ATPγN-bound, and either ATPγN/PKI- or ATPγN/VPS36-bound. Identification of inter-residue correlations by CHESCA relies on agglomerative clustering (AC) and singular value decomposition (SVD). Pairwise correlations between chemical shift variations experienced by different residues are analyzed to identify networks of coupled residues and when plotted on a correlation matrix, allows for the identification of regions that are correlated to one another. A correlation coefficient cutoff of 0.98 was used to filter non-linear residues. Residues not exhibiting a significant chemical shift (small shifts in ppm) were excluded based on linewidth. Linewidth was calculated for each resonance in each of the three forms (apo, ATPγN, ATPγN/PKI or ATPγN/VPS36). For each residue the max change in chemical shift was calculated in both the ^{1}H (*x*) and ^{15}N (*y*) dimension ($\Delta\delta_{x,y}$). Residues were included in CHESCA analysis only if they satisfied the following: $\Delta\delta_{x,y} > ½\ \Delta\delta_{xA,yA} + ½\ \Delta\delta_{xB,yB}$, where *A* and *B* correspond to two different forms analyzed (note there is no dependence on which two forms satisfied this statement).

MD Simulations.

System Setup on WT and L205R. We used the crystal structure of PKA-C^{WT} (PDB ID: 1ATP) [79] and PKA-C^{L205R} (PDB ID: 4WB6) [106] as the template, and chose a monomer (Chain A: protein, Chain I: PKI_{5-24}) from the dimer. We further aligned the current structure with the full length PKA-C^{WT} and added the missing residues 1-12 at the N terminus. The protonation state of histidine residues followed our previous settings [47]. The protein was solvated in a rhombic dodecahedron solvent box with TIP3P [245] water molecule layer extended approximately 10 Å away from the surface of the proteins. Counter ions (K^+ and Cl^-) were added to ensure electrostatic neutrality corresponding to an ionic concentration of ~150 mM. All protein covalent H-bonds were constrained with the LINCS [246] algorithm. and long-range electrostatic interactions are treated with the particle-mesh Ewald [247] method with a real-space cutoff of 10 Å. Parallel simulations on the apo form, the binary form with one Mg^{2+} ion and one ATP, and the ternary form with two Mg^{2+} ions,

one ATP and one PKI_{5-24} were performed simultaneously using GROMACS 4.6 [248] in CHARMM36a1 force fields [249]. Each system was minimized using the steepest decent algorithm to remove the bad contacts, and then gradually heated to 300K at a constant volume over 1 ns, using harmonic restraints with a force constant 1000 kJ/(mol*Å^2) on heavy atoms of both proteins and nucleotides. Over the following 12 ns of simulations at constant pressure (1 atm) and temperature (300K), the restraints were gradually released. The systems were equilibrated for an additional 20 ns without positional restraints. A Parrinello-Rahman barostat [250] was used to keep the pressure constant, while a V-rescale thermostat with a time step of 2 fs was used to keep the temperature constant. Each system was simulated for 1.05 μs, with snapshots recorded every 20 ps. A total 3.15 μs and 157500 conformations were utilized for the analyses.

Energy Landscapes using Principal Component Analysis. Cartesian principal components of the backbone atoms were calculated using the GROMACS [248] modules g_covar and g_anaeig to identify the large-scale, low-frequency conformational dynamics of the catalytic core. All the trajectories were aligned with the starting structure (minimization of the crystal structure to remove bad contacts) using helices E (Residues 140-160) and F (Residues 217-233) as a reference frame. Dominant principal components were computed from the each resulting ensemble from the individual simulations. Moreover, the distance between C^{α} atom of Ser53 and Gly186 was measured to characterize the opening and closing motions of Gly-rich loop. Different trajectories were mapped onto the 2D projection along PC1 and S53-G186 distances.

Docking and simulation of the ternary complexes bound with VPS36 peptide and ATP. The peptide sequence of QIEFYRRLSEEMTQR adopts α-helix in the crystal structure (PDB ID: 2HTH) [251]. The recognition and phosphorylation of the peptide by PKA-C, would require an extended conformation. Therefore, we unwound the helices and used HADDOCK [252] server for docking into the binding cleft of PKA-C for both WT and L205R. Specifically, we used the easy interface and selected the active residues of PKA-C, i.e., 133,168,202,198,204,205,207,230 and 330, as well as the active residues for VPS36, i.e, 3,6,7,9, and 10. The passive residues are set automatically around the active residues by the server. The top-scored structures were further solvated for MD simulations following the same protocol as the ternary complexes with PKI.

Mutual information analysis and mapping of allosteric network. To monitor the allosteric differences of the WT and L205R, MutInf [236] was used to compute mutual information between all residues. MutInf is a python package that translates the distribution of dihedral angles of residues into their conformational entropy and identifies the correlated motions between residues. The time series of dihedral angles in the MD ensemble was computed using g_chi and divided into 6 overlapped blocks, and then correlations of local motions are computed as the mutual information between selected residue pairs in each block. The results were averaged over these blocks to filter out the correlations that were not statistically significant. These matrices of mutual information and their differences were further mapped onto the crystal structure with Xpyder [253] plugin for PYMOL. Graph analysis was applied to detect hubs in the networks and key allosteric communication pathways in PKA-C.

4.6 Acknowledgements

This work was supported by the National Institutes of Health, GM100310 (G.V.) and S10 OD021536 (G.V.), and the CRC/Transregio 166 (Project C1 to D.C.) as well the IZKF Würzburg (grant B-281 to D.C.). KB was partially supported by a fellowship through a grant of the German Excellence Initiative to the Graduate School of Life Sciences, University of Würzburg. NMR experiments were carried out at the Minnesota NMR Center and MD calculations at the Minnesota Supercomputing Institute.

4.7 Author Contributions

C.W. prepared the PKA-C samples; designed, executed, and analyzed all NMR experiments and contributed to the writing of the manuscript. Y.W. carried out all MD simulations and contributed to the writing of the manuscript. C.O. carried out triple resonance NMR experiments for backbone assignment of PKA-C. A.K. carried out the initial NMR, thermodynamics, and kinetic experiments. J.C. assisted in the preparation of PKA-C samples. K.B. and D.C. contributed to the critical analysis of the data and writing of the manuscript. J.G. assisted Y.W. with setting up the MD and Markov model calculations. D.A.B. contributed to the critical analysis of the data and writing of the manuscript. S.S.T. contributed to the writing of the manuscript. G.V designed the experiments and contributed to the writing of the manuscript.

4.8 Supplementary Figures

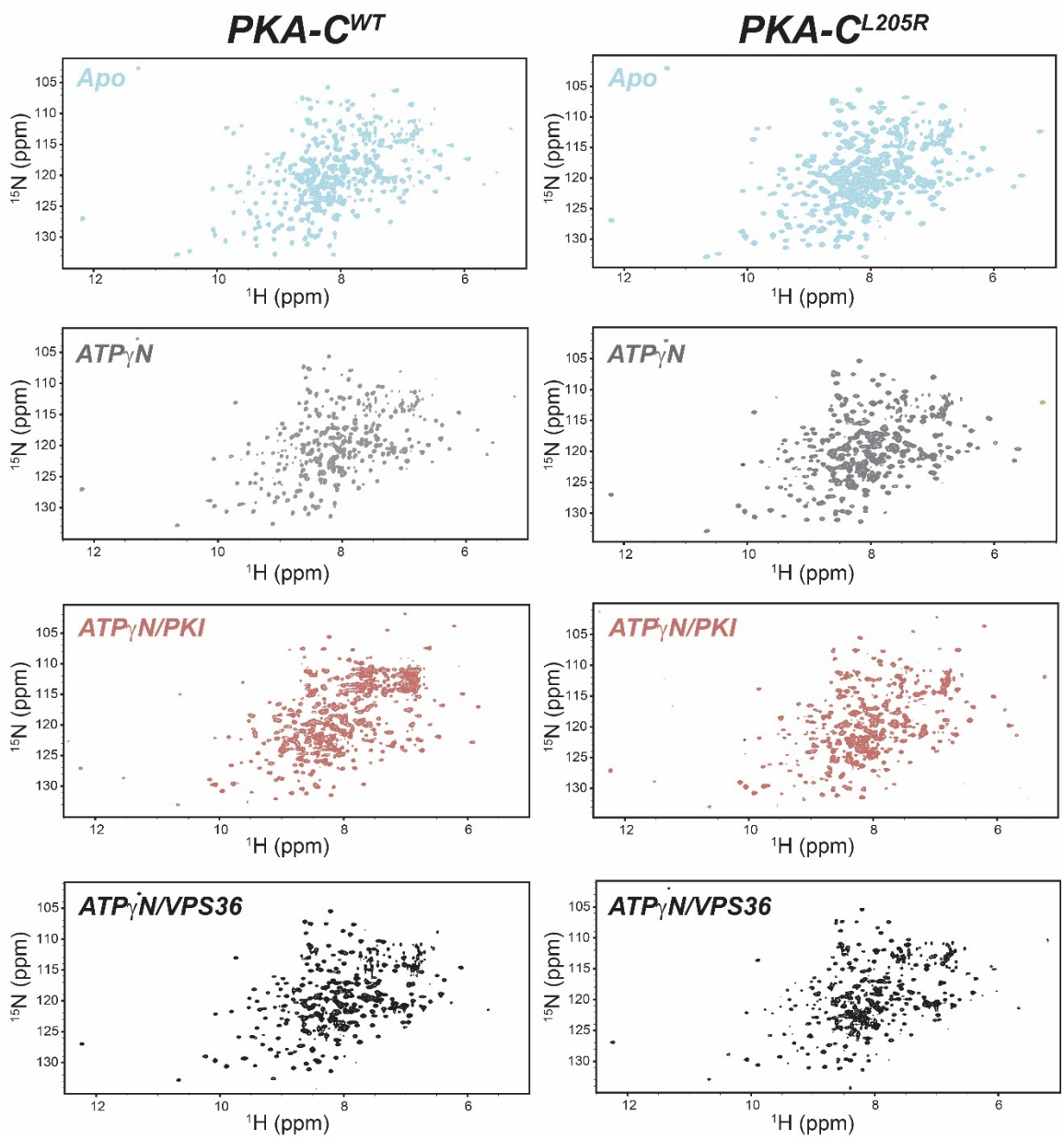

Figure 4.7. [^{1}H, ^{15}N]-TROSY-HSQC spectra for PKA-C^{WT} and PKA-C^{L205R} in apo, ATPγN, ATPγN /PKI-bound and ATPγN/VPS36-bound forms.

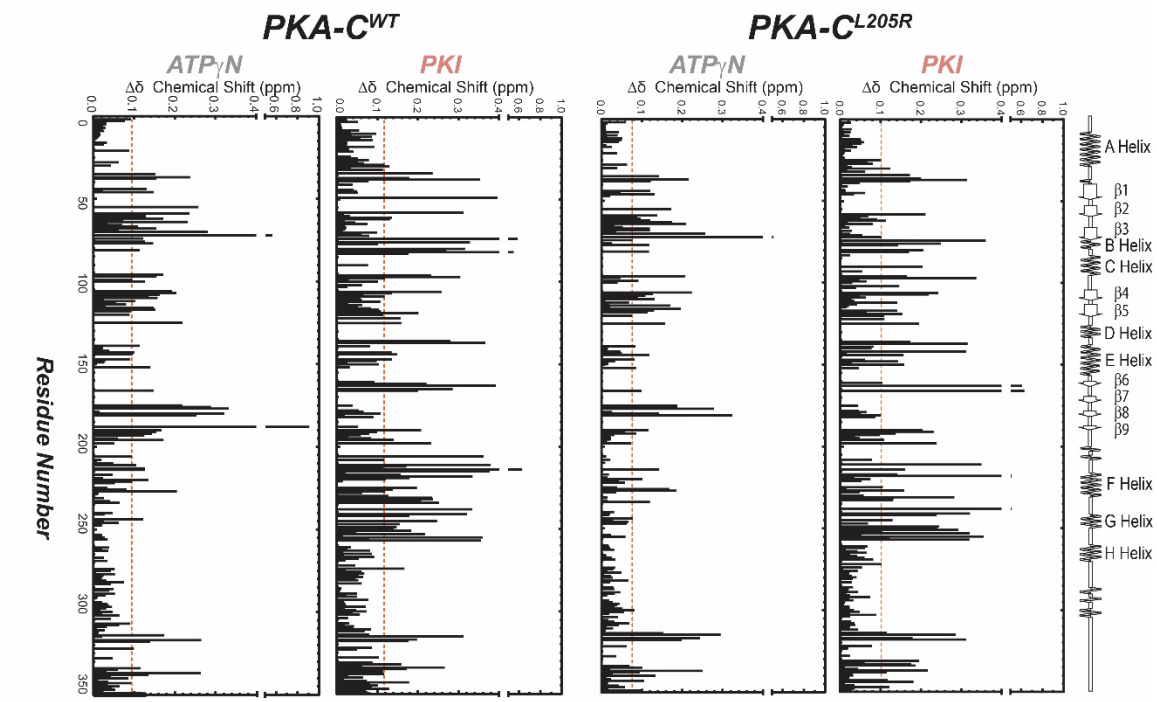

Figure 4.8. Chemical shift perturbations (CSP) observed upon ligand binding for PKA-C^{WT} and PKA-C^{L205R}.
Histograms show the combined $^{1}H/^{15}N$ chemical shift perturbations vs. residue. The cutoff for the average Δδ are given as an orange dashed line.

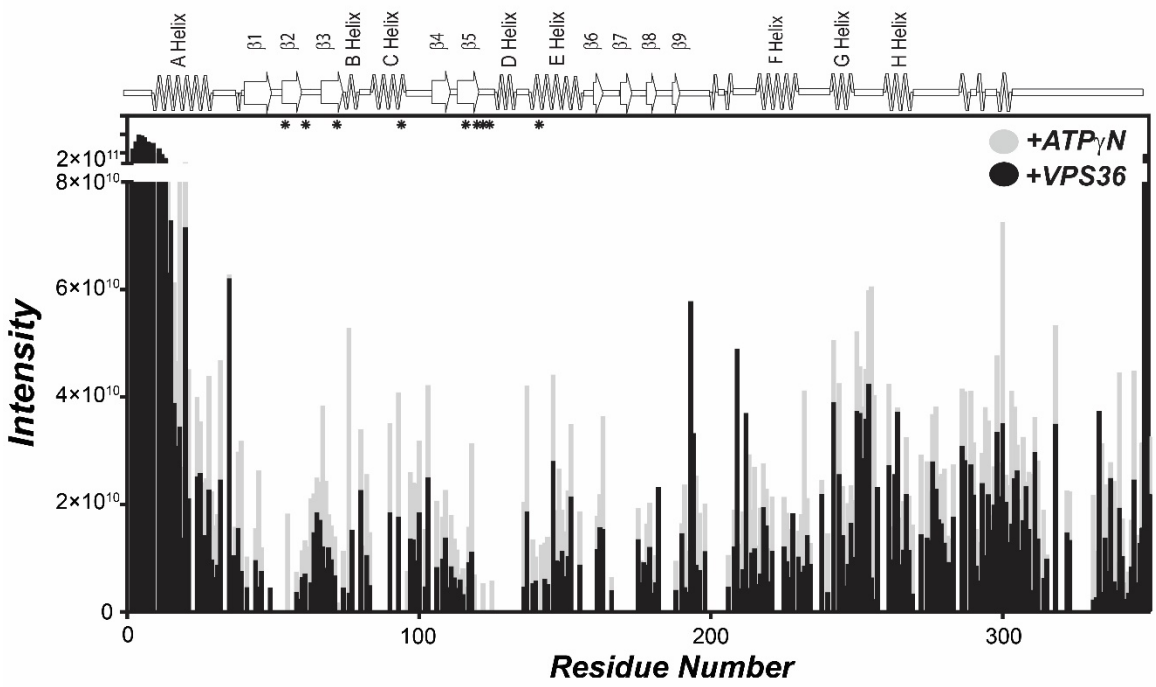

Figure 4.9. Intensity plot for the binding of VPS36 to ATPγN-saturated PKA-C^{L205R}. Asterisks indicate residues that are broadened beyond detection. Intensity was corrected to account for the increase in number of scans following addition of VPS36 and was normalized to the noise level.

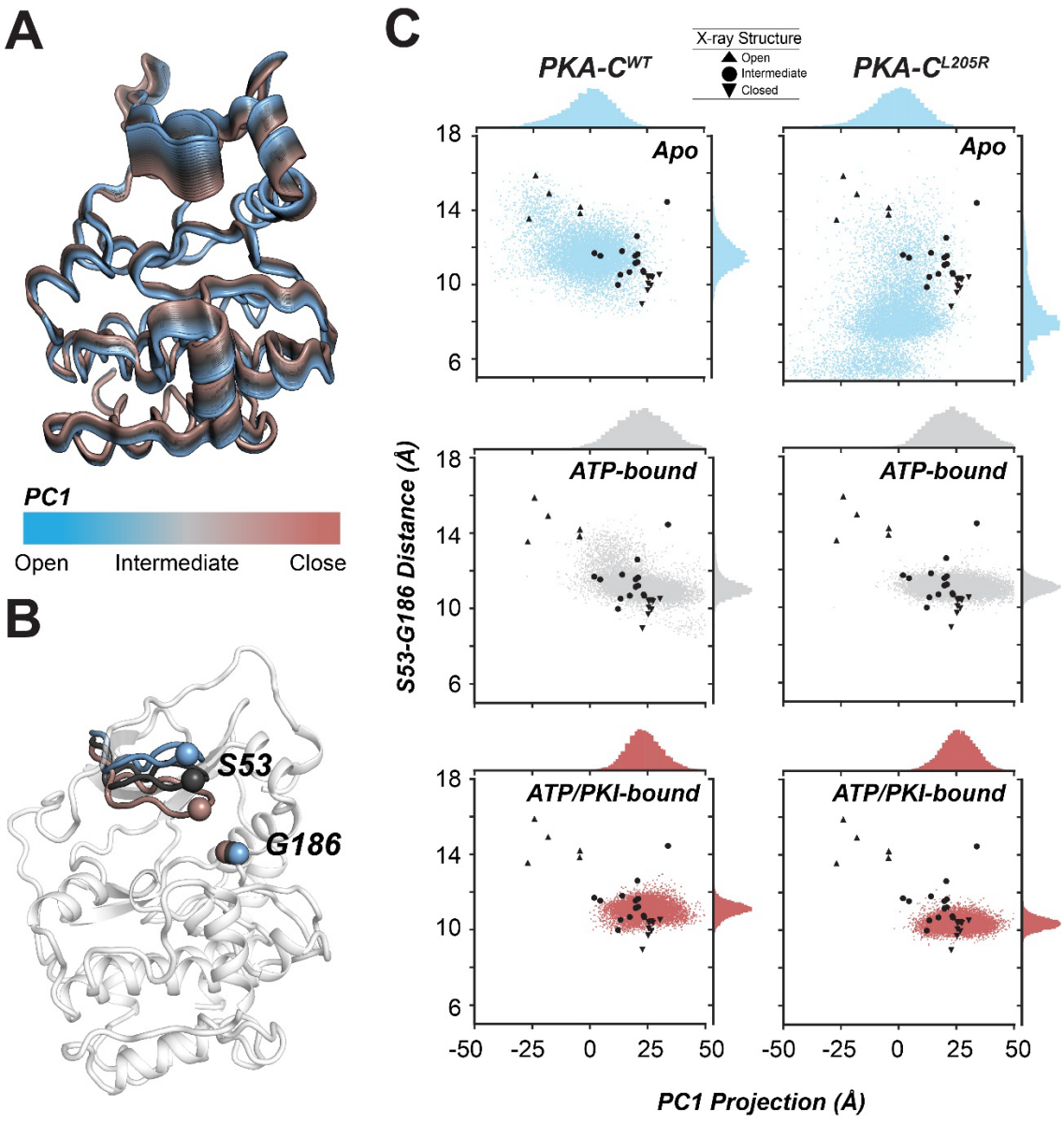

Figure 4.10. Principal component analysis (PCA) of the catalytic lobes in PKA-C^{WT} and PKA-C^{L205R}.

(**A**) The first principal component of the catalytic lobes differentiates the open, intermediate and closed conformations. (**B**) The distances between Cα of S53 and G186 characterize the motion of Gly-rich loop. (**C**) 2D-scattering plot along dS53-G186 and PC1, and the corresponding distribution plots for PKA-C^{WT} (cyan), PKA-C^{WT} /ATP (gray) and PKA-C^{WT} /ATP/PKI (dark pink). Right panel: 2D-scattering plot along dS53-G186 and PC1, and the corresponding distribution plots for PKA-C^{L205R} (cyan), PKA-C^{L205R}/ATP (gray) and PKA-C^{L205R}/ATP/PKI (dark pink). The black shapes correspond to the projection of crystallographic conformations.

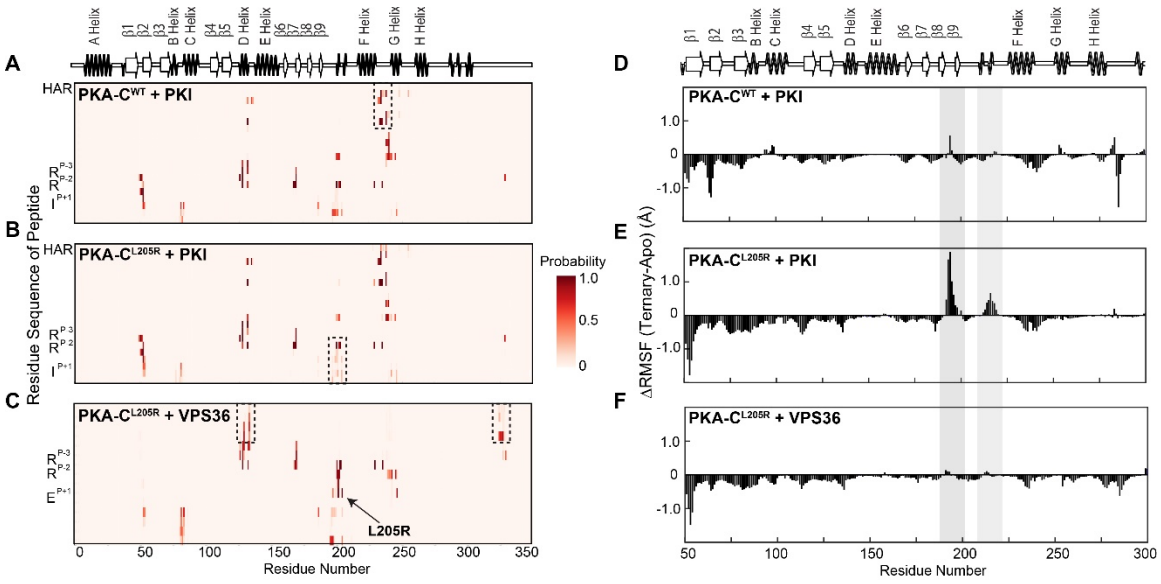

Figure 4.11. Probability of the formation of inter-residue contact and ΔRMSF of PKA-C upon forming ternary complexes with PKI_{5-24} or VPS36.

The probability distribution of the distances for (**A**) PKA-C^{WT} and PKI highlighting stable contact between HAR of PKI and C-lobe of PKA-C^{WT}, (**B**) PKA-C^{L205R} and PKI highlighting the weakened interaction around the activation loop of PKA-C^{L205R}, and (**C**) PKA-C^{L205R} and VPS36 highlighting the stable contact at R205 and the transient contact of the N-terminal region of VPS36 with the hinge region and C-terminal tail of PKA-C^{L205R}. The probability distribution of the distances is defined by a cutoff of 5 Å between heavy atoms of residue pairs. The ΔRMSF of (**D**) PKA-C^{WT} against the apo state upon forming ternary complex with PKI, (**E**) PKA-C^{L205R} against apo state upon forming ternary complex with PKI, and (**F**) PKA-C^{L205R} against apo state upon forming ternary complex with VPS36.

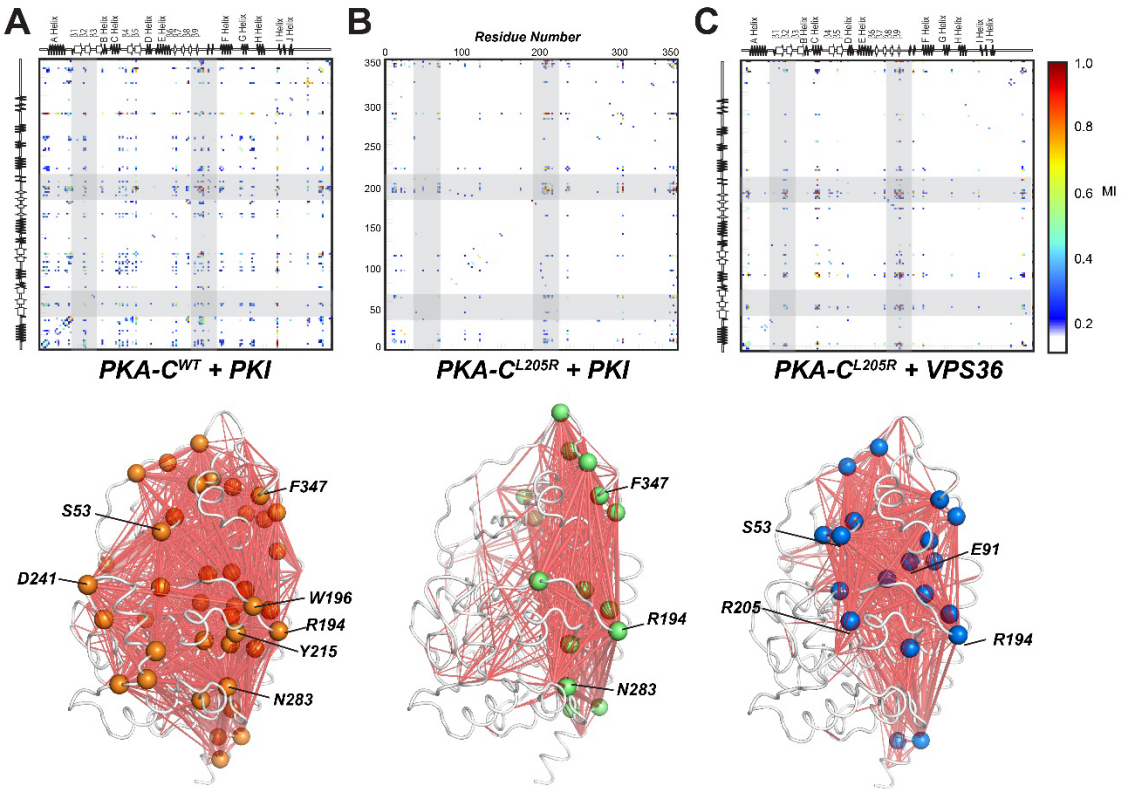

Figure 4.12. Allosteric changes upon peptide binding revealed by MD simulation and mutual information (Mutinf) analysis.
Mufinf matrices of (**A**) PKA-C^{WT} in complex with PKI, (**B**) PKA-C^{L205R} in complex with PKI, and (**C**) PKA-C^{L205R} in complex with VPS36. Mutinf matrices are mapped to the structures of PKA-C^{WT} and PKA-C^{L205R} with a cutoff of 0.15.

4.9 Supplementary Tables

Table 4.1. Changes in enthalpy, entropy, free energy, and dissociation constant of binding ATPγN, PKI_{5-24} and VPS36 for PKA-C^{WT} and PKA-C^{L205R}.
Errors in ΔG, ΔH, -TΔS, and K_d were calculated using triplicate measurements. Errors in σ were propagated from error in K_d. ND (not detected) indicates that the heat released upon binding is below the detection of the instrument. N/A indicates the value is not applicable to the particular measurements.

ATPγN to apo forms					
	K_d (μM)	**ΔG (kcal/mol)**	**ΔH (kcal/mol)**	**-TΔS (kcal/mol)**	**σ**
PKA-C^{WT}	83 ± 8	-5.61 ± 0.06	-3.6 ± 0.1	- 2.0 ± 0.1	N/A
PKA-C^{L205R}	215 ± 15	-5.04 ± 0.04	-6.2 ± 0.3	1.1 ± 0.2	N/A
PKI_{5-24} to apo forms					
	K_d (μM)	**ΔG (kcal/mol)**	**ΔH (kcal/mol)**	**-TΔS (kcal/mol)**	**σ**
PKA-C^{WT}	17 ± 2	-6.57 ± 0.08	-10.8 ± 0.5	4.2 ± 0.5	N/A
PKA-C^{L205R}	61 ± 5	-5.79 ± 0.04	-9.7 ± 0.1	3.9 ± 0.1	N/A
PKI_{5-24} to ATPγN saturated forms					
	K_d (μM)	**ΔG (kcal/mol)**	**ΔH (kcal/mol)**	**-TΔS (kcal/mol)**	**σ**
PKA-C^{WT}	0.16 ± 0.02	-9.33 ± 0.07	-13.9 ± 0.5	4.6 ± 0.4	106 ± 18
PKA-C^{L205R}	10 ± 3	-6.9 ± 0.2	-8.8 ± 0.8	1.9 ± 0.6	6 ± 2
VPS36 to ATPγN saturated forms					
	K_d (μM)	**ΔG (kcal/mol)**	**ΔH (kcal/mol)**	**-TΔS (kcal/mol)**	**σ**
PKA-C^{WT}	ND	ND	ND	ND	N/A
PKA-C^{L205R}	3.5 ± 0.1	-7.51 ± 0.03	-3.2 ± 0.6	-4.3 ± 0.6	N/A

Table 4.2. Kinetic parameters of Kemptide and VPS36 phosphorylation by PKA-C^{WT} and PKA-C^{L205R}.

Values for K_M and k_{cat} were obtained from a non-linear least squares analysis of the concentration-dependent initial phosphorylation rates using a standard coupled enzyme activity assay (related to **Figure 4.3**). Error in k_{cat}/K_M was propagated from error in K_M and k_{cat}.

Kemptide		
	PKA-C^{WT}	**PKA-C^{L205R}**
V_{max} (μM/sec)	0.42 ± 0.02	0.90 ± 0.02
K_M (μM)	29 ± 1	335 ± 17
k_{cat} (s^{-1})	19 ± 1	41 ± 1
k_{cat}/K_M	0.66 ± 0.04	0.12 ± 0.01
VPS36		
	PKA-C^{WT}	**PKA-C^{L205R}**
V_{max} (μM/sec)	0.12 ± 0.02	0.39 ± 0.01
K_M (μM)	224 ± 48	326 ± 20
k_{cat} (s^{-1})	5 ± 1	18 ± 1
k_{cat}/K_M	0.022 ± 0.006	0.055 ± 0.004

Table 4.3. PCA and standard deviation of the CONCISE analysis of the structural states analyzed.

	PCA1	SD	% Closed
PKA-C^{WT} *Apo*	-1.213	0.56	0%
PKA-C^{L205R} *Apo*	-1.042	0.57	7%
PKA-C^{WT} *ATPγN*	-0.059	0.56	45%
PKA-C^{L205R} *ATPγN*	-0.082	0.53	44%
PKA-C^{WT} *ATPγN/PKI*	1.335	0.61	100%
PKA-C^{L205R} *ATPγN/PKI*	0.904	0.55	83%
PKA-C^{WT} *ATPγN/VPS36*	-0.072	0.54	45%
PKA-C^{L205R} *ATPγN/VPS36*	0.229	0.79	57%

Table 4.4. Melting temperatures (T_m) as determined using circular dichroism.
All values are in °C and T_m was taken as the inflection point at which 50% of the enzyme complex was folded. Error was calculated using triplicate measurements.

	Apo	**Binary (MgATP)**	**Ternary (MgATP + PKI_{5-24})**
PKA^{WT}	53.2 ± 0.5	55.0 ± 0.7	60.2 ± 0.4
PKA^{L205R}	53.2 ± 0.4	56.7 ± 0.2	58.0 ± 0.3

Chapter 5 Defective Internal Allosteric Network Imparts Dysfunctional ATP/Substrate Binding Cooperativity in Oncogenic Chimera of Protein Kinase A

Cristina Oliveri[1†], Caitlin Walker[1†], Adak Karamafrooz[1†], Yingjie Wang[1,2‡], Manu V.S.[1], Fernando Porcelli[3], Donald K. Blumenthal[4], David D. Thomas[1], David A. Bernlohr[1], Simon M. Sandford[5], Susan S. Taylor[6,7], and Gianluigi Veglia[1,2*]

[1]Department of Biochemistry, Molecular Biology, and Biophysics and [2]Chemistry, University of Minnesota, Minneapolis, MN 55455, USA.

[3]DIBAF – University of Tuscia – Largo dell' Università, 01100 Viterbo, Italy.

[4]Department of Pharmacology and Toxicology, University of Utah, Salt Lake City, UT 84112, USA.

[5]Laboratory of Cellular Biophysics, Rockefeller University, New York, NY 10065, USA.

[6]Departments of Chemistry and Biochemistry and [7]Pharmacology, University of California San Diego, La Jolla, CA 92093, USA.

†These authors contributed equally.

‡Present address: Shenzhen Bay Laboratory, Shenzhen 518055, China.

Reprinted from *Communications Biology* 4(321).

5.1 Synopsis

An aberrant fusion of the *DNAJB1* and *PRKACA* genes generates a chimeric protein kinase (PKA-C^{DNAJB1}) in which the J-domain of the heat shock protein 40 is fused to the catalytic α subunit of cAMP-dependent protein kinase A (PKA-C). Deceivingly, this chimeric construct appears to be fully functional, as it phosphorylates canonical substrates, forms holoenzymes, responds to cAMP activation, and recognizes the endogenous inhibitor PKI. Nonetheless, PKA-C^{DNAJB1} has been recognized as the primary driver of fibrolamellar hepatocellular carcinoma and is implicated in other neoplasms for which the molecular mechanisms remain elusive. Here we determined the chimera's allosteric response to nucleotide and pseudo-substrate binding. We found that the fusion of the dynamic J-domain to PKA-C disrupts the internal allosteric network, causing dramatic attenuation of the nucleotide/PKI binding cooperativity. Our findings suggest that the reduced allosteric cooperativity exhibited by PKA-C^{DNAJB1} alters specific recognitions and interactions between substrates and regulatory partners contributing to dysregulation.

5.2 Introduction

Fibrolamellar hepatocellular carcinoma (FL-HCC) is a rare and aggressive form of liver cancer that predominantly affects young patients without underlying cirrhosis or disease[254]. Treatment is limited, as FL-HCC does not respond to chemotherapy[255, 256], and surgical excision remains the only therapy[257, 258]. Sequencing the tumor genomes of FL-HCC patients identified a recurrent chimeric gene[31, 32, 259, 260] that originates from a ~400kb deletion in chromosome 19. This deletion causes an in-frame fusion of exon 1 from the *DNAJB1* gene, which encodes a member of the heat-shock protein 40 family, with exons 2-to-10 of the *PRKACA* gene, encoding for the catalytic subunit of cAMP-dependent protein kinase A (PKA-C)[31]. The resulting chimeric enzyme (PKA-C^{DNAJB1}) is fully functional and comprises 405 residues with 69 amino acids of DNAJB1 (J-domain), replacing the first 14 residues of the N-terminal αA-helix of PKA-C[31]. The N-terminal deletion of part of the αA-helix prevents essential post-translational modifications such as N-myristoylation, deamidation, as well as phosphorylation at Ser10, which are responsible for the spatiotemporal localization of the kinase[42, 261].

The fusion of the J-domain does not alter the structure of the catalytic core of PKA-C^{DNAJB1}, which remains virtually identical to the wild-type kinase (PKA-C^{WT}). Instead, the αA-helix of PKA-C^{DNAJB1} is extended with the J-domain tucked under the large lobe of the enzyme (**Figure 5.1 panel A**)[106]. Moreover, PKA-C^{DNAJB1} retains the ability to form stable holoenzymes with all regulatory (R) subunit isoforms, although with non-canonical arrangements, and more importantly, responds to cAMP activation[262, 263]. *In vivo* enzymatic assays, as well as conventional *in vitro* coupled assays, have shown that the kinetic parameters of PKA-C^{WT} and PKA-C^{DNAJB1} are similar[31, 262, 264]. Furthermore, PKA-C^{DNAJB1} binds the endogenous inhibitor PKI (both full-length and derived peptides) with an affinity comparable to wild-type[264].

Despite little differences conferred to the structure and activity of the kinase by the fusion of the J-domain, *in vivo* studies have shed light on the signaling changes induced by the chimeric fusion. Recently, Scott and co-workers suggested that the J-domain is able to recruit Hsp70, stabilizing the chimeric fusion protein[108]. Together with the higher expression levels due to the *DNAJB1* gene[31], the enhanced stability of the enzyme in complex with Hsp70 may explain the dominant expression in FL-HCC cells. Furthermore, these researchers showed that the phosphoproteomics of PKA-C^{DNAJB1} is different from

that of the wild-type, implying that the J-domain skews the phosphorylation profile of cells toward alternative pathways[108]. According to this study, the J-domain is directly implicated in the oncogenicity of PKA-C^{DNAJB1}. However, other evidence shows that the kinase domain is also required for tumorigenesis[105]. To date, it remains unclear how this aberrant kinase contributes to the progression of the disease.

A prominent feature of PKA-C is the alternation of positive and negative binding cooperativity that drives the enzymatic cycle[83]. Positive binding cooperativity induced by ATP binding enhances the affinity for the substrate, while negative binding cooperativity of ADP facilitates the release of the phosphorylated product. Since binding cooperativity is essential to signal transduction amplification[265], we surmised that the nucleotide/substrate binding cooperativity of the aberrant kinase is disrupted, with implications for phosphorylation profiles and regulation by R-subunits. With this in mind, we investigated local and global responses of the kinase to nucleotide and pseudo-substrate binding using a combination of NMR spectroscopy, isothermal titration calorimetry (ITC), small-angle X-ray scattering (SAXS), and molecular dynamics (MD) simulations. We found that the J-domain fused to the N-terminus of PKA-C dramatically attenuates the canonical positive nucleotide/pseudo-substrate binding cooperativity through alterations in the intramolecular network of communication. Analogous to other pathologic mutants of PKA-C[65], the concomitant loss in binding cooperativity and intramolecular communication may render highly cooperative events, such as regulation, dysfunctional, contributing to disease progression.

5.3 Results

The dynamic J-domain of PKA-C^{DNAJB1} interconverts between *in* and *out* conformations. Previous X-ray crystallographic studies[106] have shown that the core of PKA-C^{DNAJB1} adopts a conformation similar to the wild-type. The catalytic domain in complex with an ATP analog and a pseudo-substrate peptide is virtually superimposable to the structure of the wild-type enzyme[36, 106], while the J-domain of the chimera is tucked tightly under the large lobe of the enzyme (**Figure 5.1 panel A**). In contrast, our computational and solution NMR studies suggest that PKA-C^{DNAJB1} spans a large ensemble of conformations, with the J-domain undergoing fast re-orientational dynamics relative to the core of the enzyme[64]. To provide orthogonal validation, we compared the SAXS profiles of PKA-C^{WT} and PKA-C^{DNAJB1}. For both binary (ATPγN-bound) and ternary

(ATPγN/PKI-bound) complexes of PKA-C^{DNAJB1}, we fit the SAXS profiles with the compact (J-domain *in*), intermediate, and extended (J-domain *out*) conformations extracted from the trajectories of molecular dynamics (MD) simulations (**Figure 5.1 panel B,C**). We found all structures fit well with the SAXS profile with $\chi < 1.0$ in the low q region ($q < 0.2$ Å^{-1}). However, the radius of gyration (R_g) increases from 23.7 to 26.9 Å, indicating that the J-domain can dislodge from the kinase core and adopt an extended conformation. In contrast, the flexible N-terminus of PKA-C^{WT} is much smaller and does not influence the R_g of the enzyme (21.7 Å) for both binary and ternary complexes (**Figure 5.7**). The addition of PKI to nucleotide-saturated PKA-C^{WT} and PKA-C^{DNAJB1} does not change the SAXS profiles, suggesting that PKI binding does not alter the overall size and shape of the two kinases.

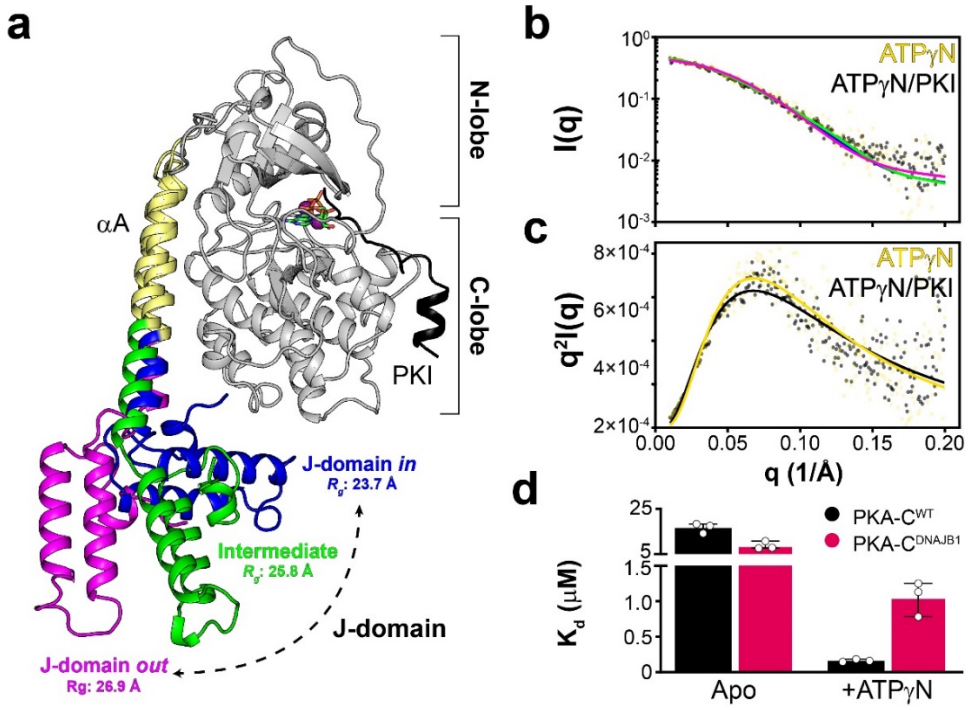

Figure 5.1. Multiple conformations adopted by the dynamic J-domain alters allosteric binding cooperativity of PKA-C.
a Overlay of selected snapshots of PKA-C^{DNAJB1} from the MD trajectories highlighting the ensemble of conformers sampled by the J-domain. **b** SAXS profiles of PKA-C^{DNAJB1}. Continuous lines show the structural fitting of the experimental SAXS data with the closed (J-domain *in*, blue), intermediate (green), and extended (J-domain *out*, magenta) conformations for binary (ATPγN-bound) and ternary (ATPγN/PKI-bound) forms. The conformations are extracted from the MD trajectories. **c** Corresponding Kratky plot of PKA-C^{DNAJB1} bound to ATPγN and ATPγN/PKI. **d** Bar graph showing the dissociation constants (K_d) calculated from the ITC titration curves of PKI$_{5-24}$ binding to the apo and ATPγN-bound forms of PKA-C^{WT} and PKA-C^{DNAJB1} (see also **Table 5.2**).

The J-domain of PKA-C^{DNAJB1} reduces the nucleotide/substrate degree of binding cooperativity (σ). Previous studies from our group have shown that PKA-C^{WT}, a K-type enzyme, exhibits positive binding cooperativity between nucleotide (ATPγN) and pseudo-substrate (PKI_{5-24}), which can be reduced by mutation while maintaining maximal rate[65, 71, 82]. Thus, we sought to understand how this canonical positive binding cooperativity is altered in PKA-C^{DNAJB1}, using isothermal titration calorimetry (ITC). For the binding of nucleotide alone, PKA-C^{DNAJB1} exhibits a 4-fold higher binding affinity for ATPγN compared to PKA-C^{WT} (K_d = 19 ± 4 μM versus 83 ± 8 μM; **Table 5.1** and **Figure 5.8**). To determine the degree of binding cooperativity (σ) for PKA-C^{DNAJB1}, we monitored the binding affinity of PKI_{5-24} in the absence and presence of nucleotide. In the absence of nucleotide, PKA-C^{DNAJB1} binds PKI_{5-24} with a 2-fold higher affinity compared to wild-type (K_d =9 ± 2 μM versus 17 ± 2 μM; **Figure 5.1 panel D** and **Figure 5.8**). In contrast, upon saturation with nucleotide, the PKA-C^{DNAJB1}/ATPγN complex binds PKI_{5-24} with a 7-fold decrease in binding affinity (K_d =1.1 ± 0.2 μM versus 0.16 ± 0.02 μM). Together, these data show that addition of the J-domain causes a sizeable decrease (13-fold) in nucleotide/pseudo-substrate binding cooperativity (**Table 5.2**).

To evaluate the effect of the dramatic reduction in binding cooperativity on the ability of PKA-C^{DNAJB1} to perform phosphoryl transfer, we used steady-state coupled enzyme assays. Specifically, we evaluated the catalytic efficiencies of PKA-C^{WT} and PKA-C^{DNAJB1} toward the standard peptide substrate, Kemptide, physiological substrate, CREB, and a known hyper-phosphorylated substrate identified by Scott and coworkers, KSR1[108] (**Figure 5.2 panel A**). Though the substrates displayed different maximal velocities (V_{max} = 0.21 – 0.35 μM/s) and Michaelis constants (K_M = 29-56 μM), PKA-C^{DNAJB1} consistently displayed higher V_{max} values resulting in slightly higher catalytic efficiencies (k_{cat}/K_M) compared to wild-type for all substrates tested (**Figure 5.2 panel B**, **Table 6.3**, and **Figure 5.9**). While the binding cooperativity is affected by the presence of the J-domain, these assays with peptides encompassing the recognition sequences of different substrates demonstrate that the kinetic parameters are only marginally altered as reported previously[264].

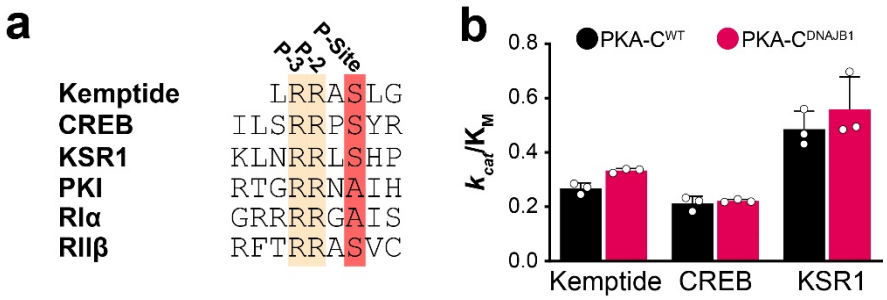

Figure 5.2. Attenuation in binding cooperativity does not influence phosphoryl transfer. **a** Comparison of the substrate recognition sequences of substrates Kemptide, CREB, and KSR1, regulatory subunits, RIα and RIIβ, and endogenous inhibitor, PKI. **b** Bar graph displaying the catalytic efficiencies (k_{cat}/K_M) of PKA-C^{WT} and PKA-C^{DNAJB1} towards Kemptide, CREB, and KSR1. Errors were calculated from triplicate measurements. All kinetics parameters are summarized in **Table 5.3** and shown in **Figure 5.9**.

The J-domain disrupts the internal allosteric network of PKA-C^{DNAJB1}. To determine the origin of the decreased allosteric binding cooperativity, we analyzed the structural response of the kinases to ligand binding using solution NMR spectroscopy. Specifically, we mapped the amide fingerprints of both enzymes using [^{1}H, ^{15}N]-TROSY-HSQC experiments[266] upon addition of nucleotide and PKI$_{5-24}$ (**Figure 5.10**). The amide fingerprints of PKA-C^{WT} and the PKA-C^{DNAJB1} kinase core are almost superimposable, reflecting their identical structures. This similarity enabled us to transfer the previously assigned PKA-C^{WT} amide resonances[82] to the PKA-C^{DNAJB1} spectrum (**Figure 5.10 panel A**). To assign the remaining resonances of the J-domain, we expressed the 69-residue construct (DNAJB1$_{1-69}$) uniformly labeled with ^{15}N and ^{13}C in *E. coli* bacteria and assigned the resonances in the [^{1}H, ^{15}N]-TROSY-HSQC spectrum using the classical *out-and-back* triple-resonance experiments (**Figure 5.11**). A total of 340 amide resonances were assigned over the 388 expected. As previously reported[267], the DNAJB1$_{1-69}$ domain folds autonomously, and its resonances overlay with those of the J-domain fused to PKA-C^{DNAJB1} (**Figure 5.10 panel B**). To analyze the kinases response to ATPγN and PKI$_{5-24}$ binding, we followed the ^{1}H and ^{15}N chemical shift perturbations (CSPs) of the amide fingerprints for the two kinases. We found that the fingerprints of both PKA-C^{WT} and PKA-C^{DNAJB1} show similar CSPs upon binding ATPγN (**Figure 5.12 panel A**). However, residues of PKA-C^{DNAJB1} encompassing the Gly-rich loop, activation loop, αF-helix, αG-helix, and the C-terminal tail show greater CSPs compared to PKA-C^{WT}. Notably, these domains undergo the largest structural rearrangements from the open (apo) to closed

(ternary) form. The J-domain is not directly involved in the binding events as it experiences CSPs well below one standard deviation. As for PKA-C^{WT}, the binding of ATPγN causes broadening of amide resonances throughout the core of PKA-C^{DNAJB1}, suggesting the presence of conformational dynamics in the μs-ms timescale[268]. Upon binding PKI_{5-24} to the ATPγN-saturated kinase, the CSPs of the kinase cores are similar, with effects propagated from the substrate-binding sites to both small and large lobes (**Figure 5.12 panel B**). The J-domain remains structurally isolated from the core as we observe only a few chemical shift changes upon binding PKI_{5-24}. As found for PKA-C^{WT}, PKI_{5-24} binding sharpens the amide fingerprint resonances, indicating that the enzyme is trapped in a well-defined conformational minimum[82]. The linewidths of the J-domain, on the other hand, are unperturbed, suggesting that pseudo-substrate binding does not change its conformational dynamics.

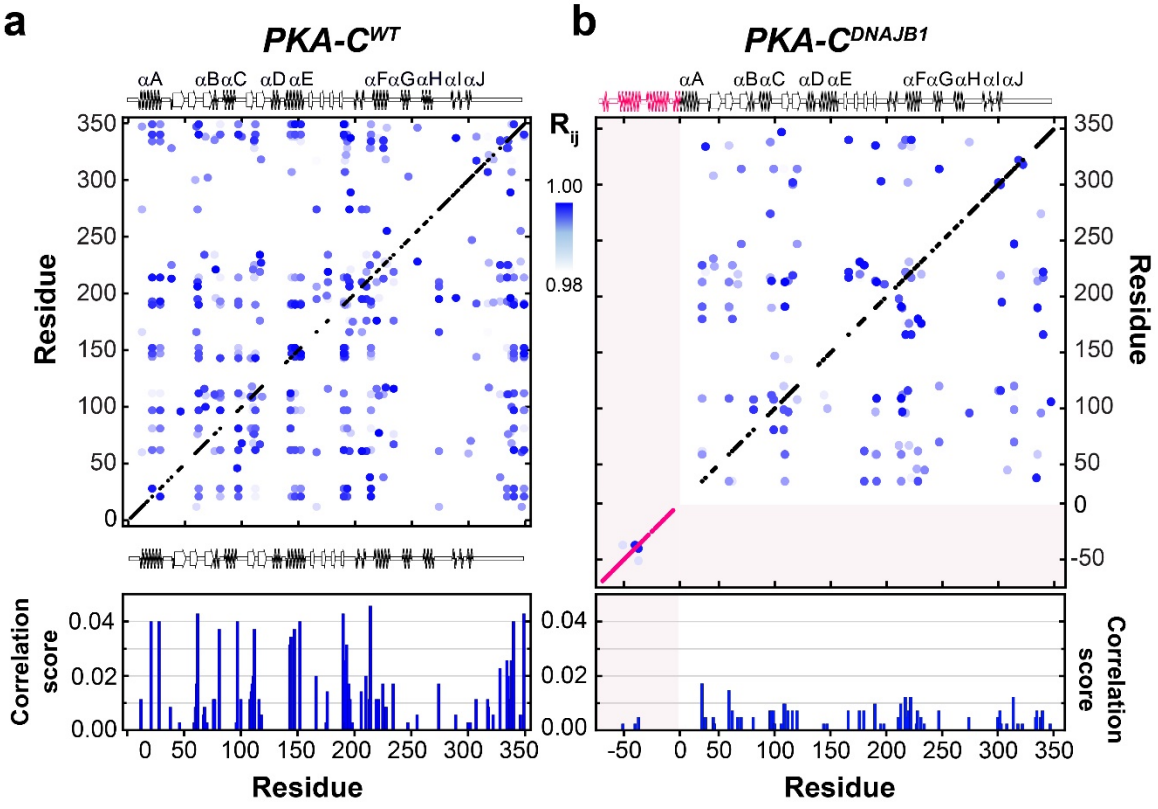

Figure 5.3. Defective internal allosteric network of PKA-C^{DNAJB1}.
Chemical shift correlation matrices for **a** PKA-C^{WT} and **b** PKA-C^{DNAJB1}. The cross-peaks represent pairs of residues with the absolute value of the Pearson's coefficient ≥ 0.98. The secondary structures for the two kinases are reported above and below the matrix. The bar graphs shown below each matrix report the average correlation scores per residue (see Materials and Methods section).

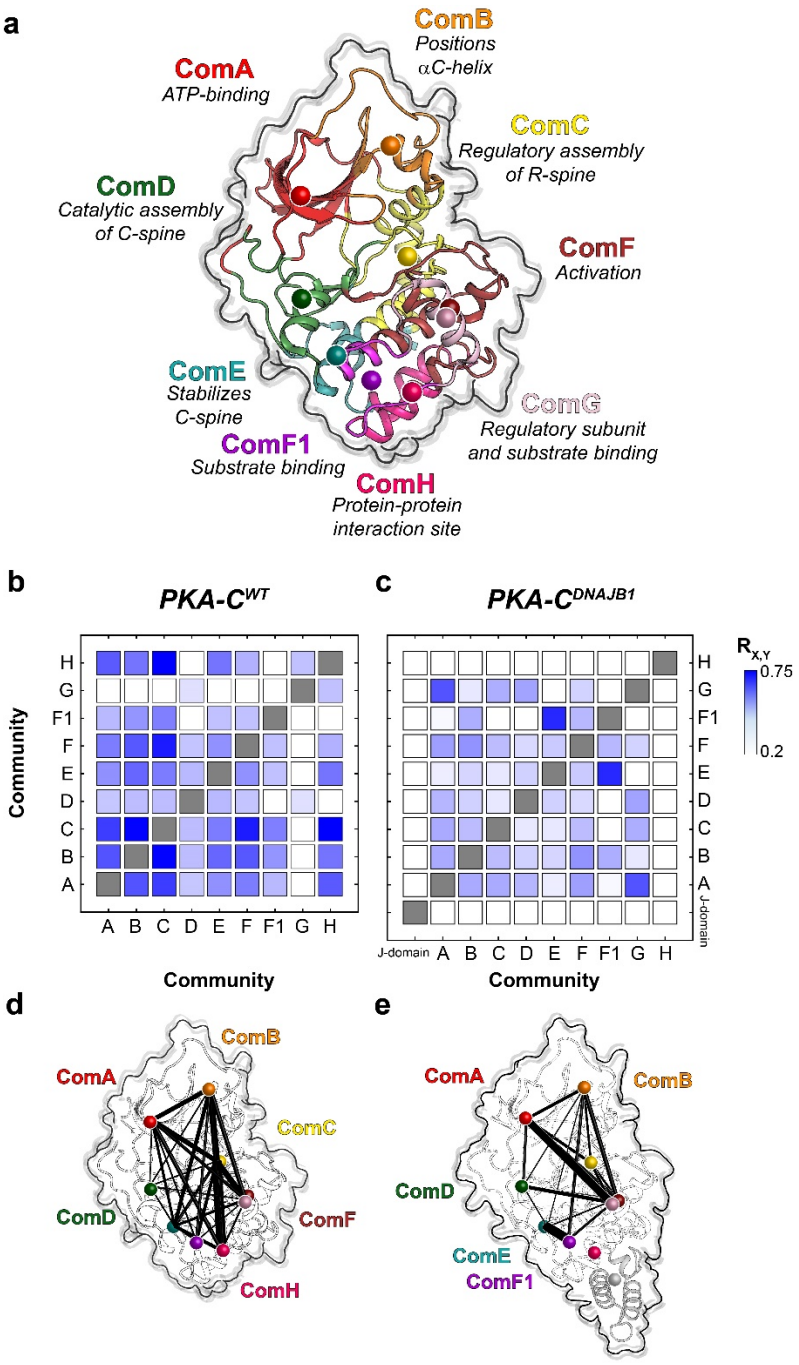

Figure 5.4. Reduced crosstalk amongst structural communities of chimeric PKA-C^{DNAJB1} relative to PKA-C^{WT}.

a Structure of PKA-C highlighting all communities and their roles in various functions and regulatory mechanisms. CHESCA community matrices for **b** PKA-C^{WT} and **c** PKA-C^{DNAJB1} upon binding PKI$_{5-24}$. **d-e** CHESCA community matrices plotted on their corresponding structures. The size of each node is independent of the number of residues it encompasses, meanwhile the weight of each line indicates the strength of coupling between the individual communities.

To analyze the internal network of communication of both PKA-C^{DNAJB1} and PKA-C^{WT}, we used CHEmical Shift Covariance Analysis (CHESCA)[129, 132]. This method identifies allosteric networks among the protein residues by tracking each residue's coordinated changes of chemical shifts in response to ligand binding or mutations. For a binding process occurring in the fast NMR timescale, the resonances associated with allosterically coupled residues exhibit a correlated linear response. When plotted on a correlation matrix, changes in allosteric networks manifest as variations in the number and extent of inter-residue correlations[131, 132]. We analyzed the chemical shift responses of four different forms of the kinase: apo, ATPγN-bound, ADP-bound, and ATPγN/PKI_{5-24}-bound. The CHESCA matrix of PKA-C^{WT} shows a coordinated response for many residues spanning the entire enzyme, with a higher density of correlations in the N-lobe near the nucleotide-binding site and the substrate-binding groove at the interface between the N- and C-lobes (**Figure 5.3 panel A**). These correlations constitute central allosteric nodes necessary for binding cooperativity[65, 81, 83]. Additionally, allosteric crosstalk exists between residues in the C-terminal tail and residues in the αA-helix (K21, K28), αE-helix (R144, A147, L152), activation loop (R190, V191, G193), and αF-helix (G214, G225). In contrast, the matrix of PKA-C^{DNAJB1} exhibits an overall attenuation in CHESCA correlations throughout the entire kinase, with a rewiring of the network between nucleotide and substrate binding sites. Specific structural domains such as the αA-helix (K21, K27), αE-helix (A143, R144, A147, L152), αC-helix (Q96, A97), and C-terminal tail (I335, N340, E349) are more noticeably attenuated (**Figure 5.3 panel B**). The functional relevance of this extensive rewiring of the intramolecular communication is apparent when we combined CHESCA with the definition of the structural and functional communities (community CHESCA)[140]. Upon dividing the kinase into nine different communities defined by McClendon *et al* (**Figure 5.4 panel A**)[140], each with different structural and functional roles, we observe a clear parallel between experimental data and theory[81, 140]. The correlation matrix for community CHESCA for PKA-C^{WT} (**Figure 5.4 panel B**) shows that structurally adjacent communities in the N-lobe and at the N/C lobe interface (ComA, ComB, ComC, and ComE) are strongly coupled with distal communities (ComH) as they exhibit high correlation coefficients ($R_{X,Y}$). A structural representation of the extent of coupling is reported in **Figure 5.4 panel D**, where crosstalk between the nucleotide-binding (ComA) with the positioning of the αC-helix (ComB), the R-spine assembly (ComC) and the activation loop (ComF) is apparent. Although attenuated, there is

substantial coupling between these communities and the more peripheral communities that have structural roles, such as ComH. The cooperative response to nucleotide and PKI_{5-24} binding involves the entire enzyme, causing coordinated CSPs interspersed throughout its three-dimensional structure. In contrast, the community CHESCA for PKA-C^{DNAJB1} exhibits a dramatic decrease in inter-community coupling (**Figure 5.4 panel C, E**). The coupling network between the ATP-binding site (ComA) and the αC-helix (ComC) or the activation loop (ComF) is sparse. Notably, the correlations between the N-lobe communities with peripheral communities in the C-lobe (ComD and ComE) are either notably reduced or lost. This phenomenon is especially evident for ComH located near the J-domain, which includes residues that are involved in docking of the R-subunits or kinase binding partners. Other correlations not found in the wild-type are observed between ComG and ComA, ComB, ComD, and ComF; and stronger correlations are observed between ComE and ComF1. Overall, the community CHESCA show that the reduced degree of cooperativity determined thermodynamically corresponds to a decrease in coordinated structural changes upon ligand binding in PKA-C^{DNAJB1}.

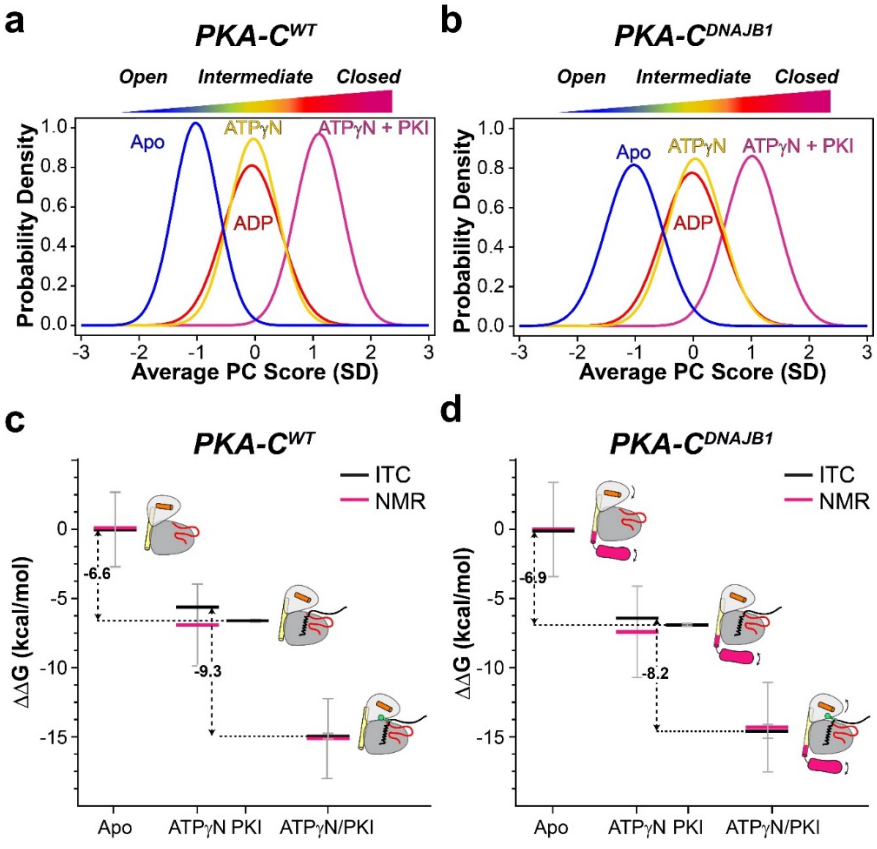

Figure 5.5. Global coordinated response of PKA-C^{WT} and PKA-C^{DNAJB1} to ligand binding.

Coordinated chemical shift changes analyzed with CONCISE for **a** PKA-C^{WT} and **b** PKA-C^{DNAJB1}. Changes in the free energy of binding of **c** PKA-C^{WT} and **d** PKA-C^{DNAJB1} to ATPγN and PKI_{5-24}. Black lines indicate the values obtained from ITC and pink lines correspond to values obtained from NMR measurements.

Global versus community-specific responses to ligand binding. While CHESCA provides an estimate of the correlated response for individual residues (or communities) to ligand binding, the analysis of the amide chemical shifts with CONCISE (COordiNated ChemIcal Shifts bEhavior)[235] provides the probability density (population) of each state along the conformational equilibrium. According to CONCISE analysis, the probability density of the amide resonances for the *apo* form of the enzyme (open state) is clustered around an average principal component (PC) score (<PC>) of ~-1.2 (**Figure 5.5 panel A**)[269]. Upon binding ATPγN, ADP, and PKI_{5-24}, the probability densities for the amide resonances of PKA-C^{WT} progressively shift toward more positive <PC> values, with the density for the binary complex (intermediate state) showing a <PC> ~ 0, and the ternary complex an <PC> ~1.3 (closed state). A similar trend is observed for PKA-C^{DNAJB1}, though the probability densities are broader, indicating that the amide resonances follow a less coordinated response[235]. Also, the maximum of the probability density for the intermediate state of PKA-C^{DNAJB1} is slightly shifted toward the closed conformation, while the probability density for the ternary complex is slightly more open than the corresponding wild-type (**Figure 5.5 panel B**). These probability densities or populations of each state can be converted into free energy, and the shift of the maxima from free to bound state along the <PC> axis reflects the free energy of binding[235]. Indeed, the $\Delta\Delta G$ values obtained from ITC data are very similar to those calculated from CONCISE (**Figure 5.5 panel C, D** and **Table 5.4**). Consequently, the attenuation in the collective response of the amide resonances of the PKA-C^{DNAJB1} is correlated with the reduced extent of binding cooperativity. Interestingly, we found that the two enzymes respond to ligand binding in a community-specific manner (**Figure 5.6 panel A, B**). For PKA-C^{WT}, the resonances associated to ComA have the most prominent response upon nucleotide binding. Also, large conformational transitions are observed for ComB, ComC, ComD, and ComE, while the remaining communities, located mostly in the C-lobe, show only marginal changes, with an <PC1> of approximately -0.4. Binding of PKI_{5-24} to the PKA-C/ATPγN complex shifts all the communities toward a fully closed state (<PC1> ~1) (**Figure 5.6 panel C** and **Figure 5.13 panel A**). In contrast, the probability densities for ComA, ComB, ComC,

ComD, and ComE for PKA-C^{DNAJB1} are shifted to a more closed intermediate state (<PC1> ~0). Moreover, PKI$_{5-24}$ binding to PKA-C^{DNAJB1}/ATPγN complex shifts the probability densities of the various communities toward the closed state to different extents (<PC1> ~ 0.75), with only ComF, ComF1, ComG, and ComH reaching a fully closed state. The remaining communities located in the N-lobe cluster around PC1 ~0.65, adopting a slightly more open conformation (**Figure 5.6 panel D** and **Figure 5.13 panel B**). Overall, the J-domain fused to the catalytic core decreases the number of correlated chemical shift responses, *i.e.,* the community of the kinase no longer transition in a correlated fashion, and prevents several communities (ComA, ComB, ComC, ComD, and ComE) from reaching a fully closed state, which explains the reduced extent of nucleotide/substrate binding cooperativity[71].

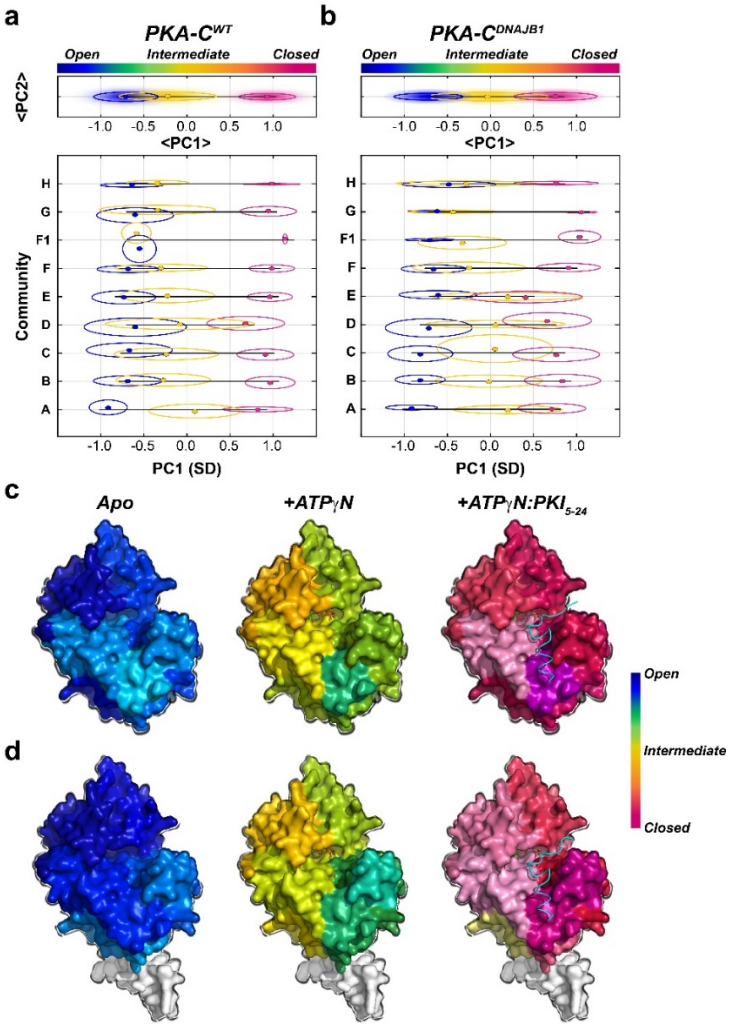

Figure 5.6. Community-specific responses of PKA-C^{WT} and PKA-C^{DNAJB1} upon ATPγN and PKI$_{5-24}$ binding.

CONCISE analysis for each individual community for **a** PKA-C^{WT} and **b** PKA-C^{DNAJB1}. The top panel on the graphs shows the average PC1 (<PC1>) over all communities, while the bottom panel shows the PC1 scores of each individual community. CONCISE scores of each community mapped onto the surface of **c** PKA-C^{WT} (PDB: 4WB5) and **d** PKA-C^{DNAJB1} (PDB: 4WB7) for each state (apo, +ATPγN, and +ATPγN/PKI_{5-24}).

5.4 Discussion

There is mounting evidence that PKA-C^{DNAJB1} is the primary driver of FL-HCC[31, 32, 259] and may be involved in other pathologies[270, 271]. Despite its link to tumorigenesis, initial structural and functional studies have left more questions than answers regarding the molecular etiology of this rare liver carcinoma. Similar to other oncogenic kinases involved in Cushing's syndrome, the X-ray structure of PKA-C^{DNAJB1} does not reveal any structural anomalies in the catalytic core (RMSD < 0.4 Å)[106]. In solution, however, NMR and SAXS have shown that the J-domain is flexible, assuming both *in* and *out* conformations[64]. The inherent flexibility of the J-domain enables the kinase to form hetero-tetrameric holoenzymes with RIα subunits, although with two alternative conformations[263]. Interestingly, the RIα subunit is overexpressed in carcinoma cells, presumably to 'buffer' the PKA-C^{DNAJB1} overexpression[259, 262, 272]. In rare cases of FL-HCC, lack of PKA-C regulation by RIα may result in the progression of the disease[273], like the dysregulation of PKA-C in Carney Complex[95]. These data alone do not adequately explain the aberrant function of PKA-C^{DNAJB1}.

It is possible, however, that the functional repercussion of the J-domain fusion to PKA-C is multifaceted. First, the deletion of 14 residues in the αA-helix and N-terminus prevents post-translational modifications such as myristoylation, deamidation, and phosphorylation of Ser10. These modifications are essential for intracellular membrane localization[274, 275]; therefore, the J-domain may interfere with the localization of the enzyme in the proximity of natural substrates. Second, the phosphorylation profile of PKA-C^{DNAJB1} is considerably different from the wild-type[108]. Third, the presence of the J-domain may interfere with the formation of localization complexes with A-kinase anchoring proteins (AKAPs)[272]. Fourth, PKA-C^{DNAJB1} may form stable complexes with Hsp70, with the J-domain acting as a scaffold for this chaperonin[108].

Irrespective of these putative mechanisms, our studies reveal that the fusion of the J-domain to the kinase reduces canonical positive binding cooperativity between

nucleotide and substrate[71], and alters the kinases' conformational equilibrium via disruptions of the intramolecular allostery. Indeed, cooperativity plays an essential role in macromolecular assembly, regulation, and signal transduction[276, 277]. Therefore, the attenuation in allosteric binding cooperativity is likely to be implicated in the altered interactome and phosphoproteome[108]. Since the recognition sequences of R-subunits are highly homologous to PKI, the reduced nucleotide/PKI binding cooperativity of PKA-C^{DNAJB1} suggests an aberrant regulation of the holoenzyme as well. It is worth noting that a reduction in cooperativity is also a prominent feature of a single mutation in the P+1 loop of the catalytic subunit (PKA-C^{L205R}) in patients affected by Cushing's syndrome[65],[53,54].

Consistent with our previous analyses of PKA-C^{L205R}, the allosteric network of PKA-C^{DNAJB1} exhibits an overall attenuation in the density of correlations across the kinase with a marked reduction near the nucleotide-binding site and substrate-binding groove. The introduction of community-specific analyses assists in deciphering how the fusion of the J-domain perturbs the allosteric network and further underscores the linkage between the reduced binding cooperativity and the decrease in crosstalk among the structural communities[140]. The coupling between ComH, responsible for the docking of proteins such as PKI or R-subunits, to other communities is completely ablated, explaining the lower degree of binding cooperativity observed for PKA-C^{DNAJB1}, and further suggesting that the R/C-interactions may be altered. Moreover, the dramatic decrease in the inter-community coupling of ComC, adjacent to the αA-helix, reflects the structural and/or dynamic changes caused by the J-domain fusion to the αA-helix. Overall, the similarities observed between PKA-C^{L205R} and PKA-C^{DNAJB1} suggest a common mechanism, involving concomitant reductions in binding cooperativity and intramolecular allostery that may elicit their aberrant function.

Indeed both computational and experimental methods have successfully elucidated allosteric pathways in a variety of different systems outside of protein kinase A[77, 134, 146, 278-282]. Perhaps more importantly, many of these studies have shown how disruptions in these pathways act to change function. Taken with our previous studies, nucleotide/substrate binding cooperativity emerges as a critical function in protein kinase A that arises from the structural changes of multiple domains (*i.e.*, communities) that must be coordinated and synchronized to ensure a cooperative binding response[65, 83]. Like other tumorigenic transcriptomes that result in a fully active PKA-C, it is likely

that alterations in the allosteric network impart defective binding cooperativity and may play a role in their aberrant functions[270, 271, 283]. As for the chimeric PKA-C^{DNAJB1}, attenuated or dysfunctional responses to allosteric effectors (such as ATP) may result in defective spatial and temporal control of phosphorylation-mediated signaling in other protein kinases, leading to disease.

5.5 Materials and Methods

Sample Preparation of PKA-C^{WT} and PKA-C^{DNAJB1}. Recombinant PKA-C^{WT} was expressed and purified as described in Walker *et al.* [65]. PKA-C^{DNAJB1} was cloned into a pET-28a (+) vector. A tobacco etch virus (TEV) cleavage site was incorporated via mutagenesis into the vector between the cDNA coding for the kinase and a thrombin cleavage site. Transformed *E.coli BL21 (DE3) pLyss* (Agilent) cells were cultured in M9 minimal media supplemented with $^{15}NH_4Cl$. Protein overexpression was induced with 0.4 mM isopropyl β-D-thiogalactopyranoside (IPTG) and carried out overnight at 20°C. Following harvest, the cell pellet was resuspended in 50 mM Tris-HCl, 30 mM KH_2PO_4, 300 mM NaCl, 5 mM 2-mercaptoethanol, 0.15 mg/mL Lysozyme, 200 µM ATP, DNaseI, Roche EDTA-free protease inhibitor tablet (pH 8.0) and lysed using French press. The solution was cleared by centrifugation (16000 rpm, 4°C, 45 min) and the supernatant incubated with Ni^{2+} nitrilotriacetic acid resin (Thermo Scientific, 1 ml of resin per liter of culture) at 4°C overnight. The resin was then washed with 50 mM Tris-HCl, 30 mM KH_2PO_4, 300 mM NaCl, 5 mM 2-mercaptoethanol, 0.5 mM phenylmethylsulfonyl fluoride (PMSF) (pH 8.0). The resin was further washed with the same buffer supplemented with 10 mM imidazole. PKA-C^{DNAJB1} was eluted using the same buffer with 250 mM imidazole. SDS-PAGE electrophoresis samples were taken at each purification step listed and are shown in **Figure 5.14 panel A**. Fractions containing PKA-C^{DNAJB1} were cleaved for 18 hours at 4°C in a dialysis buffer composed of 20 mM KH_2PO_4, 25 mM KCl, 5 mM 2-mercaptoethanol, 0.1 mM PMSF (pH 7.0). The phosphorylation states of PKA-C^{DNAJB1} were separated using a cation exchange column (HiTrap Q-SP, GE Healthcare Life Sciences using a linear gradient of KCl in 20 mM KH_2PO_4.

Sample Preparation of DNAJB1. The 69 amino acid sequence corresponding to the DNAJB1 heat shock protein fragment, $DNAJB1_{1-69}$, was cloned into the pET-28a (+) vector. $DNAJB1_{1-69}$ was expressed in *E.coli BL21 (DE3)* (Agilent) in M9 minimal media containing $^{15}NH_4Cl$ and ^{13}C-glucose as the sole source of nitrogen and carbon,

respectively. Overexpression was induced with 0.4 mM IPTG and carried out for 5 hours at 30°C. The cell pellet was resuspended in 20 mM Tris-HCl, 300 mM NaCl, 5 mM 2-mercaptoethanol, 15 mg/mL Lysozyme, DNaseI, Roche EDTA-free protease inhibitor tablet (pH 8.0) and lysed using sonication. The lysate was cleared by centrifugation (18000 rpm, 4°C, 30 min,) and the supernatant was incubated with Ni^{2+} nitrilotriacetic acid resin at 4°C overnight. Resin was washed with 20 mM Tris-HCl, 300 mM NaCl, 5 mM 2-mercaptoethanol, 0.5 mM PMSF (pH 8.0). $DNAJB1_{1-69}$ was eluted using the same buffer supplemented with 250 mM imidazole. SDS-PAGE electrophoresis samples were taken at each purification step listed as shown in **Figure 5.14 panel B**. The elution was dialyzed for 3 hours at 4°C into 20 mM Tris-HCl, 150 mM NaCl and 5 mM 2-mercaptoethanol (pH 8.0). To cleave the His-tag, an appropriate amount of thrombin was added to the solution and allowed to occur at RT for 4 hours. The cleavage reaction was monitored by SDS-PAGE, and upon completion, thrombin was inactivated by adding 1 mM PMSF. To purify the protein, the cleavage solution was passed through a Ni^{2+} nitrilotriacetic acid resin. The flowthrough was collected, concentrated using a 10 kDa, and subsequently a 3 kDa spin concentrator and stored at 4°C in 20 mM Tris-HCl, 150 mM NaCl and 2 mM DTT supplemented with 0.5 mM of PMSF (pH 8.0).

Sample Preparation of Peptides. Kemptide (LRRASLG), CREB (^{123}KRREILSRRPSYR^{135}), and KSR1 (^{880}LPKLNRRLSHPGHFWKS^{896}), and PKI_{5-24} were synthesized on a CEM Liberty Blue microwave synthesizer. All peptides were purified using reverse-phase high-pressure liquid chromatography. The purified peptide was concentrated, lyophilized, and stored at -20°C. All peptides molecular weight was verified by MALDI-TOF. Kemptide's molecular weight quantity was verified by amino acid analysis (Texas A&M University).

ITC Measurements. ITC measurements were performed with a low-volume NanoITC (TA Instruments). PKA-C^{WT} and PKA-C^{DNAJB1} were dialyzed into 20 mM MOPS, 90 mM KCl, 10 mM DTT, 10 mM $MgCl_2$, and 1 mM NaN_3 (pH 6.5). PKA-C^{WT} and PKA-C^{DNAJB1} concentrations for ITC measurements were between 80-130 μM as confirmed by A_{280} = 53,860 M^{-1} cm^{-1} and A_{280} = 62,800 M^{-1} cm^{-1}, respectively. Approximately 300 μL of the kinase was used for each experiment, with 50 μL of 2 mM ATPγN and/or 0.6-1 mM PKI_{5-24} in the titrant syringe. The heat of dilution of the ligand into the buffer was taken into account for all experiments and subtracted. For experiments with saturated nucleotide, 2

mM ATPγN was added. All measurements were performed at 300 K in triplicates. The binding was assumed to be 1:1, and curves were analyzed with the NanoAnalyze software (TA Instruments) using the Wiseman Isotherm[242]:

$$\frac{d[MX]}{d[X_{tot}]} = \Delta H° V_0 \left[\frac{1}{2} + \frac{1-\frac{1-r}{2}-R_m/2}{(R_m^2-2R_m(1-r)+(1+r)^2)^{1/2}}\right] \quad (1)$$

where *d[MX]* is the change in total complex relative to the change in total protein concentration, *d[X_{tot}]* is dependent on *r*, the ratio of K_d relative to the total protein concentration, and R_m, the ratio between total ligand and total protein concentration. The free energy of binding was determined using the following:

$$\Delta G = RT \ln K_d$$

where R is the universal gas constant, and T is the temperature at measurement (300 K). The entropic contribution to binding was calculated using the following:

$$T\Delta S = \Delta H - \Delta G.$$

The degree of cooperativity (σ) was calculated as follows:

$$\sigma = \frac{K_{d\ Apo}}{K_{d\ Nucleotide}}$$

where $K_{d\ Apo}$ is the dissociation constant of PKI_{5-24} binding to the apoenzyme, and $K_{d\ Nucleotide}$ is the *corresponding dissociation constant for* PKI_{5-24} binding to the nucleotide-bound PKA-C.

Enzyme Assays. Steady-state activity assays with Kemptide, CREB, and KSR1 were performed under saturating ATP concentrations and spectrophotometrically at 298 K as described by Cook *et al.* [85]. The values of V_{max} and K_M were obtained from a non-linear fit of the initial velocities to the Michaelis-Menten equation.

Small-angle X-ray scattering (SAXS). Following the purification method outlined above, PKA-C^{DNAJB1} was buffer exchanged into 20 mM MOPS, 90 mM KCl, 60 mM $MgCl_2$, 10 mM DTT, and 1 mM NaN_3 (pH 6.5) and concentrated to 70 μM. For binary and ternary samples, 12 mM ATPγN and/or 70 μM PKI (1:1 ratio) was added to PKA-C^{DNAJB1}. Fitting of structures

from MD simulations against the experimental SAXS curves was performed using the FoXS web server[284]. One hundred random snapshots from MD simulations for PKA-C^{WT} and PKA-C^{DNAJB1} were chosen as representative structures for the conformational ensembles, and the fitting of the SAXS data was carried out for a range of *q* values spanning from 0.01 to 0.2.

NMR Spectroscopy. Uniformly ^{15}N-labeled PKA-C^{WT} and PKA-C^{DNAJB1} were overexpressed and purified as described above. NMR experiments were performed in 90 mM KCl, 20 mM KH_2PO_4, 10 mM dithiothreitol (DTT), 60 mM $MgCl_2$, and 1 mM NaN_3 at pH 6.5. Standard [^{1}H-^{15}N]-TROSY-HSQC experiments were carried out for PKA-C^{WT} and PKA-C^{DNAJB1} on an 850-MHz Bruker Advance III spectrometer equipped with a TCI cryoprobe, respectively. Concentrations for samples were 0.1-0.3 mM as determined by A_{280} measurements, 12 mM ATPγN or ADP was added for the nucleotide-bound form, and 0.2-0.4 mM PKI_{5-24} for the ternary complex. Spectra were collected at 300K, processed using NMRPipe[243], and visualized using Sparky[244].

All [^{1}H-^{15}N]-TROSY-HSQC experiments were acquired with 2048 (proton) and 256 (nitrogen) complex points. Combined chemical shift perturbations were calculated using ^{1}H and ^{15}N chemical shifts according to the following:

$$\Delta\delta = \sqrt{(\Delta\delta H)^2 + (0.154 \times \Delta\delta N)^2} \qquad (2)$$

Backbone resonance assignment of $DNAJB1_{1-69}$. Uniformly ^{13}C,^{15}N-labeled $DNAJB1_{1-69}$ was overexpressed and purified as described above. NMR experiments were performed in 90 mM KCl, 20 mM KH_2PO_4, 10 mM dithiothreitol (DTT), 60 mM $MgCl_2$, and 1 mM NaN_3 (pH 6.5). Standard 3D triple resonance experiments were carried out for $DNAJB1_{1-69}$ on a 600 MHz Bruker Avance NEO spectrometer equipped with a triple resonance cryogenic probe at 300 K. Concentrations for samples were 0.3 mM as determined by A_{280} measurements. All NMR data were processed using NMRPipe[243] and visualized using Sparky[244].

Chemical Shift Analyses. ***COordiNated ChemIcal Shift bEhavior (CONCISE).*** CONCISE was used to measure the change in equilibrium position using the following PKA-C constructs: apo, ATPγN, ADP, and ATPγN/PKI_{5-24}. This method identifies sets of residues whose chemical shifts respond linearly to the conformational transition using

principal component analysis (PCA). Community-based and domain-based CONCISE analyses use similar methods using only select residues that comprise either an individual community or domain as defined by McClendon *et al.* [40, 140]. $\Delta\Delta G$ values from NMR derived from CONCISE analysis and based on extent of closure (% closed). Values used for the calculations can be found in **Table 5.4**. PKA-C^{WT} ITC values were used as a reference with apo PKA-C^{WT}: $\Delta\Delta G$=0 and 0% closed; and +ATPγN/PKI-bound PKA-C^{WT}: $\Delta\Delta G$ = -15 and 100% closed. Error was calculated by using the standard deviation of the gaussian fits from CONCISE analysis

CHEmical Shift Covariance Analysis (CHESCA). CHESCA was used to identify and functionally characterize allosteric networks of residues eliciting concerted responses to, in this case, nucleotide and pseudo-substrate. A total of four states were used to identify inter-residue correlations: apo, ATPγN-bound, ADP-bound, and ATPγN/PKI_{5-24}. The identification of inter-residue correlations by CHESCA relies on agglomerative clustering (AC) and singular value decomposition (SVD). Pairwise correlations between chemical shift variations experienced by different residues were calculated to identify networks. When plotted on a correlation matrix, this allows for the identification of regions that are correlated to one another. For each residue, the max change in chemical shift was calculated in both the ^{1}H (*x*) and ^{15}N (*y*) dimension ($\Delta\delta_{x,y}$). Residues were included in CHESCA analysis only if they satisfied the following: $\Delta\delta_{x,y} > ½\ \Delta v_{xA,yA} + ½\ \Delta v_{xB,yB}$, where *A* and *B* correspond to two different forms analyzed. (Note that there is no dependence on which two forms satisfied this statement) For every residue x, correlation scores were calculated by finding the total # of residues correlated (with $R_{ij} > 0.98$) to residue x and dividing by the total # of residues in the kinase (350). Community CHESCA analysis is a chemical shift-based correlation map between various functional communities within the kinase. Each community is a group of residues (McClendon *et al*.[140]) associated with a function or regulatory mechanism. Mathematically, this community-based CHESCA analysis is a selective interpretation of CHESCA, where we evaluate a correlation score between residues in various communities, as shown below. To represent community-based CHESCA analysis, we lowered the correlation cutoff such that $R_{cutoff} > 0.8$. Suppose community X and community Y has n_X and n_Y number of assigned residues respectively, the correlation score between X and Y is defined as,

$$R_{X,Y} = \text{Number of } (R_{ij} > R_{cutoff}) / (n_X * n_Y).$$

Where R_{ij} is the CHESCA correlation coefficient between residue i (belongs to community A) and residue j (belongs to community B). R_{cutoff} is the correlation value cutoff. $R_{X,Y}$ can assume values ranging from 0 (no correlation between residues in X and Y) to 1 (all residues in X are correlated with all residues in Y).

Molecular Dynamics Simulations. Parallel MD simulations were set up to compare PKA-C^{WT} and PKA^{DNAJB1}. These simulations were repeated for the apo, the binary (ATP-bound), and the ternary complexes (ATP/PKI_{5-24}). The systems with PKA-C^{WT} and PKA-C^{DNAJB1} were built directly from the X-ray structures starting from the closed configurations (PDB ID: 1ATP and 4WB7, respectively)[79, 106]. All simulations were performed using GROMACS 4.6[285] in the CHARMM36 force field [286]. The all-atom structures were solvated in a rhombic dodecahedron solvent box with a TIP3P[245] water molecule layer extending approximately 10Å away from the surface of the proteins. Counter ions (K^+ and Cl^-) were added to ensure electrostatic neutrality corresponding to an ionic concentration of ~150 mM. The LINCS[287] algorithm was applied to constrain all covalent H-bonds to the equilibrium length, and particle-mesh Ewald [288] was used to treat long-range electrostatic interactions with a real-space cutoff of 10 Å. All systems were minimized using steepest descent algorithm, and then were gradually heated to 300 K at a constant volume over 1 ns, using harmonic restraints with force constant of 1000 kJ/(mol*$Å^2$) on heavy atoms of both proteins and nucleotides. Over the following 12 ns of simulations at constant pressure (1 atm) and temperature (300 K), the restraints were gradually released. The systems were equilibrated for an additional 20 ns without positional constraints. A Parrinello-Rahman barostat[289] was used to keep the pressure constant, while a V-rescale thermostat with a time step of 2 fs was used to maintain constant temperature. Each system was simulated for 1.05 μs, with snapshots recorded every 20 ps. A total of 6.3 μs and 315000 conformations were utilized for the analyses.

Statistics and Reproducibility. Numerical ΔG, ΔH, $-T\Delta S$, and K_d values shown in Supplementary Tables 1 and 2 are averages of three independent ITC experiments with errors calculated as the standard deviation between these three measurements. Numerical values of V_{max} and K_M were determined with a nonlinear regression function assuming Michaelis-Menten kinetics for substrate concentration versus velocity using GraphPad Prism 8.0.1. Error in k_{cat}/K_M values was propagated from error in k_{cat} and K_M.

5.6 Acknowledgements

This work was supported by the National Institutes of Health, GM100310 (G.V.), S10 OD021536 (G.V.), HL139065 (D.D.T.) and AG26160 (D.D.T); and the American Heart Association, 20PRE35120253 (C.W.). NMR experiments were carried out at the Minnesota NMR Center and MD simulations using the Minnesota Supercomputing Institute. The SAXS instrument at the University of Utah was funded by the Department of Energy (Dr. J. Trewhella).

5.7 Author Contributions

C.O. and C.W. collected and analyzed activity assays, NMR, and ITC data and contributed to the writing of the manuscript. A.K carried out preliminary experiments. Y.W. analyzed SAXS data and completed MD simulations. D.K.B collected the SAXS data. M.V.S wrote all scripts for CHESCA and CONCISE analyses. F.P., D.D.T., D.A.B., S.M.S., and S.S.T. contributed to the critical analysis of the data and writing of the manuscript. G.V. conceived and directed the project, along with helping with data analysis and writing the manuscript.

5.8 Supplementary Figures

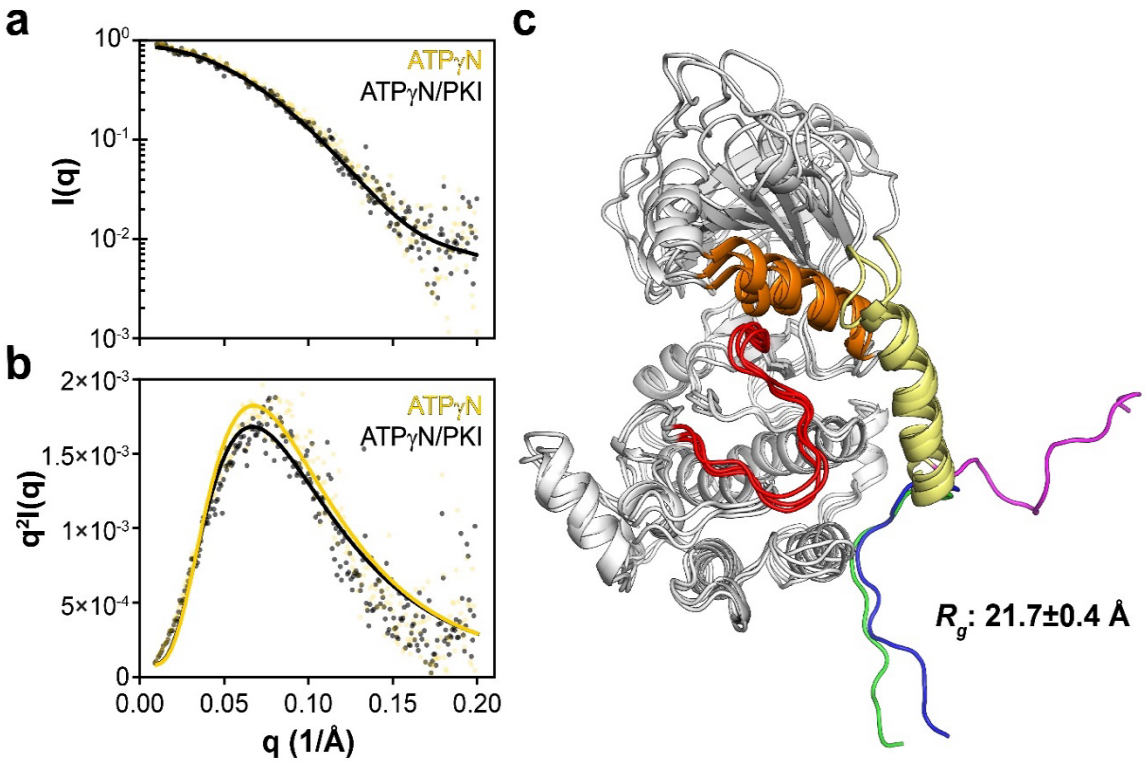

Figure 5.7. SAXS profiles for PKA-C^{WT}.
a SAXS profiles of PKA-C^{WT} in the binary (ATPγN-bound, yellow) and ternary (ATPγN/PKI-bound, black) forms. Continuous lines show the fitting of the experimental SAXS data. **b** Corresponding Kratky plot of PKA-C^{WT} bound to ATPγN and ATPγN/PKI. **c** Overlay of selected snapshots of PKA-C^{WT}.

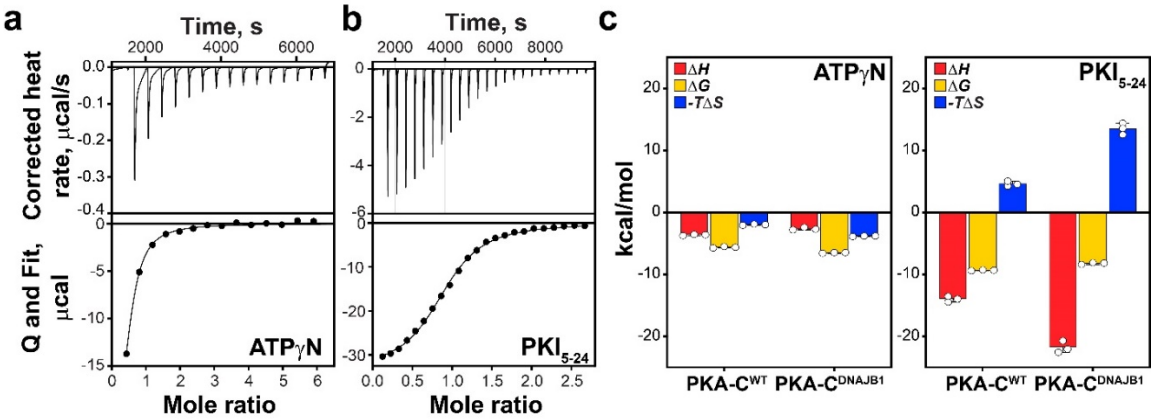

Figure 5.8. Thermodynamics of PKA-C^{DNAJB1} binding nucleotide and pseudo-substrate. Representative ITC thermographs of apo PKA-C^{DNAJB1} binding **a** ATPγN, and **b** PKI$_{5-24}$. Corresponding thermodynamic values are found in **Table 5.1, 5.2**. **c** Graphical representation of the values of ΔH (red), ΔG (yellow), and -TΔS (blue). Errors are calculated as SD from triplicate measurements.

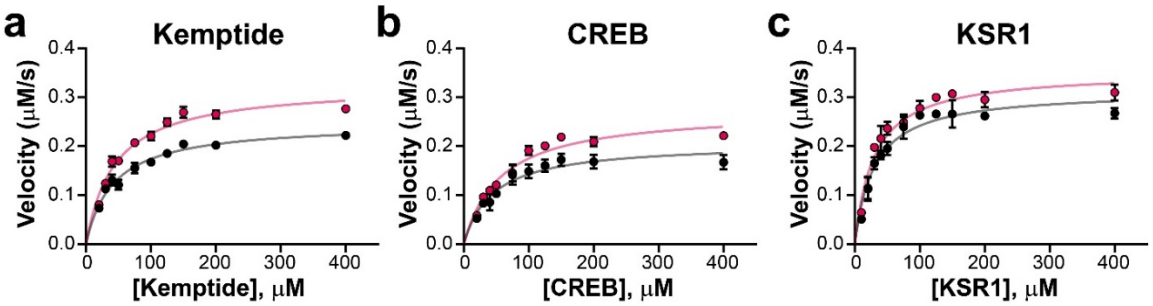

Figure 5.9. Steady state kinetics of phosphoryl transfer.
Steady state phosphorylation kinetics of PKA-C^{WT} (black) and PKA-C^{DNAJB1} (pink) towards **a** Kemptide, **b** CREB, and **c** KSR1. See Supplementary Table 3 for corresponding kinetic parameters following fitting with the Michaelis-Menten equation.

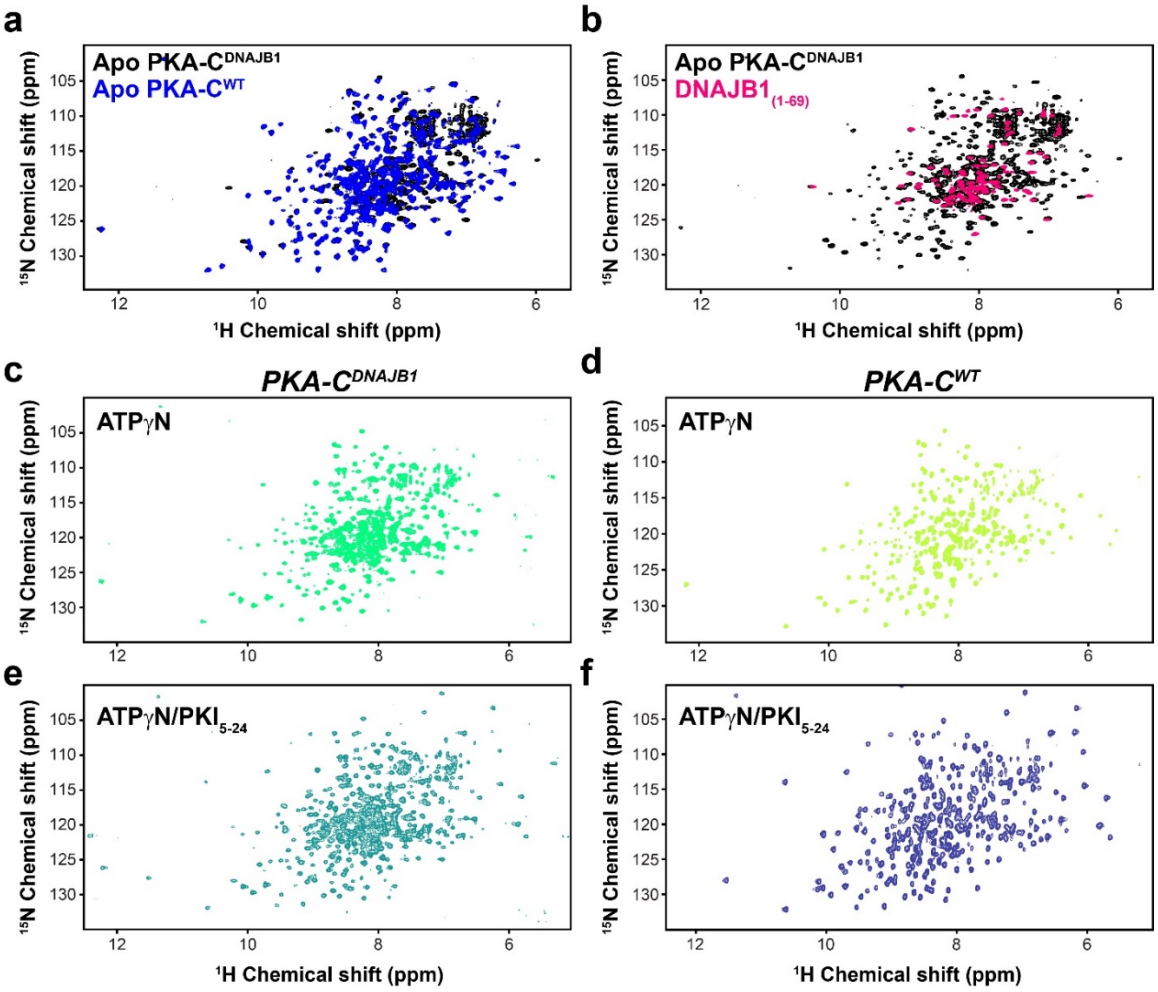

Figure 5.10. NMR amide fingerprints of PKA-C^{DNAJB1} and PKA-C^{WT}.
[^{1}H,^{15}N]-TROSY-HSQC spectrum overlay of apo PKA-C^{DNAJB1} to **a** apo PKA-C^{WT} and **b** DNAJB1$_{(1-69)}$. [^{1}H,^{15}N]-TROSY-HSQC spectrum of PKA-C^{DNAJB1} bound to **c** ATPγN and **e** ATPγN/PKI$_{5-24}$, and of PKA-C^{WT} bound to **d** ATPγN and **f** ATPγN/PKI$_{5-24}$.

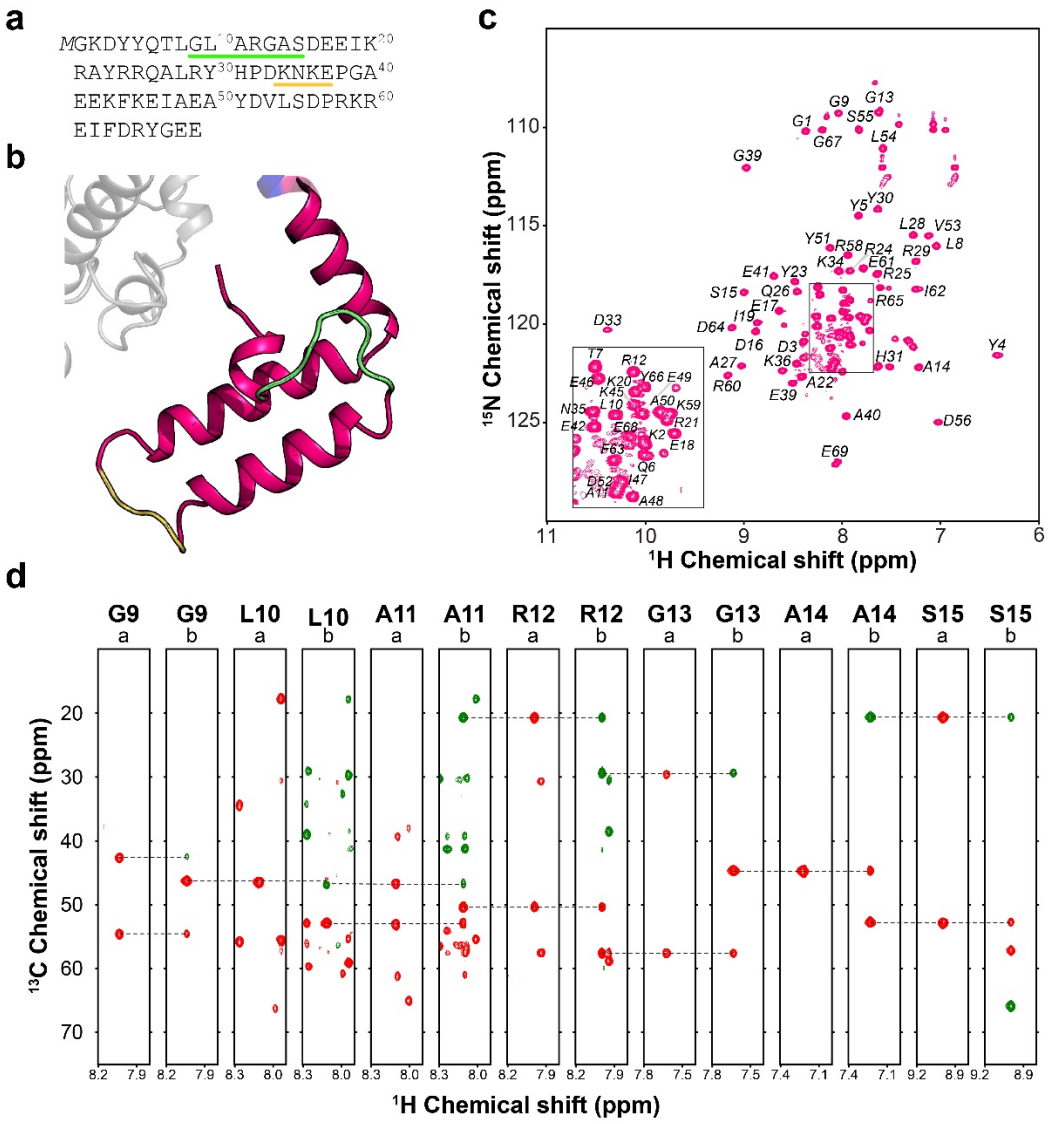

Figure 5.11. NMR backbone assignment of DNAJB1$_{1\text{-}69}$.
a Primary sequence of DNAJB1 (Uniprot 25685). The sequence underlined in green are the residues which through-bound connectivity is reported in panel D. Residues that could not be assigned are underlined in yellow. **b** The three-dimensional structure of the J-domain (DNAJB1) of PKA-C^{DNAJB1} (PDB 4WB7). **c** [^{1}H,^{15}N]-Heteronuclear single quantum correlation (HSQC) spectrum of DNAJB1$_{1\text{-}69}$ with resonance assignment. **d** Series of strip plots from the CBCA(CO)HN (a) and HNCACB (b) experiments that illustrates the sequential connections between residue G9 and S15.

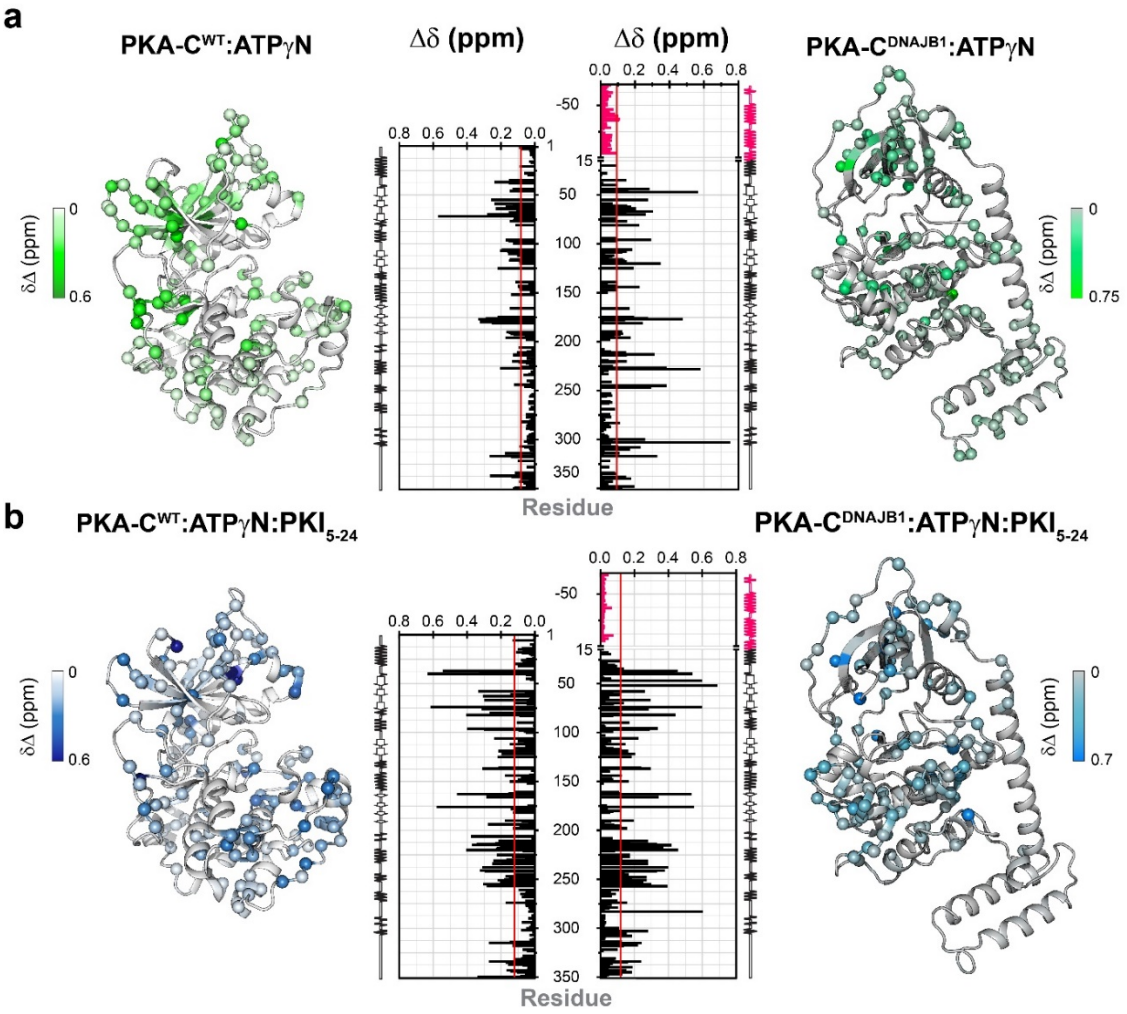

Figure 5.12. Chemical shift perturbations (CSP) observed upon ligand binding for PKA-C^{WT} and PKA-C^{DNAJB1}.

Histograms show the combined ^{1}H-^{15}N chemical shift perturbations vs. residue for PKA-C^{WT} and PKA-C^{DNAJB1} in response to **a** ATPγN-binding and **b** ATPγN/PKI$_{5-24}$-binding. Each CSP is plotted on the structures of either PKA-C^{WT} (PDB: 4WB5) or PKA-C^{DNAJB1} (PDB: 4WB7). The red line on the histograms indicate one standard deviation from the average CSP. Note that the CSP values for PKA-C^{WT} are from [65].

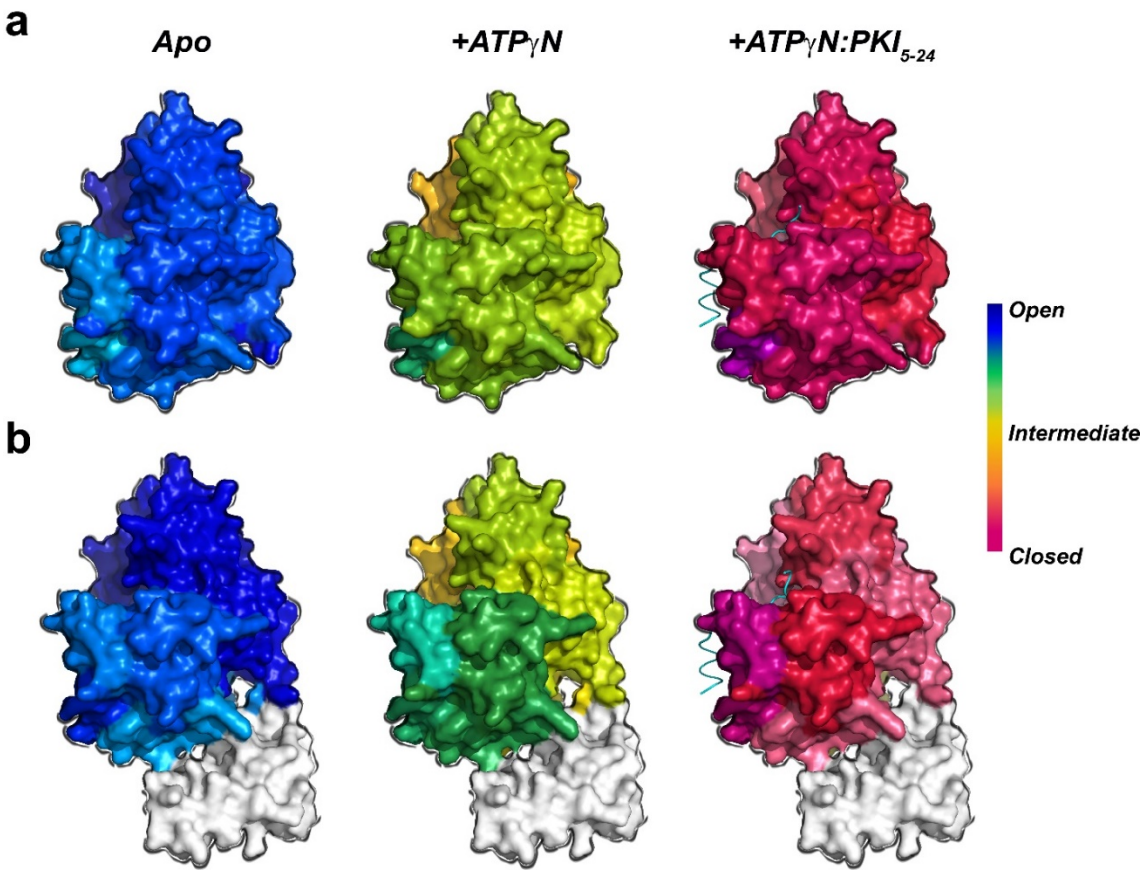

Figure 5.13. CONCISE scores of each individual community mapped onto the surface of a **PKA-C^{WT} and** b **PKA-C^{DNAJB1}.**

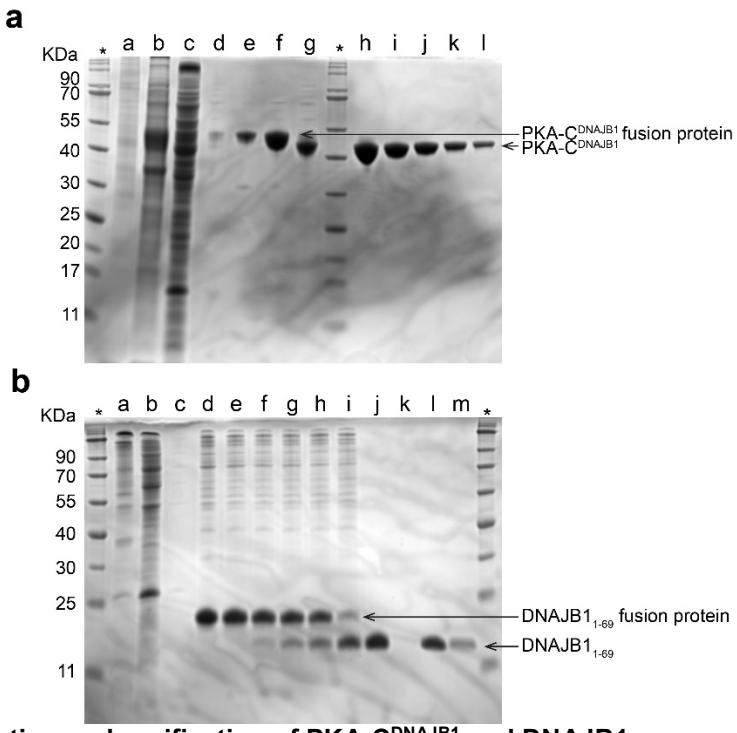

Figure 5.14. Isolation and purification of PKA-C^{DNAJB1} and DNAJB1$_{1-69}$.
a Coomassie-stained 12% Acrylamide/bis-acrylamide SDS-PAGE of the expression and purification (a-g), and protein integrity test (i-k) of U-^{15}N PKA-C^{DNAJB1}. (*) BLUEstain™ Protein ladder (GoldBio), 11-245 kDa; (a) before induction of expression with 0.4 mM of IPTG; (b) after 12 hour expression; (c) Ni^{+}-NTA flow through; (d) wash 1; (e) wash 2; (f) elution; (g) after 18 hours of cleavage; (h) 15 µM of U-^{15}N *PKA-C^{DNAJB1}* used for the NMR titration; (i-l) serial dilutions of sample *h*. **b** Coomassie-stained 18% Acrylamide/bis-acrylamide SDS-PAGE of the purification of U-^{13}C/^{15}N DNAJB1$_{1-69}$. (*) BLUEstain™ Protein ladder (GoldBio), 11-245 kDa; (a) cell pellet; (b) Ni^{+}-NTA flow through; (c) wash; (d) elution; (e) before thrombin cleavage; (f) 1 hour into cleavage reaction; (g) 2 hours into cleavage reaction; (h) 3 hours into cleavage reaction; (i) 4 hours into cleavage reaction; (j) flow through from 10 kDa concentrator; (k) flow through from 3 kDa concentrator; (l) supernatant of 3 kDa concentrator; (m) NMR sample.

5.9 Supplementary Tables

Table 5.1. Changes in enthalpy, entropy, free energy, and dissociation constant of binding ATPγN for PKA-C^{WT} and PKA-C^{DNAJB1} derived from ITC experiments.
All errors were calculated using triplicate measurements. Note that the values of K_d for PKA-C^{WT} are taken from Walker *et al*. [65].

	K_d (μM)	ΔG (kcal/mol)	ΔH (kcal/mol)	-TΔS (kcal/mol)
PKA-C^{WT}	83 ± 8	-5.61 ± 0.06	-3.6 ± 0.1	- 2.0 ± 0.1
PKA-C^{DNAJB1}	19 ± 4	-6.5 ± 0.1	-2.7 ± 0.2	-3.8 ± 0.1

Table 5.2. Changes in enthalpy, entropy, free energy, and dissociation constant for the binding of PKI_{5-24} to the apo and nucleotide-saturated forms of PKA-C^{WT} and PKA-C^{DNAJB1} derived from ITC experiments.

All errors were calculated using triplicate measurements. Errors in σ were propagated from errors in K_d. N/A indicates the value is not applicable to the particular measurements. Note that the values of K_d for PKA-C^{WT} are taken from Walker *et al*. [65].

Binding of PKI_{5-24} to apo forms of kinases					
	K_d (μM)	ΔG (kcal/mol)	ΔH (kcal/mol)	-TΔS (kcal/mol)	σ
PKA-C^{WT}	17 ± 2	-6.6 ± 0.1	-10.8 ± 0.5	4.2 ± 0.5	N/A
PKA-C^{DNAJB1}	9 ± 2	-6.9 ± 0.1	-20.1 ± 0.4	13.1 ± 0.4	N/A
Binding of PKI_{5-24} to the $ATP\gamma N$ saturated forms of kinases					
	K_d (μM)	ΔG (kcal/mol)	ΔH (kcal/mol)	-TΔS (kcal/mol)	σ
PKA-C^{WT}	0.16 ± 0.02	-9.33 ± 0.07	-13.9 ± 0.5	4.6 ± 0.4	106 ± 18
PKA-C^{DNAJB1}	1.1 ± 0.2	-8.2 ± 0.1	-22 ± 1	14 ± 1	8 ± 2

Table 5.3. Kinetic parameters of Kemptide, CREB, and KSR1 phosphorylation for PKA-C^{WT} and PKA-C^{DNAJB1}.

Values for K_M and k_{cat} were obtained from a non-linear least-squares analysis of the concentration-dependent initial phosphorylation rates using a standard coupled enzyme activity assay (related to **Figure 5.2 panel B** and **Figure 5.9**). Error in k_{cat}/K_M was propagated from the error in K_M and k_{cat}.

Kemptide		
	PKA-C^{WT}	PKA-C^{DNAJB1}
V_{max} (μM/s)	0.25 ± 0.01	0.33 ± 0.01
K_M (μM)	42 ± 5	44 ± 6
k_{cat} (s^{-1})	11.4 ± 0.5	15 ± 0.5
k_{cat}/K_M	0.27 ± 0.03	0.34 ± 0.05

CREB		
	PKA-C^{WT}	PKA-C^{DNAJB1}
V_{max} (μM/s)	0.21 ± 0.01	0.27 ± 0.02
K_M (μM)	45 ± 8	56 ± 10
k_{cat} (s^{-1})	9.5 ± 0.5	12.3 ± 0.9
k_{cat}/K_M	0.21 ± 0.04	0.22 ± 0.04

KSR1		
	PKA-C^{WT}	PKA-C^{DNAJB1}
V_{max} (μM/s)	0.31 ± 0.01	0.35 ± 0.02
K_M (μM)	30 ± 5	29 ± 5
k_{cat} (s^{-1})	14.1 ± 0.5	15.9 ± 0.9
k_{cat}/K_M	0.47 ± 0.08	0.6 ± 0.1

Table 5.4. CONCISE analysis of PKA-C^{WT} and PKA-C^{DNAJB1}.
Value of % closed was calculated as a function of average PC scores. See the Methods section for calculation of $\Delta\Delta$G based on CONCISE analysis.

	Average PC Score	% Closed	$\Delta\Delta$G (kcal/mol)
PKA-C^{WT} Apo	-1.02	0%	0
PKA-C^{DNAJB1} Apo	-1.02	0%	0
PKA-C^{WT} ATPγN	-0.03	46%	-6.9
PKA-C^{DNAJB1} ATPγN	0.03	49%	-7.4
PKA-C^{WT} ADP	-0.06	45%	N/A
PKA-C^{DNAJB1} ADP	-0.02	47%	N/A
PKA-C^{WT} ATPγN/PKI$_{5-24}$	1.11	100%	-15.0
PKA-C^{DNAJB1} ATPγN/PKI$_{5-24}$	1.01	95%	-14.3

Chapter 6 Is Disrupted Nucleotide-Substrate Cooperativity a Common Trait for Cushing's Syndrome Driving Mutations of Protein Kinase A?

Caitlin Walker[1], Yingjie Wang[1,2], Cristina Olivieri[1], Manu V.S.[1], Jiali Gao[2,3], David A. Bernlohr[1], Davide Calebiro[4,5], Susan S. Taylor[6,7], and Gianluigi Veglia[1,2,*]

[1]*Department of Biochemistry, Molecular Biology, and Biophysics, University of Minnesota, Minneapolis, MN 55455, USA.*

[2]*Department of Chemistry and Supercomputing Institute, University of Minnesota, Minneapolis, MN 55455, USA.*

[3]*Institute of Systems and Physical Biology, Shenzhen Bay Laboratory, Shenzhen, 518055, China.*

[4]*Institute of Metabolism and Systems Research, University of Birmingham, B15 2TT, Birmingham, UK.*

[5]*Centre of Membrane Proteins and Receptors, Universities of Birmingham and Nottingham, B15 2TT, Birmingham, UK.*

[6]*Department of Chemistry and Biochemistry, University of California at San Diego, La Jolla, CA 92093, USA.*

[7]*Department of Pharmacology, University of California at San Diego, La Jolla, CA 92093, USA.*

Submitted.

6.1 Synopsis

Somatic mutations in the *PRKACA* gene encoding the catalytic α subunit of protein kinase A (PKA-C) are responsible for cortisol-producing adrenocortical adenomas. These benign neoplasms contribute to the development of Cushing's syndrome. The majority of these mutations occur at the interface between the two lobes of PKA-C and interfere with the enzyme's ability to recognize substrates and regulatory subunits, leading to aberrant phosphorylation patterns and activation. Rarely, patients with similar phenotypes carry an allosteric mutation, E31V, located at the αA-helix's C-terminal end and adjacent to the αC-helix, a critical element in assembling the active conformation of kinases, but structurally distinct from the PKA-C interface mutations. Using a combination of solution NMR, thermodynamics, and kinetic assays, and molecular dynamics simulations, we show that the E31V allosteric mutation disrupts central communication nodes between the N- and C- lobes of the enzyme as well as the nucleotide-substrate binding cooperativity, a hallmark for kinases' substrate fidelity and regulation. For both orthosteric (L205R and W196R) and allosteric (E31V) Cushing's syndrome mutants the loss of binding cooperativity is proportional to the density of the intramolecular allosteric network. This structure-activity relationship suggests a possible common mechanism for Cushing's syndrome driving mutations in which decreased nucleotide/substrate binding cooperativity is linked to loss in substrate fidelity and dysfunctional regulation.

6.2 Introduction

Cushing's syndrome is defined by a collection of symptoms that result from prolonged exposure to high cortisol levels, leading to cardiovascular and metabolic complications [98]. Playing a fundamental role in regulating metabolism and cell proliferation in endocrine tissues, the cAMP signaling pathway and its aberrant activation are linked to several endocrine diseases [99, 226, 227]. The role of one component of this signaling cascade, cAMP-dependent protein kinase A (PKA), in Cushing's syndrome was not appreciated until recently when somatic mutations were identified in the *PRKACA* gene encoding the catalytic α subunit of PKA (PKA-C) [26-30, 102, 290, 291]. To date, a total of eight mutations have been discovered. Except for one mutation, E31V, all mutations are located near the substrate-binding cleft adjacent to the catalytic/regulatory (R) subunit interface (**Figure 6.1 panel A**).

PKA is the principal intracellular effector of the second messenger, cAMP. Inactive PKA exists as a holoenzyme (R_2:C_2) containing an R-subunit dimer bound to two catalytic (C) subunits [229]. Each R-subunit contains an inhibitory sequence that occupies the active site of the enzyme. Following stimulation of adenylate cyclase, two cAMP molecules bind to each R-subunit, initiating a conformational change and releasing active PKA-C. While R-subunits are the primary intracellular regulator of PKA-C, an endogenous inhibitor (PKI) inhibits PKA-C activity within the nucleus and controls nuclear exportation [229]. Spatiotemporal regulation is controlled by various ancillary proteins such as A-kinase anchoring proteins (AKAPs) that, via interactions with R-subunits, localize PKA-C near substrates [55].

PKA-C toggles between three major conformational states: open (apo), intermediate (nucleotide-bound), and closed (nucleotide/substrate-bound) [42]. This bean-shaped enzyme consists of a conserved catalytic core comprised of two lobes. The N-lobe of the kinase is smaller and contains mostly β-sheets and the αC-helix and harboring the ATP binding site, while the C-lobe comprises mostly α-helices and contains the substrate-binding cleft [35]. In contrast to other Ser/Thr kinases, PKA-C contains an αA-helix at its N-terminus, which anchors the N-lobe to the C-lobe and contributes to the tethering/positioning of the αC-helix. This important structural motif is recognized for its role in the activation and inactivation of protein kinases [42]. E31V is located at the C-

terminus of the αA-helix and adjacent to the C-terminus of the αC-helix. While other Cushing's syndrome mutations have been shown to disrupt R-subunit/PKA-C interactions, alter the enzyme's catalytic efficiency, and/or change its substrate specificity, the mechanism of dysfunction for PKA-C^{E31V} has remained elusive [20, 65, 230].

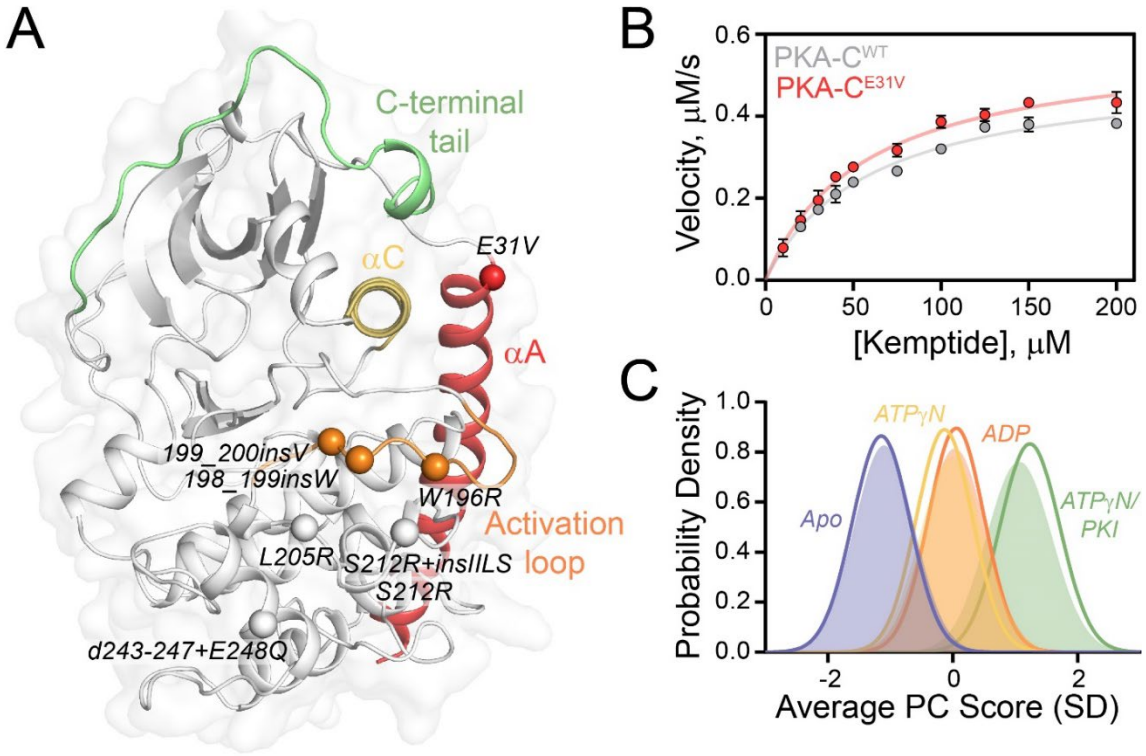

Figure 6.1. Structural and kinetic characterization of PKA-C^{E31V}.
(**A**) Structure of PKA-C bound to endogenous inhibitor, PKI (PDB: 1ATP) highlighting important structural elements and locations of Cushing's syndrome mutations in relation to E31V. (**B**) Steady state phosphorylation kinetics of PKA-C^{E31V} with Kemptide. (**C**) CONCISE analysis on the apo, ATPγN-, ADP- and ATPγN/PKI-bound forms of PKA-C^{WT} (opaque gaussian) and PKA-C^{E31V} (outlined gaussian).

Recently, we discovered that the most common Cushing's syndrome mutation, PKA-C^{L205R}, abrogates the nucleotide/pseudosubstrate binding cooperativity by reducing the intramolecular allostery between the small and large lobe [65]. Based on these findings, we suggested that this dysfunctional binding cooperativity and altered allostery disrupts substrate recognition and interactions with R-subunits, thereby altering canonical cAMP signaling. Despite E31V and L205R being spatially distant, our previous NMR analysis suggested they are allosterically coupled [65]. Therefore, we surmised that E31V

may affect the kinase's function in a manner similar to L205R, *i.e.*, the non-conservative mutation may disrupt the allosteric network and the binding cooperativity.

To dissect this allosteric mutation's effects, we carried out solution NMR spectroscopy along with isothermal titration calorimetry (ITC), kinetic assays, and molecular dynamics (MD) simulations. We found that the E31V mutation ablates the canonical positive cooperativity, typically seen for PKA-C while maintaining the kinase's catalytic efficiency. Specifically, the E31V mutation directly affects the allosteric node that connects the αA-, αC-helix, and activation loop, thereby disrupting nucleotide-substrate binding cooperativity. Finally, by comparing PKA-C^{WT} with three drivers for Cushing's syndrome, PKA-C^{E31V}, PKA-C^{L205R}, and PKA-C^{W196R}, we found a direct relationship between the loss of binding cooperativity and the reduction of allosteric communication within the enzyme. Altogether, our results suggest the existence of a common dysfunctional mechanism for PKA-C Cushing's mutations discovered thus far.

6.3 Results

E31V mutation ablates nucleotide-substrate binding cooperativity in PKA-C. To evaluate the effects of E31V on the thermodynamics of nucleotide (ATPγN) and pseudosubstrate (PKI) binding, we used isothermal titration calorimetry (ITC) [242]. Values of ΔG, ΔH, -TΔS, K_d, and cooperativity coefficients (σ) obtained for PKA-C^{E31V} are summarized in **Table 6.1, 6.2** [65]. We found PKA-C^{WT} and PKA-C^{E31V} have similar binding affinities for ATPγN (K_d = 83 ± 8 and 91 ± 9 μM, respectively). A 7-fold higher binding affinity is observed for PKA-C^{E31V} compared to PKA-C^{WT} when binding PKI_{5-24} to their apo forms (K_d = 2.5 ± 0.5 and 17 ± 2 μM, respectively). In contrast to PKA-C^{WT}, upon saturation with ATPγN, PKA-C^{E31V} displays a 12-fold reduction in binding affinity (K_d = 0.16 ± 0.02 and 2 ± 1 μM, respectively). As previously determined, the binding of PKI_{5-24} to PKA-C^{WT} is highly cooperative (σ = 106 ± 18); in contrast, PKA-C^{E31V} displays no cooperativity with σ = 1.3 ± 0.7. To evaluate the effects of E31V on the kinase's catalytic efficiency, we carried out steady-state coupled enzyme assays using the standard substrate, Kemptide. Despite the dramatic effects on binding cooperativity, PKA-C^{E31V} displayed only a slight increase in V_{max} and a slight decrease in K_M, resulting in similar catalytic efficiencies (k_{cat}/K_M = 0.41 ± 0.05 and 0.46 ± 0.04 for PKA-C^{WT} and PKA-C^{E31V}, respectively; **Figure 6.1 panel B** and **Table 6.3**). Interestingly, mutagenesis of residues adjacent to the E31 site has shown similar kinetic behavior [48].

NMR mapping of nucleotide/PKI binding response. To analyze the binding response of PKA-C^{E31V} to nucleotide and pseudosubstrate, we mapped the amide backbone fingerprint of the enzyme using [^{1}H, ^{15}N]-TROSY-HSQC experiments [125]. The amide fingerprints of the kinase in different ligated forms are displayed in **Figure 6.7**. The global response of the two kinases to ligand binding was determined using CONCISE (COordiNated ChemIcal Shifts bEhavior) [235], which performs a statistical analysis on linear chemical shift trajectories of amide resonances to identify the position of each state along the conformational equilibrium, shows that nucleotide and pseudosubstrate shift the overall populations from an open state to an intermediate and fully closed state. Upon binding the nucleotide, the probability density of the amide resonances from the apo shifts toward an intermediate state, and the subsequent saturation with PKI peptide further shifts toward the fully closed state (**Figure 6.1 panel C**). Globally wild-type and mutant behave similarly; however, upon binding ATPγN, PKA-C^{E31V} adopts a more open conformation compared to PKA-C^{WT} and subsequent binding of PKI shifts the probability distribution toward a more closed state.

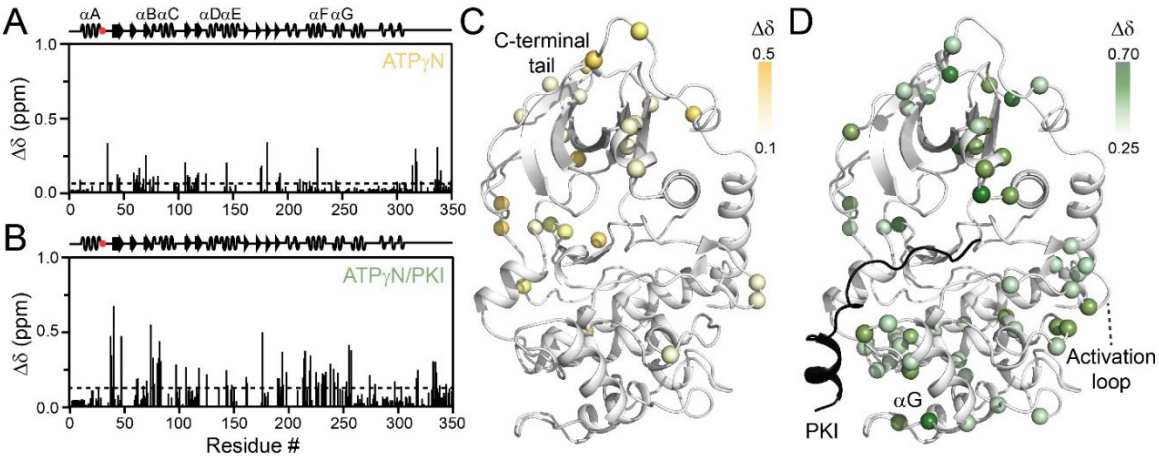

Figure 6.2. Chemical shift perturbation of PKA-C^{E31V}.
Chemical shift perturbation (CSP) of amide fingerprint of PKA-C^{E31V} upon binding (**A**) ATPγN and subsequent binding of (**B**) PKI. The average CSP is shown as a dashed line. CSPs of PKA-C^{E31V} amide resonances mapped onto the structure (PDB: 1ATP).

To further confirm the changes in the global response of PKA-C induced by E31V, we mapped the chemical shift perturbations (CSP, $\Delta\delta$) of PKA-C^{E31V}. Upon binding ATPγN, PKA-C^{E31V} exhibits similar CSP patterns as wild-type (**Figure 6.2 panel A,C**) with larger

CSPs occurring throughout the N-lobe and in the c-terminal tail, though to a lesser extent than PKA-C^{WT}. Further analysis of the ΔCSP ($\Delta\delta_{WT}$-$\Delta\delta_{E31V}$) shows regions of positive ΔCSP confirming that upon binding ATPγN, PKA-C^{E31V} does not adopt as closed of a conformation as the wild-type kinase (**Figure 6.8 panel A**). Subsequent binding of PKI to ATPγN-saturated PKA-C^{E31V} also exhibits similar CSPs compared to wild-type (**Figure 6.2 panel B,D**), though to a larger extent as reflected in the negative ΔCSP values (**Figure 6.7 panel B**).

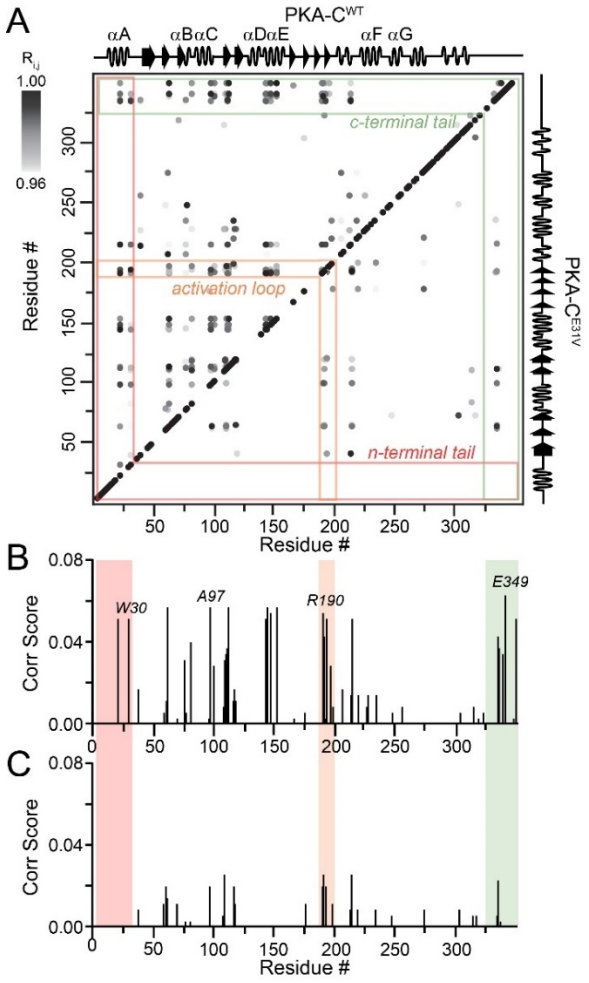

Figure 6.3. The reduction in binding cooperativity corresponds to a decrease in intramolecular allosteric connectivities.
(**A**) CHESCA correlation matrix of PKA-C^{WT} (top diagonal) and PKA-C^{E31V} (bottom diagonal) upon binding PKI highlighting the notable reductions in correlations within the n-terminal tail (red), activation loop (orange), and c-terminal tail (green). Only correlations with R_{ij}> 0.98 are shown. Plot of correlation score vs. residue for (**B**) PKA-C^{WT} and (**C**) PKA-C^{E31V} emphasizing the residues that show the largest reductions in correlation score that make contacts with the □C-helix. See material and methods for the calculation of correlation scores.

Rearrangement of the allosteric network of PKA-C^{E31V} is linked to a decrease in nucleotide-substrate binding cooperativity. Since cooperativity is often manifested as structural rearrangements upon ligand binding, we further analyzed the chemical shift perturbations of PKA-C^{WT} and PKA-C^{E31V} using CHEmical Shift Covariance Analysis (CHESCA). This statistical method identifies covariant residues networks involved in a concerted response upon ligand binding and help tracing allosteric pathways [129, 130, 132]. The [^{1}H, ^{15}N]-TROSY-HSQC spectra of four forms of wild-type and PKA-C^{E31V} (apo, ATPγN-bound, ADP-bound, and ATPγN/PKI-bound) were used for CHESCA. When we analyzed the chemical shifts changes of PKA-C^{WT}, we identified a well-organized communication network in which spatially distinct clusters of residues responding to ATP and PKI binding in a coordinated manner [65]. In contrast, we observed a dramatic reduction in the intramolecular allosteric network of PKA-C^{E31V} similar to PKA-C^{L205R}, a Cushing's syndrome mutation with significantly higher occurrence [65, 228, 230]. In particular, highly correlated groups of residues in the N-lobe of PKA-C^{E31V}, including the αA-helix (K28, W30) and αC-helix (A97), display a dramatic reduction in the number of correlations for distal regions of the kinase, including the activation loop (R190, G193, L198), αF-helix (K217, V219, G225), and C-terminal tail (E334, N340, E349) (**Figure 6.3**). Notably, the loss of correlations occurs in structural elements surrounding the αC-helix.

The typical CHESCA analysis gives pairwise correlations along the primary protein sequences. Therefore, we adopted the definition of structural 'communities' introduced by McClendon *et al.* [140] to obtain a three-dimensional view of the correlated structural changes. Using this analysis, we found strong correlations among the major communities in response to nucleotide and pseudosubstrate binding (**Figure 6.4**) [140]. In particular, ComA, ComB, and ComC show average correlation coefficients higher than 0.95, indicating that these communities respond to ligand binding in a concerted manner. Notably, there are long-range correlations between ComA, ComB, and ComC with ComE, ComF and ComF1. ComC, which encompasses the αA- and αC-helix including E31, acts as a central hub, connecting six other communities as it is centered around a critical allosteric mediator the αC-helix, which bridges both lobes of the kinase. The density of these correlations underscores the concerted response of the N- and C-lobe to ligand binding. While the E31V mutation exhibits some of the local and long-range correlations, the values of the correlation coefficients are lower. ComC and parts of the activation loop of the mutant exhibit the most noticeable reduction in correlation to both local (ComA and

ComB) and distal (ComE and ComF) communities. Indeed ComC acts as a hub in the wild-type community map, having connections to six other communities and centered around a critical allosteric mediator of the kinase regulation, the αC-helix.

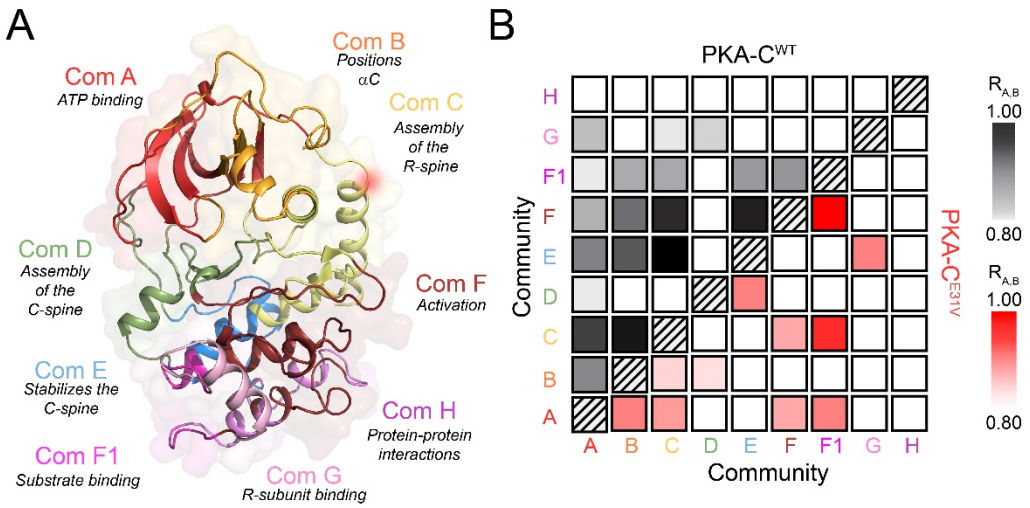

Figure 6.4. Community analysis of PKA-C^{E31V}.
(**A**) Community map of PKA-C highlighting functional/regulatory role of each community as defined by [140]. (**B**) Community CHESCA analysis of PKA-C^{WT} (top diagonal, black) and PKA-C^{E31V} (bottom diagonal, red). Only correlations with $R_{A,B}$ > 0.8 are shown.

MD simulations corroborate attenuation of allosteric network of PKA-C^{E31V}. To determine the effects of the E31V mutation on the conformational energy landscape of nucleotide-bound PKA-C, we carried out parallel MD simulations in explicit water. We set up the simulations starting from the X-ray coordinates of PKA-C^{WT} (PDB: 4WB5 [106]) mutating E31 into a valine and removing PKI [35]. After initial equilibration, we produced an MD trajectory and analyzed the conformational dynamics of PKA-C^{E31V}. Relative to PKA-C^{WT}, we observed large changes of root mean squared fluctuations (RMSF) of the backbone coordinates with effects that propagate to distal domains [80], including the αA-helix, αC-helix, as well as the C-terminal tail (**Figure 6.5 panel A**). The most noticeable effect of the E31V mutation is the increase in the αA-helix and αC-helix motions, presumably due to V31 moving towards the kinase's hydrophobic interior and disrupting the cation- π interactions between W30, R93 and R190. These 'sandwiched' cation-π interactions have been shown to be partially responsible for positioning the indole ring of W30 in a conserved pocket that can be exploited to regulate kinases activity [48, 292]. As the αA-helix is displaced, the indole ring of W30 undergoes a 180° flip, maintaining only

one cation-π interaction with R190 (**Figure 6.5 panel B**). The alteration of local structure is accompanied by the reduction of the global allostery in PKA-C^{E31V} with respect to PKA-C^{WT}, as is characterized by the dihedral mutual information of all residue pairs. The most prominent changes are the loss of correlation between N-terminal αA-helix and other regions (**Figure 6.9 panel A**). The mutual information matrices are further mapped onto the kinase structure via graph analysis, highlighting the attenuated network and vanish of key hubs throughout the kinase, particularly for S10 at the tip of αA-helix, N216 at αF-helix, D241 at αG-helix, and N340, F347 at the C-terminal tail(**Figure 6.9 panel B**), in good accordance with the CHESCA analysis. How does the attenuated allosteric network between N-lobe and C-lobe affect the binding of pseudosubstrate PKI_{5-24} and cooperativity? We first compared the dynamics of PKI in the ternary complexes. Whereas PKI_{5-24} is rather rigid with an average RMSF of about 1 Å for PKA-C^{WT}, the short peptide is much more dynamic for PKA-C^{E31V}, especially in its C-terminal end (**Figure 6.5 panel C**). We next analyzed interaction profile of PKI_{5-24} by computing the contact probability of all residue pairs between the short peptide and kinase. The stable interaction at the high affinity region (HAR) and the recognition sequence (P-3, P-2 and P+1 sites) is largely preserved, yet the contact probability between the C-terminal end of PKI and the peptide-positioning loop (residues 198-208) decreases (**Figure 6.10**), indicative of dynamic C-terminal flipping out of the hydrophobic pocket. Loss of anchoring of C-terminal end echoes the over 100-fold reduction of binding affinity measured by ITC.

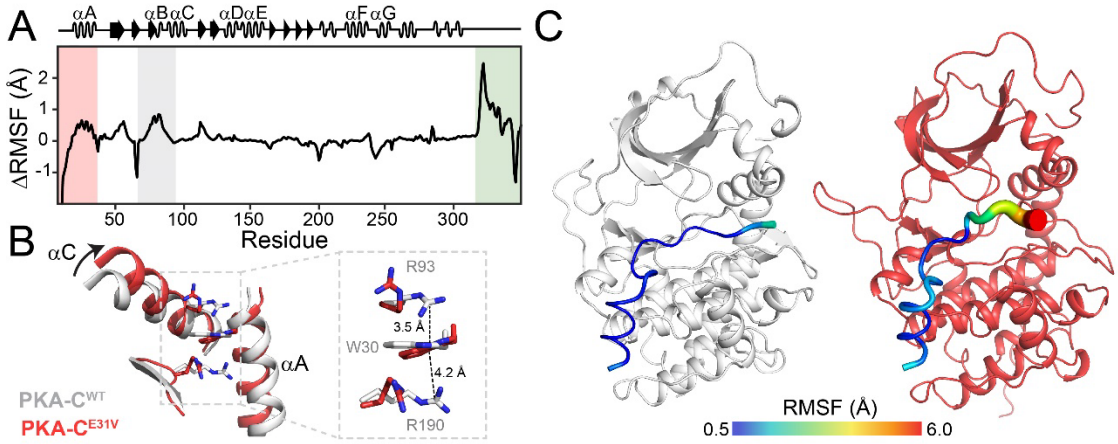

Figure 6.5. Altered dynamics of PKA-C^{E31V} reveled by MD simulations.
(**A**) ΔRMSF of PKA-C^{E31V} in the binary form over 1.0 μs of simulation. (**B**) Overlay of PKA-C^{WT} (PDB: 1ATP; gray) and PKA-C^{E31V} (from MD simulations; red) highlighting the structural rearrangements of the αA- and αC-helices caused by the E31V mutation. The inset shows the cation-π stacking interactions altered in response to the mutation. (**C**) Distinct dynamics of the

pseudosubstrate, PKI_{5-24}, in the ternary complex. Putty representation of RMSF for PKI_{5-24} for a typical MD snapshot of PKA-C^{WT} (gray) and PKA-C^{E31V} (red).

To link the MD simulations to the binding thermodynamics derived from the ITC experiments, we computed the difference in free energy of binding ($\Delta\Delta G_{binding}$) for PKA-C^{WT} and PKA-C^{E31V} using the free energy perturbation (FEP) method [293], as detailed in the thermodynamic cycle shown in **Figure 6.11**. The ratio of the cooperativity coefficients can be expressed in terms of free energy:

$$\frac{\sigma_{PKI}^{WT}}{\sigma_{PKI}^{E31V}} = \frac{K_{d\ Apo}^{WT} * K_{d\ Nucleotide}^{E31V}}{K_{d\ Nucleotide}^{WT} * K_{d\ Apo}^{E31V}} = \frac{K_{d\ Apo}^{WT}}{K_{d\ Apo}^{E31V}} \times \frac{K_{d\ Nucleotide}^{E31V}}{K_{d\ Nucleotide}^{WT}} = e^{-\frac{\Delta\Delta G_{Nucleotide} - \Delta\Delta G_{Apo}}{RT}}$$

$$= e^{-\frac{\left(\Delta G_4 - \Delta G_3\right) - \left(\Delta G_2 - \Delta G_1\right)}{RT}}$$

Where $\frac{\sigma_{PKI}^{WT}}{\sigma_{PKI}^{E31V}}$ represents the ratio of the cooperativity coefficients for wild-type and E31V, and the free energy change of a mutation in different states ΔG_1 to ΔG_4 is illustrated in **Figure 6.11 panel A**. Using this expression for the binding of PKI to apo PKA-C^{E31V}, the FEP method calculates a free energy difference between the free and bound state of -1.1 ± 0.3 kcal/mol, corresponding to a ~7-fold reduction in the binding affinity of PKA-C^{E31V} for PKI. This value is in excellent agreement with the experimental results (**Table 6.4**). On the other hand, the binding of PKI to the nucleotide-bound E31V mutant resulted in a free energy perturbation of 0.3 ± 0.2 kcal/mol, indicating a reduction in binding affinity. From the differences of these two values, it is possible to estimate approximately a 11-fold reduction in the nucleotide/PKI binding cooperativity (**Figure 6.3 panel B**), which is in qualitative agreement with ITC experiments. We also calculated the change in cooperativity for binding PKI first and then the nucleotide (**Figure 6.3 panel C**). These calculations confirmed the reduction in cooperativity with a value that is approximately 24-fold lower for the ATP binding by PKA-C^{E31V}, further supporting the experimentally observed loss in cooperativity for PKA-C^{E31V} (**Table 6.4**).

Nucleotide-substrate binding cooperativity and extent of allosteric communication are directly correlated. Both thermodynamic and NMR data show that Cushing's syndrome mutants, PKA-C^{L205R} and PKA-C^{E31V}, exhibit reduced binding cooperativity and decreased intramolecular allosteric communication. Therefore, we hypothesized that the coordinated structural changes might be correlated to the nucleotide-substrate

cooperative binding response. Hence, a disruption of the allosteric network would directly affect the nucleotide-substrate binding cooperativity. To test this, we analyzed the thermodynamics and structural response of PKA-C^{W196R}, another mutant that was found in 3% of Cushing's patients [20]. This mutation is located in the activation loop and is adjacent to the T197 phosphorylation site. We repeated both ITC and NMR analysis for PKA-C^{W196R}, and similarly to PKA-C^{E31V} we found a significant attenuation in both binding cooperativity and extent of intramolecular allosteric communication (**Table 6.5**, **Figure 6.12**). From the CHESCA matrices of these three mutants and PKA-C^{WT}, we extracted the relative correlation score (see Material and Methods), which can be used to estimate the density of the intramolecular allosteric networks. We then plot the relative correlation scores versus ln(σ). We found that these parameters are linearly correlated (R^2 = 0.98, **Figure 6.6**). This relationship suggests that the extent of the nucleotide-substrate binding cooperativity depends on the coordinated structural changes of the two lobes of the enzyme upon nucleotide and substrate binding.

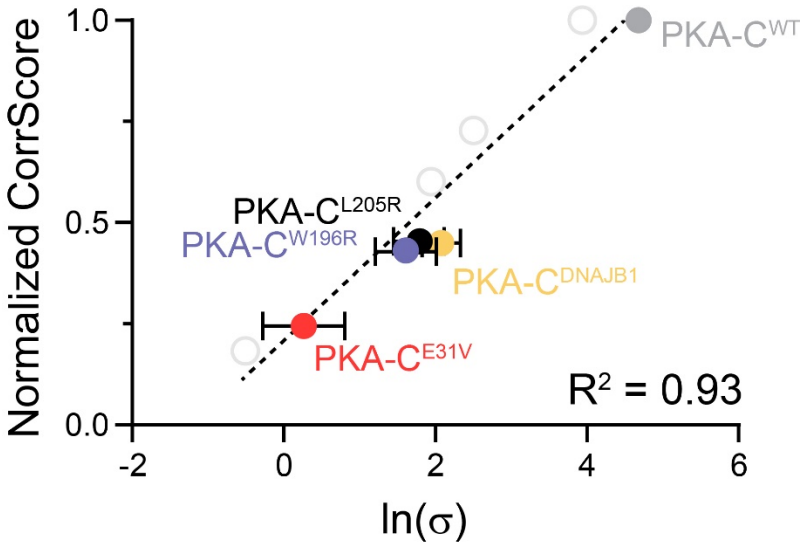

Figure 6.6. Relationship between coordinated structural changes identified by CHESCA and the nucleotide-substrate binding cooperativity (σ) determined by ITC measurements.
Values used for plotting σ of PKA-C^{L205R} and PKA-C^{DNAJB1} have been published in [65] and [107], respectively.

6.4 Discussion

The cAMP/PKA pathway plays a central role in the regulation of adrenocortical growth and steroidogenesis [99, 227]. Although multiple components of the cAMP/PKA pathway have

been implicated in various endocrine disease states, it was not until recently that PKA-C was discovered to play a central role [294]. To date, eight mutations have been discovered in *PRKACA* in cortisol-producing ACA's responsible for Cushing's syndrome [26-30, 102, 290, 291]. Except for E31V, all mutations are positioned in the substrate binding cleft or at the R/C interface, providing a justification for the loss of substrate fidelity and regulation of the kinase [20, 65]. However, it has been difficult to rationalize why the E31V mutant results in the same phenotype of the other orthosteric Cushing's syndrome driving mutations. This present study shows that local conformational changes caused by the E31V mutation alter key allosteric interactions that link the terminal regions of the C-terminal tail, αA- and αC-helix. MD simulations revealed that the E31V mutation increases the conformational dynamics within the αA-helix, causing it to dislodge from the kinase core and thereby disrupting canonical cation-π interactions between W30 and R93 and R190 [46, 47]. These structural alterations cause the N-lobe of the kinase to swing outward adopting a more open conformation, with the activation loop in a *flipped* conformation, forming a stable salt bridge with the αC-helix and disrupting a critical allosteric node responsible for inter-lobe allosteric communication and binding cooperativity [46].

Cooperativity is fundamental factor for macromolecular assembly and signal amplification [3, 113, 265]. For PKA-C, binding cooperativity has been used to define the role of ATP as an allosteric effector, able to amplify the substrate's binding affinity [82]. However, PKA-C interacts with other binding partners including the R-subunits that keep its function under strict control. Notably, the R-subunits recognition sequences are highly homologous to those of substrates and PKI. Therefore, it is likely that the loss in nucleotide/PKI binding cooperativity we observed for these Cushing's syndrome mutants may negatively affect the assembly of the R:C complex and the entire cAMP signaling pathway.

In conclusion, we identified a common trait between orthosteric and allosteric mutations linked to Cushing's syndrome. These mutations display a reduced binding cooperativity with a concomitant loss in intramolecular allosteric communication. The effects derived by these events are manifested as a loss of substrate fidelity and regulation by the R-subunit, while the catalytic activity of these mutants remains essentially unaltered. These results may explain how these aberrant enzymes give rise to anomalous phosphoproteomic profiles [20].

6.5 Materials and Methods

Sample Preparation. Recombinant human Cα subunit of cAMP-dependent protein kinase A cDNA (PKA-C^{WT} and PKA-C^{E31V}) was cloned into a pET-28a vector. A tobacco etch virus (TEV) cleavage site was incorporated via mutagenesis into the vector between the cDNA coding for the kinase and a thrombin cleavage site. The kinase was expressed in *Escherichia coli* BL21 (DE3) according to procedures previously published [65]. PKI (full-length) was expressed and purified according to procedures previously published [60]. Peptides (Kemptide/PKI_{5-24}) were synthesized using standard Fmoc chemistry on a CEM Liberty Blue microwave synthesizer, cleaved with Reagent K (82.5% TFA, 5% phenol, 5% thioanisole, 2.5% ethanedithiol, and 5% water) for 3 h and purified using a semipreparative Supelco C18 reverse-phase HPLC column at 3 mL/min. Molecular weight and the quantity of the peptides were verified by LC-MS and/or amino acid analysis (Texas Tech Protein Chemistry Laboratory).

ITC Measurements. ITC measurements were performed with a low-volume NanoITC (TA Instruments). PKA-C^{WT} and PKA-C^{E31V} were dialyzed into 20 mM MOPS, 90 mM KCl, 10 mM DTT, 10 mM $MgCl_2$, and 1 mM NaN_3 (pH 6.5). PKA-C concentrations for ITC measurements were between 100-110 μM as confirmed by A_{280} = 53860 $M^{-1}cm^{-1}$. All measurements with ATPγN saturated PKA-C^{WT} and PKA-C^{E31V} were performed at 2 mM ATPγN. ITC measurements were performed at 300K in triplicates. Approximately 300 μL of PKA-C was used for each experiment, and 50 μL of 2 mM ATPγN and 0.6-0.8 mM PKI in the titrant syringe. The heat of dilution of the ligand into the buffer was taken into account for all experiments and subtracted. Curves were analyzed with the NanoAnalyze software (TA Instruments) using the Wiseman Isotherm [242]:

$$\frac{d[MX]}{d[X_{tot}]} = \Delta H^{\circ} V_0 \left[\frac{1}{2} + \frac{1 - \frac{1-r}{2} - R_m/2}{(R_m^2 - 2R_m(1-r) + (1+r)^2)^{1/2}}\right] \qquad (1)$$

where *d[MX]* is the change in total complex with respect to change in total protein concentration, $d[X_{tot}]$ is dependent on *r*, the ratio of K_d with respect to the total protein concentration, and R_M, the ratio between total ligand and total protein concentration. The free energy of binding was determined using the following:

$$\Delta G = RT \ln K_d$$

where R is the universal gas constant and T is the temperature at measurement (300K). The entropic contribution to binding was calculated using the following:

$$T\Delta S = \Delta H - \Delta G.$$

Calculations for the cooperativity constant (σ) were calculated as follows:

$$\sigma = \frac{K_{d\ Apo}}{K_{d\ Nucleotide}}$$

where $K_{d\ Apo}$ is the K_d of PKI_{5-24} binding to the apoenzyme and $K_{d\ Nucleotide}$ is the K_d of PKI_{5-24} binding to the nucleotide-bound enzyme.

Enzyme Assays. Steady-state activity assays with Kemptide were performed under saturating ATP concentrations and spectrophotometrically at 298K as described by Cook et al [85]. The values of V_{max} and K_M were obtained from a nonlinear fit of the initial velocities to the Michaelis-Menten equation.

NMR Spectroscopy. Uniformly ^{15}N-labeled PKA-C^{WT} and PKA-C^{E31V} were overexpressed and purified as described above. NMR experiments were performed in 90 mM KCl, 20 mM KH_2PO_4, 10 mM dithiothreitol (DTT), 10 mM $MgCl_2$, and 1 mM NaN_3 at pH 6.5. Standard [^1H-^{15}N]-TROSY-HSQC experiments were carried out for PKA-C^{E31V} and PKA-C^{WT} on a 900-MHz Bruker Advance III spectrometer equipped with a TCI cryoprobe. Concentrations for samples were 0.2-0.3 mM as determined by A_{280} measurements, 12 mM ATPγN was added for the nucleotide-bound form, and 0.2-1.2 mM PKI for the ternary complex. Spectra were collected at 300K, processed using NMRPipe [243], and visualized using Sparky [244].

All [^1H-^{15}N]-TROSY-HSQC experiments were acquired with 2048 (proton) and 256 (nitrogen) complex points. Combined chemical shift perturbations were calculated using ^1H and ^{15}N chemical shifts according to the following:

$$\Delta\delta = \sqrt{(\Delta\delta H)^2 + 0.154(\Delta\delta N)^2}$$

Chemical Shift Analyses.

COordiNated ChemIcal Shift bEhavior (CONCISE). CONCISE was used to monitor chemical shift trajectories and measure the change in equilibrium position using each PKA-C construct (apo, ATPγN, ADP, ATPγN/PKI). This method uses principal component

analysis to identify sets of residues whose chemical shifts respond linearly to a conformational transition (i.e. open, intermediate, and closed). Each residue provides a measure of the equilibrium position for each PKA-C construct in the form of scores along the first principal component (PC1). To identify the residues whose chemical shifts follow a linear trajectory, a threshold of 3.0 for the ratio of the standard deviations of PC1 over PC2 was used, and residues not exhibiting a significant chemical shift were excluded based on the linewidth.

CHEmical Shift Covariance Analysis (CHESCA). CHESCA was used to identify and functionally characterize allosteric networks of residues eliciting concerted responses to, in this case, nucleotide and pseudosubstrate. A total of four states were used to identify inter-residue correlations: apo, ADP-bound, ATPγN-bound, and ATPγN/PKI-bound. Identification of inter-residue correlations by CHESCA relies on agglomerative clustering (AC) and singular value decomposition (SVD). Pairwise correlations between chemical shift variations experienced by different residues are analyzed to identify networks of coupled residues and when plotted on a correlation matrix, allows for the identification of regions that are correlated to one another. A correlation coefficient (R_{ij}) cutoff of 0.96 was used to filter non-linear residues. Residues not exhibiting a significant chemical shift (small shifts in ppm) were excluded based on linewidth. For each residue the max change in chemical shift was calculated in both the ^{1}H (*x*) and ^{15}N (*y*) dimension ($\Delta\delta_{x,y}$). Residues were included in CHESCA analysis only if they satisfied the following: $\Delta\delta_{x,y} > ½\ \Delta v_{xA,yA} + ½\ \Delta v_{xB,yB}$, where *A* and *B* correspond to two different forms analyzed (note there is no dependence on which two forms satisfied this statement). Correlation scores were used to quantify the CHESCA correlation of a single residue or a group of residues with another group. Correlation scores were evaluated for both (a) a single residue and (b) the full protein. The generalized mathematical expression for evaluating either case is given as follows:

$$Corr\ Score = \frac{number\ of\ (R_{ij} > cutoff)}{total\ number\ of\ R_{ij}}$$

where *R* is the CHESCA correlation matrix and *i* and *j* denote (a) a single residue and all other assigned residues in the protein, respectively, or (b) both represent all the assigned residues in the protein. Community CHESCA analysis is a chemical shift based correlation map between various functional communities within the kinase. Each community is a

group of residues (McClendon et al.[140]) associated with a function or regulatory mechanism. Mathematically, this community-based CHESCA analysis is a selective interpretation of CHESCA, where we evaluate a correlation score between residues in various communities as shown below. In order to represent community-based CHESCA analysis we lowered the correlation cutoff such that $R_{cutoff} > 0.8$. Suppose community A and community B has n_A and n_B number of assigned residues respectively, the correlation score between A and B is defined as,

$$R_{A,B} = \text{Number of } (R_{ij} > R_{cutoff}) / (n_A * n_B).$$

Where R_{ij} is the CHESCA correlation coefficient between residue i (belongs to community A) and residue j (belongs to community B). R_{cutoff} is the correlation value cutoff. $R_{A,B}$ can take values from 0 (no correlation between residues in A and B) to 1 (all residues in A has correlation > cutoff with all residues in B).

MD Simulations. We used the crystal structure of PKA-C^{WT} (PDB ID: 4WB5[106]) as the template. We further aligned the current structure with the full length PKA-C^{WT} and added the missing residues 1-12 at the N terminus. The protonation state of histidine residues followed our previous settings [80]. The protein was solvated in a rhombic dodecahedron solvent box with TIP3P water molecule layer extended approximately 10 Å away from the surface of the proteins. Counter ions (K^+ and Cl^-) were added to ensure electrostatic neutrality corresponding to an ionic concentration of ~150 mM. All covalent bonds involving a hydrogen atom of the protein were constrained with the LINCS[287]algorithm. and long-range electrostatic interactions were treated with the particle-mesh Ewald [288] method with a real-space cutoff of 10 Å. Parallel simulations on the apo form, the binary form with one Mg^{2+} ion and one ATP, and the ternary form with two Mg^{2+} ions, one ATP and one PKI_{5-24} were performed simultaneously using GROMACS 5.1.4 [285] with the CHARMM36a1 force field [286]. Each system was minimized using the steepest decent algorithm to remove bad contacts, and then gradually heated to 300K at a constant volume over 1 ns, using harmonic restraints with a force constant 1000 kJ/(mol*Å^2) on heavy atoms of both proteins and nucleotides. Over the following 12 ns of simulations at constant pressure (1 atm) and temperature (300K), the restraints were gradually released. The systems were equilibrated for an additional 20 ns without positional restraints. The Parrinello-Rahman[289] barostat was used to keep the pressure constant, while a V-rescale thermostat with a time step of 2 fs was used to keep the temperature constant.

Each system was simulated for 1.0 μs, with snapshots recorded every 50 ps. To characterize the allosteric network, the dihedral mutual information was computed using MDEntropy [295] for every residue pair, and the normalized mutual information matrix was mapped onto the structure for graph analysis using Xpyder [296] with MI_{cutoff} = 0.3.

Relative change of cooperativity from free energy perturbation calculations. The cooperativity can be defined for both nucleotide and pseudosubstrate PKI, respectively. For nucleotide, the change of cooperativity upon mutation can be rewritten as the difference in ΔΔG between the apo and the PKI-bound state, as shown in the following equation and illustrated in **Figure 6.11**:

$$\frac{\sigma^{WT}_{Nucleotide}}{\sigma^{E31V}_{Nucleotide}} = \frac{K^{WT}_{d\ Apo} * K^{E31V}_{d\ PKI}}{K^{WT}_{d\ PKI} * K^{E31V}_{d\ Apo}} = \frac{K^{WT}_{d\ Apo}}{K^{E31V}_{d\ Apo}} \times \frac{K^{E31V}_{d\ PKI}}{K^{WT}_{d\ PKI}} = e^{-\frac{(\Delta G_1\ -\Delta G_3\ )+(\Delta G_4\ -\Delta G_2\ )}{RT}}$$

The free energies ΔG due to amino acid mutations were determined following a protocol based on the Bennett acceptance ratio (BAR) implemented in the GROMACS and PMX [293]. To avoid the artifacts by introducing a charged mutation, the double-system/single-box setup was used. The procedure employs dual protein topologies that include both residues of the wild-type (λ = 0) and the mutant protein (λ = 1) coupled by the progressing variable λ. Of course, both the complex and unbound structures were used to obtain the change in binding free energies using standard thermodynamic cycle approach. Single-site mutations were performed based on the well-equilibrated structure of PKA-C^{WT} from simulations. The computational details are identical to those detailed above, except that after 40 ns of equilibration of both initial and final states for each mutation, 200 additional trajectories, each lasting 100 ps, were initiated from the last 20 ns simulations both in the forward and in the backward transformations to accumulate statistical averages and fluctuations.

6.6 Acknowledgements

This work was supported by the National Institutes of Health, GM100310 (G.V.), S10 OD021536 (G.V.) and GM046736 (J.G), the American Heart Association, 20PRE35120253 (C.W), and the National Natural Science Foundation of China, No. 22007069 (Y.W.), for additional analysis performed at Shenzhen Bay Laboratory. NMR experiments were carried out at the Minnesota NMR Center and MD calculations at the Minnesota Supercomputing Institute.

6.7 Author Contributions

C.W. collected and analyzed activity assay, NMR, and ITC data and contributed to the writing of the manuscript. Y.W. carried out and analyzed MD simulations, with J.G. directing and assisting with analysis of the MD simulations. D.C, D.A.B and S.S.T contributed to critical analysis of the data and writing of the manuscript. G.V. conceived and directed the project, along with assisting with data analysis and writing the manuscript.

6.8 Supplementary Figures

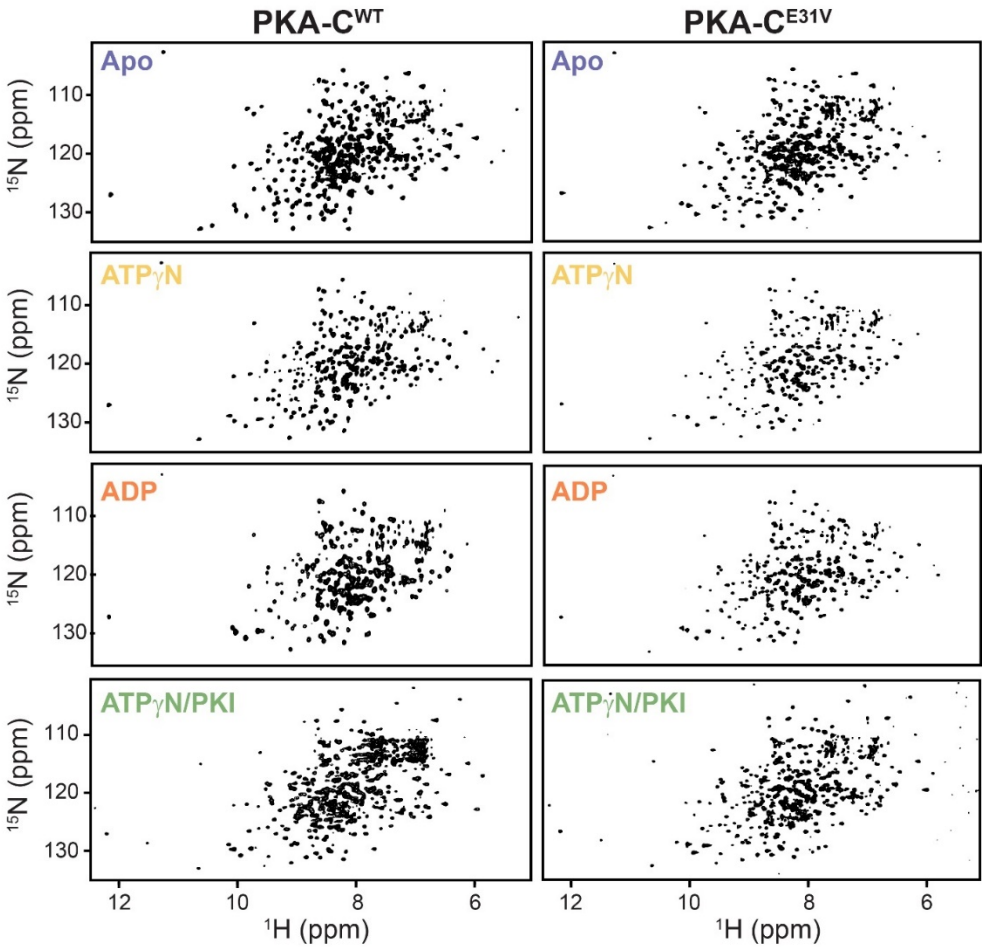

Figure 6.7. [^{1}H, ^{15}N]-TROSY-HSQC spectra for PKA-C^{WT} and PKA-C^{E31V} in the apo, ATPγN-, ADP-, and ATPγN/PKI-bound forms.

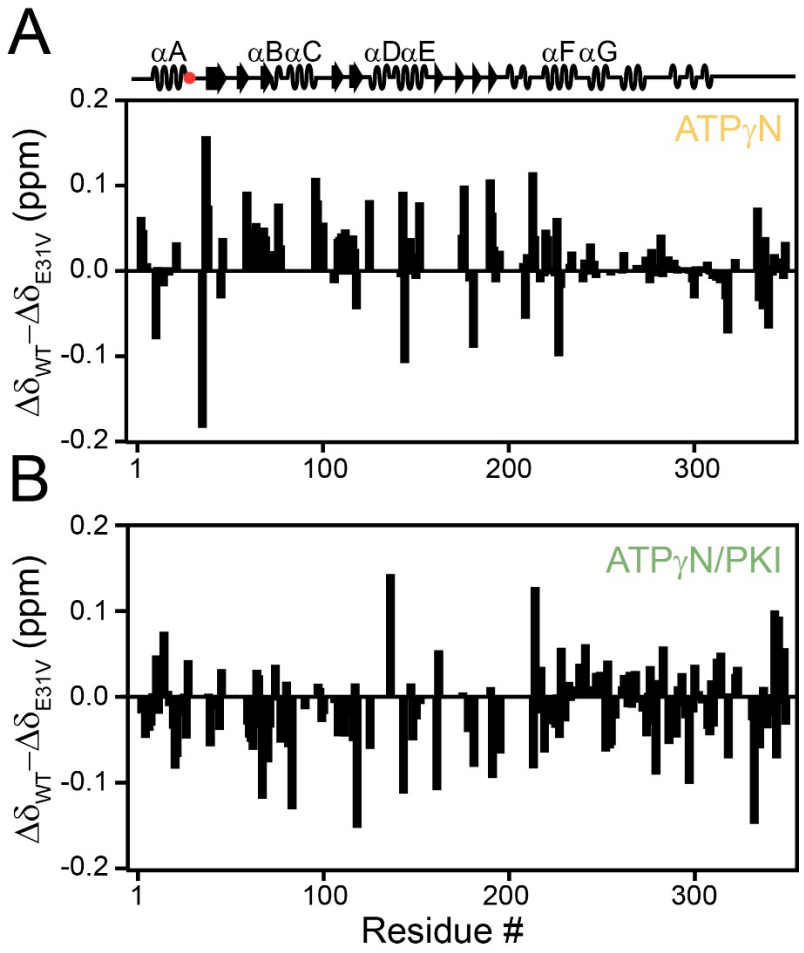

Figure 6.8. Change in chemical shift perturbation between PKA-C^{WT} and PKA-C^{E31V}. Change in CSP ($\Delta\delta_{WT}$-$\Delta\delta_{E31V}$) upon binding (**A**) ATPγN. and subsequent binding of (**B**) PKI.

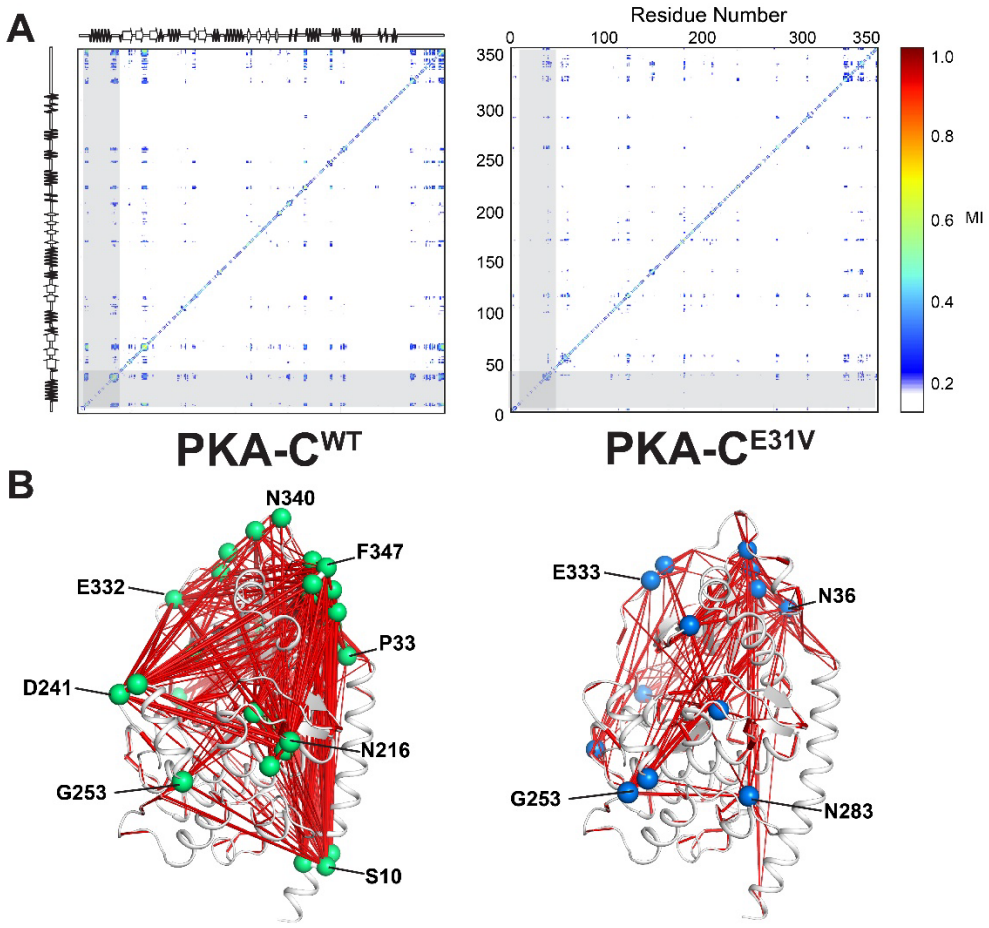

Figure 6.9. Attenuated allostery of PKA-C^{E31V} revealed by MD simulations.
(**A**) Dihedral mutual information matrices of PKA-C^{WT} and PKA-C^{E31V}, highlighting the prominent reduction of allostery in the N-terminus of PKA-C^{E31V}. (**B**) Comparison of allosteric network mapping from the mutual information matrices (MI_{cutoff} = 0.3), with the key hub residues labeled for PKA-C^{WT} and PKA-C^{E31V}.

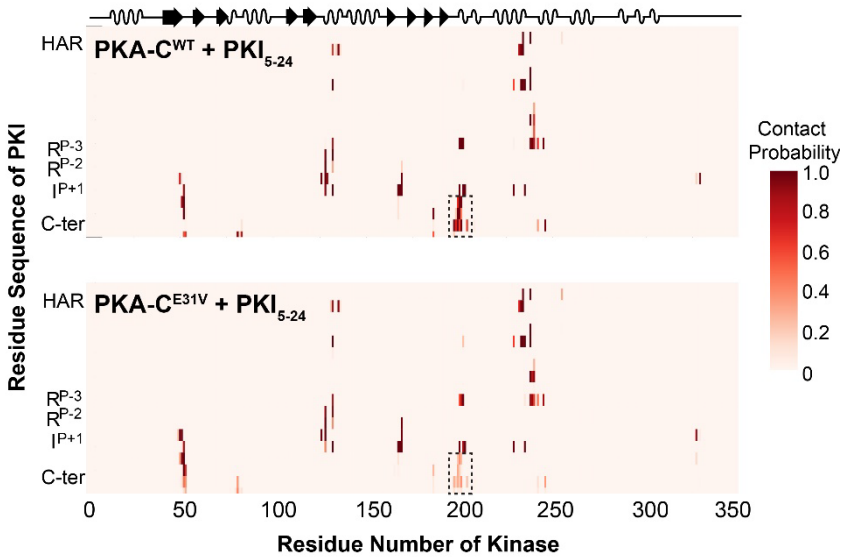

Figure 6.10. Distinct interaction profile of PKI_{5-24} in the ternary complex with PKA-C^{WT} and PKA-C^{E31V}.
Probability of the formation of inter-residue contact between PKA-C^{WT} (above) and PKI_{5-24} and PKA-C^{E31V} (below) ternary complex, highlighting a prominent reduction of interaction between the C-terminus of PKI_{5-24} and the peptide positioning loop of the kinase.

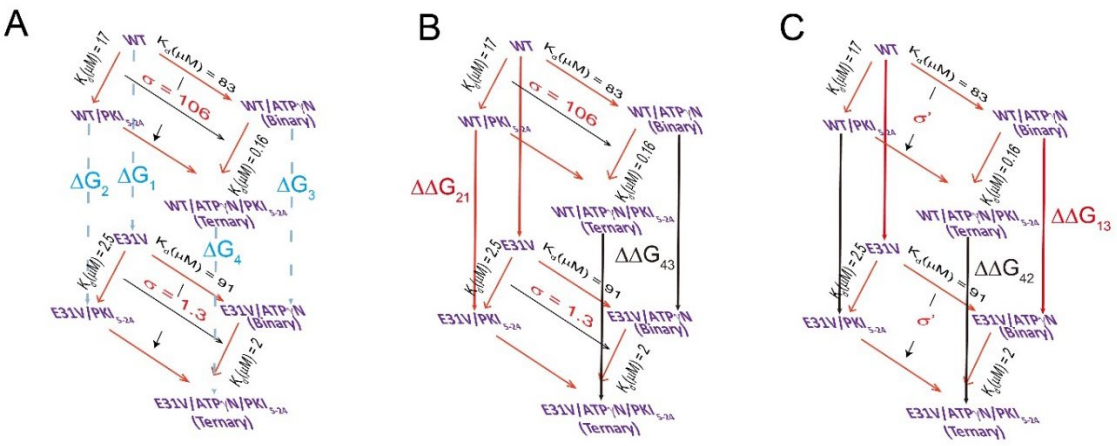

Figure 6.11. Thermodynamic cycle linking the free energy perturbation (FEP) calculation to ratio of K_d and σ.

(**A**). Alchemical transition steps that determine the relative change of binding free energy. The change in PKI-binding to the apo state upon mutation can either be obtained from the experimental ratio $\frac{K_{d\ Apo}^{E31V}}{K_{d\ Apo}^{WT}}$, or be computed from the difference between the two alchemical transition ΔG_2-ΔG_1. (**B**). Computational scheme used to determine the ratio of the cooperativity coefficients (σ). $\Delta\Delta G_{21}$ is directly computed by grouping the two alchemical transitions in the same simulation box with forward transition of WT -> E31V, along with the reverse transition of E31V/$PKI_{5\text{-}24}$ -> WT/$PKI_{5\text{-}24}$. The same computational scheme was used to determine $\Delta\Delta G_{43}$. The ratio of σ was derived from the difference between $\Delta\Delta G_{21}$ and $\Delta\Delta G_{43}$. (**C**). Computational scheme used to determine the ratio of the cooperativity coefficients σ' calculating $\Delta\Delta G_{13}$ and $\Delta\Delta G_{42}$, respectively.

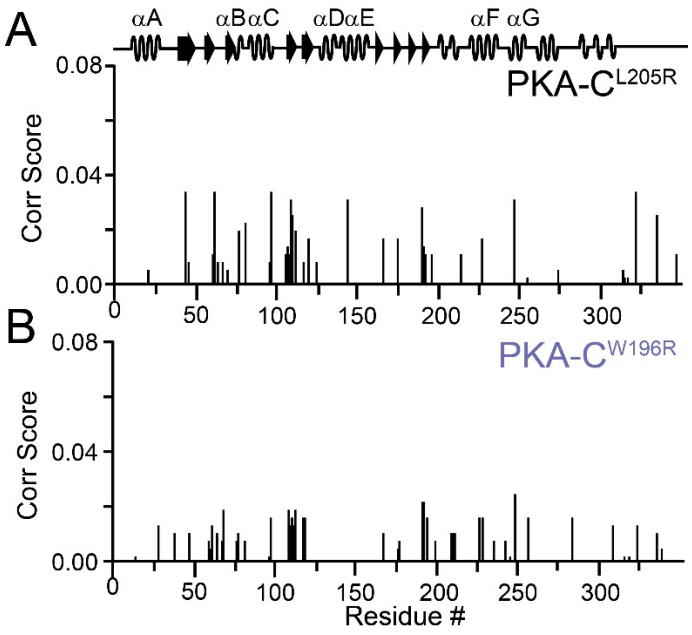

Figure 6.12. Correlation score analysis of PKA-C^{L205R} and PKA-C^{W196R}.
Plot of correlation score vs. residue for (**A**) PKA-C^{L205R} and (**B**) PKA-C^{W196R}. See materials and methods for the calculation of correlation scores.

6.9 Supplementary Tables

Table 6.1. Changes in enthalpy, entropy, free energy, and dissociation constant for the binding of nucleotide to PKA-C^{E31V}.
All errors were calculated using triplicate measurements. Values for PKA-C^{WT} are published in [65].

	K_d (μM)	ΔG (kcal/mol)	ΔH (kcal/mol)	-TΔS (kcal/mol)
PKA-C^{E31V}	91 ± 9	-5.56 ± 0.06	-3.7 ± 0.2	-1.9 ± 0.2

Table 6.2. Changes in enthalpy, entropy, free energy, and dissociation constant for the binding of PKI_{5-24} to apo and nucleotide-saturated PKA-C^{E31V}.

Errors in ΔG, ΔH, $-T\Delta S$, and K_d were calculated using triplicate measurements. Errors in σ were propagated from error in K_d. Values for PKA-C^{WT} are published in [65].

	K_d (μM)	ΔG (kcal/mol)	ΔH (kcal/mol)	$-T\Delta S$ (kcal/mol)	σ
Apo	2.5 ± 0.5	-7.7 ± 0.1	-19.8 ± 0.4	12.1 ± 0.5	N/A
+ATPγN	2 ± 1	-7.9 ± 0.3	-17 ± 1	9 ± 1	1.3 ± 0.7

Table 6.3. Kinetic parameters of Kemptide phosphorylation by PKA-C^{WT} and PKA-C^{E31V}.
Values for K_m and k_{cat} were obtained from a non-linear least squares analysis of the concentration-dependent initial phosphorylation rates using a standard coupled enzyme activity assay. Error in k_{cat}/K_M was propagated from error in K_M and k_{cat}.

	PKA-C^{WT}	PKA-C^{E31V}
V_{max} (μM/sec)	0.52 ± 0.02	0.58 ± 0.02
K_M (μM)	59 ± 7	56 ± 5
k_{cat} (s^{-1})	24 ± 1	26 ± 1
k_{cat}/K_M	0.41 ± 0.05	0.46 ± 0.04

Table 6.4. Changes in relative binding free energy, $\Delta\Delta G$, and cooperativity from PKA-C^{WT} to PKA-C^{E31V} for the binding of PKI_{5-24} and the binding of ATP in the apo and binary states.

	$\Delta\Delta G_{apo}$ (kcal/mol)	$\Delta\Delta G_{binary}$ (kcal/mol)	Reduction in σ
PKI_{5-24} binding	-1.1 ± 0.3	0.3 ± 0.2	11 ± 5
ATP binding	-0.8 ± 0.2	1.1 ± 0.3	24 ± 9

Table 6.5. Changes in enthalpy, entropy, free energy, and dissociation constant for the binding of PKI_{5-24} to apo and nucleotide-saturated PKA-C^{W196R}.

Errors in ΔG, ΔH, -TΔS, and K_d were calculated using triplicate measurements. Errors in σ were propagated from error in K_d.

	K_d (μM)	ΔG (kcal/mol)	ΔH (kcal/mol)	-TΔS (kcal/mol)	σ
Apo	5 ± 2	-7.3 ± 0.2	-21.1 ± 0.8	13.8 ± 0.5	N/A
+ATPγN	0.95 ± 0.05	-8.28 ± 0.03	-19.2 ± 0.5	10.9 ± 0.5	5 ± 2

Perspectives

Since it was articulated nearly half a century ago, allostery has remained essential in understanding processes beyond the molecular level such as signal propagation and disease. Despite the substantial progress in understanding the complexities, many aspects underlying allosteric control are still poorly understood. Nonetheless, studies of allostery in relation to enzymology and pharmacology continue to be intense focal points due its expanding role in disease and drug discovery.

Biomolecules that exist in a range of closely related conformational states are defined as allosteric, as perturbation to any site in the structure leads to shifts in the distribution of the conformational states across the ensemble. In the cell, allosteric perturbations are common, typically arising from effector (ions, lipids, cAMP, drugs, proteins, RNA, DNA) binding; or covalent events such as phosphorylation or point mutations. With detailed mechanistic studies now being achievable thanks to advances in experimental and computational methods, recent studies have considered the impact of allosteric perturbations with a particular interest on how they impact cellular function and disease pathogenesis. Interestingly, although many characterized disease-causing mutations are located in binding sites, genetic analyses suggest that a majority of these mutations occur in locations distant from binding sites in proteins making allostery critical our understanding. Mutations are known to cause disease by either one of the following mechanisms: 1) a shift in the free-energy landscape (ensemble populations) leading to changing populations of the ‘on’ or ‘off’ states or leading to a change in the active site shape or dynamics or 2) the redistribution of the allosteric network in the protein. This extensive list illustrates how diverse mechanisms can be exploited to elicit dysfunction.

This thesis presents a series of studies highlighting the intricate regulation of allosteric information transfer and demonstrating that small perturbations in the form of mutations (see Chapter 4, 5, and 6) or ligand architectures (see Chapter 4) can disrupt enzymatic function through alteration of allosteric pathways or conformational ensembles. The studies presented herein highlight the fundamental role of allostery in cellular function and its relevance to disease, particularly in relation to Cushing’s Syndrome and Fibrolamellar Hepatocellular Carcinoma. Furthermore, cumulatively these studies suggest that attenuated allosteric cooperativity underlies the dysfunction of protein kinase A in disease pathogenesis. Together these studies lay the foundation for future work

addressing the implications of dysfunctional allostery in the context of regulation of PKA. In particular: How do changes in allosteric cooperativity manifest as alterations in the regulation of PKA? Do changes in the intramolecular allosteric network drive non-canonical protein-protein interactions? Moreover, what are the implications of allostery on the cellular level?

From the simplest perspective, allostery takes place on a single-molecule level, but to understand its effects it is necessary to put allostery in the context of the cell. The significant crosstalk amongst signaling pathways alone suggests that dysfunction of one component can elicit multiple disease consequences. Despite this, the implications of dysfunctional allostery and cooperativity on regulation are currently not well established. Thus, future studies focusing on the consequences of dysfunctional allostery in the context of the cellular network and organism will be essential to fully grasp the significance of allostery. Furthermore, studies looking at the implications of allostery from a systems biology perspective would assist in linking aberrant allosteric events on the single-molecule level to disease pathogenesis on the cellular level.

List of Publications

Publications directly related to thesis work:

Larsen, E.K.; Olivieri, C.; **Walker, C.;** V.S., M.; Gao, J.; Bernlohr, D.A.; Tonelli, M.; Markley, J.L.; Veglia, G. "Probing Protein-Protein Interactions Using Asymmetric Labeling and Carbonyl-Carbon Selective Heteronuclear NMR Spectroscopy." ***Molecules*** 2018, *23*, 1937. PMCID: PMC6205158

Walker, C.; Wang, Y.; Olivieri, C.; Karamafrooz, A.; Casby, J.; Bathon, K.; Calebiro, D.; Gao, J.; Bernlohr, D.A.; Taylor, S.S.; Veglia, G. "Cushing's Syndrome Driver Mutation Disrupts Protein Kinase A Allosteric Network Altering Both Regulation and Substrate Specificity." ***Science Advances*** 2019, 5, eaaw9298. PMCID: PMC6713507

Olivieri, C.*; **Walker, C.*;** Karamafrooz, A.*; Wang, Y.; V.S., M.; Porcelli, F.; Blumenthal, D.K.; Thomas, D.D.; Bernlohr, D.A.; Sandford, S.M.; Taylor, S.S.; Veglia, G. "Defective Internal Allosteric Network Imparts Dysfunctional ATP/Substrate Binding Cooperativity in Oncogenic Chimera of Protein Kinase A." ***Communications Biology*** 2021, 4, 321. PMCID: PMC7946884 *authors contributed equally

Walker, C.; Wang, Y.; Olivieri, C.; V.S., Manu; Gao, J.; Bernlohr, D.A.; Calebiro, D.; Taylor, S.S.; Veglia, G. "Is Disrupted Nucleotde-Substrate Cooperativity a Common Trait for Cushing's Syndrome Driving Mutations of Protein Kinase A?" ***Submitted***.

Olivieri, C.; Li, G.L.; V.S., M.; Wang, Y.; **Walker, C.;** Camilloni, C.; De Simone, A.; Vendruscolo, M.; Kim, J.; Bernlohr, D.A.; Taylor, S.S.; Veglia, G. "ATP-Competitive Inhibitors Modulate the Substrate Binding Cooperativity of a Kinase by Altering its Conformational Entropy." ***Submitted***.

Olivieri, C.; **Walker, C.;** V.S., M.; Bernlohr, D.A.; Melacini, G.; Taylor, S.S.; Veglia, G. "Intrinsic Equilibrium of the RIIβ PKA Holoenzyme Governs Cooperative cAMP Response." ***In preparation.***

Walker, C.; Veglia, G. "An NMR Perspective on Intramolecular Allosteric Communication in PKA." ***In preparation.***

Publications addressing different topics:

Wang, S.; Gopinath, T.; Larsen, E.K.; Weber, D.K.; **Walker, C**.; Uddigiri, V.R.; Mote, K.R.; Sahoo, S.K.; Periasamy, M.; Veglia, G. "Structural Basis for Sarcolipin's Regulation of Muscle Thermogenesis by the Sarcoplasmic Reticulum Ca^{2+}-ATPase." ***Under Review*.**

References

1. Nussinov, R. and C.J. Tsai, *Allostery in disease and in drug discovery.* Cell, 2013. **153**(2): p. 293-305.
2. Nussinov, R., C.J. Tsai, and J. Liu, *Principles of allosteric interactions in cell signaling.* J Am Chem Soc, 2014. **136**(51): p. 17692-701.
3. Wu, H., *Higher-Order Assemblies in a New Paradigm of Signal Transduction.* Cell, 2013. **153**(2): p. 287-292.
4. Monod, J., J. Wyman, and J.P. Changeux, *ON THE NATURE OF ALLOSTERIC TRANSITIONS: A PLAUSIBLE MODEL.* J Mol Biol, 1965. **12**: p. 88-118.
5. Koshland, D.E., Jr., G. Némethy, and D. Filmer, *Comparison of experimental binding data and theoretical models in proteins containing subunits.* Biochemistry, 1966. **5**(1): p. 365-85.
6. Colombo, M.F., D.C. Rau, and V.A. Parsegian, *Protein solvation in allosteric regulation: a water effect on hemoglobin.* Science, 1992. **256**(5057): p. 655-9.
7. Tsai, C.J., et al., *Folding funnels, binding funnels, and protein function.* Protein Sci, 1999. **8**(6): p. 1181-90.
8. Kumar, S., et al., *Folding funnels and conformational transitions via hinge-bending motions.* Cell Biochem Biophys, 1999. **31**(2): p. 141-64.
9. Shan, Y., et al., *Oncogenic mutations counteract intrinsic disorder in the EGFR kinase and promote receptor dimerization.* Cell, 2012. **149**(4): p. 860-70.
10. Lu, S., et al., *The Structural Basis of Oncogenic Mutations G12, G13 and Q61 in Small GTPase K-Ras4B.* Scientific Reports, 2016. **6**(1): p. 21949.
11. Tsai, C.J. and R. Nussinov, *Allostery modulates the beat rate of a cardiac pacemaker.* J Biol Chem, 2017. **292**(15): p. 6429-6430.
12. Wan, P.T., et al., *Mechanism of activation of the RAF-ERK signaling pathway by oncogenic mutations of B-RAF.* Cell, 2004. **116**(6): p. 855-67.
13. Kravats, A.N., S. Tonddast-Navaei, and G. Stan, *Coarse-Grained Simulations of Topology-Dependent Mechanisms of Protein Unfolding and Translocation Mediated by ClpY ATPase Nanomachines.* PLoS Comput Biol, 2016. **12**(1): p. e1004675.
14. Guarnera, E. and I.N. Berezovsky, *Structure-Based Statistical Mechanical Model Accounts for the Causality and Energetics of Allosteric Communication.* PLoS Comput Biol, 2016. **12**(3): p. e1004678.
15. Kalescky, R., et al., *Rigid Residue Scan Simulations Systematically Reveal Residue Entropic Roles in Protein Allostery.* PLoS Comput Biol, 2016. **12**(4): p. e1004893.
16. Grutsch, S., S. Brüschweiler, and M. Tollinger, *NMR Methods to Study Dynamic Allostery.* PLoS Comput Biol, 2016. **12**(3): p. e1004620.
17. Tzeng, S.-R. and C.G. Kalodimos, *Protein dynamics and allostery: an NMR view.* Current Opinion in Structural Biology, 2011. **21**(1): p. 62-67.
18. Lisi, G.P. and J.P. Loria, *Solution NMR Spectroscopy for the Study of Enzyme Allostery.* Chem Rev, 2016.
19. Draznin, B., *Molecular Mechanisms of Insulin Resistance: Serine Phosphorylation of Insulin Receptor Substrate-1 and Increased Expression of p85α.* The Two Sides of a Coin, 2006. **55**(8): p. 2392-2397.
20. Bathon, K., et al., *Alterations in Protein Kinase A Substrate Specificity as a Potential Cause of Cushing's Syndrome.* Endocrinology, 2019: p. en.2018-00775-en.2018-00775.

21. Minamoto, T., et al., *Distinct pattern of p53 phosphorylation in human tumors.* Oncogene, 2001. **20**(26): p. 3341-3347.
22. Schett, G., J. Zwerina, and G. Firestein, *The p38 mitogen-activated protein kinase (MAPK) pathway in rheumatoid arthritis.* Ann Rheum Dis, 2008. **67**(7): p. 909-16.
23. Walker, L.A., D.A. Fullerton, and P.M. Buttrick, *Contractile protein phosphorylation predicts human heart disease phenotypes.* Am J Physiol Heart Circ Physiol, 2013. **304**(12): p. H1644-50.
24. Hu, R., et al., *KinaseMD: kinase mutations and drug response database.* Nucleic Acids Research, 2020. **49**(D1): p. D552-D561.
25. Torkamani, A., G. Verkhivker, and N.J. Schork, *Cancer driver mutations in protein kinase genes.* Cancer Lett, 2009. **281**(2): p. 117-27.
26. Goh, G., et al., *Recurrent activating mutation in PRKACA in cortisol-producing adrenal tumors.* Nature Genetics, 2014. **46**: p. 613.
27. Sato, Y., et al., *Recurrent somatic mutations underlie corticotropin-independent Cushing's syndrome.* Science, 2014. **344**(6186): p. 917-20.
28. Beuschlein , F., et al., *Constitutive Activation of PKA Catalytic Subunit in Adrenal Cushing's Syndrome.* New England Journal of Medicine, 2014. **370**(11): p. 1019-1028.
29. Cao, Y., et al., *Activating hotspot L205R mutation in PRKACA and adrenal Cushing's syndrome.* Science, 2014. **344**(6186): p. 913-7.
30. Di Dalmazi, G., et al., *Novel somatic mutations in the catalytic subunit of the protein kinase A as a cause of adrenal Cushing's syndrome: a European multicentric study.* J Clin Endocrinol Metab, 2014. **99**(10): p. E2093-100.
31. Honeyman, J.N., et al., *Detection of a recurrent DNAJB1-PRKACA chimeric transcript in fibrolamellar hepatocellular carcinoma.* Science, 2014. **343**(6174): p. 1010-4.
32. Graham, R.P., et al., *DNAJB1-PRKACA is specific for fibrolamellar carcinoma.* Modern Pathology, 2015. **28**(6): p. 822-829.
33. Manning, G., et al., *The Protein Kinase Complement of the Human Genome.* Science, 2002. **298**(5600): p. 1912-1934.
34. Knighton, D.R., et al., *Crystallization studies of cAMP-dependent protein kinase. Cocrystals of the catalytic subunit with a 20 amino acid residue peptide inhibitor and MgATP diffract to 3.0 A resolution.* J Mol Biol, 1991. **220**(2): p. 217-20.
35. Knighton, D.R., et al., *Crystal structure of the catalytic subunit of cyclic adenosine monophosphate-dependent protein kinase.* Science, 1991. **253**(5018): p. 407-14.
36. Knighton, D.R., et al., *Structure of a peptide inhibitor bound to the catalytic subunit of cyclic adenosine monophosphate-dependent protein kinase.* Science, 1991. **253**(5018): p. 414-20.
37. Zheng, J., et al., *2.2 A refined crystal structure of the catalytic subunit of cAMP-dependent protein kinase complexed with MnATP and a peptide inhibitor.* Acta Crystallographica Section D, 1993. **49**(3): p. 362-365.
38. Kornev, A.P., et al., *Surface comparison of active and inactive protein kinases identifies a conserved activation mechanism.* Proc Natl Acad Sci U S A, 2006. **103**(47): p. 17783-8.
39. Kornev, A.P., S.S. Taylor, and L.F. Ten Eyck, *A helix scaffold for the assembly of active protein kinases.* Proc Natl Acad Sci U S A, 2008. **105**(38): p. 14377-82.
40. Hanks, S., A. Quinn, and T. Hunter, *The protein kinase family: conserved features and deduced phylogeny of the catalytic domains.* Science, 1988. **241**(4861): p. 42-52.

41. Hanks, S.K. and T. Hunter, *The eukaryotic protein kinase superfamily: kinase (catalytic) domain structure and classification1.* The FASEB Journal, 1995. **9**(8): p. 576-596.
42. Johnson, D.A., et al., *Dynamics of cAMP-dependent protein kinase.* Chem Rev, 2001. **101**(8): p. 2243-70.
43. Meharena, H.S., et al., *Deciphering the Structural Basis of Eukaryotic Protein Kinase Regulation.* PLOS Biology, 2013. **11**(10): p. e1001680.
44. Meharena, H.S., et al., *Decoding the Interactions Regulating the Active State Mechanics of Eukaryotic Protein Kinases.* PLOS Biology, 2016. **14**(11): p. e2000127.
45. Taylor, S.S., et al., *Evolution of the eukaryotic protein kinases as dynamic molecular switches.* Philos Trans R Soc Lond B Biol Sci, 2012. **367**(1602): p. 2517-28.
46. Taylor, S.S. and A.P. Kornev, *Protein kinases: evolution of dynamic regulatory proteins.* Trends Biochem Sci, 2011. **36**(2): p. 65-77.
47. Cembran, A., et al., *Conformational equilibrium of N-myristoylated cAMP-dependent protein kinase A by molecular dynamics simulations.* Biochemistry, 2012. **51**(51): p. 10186-96.
48. Herberg, F.W., et al., *Importance of the A-helix of the catalytic subunit of cAMP-dependent protein kinase for stability and for orienting subdomains at the cleft interface.* Protein science : a publication of the Protein Society, 1997. **6**(3): p. 569-579.
49. Kannan, N., et al., *The hallmark of AGC kinase functional divergence is its C-terminal tail, a cis-acting regulatory module.* Proceedings of the National Academy of Sciences, 2007. **104**(4): p. 1272-1277.
50. Romano, R.A., et al., *A chimeric mechanism for polyvalent trans-phosphorylation of PKA by PDK1.* Protein Sci, 2009. **18**(7): p. 1486-97.
51. Batkin, M., I. Schvartz, and S. Shaltiel, *Snapping of the Carboxyl Terminal Tail of the Catalytic Subunit of PKA onto Its Core: Characterization of the Sites by Mutagenesis.* Biochemistry, 2000. **39**(18): p. 5366-5373.
52. Pearce, L.R., D. Komander, and D.R. Alessi, *The nuts and bolts of AGC protein kinases.* Nature Reviews Molecular Cell Biology, 2010. **11**(1): p. 9-22.
53. Taylor, S.S., et al., *Dynamics of signaling by PKA.* Biochimica et Biophysica Acta (BBA) - Proteins and Proteomics, 2005. **1754**(1): p. 25-37.
54. Carnegie, G.K., C.K. Means, and J.D. Scott, *A-kinase anchoring proteins: from protein complexes to physiology and disease.* IUBMB Life, 2009. **61**(4): p. 394-406.
55. Langeberg, L.K. and J.D. Scott, *Signalling scaffolds and local organization of cellular behaviour.* Nat Rev Mol Cell Biol, 2015. **16**(4): p. 232-44.
56. Housden, B.E. and N. Perrimon, *Spatial and temporal organization of signaling pathways.* Trends Biochem Sci, 2014. **39**(10): p. 457-64.
57. Scott, J.D., et al., *Identification of an inhibitory region of the heat-stable protein inhibitor of the cAMP-dependent protein kinase.* Proc Natl Acad Sci U S A, 1985. **82**(13): p. 4379-83.
58. Hauer, J.A., et al., *Two well-defined motifs in the cAMP-dependent protein kinase inhibitor (PKIalpha) correlate with inhibitory and nuclear export function.* Protein Sci, 1999. **8**(3): p. 545-53.
59. Hauer, J.A., S.S. Taylor, and D.A. Johnson, *Binding-dependent disorder-order transition in PKI alpha: a fluorescence anisotropy study.* Biochemistry, 1999. **38**(21): p. 6774-80.

60. Olivieri, C., et al., *Multi-state Recognition Pathway of the Intrisically Disordered Protein Kinase Inhibitor by Protein Kinase A.* Under Review, 2020.
61. Sastri, M., et al., *A-kinase-interacting protein localizes protein kinase A in the nucleus.* Proceedings of the National Academy of Sciences of the United States of America, 2005. **102**(2): p. 349-354.
62. Masterson, L.R., et al., *Backbone NMR resonance assignment of the catalytic subunit of cAMP-dependent protein kinase A in complex with AMP-PNP.* Biomolecular NMR Assignments, 2009. **3**(1): p. 115-117.
63. Masterson, L.R., et al., *cAMP-dependent protein kinase A selects the excited state of the membrane substrate phospholamban.* J Mol Biol, 2011. **412**(2): p. 155-64.
64. Tomasini, M.D., et al., *Conformational Landscape of the PRKACA-DNAJB1 Chimeric Kinase, the Driver for Fibrolamellar Hepatocellular Carcinoma.* Sci Rep, 2018. **8**(1): p. 720.
65. Walker, C., et al., *Cushing's syndrome driver mutation disrupts protein kinase A allosteric network, altering both regulation and substrate specificity.* Science Advances, 2019. **5**(8): p. eaaw9298.
66. Kim, J., et al., *A dynamic hydrophobic core orchestrates allostery in protein kinases.* Sci Adv, 2017. **3**(4): p. e1600663.
67. Masterson, L.R., et al., *Dynamics connect substrate recognition to catalysis in protein kinase A.* Nat Chem Biol, 2010. **6**(11): p. 821-8.
68. Kim, J., et al., *Dysfunctional conformational dynamics of protein kinase A induced by a lethal mutant of phospholamban hinder phosphorylation.* Proc Natl Acad Sci U S A, 2015. **112**(12): p. 3716-21.
69. Li, G.C., et al., *Mapping the Hydrogen Bond Networks in the Catalytic Subunit of Protein Kinase A Using H/D Fractionation Factors.* Biochemistry, 2015. **54**(26): p. 4042-4049.
70. Srivastava, Atul K., et al., *Synchronous Opening and Closing Motions Are Essential for cAMP-Dependent Protein Kinase A Signaling.* Structure, 2014. **22**(12): p. 1735-1743.
71. Kim, J., et al., *Uncoupling Catalytic and Binding Functions in the Cyclic AMP-Dependent Protein Kinase A.* Structure, 2016. **24**(3): p. 353-63.
72. Xiao, Y., et al., *Phosphorylation releases constraints to domain motion in ERK2.* Proceedings of the National Academy of Sciences, 2014. **111**(7): p. 2506-2511.
73. Majumdar, A., et al., *Allostery governs Cdk2 activation and differential recognition of CDK inhibitors.* Nature Chemical Biology, 2021. **17**(4): p. 456-464.
74. Kumar, G.S., et al., *Dynamic activation and regulation of the mitogen-activated protein kinase p38.* Proceedings of the National Academy of Sciences, 2018. **115**(18): p. 4655-4660.
75. Vogtherr, M., et al., *NMR backbone assignment of the mitogen-activated protein (MAP) kinase p38.* Journal of Biomolecular NMR, 2005. **32**(2): p. 175-175.
76. Vogtherr, M., et al., *NMR Characterization of Kinase p38 Dynamics in Free and Ligand‐Bound Forms.* Angewandte Chemie International Edition, 2006. **45**(6): p. 993-997.
77. Xie, T., et al., *Conformational states dynamically populated by a kinase determine its function.* Science, 2020. **370**(6513): p. eabc2754.
78. Herberg, F.W. and S.S. Taylor, *Physiological inhibitors of the catalytic subunit of cAMP-dependent protein kinase: effect of magnesium-ATP on protein-protein interactions.* Biochemistry, 1993. **32**(50): p. 14015-14022.

79. Zheng, J., et al., *2.2 A refined crystal structure of the catalytic subunit of cAMP-dependent protein kinase complexed with MnATP and a peptide inhibitor.* Acta Crystallogr D Biol Crystallogr, 1993. **49**(Pt 3): p. 362-5.
80. Masterson, L.R., et al., *Dynamically committed, uncommitted, and quenched states encoded in protein kinase A revealed by NMR spectroscopy.* Proceedings of the National Academy of Sciences, 2011. **108**(17): p. 6969-6974.
81. Ahuja, L.G., et al., *Mutation of a kinase allosteric node uncouples dynamics linked to phosphotransfer.* Proceedings of the National Academy of Sciences, 2017. **114**(6): p. E931-E940.
82. Masterson, L.R., et al., *Allosteric cooperativity in protein kinase A.* Proc Natl Acad Sci U S A, 2008. **105**(2): p. 506-11.
83. Wang, Y., et al., *Globally correlated conformational entropy underlies positive and negative cooperativity in a kinase's enzymatic cycle.* Nature Communications, 2019. **10**(1): p. 799.
84. Adams, J.A., *Kinetic and catalytic mechanisms of protein kinases.* Chem Rev, 2001. **101**(8): p. 2271-90.
85. Cook, P.F., et al., *Adenosine cyclic 3',5'-monophosphate dependent protein kinase: kinetic mechanism for the bovine skeletal muscle catalytic subunit.* Biochemistry, 1982. **21**(23): p. 5794-9.
86. Kong, C.T. and P.F. Cook, *Isotope partitioning in the adenosine 3',5'-monophosphate dependent protein kinase reaction indicates a steady-state random kinetic mechanism.* Biochemistry, 1988. **27**(13): p. 4795-4799.
87. Whitehouse, S., et al., *Studies on the kinetic mechanism of the catalytic subunit of the cAMP-dependent protein kinase.* J Biol Chem, 1983. **258**(6): p. 3693-701.
88. Bastidas, A.C., et al., *Phosphoryl transfer by protein kinase A is captured in a crystal lattice.* J Am Chem Soc, 2013. **135**(12): p. 4788-98.
89. Khavrutskii, I.V., et al., *A transition path ensemble study reveals a linchpin role for Mg(2+) during rate-limiting ADP release from protein kinase A.* Biochemistry, 2009. **48**(48): p. 11532-45.
90. Grant, B.D. and J.A. Adams, *Pre-Steady-State Kinetic Analysis of cAMP-Dependent Protein Kinase Using Rapid Quench Flow Techniques.* Biochemistry, 1996. **35**(6): p. 2022-2029.
91. Zhou, J. and J.A. Adams, *Participation of ADP Dissociation in the Rate-Determining Step in cAMP-Dependent Protein Kinase.* Biochemistry, 1997. **36**(50): p. 15733-15738.
92. Shaffer, J. and J.A. Adams, *Detection of conformational changes along the kinetic pathway of protein kinase A using a catalytic trapping technique.* Biochemistry, 1999. **38**(37): p. 12072-9.
93. Weinstein, L.S., et al., *Activating mutations of the stimulatory G protein in the McCune-Albright syndrome.* N Engl J Med, 1991. **325**(24): p. 1688-95.
94. Kirschner, L.S., et al., *Mutations of the gene encoding the protein kinase A type I-alpha regulatory subunit in patients with the Carney complex.* Nat Genet, 2000. **26**(1): p. 89-92.
95. Kamilaris, C.D.C., et al., *Carney Complex.* Exp Clin Endocrinol Diabetes, 2019. **127**(2-03): p. 156-164.
96. Horvath, A., et al., *Mutations and polymorphisms in the gene encoding regulatory subunit type 1-alpha of protein kinase A (PRKAR1A): an update.* Hum Mutat, 2010. **31**(4): p. 369-79.
97. Nieman, L.K., *Recent Updates on the Diagnosis and Management of Cushing's Syndrome.* Endocrinol Metab (Seoul), 2018. **33**(2): p. 139-146.

98. Lacroix, A., et al., *Cushing's syndrome.* Lancet, 2015. **386**(9996): p. 913-27.
99. Calebiro, D., et al., *cAMP signaling in cortisol-producing adrenal adenoma.* European Journal of Endocrinology, 2015. **173**(4): p. M99-M106.
100. Rothenbuhler, A., et al., *Identification of novel genetic variants in phosphodiesterase 8B (PDE8B), a cAMP-specific phosphodiesterase highly expressed in the adrenal cortex, in a cohort of patients with adrenal tumours.* Clin Endocrinol (Oxf), 2012. **77**(2): p. 195-9.
101. Tissier, F., et al., *Mutations of beta-catenin in adrenocortical tumors: activation of the Wnt signaling pathway is a frequent event in both benign and malignant adrenocortical tumors.* Cancer Res, 2005. **65**(17): p. 7622-7.
102. Ronchi, C.L., et al., *Genetic Landscape of Sporadic Unilateral Adrenocortical Adenomas Without PRKACA p.Leu206Arg Mutation.* Journal of Clinical Endocrinology & Metabolism, 2016. **101**(9): p. 3526-3538.
103. Kassahun, W.T., *Contemporary management of fibrolamellar hepatocellular carcinoma: diagnosis, treatment, outcome, prognostic factors, and recent developments.* World Journal of Surgical Oncology, 2016. **14**(1): p. 151.
104. Njei, B., V.R. Konjeti, and I. Ditah, *Prognosis of Patients With Fibrolamellar Hepatocellular Carcinoma Versus Conventional Hepatocellular Carcinoma: A Systematic Review and Meta-analysis.* Gastrointest Cancer Res, 2014. **7**(2): p. 49-54.
105. Kastenhuber, E.R., et al., *DNAJB1–PRKACA fusion kinase interacts with β-catenin and the liver regenerative response to drive fibrolamellar hepatocellular carcinoma.* Proceedings of the National Academy of Sciences, 2017. **114**(50): p. 13076-13084.
106. Cheung, J., et al., *Structural insights into mis-regulation of protein kinase A in human tumors.* Proc Natl Acad Sci U S A, 2015. **112**(5): p. 1374-9.
107. Olivieri, C., et al., *Defective internal allosteric network imparts dysfunctional ATP/substrate-binding cooperativity in oncogenic chimera of protein kinase A.* Communications Biology, 2021. **4**(1): p. 321.
108. Turnham, R.E., et al., *An acquired scaffolding function of the DNAJ-PKAc fusion contributes to oncogenic signaling in fibrolamellar carcinoma.* eLife, 2019. **8**: p. e44187.
109. Reynen, K., *Cardiac myxomas.* N Engl J Med, 1995. **333**(24): p. 1610-7.
110. Maleszewski, J.J., et al., *PRKAR1A in the development of cardiac myxoma: a study of 110 cases including isolated and syndromic tumors.* Am J Surg Pathol, 2014. **38**(8): p. 1079-87.
111. Tseng, I.C., et al., *Microinsertions in PRKACA cause activation of the protein kinase A pathway in cardiac myxoma.* J Pathol, 2017. **242**(2): p. 134-139.
112. Liu, J. and R. Nussinov, *Allostery: An Overview of Its History, Concepts, Methods, and Applications.* PLoS Comput Biol, 2016. **12**(6): p. e1004966.
113. Tsai, C.J., A. Del Sol, and R. Nussinov, *Protein allostery, signal transmission and dynamics: a classification scheme of allosteric mechanisms.* Mol Biosyst, 2009. **5**(3): p. 207-16.
114. Tsai, C.J. and R. Nussinov, *A unified view of "how allostery works".* PLoS Comput Biol, 2014. **10**(2): p. e1003394.
115. Wodak, S.J., et al., *Allostery in Its Many Disguises: From Theory to Applications.* Structure, 2019. **27**(4): p. 566-578.
116. Cui, Q. and M. Karplus, *Allostery and cooperativity revisited.* Protein Sci, 2008. **17**(8): p. 1295-307.

117. Lange, O.F., et al., *Recognition Dynamics Up to Microseconds Revealed from an RDC-Derived Ubiquitin Ensemble in Solution.* Science, 2008. **320**(5882): p. 1471-1475.
118. Kern, D. and E.R.P. Zuiderweg, *The role of dynamics in allosteric regulation.* Current Opinion in Structural Biology, 2003. **13**(6): p. 748-757.
119. Volkman, B.F., et al., *Two-State Allosteric Behavior in a Single-Domain Signaling Protein.* Science, 2001. **291**(5512): p. 2429-2433.
120. Gsponer, J., et al., *A Coupled Equilibrium Shift Mechanism in Calmodulin-Mediated Signal Transduction.* Structure, 2008. **16**(5): p. 736-746.
121. Tang, C., C.D. Schwieters, and G.M. Clore, *Open-to-closed transition in apo maltose-binding protein observed by paramagnetic NMR.* Nature, 2007. **449**(7165): p. 1078-1082.
122. Yang, J., et al., *Allosteric network of cAMP-dependent protein kinase revealed by mutation of Tyr204 in the P+1 loop.* J Mol Biol, 2005. **346**(1): p. 191-201.
123. Loh, S.N. and J.L. Markley, *Measurement of Amide Hydrogen D/H Fractionation Factors in Proteins by NMR Spectroscopy*, in *Techniques in Protein Chemistry IV*, R.H. Angeletti, Editor. 1993, Academic Press. p. 517-524.
124. Barbara Schowen, K. and R.L. Schowen, *[29] Solvent isotope effects on enzyme systems*, in *Methods in Enzymology*, D.L. Purich, Editor. 1982, Academic Press. p. 551-606.
125. Pervushin, K., et al., *Attenuated T2 relaxation by mutual cancellation of dipole–dipole coupling and chemical shift anisotropy indicates an avenue to NMR structures of very large biological macromolecules in solution.* Proceedings of the National Academy of Sciences, 1997. **94**(23): p. 12366-12371.
126. Loh, S.N. and J.L. Markley, *Hydrogen Bonding in Proteins As Studied by Amide Hydrogen D/H Fractionation Factors: Application to Staphylococcal Nuclease.* Biochemistry, 1994. **33**(4): p. 1029-1036.
127. Li, F., et al., *Evidence for an internal entropy contribution to phosphoryl transfer: a study of domain closure, backbone flexibility, and the catalytic cycle of cAMP-dependent protein kinase.* J Mol Biol, 2002. **315**(3): p. 459-69.
128. Gangal, M., et al., *Backbone flexibility of five sites on the catalytic subunit of cAMP-dependent protein kinase in the open and closed conformations.* Biochemistry, 1998. **37**(39): p. 13728-35.
129. Selvaratnam, R., et al., *Mapping allostery through the covariance analysis of NMR chemical shifts.* Proc Natl Acad Sci U S A, 2011. **108**(15): p. 6133-8.
130. Byun, J.A. and G. Melacini, *NMR methods to dissect the molecular mechanisms of disease-related mutations (DRMs): Understanding how DRMs remodel functional free energy landscapes.* Methods, 2018. **148**: p. 19-27.
131. Boulton, S., et al., *Implementation of the NMR CHEmical Shift Covariance Analysis (CHESCA): A Chemical Biologist's Approach to Allostery.* Methods Mol Biol, 2018. **1688**: p. 391-405.
132. Boulton, S., et al., *A tool set to map allosteric networks through the NMR chemical shift covariance analysis.* Sci Rep, 2014. **4**: p. 7306.
133. Xu, Y., et al., *Identifying coupled clusters of allostery participants through chemical shift perturbations.* Proceedings of the National Academy of Sciences, 2019. **116**(6): p. 2078-2085.
134. Wang, J., et al., *Mapping allosteric communications within individual proteins.* Nature Communications, 2020. **11**(1): p. 3862.

135. Masterson, L.R., et al., *Allostery and binding cooperativity of the catalytic subunit of protein kinase A by NMR spectroscopy and molecular dynamics simulations.* Adv Protein Chem Struct Biol, 2012. **87**: p. 363-89.
136. Selvaratnam, R., et al., *The Auto-Inhibitory Role of the EPAC Hinge Helix as Mapped by NMR.* PLoS ONE, 2012. **7**(11): p. e48707.
137. Axe, J.M., et al., *Amino Acid Networks in a (ß/α)8 Barrel Enzyme Change during Catalytic Turnover.* Journal of the American Chemical Society, 2014. **136**(19): p. 6818-6821.
138. Axe, J.M., et al., *Severing of a hydrogen bond disrupts amino acid networks in the catalytically active state of the alpha subunit of tryptophan synthase.* Protein Sci, 2015. **24**(4): p. 484-94.
139. Dawson, J.E., P.J. Farber, and J.D. Forman-Kay, *Allosteric Coupling between the Intracellular Coupling Helix 4 and Regulatory Sites of the First Nucleotide-binding Domain of CFTR.* PLOS ONE, 2013. **8**(9): p. e74347.
140. McClendon, C.L., et al., *Dynamic architecture of a protein kinase.* Proc Natl Acad Sci U S A, 2014. **111**(43): p. E4623-31.
141. Walker, C., et al., *The allosteric E31V mutation disrupts the nucleotide-substrate cooperativity in protein kinase A: is there a common mechanism for Cushing's syndrome driving mutations?* Submitted, 2021.
142. Cooper, A. and D.T. Dryden, *Allostery without conformational change. A plausible model.* Eur Biophys J, 1984. **11**(2): p. 103-9.
143. Frederick, K.K., et al., *Conformational entropy in molecular recognition by proteins.* Nature, 2007. **448**(7151): p. 325-329.
144. Petit, C.M., et al., *Hidden dynamic allostery in a PDZ domain.* Proceedings of the National Academy of Sciences, 2009. **106**(43): p. 18249-18254.
145. Popovych, N., et al., *Dynamically driven protein allostery.* Nature Structural & Molecular Biology, 2006. **13**(9): p. 831-838.
146. Shi, L. and L.E. Kay, *Tracing an allosteric pathway regulating the activity of the HslV protease.* Proceedings of the National Academy of Sciences, 2014. **111**(6): p. 2140-2145.
147. Otten, R., et al., *Rescue of conformational dynamics in enzyme catalysis by directed evolution.* Nature Communications, 2018. **9**(1): p. 1314.
148. Gardner, J.M., et al., *Manipulating Conformational Dynamics To Repurpose Ancient Proteins for Modern Catalytic Functions.* ACS Catalysis, 2020. **10**(9): p. 4863-4870.
149. Schütz, A.K., E. Rennella, and L.E. Kay, *Exploiting conformational plasticity in the AAA+ protein VCP/p97 to modify function.* Proceedings of the National Academy of Sciences, 2017. **114**(33): p. E6822-E6829.
150. Tollinger, M., et al., *Slow dynamics in folded and unfolded states of an SH3 domain.* Journal of the American Chemical Society, 2001. **123**(46): p. 11341-11352.
151. Zimmermann, B., et al., *Effect of metal ions on high-affinity binding of pseudosubstrate inhibitors to PKA.* Biochem J, 2008. **413**(1): p. 93-101.
152. Tugarinov, V., R. Sprangers, and L.E. Kay, *Probing Side-Chain Dynamics in the Proteasome by Relaxation Violated Coherence Transfer NMR Spectroscopy.* Journal of the American Chemical Society, 2007. **129**(6): p. 1743-1750.
153. Capdevila, D.A., et al., *Entropy redistribution controls allostery in a metalloregulatory protein.* Proceedings of the National Academy of Sciences, 2017. **114**(17): p. 4424-4429.

154. Marlow, M.S., et al., *The role of conformational entropy in molecular recognition by calmodulin.* Nat Chem Biol, 2010. **6**(5): p. 352-8.
155. Marintchev, A., D. Frueh, and G. Wagner, *NMR Methods for Studying Protein–Protein Interactions Involved in Translation Initiation*, in *Methods in Enzymology*, J. Lorsch, Editor. 2007, Academic Press. p. 283-331.
156. Tord, B., L. Sara, and J. Peter, *Methods for the detection and analysis of protein–protein interactions.* PROTEOMICS, 2007. **7**(16): p. 2833-2842.
157. Ngounou Wetie, A.G., et al., *Investigation of stable and transient protein-protein interactions: past, present and future.* Proteomics, 2013. **13**(0): p. 10.1002/pmic.201200328.
158. Barile, E. and M. Pellecchia, *NMR-Based Approaches for the Identification and Optimization of Inhibitors of Protein–Protein Interactions.* Chemical Reviews, 2014. **114**(9): p. 4749-4763.
159. Zuiderweg, E.R.P., *Mapping Protein−Protein Interactions in Solution by NMR Spectroscopy.* Biochemistry, 2002. **41**(1): p. 1-7.
160. Nishida, N. and I. Shimada, *An NMR Method to Study Protein–Protein Interactions*, in *Integrin and Cell Adhesion Molecules: Methods and Protocols*, M. Shimaoka, Editor. 2012, Humana Press: Totowa, NJ. p. 129-137.
161. Ishima, R. and D.A. Torchia, *Protein dynamics from NMR.* Nature Structural Biology, 2000. **7**: p. 740.
162. Kay, L.E., *Protein dynamics from NMR.* Biochemistry and Cell Biology, 1998. **76**(2-3): p. 145-152.
163. Kempf, J.G. and J.P. Loria, *Protein dynamics from solution NMR.* Cell Biochemistry and Biophysics, 2002. **37**(3): p. 187-211.
164. Olivieri, C., et al., *Simultaneous detection of intra- and inter-molecular paramagnetic relaxation enhancements in protein complexes.* J Biomol NMR, 2018. **70**(3): p. 133-140.
165. Park, S.H., et al., *Paramagnetic relaxation enhancement of membrane proteins by incorporation of the metal-chelating unnatural amino acid 2-amino-3-(8-hydroxyquinolin-3-yl)propanoic acid (HQA).* J Biomol NMR, 2015. **61**(3-4): p. 185-96.
166. Gong, Z., C.D. Schwieters, and C. Tang, *Theory and practice of using solvent paramagnetic relaxation enhancement to characterize protein conformational dynamics.* Methods, 2018.
167. Pervushin, K., et al., *Transverse Relaxation-Optimized Spectroscopy (TROSY) for NMR Studies of Aromatic Spin Systems in 13C-Labeled Proteins.* Journal of the American Chemical Society, 1998. **120**(25): p. 6394-6400.
168. Tugarinov, V., P.M. Hwang, and L.E. Kay, *Nuclear Magnetic Resonance Spectroscopy of High-Molecular-Weight Proteins.* Annual Review of Biochemistry, 2004. **73**(1): p. 107-146.
169. Gardner, K.H., et al., *Solution NMR Studies of a 42 KDa Escherichia Coli Maltose Binding Protein/β-Cyclodextrin Complex: Chemical Shift Assignments and Analysis.* Journal of the American Chemical Society, 1998. **120**(45): p. 11738-11748.
170. Walters, K.J., et al., *[11] - Characterizing Protein-Protein Complexes and Oligomers by Nuclear Magnetic Resonance Spectroscopy*, in *Methods in Enzymology*, T.L. James, V. Dötsch, and U. Schmitz, Editors. 2001, Academic Press. p. 238-258.

171. Göbl, C., et al., *NMR approaches for structural analysis of multidomain proteins and complexes in solution.* Progress in Nuclear Magnetic Resonance Spectroscopy, 2014. **80**: p. 26-63.
172. Keskin, O., N. Tuncbag, and A. Gursoy, *Predicting Protein-Protein Interactions from the Molecular to the Proteome Level.* Chem Rev, 2016. **116**(8): p. 4884-909.
173. Jones, S. and J.M. Thornton, *Principles of protein-protein interactions.* Proc Natl Acad Sci U S A, 1996. **93**(1): p. 13-20.
174. Zhang, X., et al., *Protein-protein interactions among signaling pathways may become new therapeutic targets in liver cancer.* Oncology Reports, 2016. **35**(2): p. 625-638.
175. Braun, P. and A.C. Gingras, *History of protein-protein interactions: from egg-white to complex networks.* Proteomics, 2012. **12**(10): p. 1478-98.
176. Andreani, J. and R. Guerois, *Evolution of protein interactions: from interactomes to interfaces.* Arch Biochem Biophys, 2014. **554**: p. 65-75.
177. Lage, K., *Protein-protein interactions and genetic diseases: The interactome.* Biochim Biophys Acta, 2014. **1842**(10): p. 1971-1980.
178. Bhattacharya, A., Y.C. Kim, and J. Mittal, *Protein-protein interactions in a crowded environment.* Biophys Rev, 2013. **5**(2): p. 99-108.
179. Vuister, G.W., A.C. Wang, and A. Bax, *Measurement of three-bond nitrogen-carbon J couplings in proteins uniformly enriched in nitrogen-15 and carbon-13.* Journal of the American Chemical Society, 1993. **115**(12): p. 5334-5335.
180. Montelione, G.T., et al., *Accurate measurements of long-range heteronuclear coupling constants from homonuclear 2D NMR spectra of isotope-enriched proteins.* Journal of Magnetic Resonance (1969), 1989. **82**(1): p. 198-204.
181. Wider, G., et al., *A heteronuclear three-dimensional NMR experiment for measurements of small heteronuclear coupling constants in biological macromolecules.* Journal of Magnetic Resonance (1969), 1989. **85**(2): p. 426-431.
182. Kurz, M., P. Schmieder, and H. Kessler, *HETLOC, an Efficient Method for Determining Heteronuclear Long-Range Couplings with Heteronuclei in Natural Abundance.* Angewandte Chemie International Edition in English, 1991. **30**(10): p. 1329-1331.
183. Edison, A.S., W.M. Westler, and J.L. Markley, *Elucidation of amino acid spin systems in proteins and determination of heteronuclear coupling constants by carbon-proton-proton three-dimensional NMR.* Journal of Magnetic Resonance (1969), 1991. **92**(2): p. 434-438.
184. Xu, R.X., E.T. Olejniczak, and S.W. Fesik, *Stereospecific assignments and χ1 rotamers for FKBP when bound to ascomycin from 3JHα,Hβ and 3JN,Hβ coupling constants.* FEBS Letters, 1992. **305**(2): p. 137-143.
185. Sattler, M., H. Schwalbe, and C. Griesinger, *Stereospecific assignment of leucine methyl groups with carbon-13 in natural abundance or with random 13C labeling.* Journal of the American Chemical Society, 1992. **114**(3): p. 1126-1127.
186. Tonelli, M., et al., *Carbonyl carbon label selective (CCLS) (1)H–(15)N HSQC experiment for improved detection of backbone (13)C–(15)N cross peaks in larger proteins.* Journal of biomolecular NMR, 2007. **39**(3): p. 177-185.
187. Mori, S., et al., *Improved Sensitivity of HSQC Spectra of Exchanging Protons at Short Interscan Delays Using a New Fast HSQC (FHSQC) Detection Scheme That Avoids Water Saturation.* Journal of Magnetic Resonance, Series B, 1995. **108**(1): p. 94-98.

188. Taylor, S.S., et al., *PKA: a portrait of protein kinase dynamics.* Biochimica et Biophysica Acta (BBA) - Proteins and Proteomics, 2004. **1697**(1): p. 259-269.
189. Langer, T., et al., *NMR Backbone Assignment of a Protein Kinase Catalytic Domain by a Combination of Several Approaches: Application to the Catalytic Subunit of cAMP-Dependent Protein Kinase.* ChemBioChem, 2004. **5**(11): p. 1508-1516.
190. Langer, T., et al., *Folding and activity of cAMP-dependent protein kinase mutants.* FEBS Letters, 2005. **579**(19): p. 4049-4054.
191. Dalton, G.D. and W.L. Dewey, *Protein kinase inhibitor peptide (PKI): A family of endogenous neuropeptides that modulate neuronal cAMP-dependent protein kinase function.* Neuropeptides, 2006. **40**(1): p. 23-34.
192. Masterson, L.R., et al., *Simultaneous Detection and Deconvolution of Congested NMR Spectra Containing Three Isotopically Labeled Species.* Journal of the American Chemical Society, 2008. **130**(25): p. 7818-7819.
193. Wirmer, J. and H. Schwalbe, *Angular dependence of 1J(Ni,Cα i) and 2J(Ni,Cα (i − 1)) coupling constants measured in J-modulated HSQCs.* Journal of Biomolecular NMR, 2002. **23**(1): p. 47-55.
194. Traaseth, N.J., R. Verardi, and G. Veglia, *Asymmetric methyl group labeling as a probe of membrane protein homo-oligomers by NMR spectroscopy.* J Am Chem Soc, 2008. **130**(8): p. 2400-1.
195. Verardi, R., et al., *Isotope labeling for solution and solid-state NMR spectroscopy of membrane proteins.* Adv Exp Med Biol, 2012. **992**: p. 35-62.
196. Walters, K.J., et al., *Characterizing protein-protein complexes and oligomers by nuclear magnetic resonance spectroscopy.* Methods Enzymol, 2001. **339**: p. 238-58.
197. Atreya, H.S., *Isotope labeling in biomolecular NMR*. Advances in experimental medicine and biology. 2012, Dordrecht ; New York: Springer. viii, 219 p.
198. Anglister, J., G. Srivastava, and F. Naider, *Detection of intermolecular NOE interactions in large protein complexes.* Prog Nucl Magn Reson Spectrosc, 2016. **97**: p. 40-56.
199. Anglister, J., R. Levy, and T. Scherf, *Interactions of antibody aromatic residues with a peptide of cholera toxin observed by two-dimensional transferred nuclear Overhauser effect difference spectroscopy.* Biochemistry, 1989. **28**(8): p. 3360-5.
200. Scherf, T. and J. Anglister, *A T1 rho-filtered two-dimensional transferred NOE spectrum for studying antibody interactions with peptide antigens.* Biophys J, 1993. **64**(3): p. 754-61.
201. Hansen, D.F., et al., *Probing Chemical Shifts of Invisible States of Proteins with Relaxation Dispersion NMR Spectroscopy: How Well Can We Do?* Journal of the American Chemical Society, 2008. **130**(8): p. 2667-2675.
202. Lundström, P., et al., *Fractional 13C enrichment of isolated carbons using [1-13C]- or [2-13C]-glucose facilitates the accurate measurement of dynamics at backbone Cα and side-chain methyl positions in proteins.* Journal of Biomolecular NMR, 2007. **38**(3): p. 199-212.
203. LeMaster, D.M. and D.M. Kushlan, *Dynamical Mapping of E. coli Thioredoxin via 13C NMR Relaxation Analysis.* Journal of the American Chemical Society, 1996. **118**(39): p. 9255-9264.
204. Takeuchi, K., et al., *1-13C amino acid selective labeling in a 2H15N background for NMR studies of large proteins.* Journal of Biomolecular NMR, 2007. **38**(1): p. 89-98.

205. Takeuchi, K., Z.-Y.J. Sun, and G. Wagner, *Alternate 13C−12C Labeling for Complete Mainchain Resonance Assignments using Cα Direct-Detection with Applicability Toward Fast Relaxing Protein Systems.* Journal of the American Chemical Society, 2008. **130**(51): p. 17210-17211.
206. Prestegard, J.H., C.M. Bougault, and A.I. Kishore, *Residual Dipolar Couplings in Structure Determination of Biomolecules.* Chemical Reviews, 2004. **104**(8): p. 3519-3540.
207. Lipsitz, R.S. and N. Tjandra, *Residual Dipolar Couplings in NMR Structure Analysis.* Annual Review of Biophysics and Biomolecular Structure, 2004. **33**(1): p. 387-413.
208. Bax, A. and A. Grishaev, *Weak alignment NMR: a hawk-eyed view of biomolecular structure.* Current Opinion in Structural Biology, 2005. **15**(5): p. 563-570.
209. Tolman, J.R. and K. Ruan, *NMR Residual Dipolar Couplings as Probes of Biomolecular Dynamics.* Chemical Reviews, 2006. **106**(5): p. 1720-1736.
210. Ottiger, M., F. Delaglio, and A. Bax, *Measurement ofJand Dipolar Couplings from Simplified Two-Dimensional NMR Spectra.* Journal of Magnetic Resonance, 1998. **131**(2): p. 373-378.
211. Ding, K. and A.M. Gronenborn, *Sensitivity-enhanced 2D IPAP, TROSY–anti-TROSY, and E.COSY experiments: alternatives for measuring dipolar 15N–1HN couplings.* Journal of Magnetic Resonance, 2003. **163**(2): p. 208-214.
212. Tonelli, M., et al., *One-Sample Approach to Determine the Relative Orientations of Proteins in Ternary and Binary Complexes from Residual Dipolar Coupling Measurements.* Journal of the American Chemical Society, 2009. **131**(40): p. 14138-14139.
213. Sharff, A.J., et al., *Crystallographic evidence of a large ligand-induced hinge-twist motion between the two domains of the maltodextrin binding protein involved in active transport and chemotaxis.* Biochemistry, 1992. **31**(44): p. 10657-10663.
214. Vijay-Kumar, S., C.E. Bugg, and W.J. Cook, *Structure of ubiquitin refined at 1.8Åresolution.* Journal of Molecular Biology, 1987. **194**(3): p. 531-544.
215. Clore, G.M. and J. Iwahara, *Theory, Practice, and Applications of Paramagnetic Relaxation Enhancement for the Characterization of Transient Low-Population States of Biological Macromolecules and Their Complexes.* Chemical Reviews, 2009. **109**(9): p. 4108-4139.
216. Solomon, I., *Relaxation Processes in a System of Two Spins.* Physical Review, 1955. **99**(2): p. 559-565.
217. Iwahara, J., C. Tang, and G.M. Clore, *Practical Aspects of (1)H Transverse Paramagnetic Relaxation Enhancement Measurements on Macromolecules.* Journal of magnetic resonance (San Diego, Calif. : 1997), 2007. **184**(2): p. 185-195.
218. Janowska, M.K. and J. Baum, *Intermolecular Paramagnetic Relaxation Enhancement (PRE) Studies of Transient Complexes in Intrinsically Disordered Proteins.* Methods Mol Biol, 2016. **1345**: p. 45-53.
219. Newby, F.N., et al., *Structure-Free Validation of Residual Dipolar Coupling and Paramagnetic Relaxation Enhancement Measurements of Disordered Proteins.* Biochemistry, 2015. **54**(46): p. 6876-86.
220. Eliezer, D., *Distance information for disordered proteins from NMR and ESR measurements using paramagnetic spin labels.* Methods Mol Biol, 2012. **895**: p. 127-38.

221. Mainz, A., et al., *NMR Spectroscopy of Soluble Protein Complexes at One Mega-Dalton and Beyond.* Angewandte Chemie International Edition, 2013. **52**(33): p. 8746-8751.
222. Tzakos, A.G., et al., *NMR TECHNIQUES FOR VERY LARGE PROTEINS AND RNAS IN SOLUTION.* Annual Review of Biophysics and Biomolecular Structure, 2006. **35**(1): p. 319-342.
223. Manu, V.S. and G. Veglia, *Genetic algorithm optimized triply compensated pulses in NMR spectroscopy.* Journal of Magnetic Resonance, 2015. **260**: p. 136-143.
224. Xia, Y., et al., *Enhancing the sensitivity of multidimensional NMR experiments by using triply-compensated pi pulses.* J Biomol NMR, 2017. **69**(4): p. 237-243.
225. Hunter, T., *Why nature chose phosphate to modify proteins.* Philos Trans R Soc Lond B Biol Sci, 2012. **367**(1602): p. 2513-6.
226. Lodish, M. and C.A. Stratakis, *A genetic and molecular update on adrenocortical causes of Cushing syndrome.* Nat Rev Endocrinol, 2016.
227. Calebiro, D., K. Bathon, and I. Weigand, *Mechanisms of Aberrant PKA Activation by Cα Subunit Mutations.* Horm Metab Res, 2017. **49**(04): p. 307-314.
228. Di Dalmazi, G., et al., *Adrenal function after adrenalectomy for subclinical hypercortisolism and Cushing's syndrome: a systematic review of the literature.* J Clin Endocrinol Metab, 2014. **99**(8): p. 2637-45.
229. Taylor, S.S., et al., *Assembly of allosteric macromolecular switches: lessons from PKA.* Nat Rev Mol Cell Biol, 2012. **13**(10): p. 646-58.
230. Calebiro, D., et al., *PKA catalytic subunit mutations in adrenocortical Cushing's adenoma impair association with the regulatory subunit.* Nature Communications, 2014. **5**: p. 5680.
231. Rock, R., et al., *Impact of kinase activating and inactivating patient mutations on binary PKA interactions.* Front Pharmacol, 2015. **6**: p. 170.
232. Lubner, J.M., et al., *Cushing's syndrome mutant PKA(L)(205R) exhibits altered substrate specificity.* FEBS Lett, 2017. **591**(3): p. 459-467.
233. Luzi, N.M., et al., *Kinetics and inhibition studies of the L205R mutant of cAMP-dependent protein kinase involved in Cushing's syndrome.* FEBS Open Bio, 2018. **8**(4): p. 606-613.
234. Pervushin, K., et al., *Attenuated T₂ relaxation by mutual cancellation of dipole–dipole coupling and chemical shift anisotropy indicates an avenue to NMR structures of very large biological macromolecules in solution.* Proc Natl Acad Sci U S A 1997. **94**(23): p. 12366-12371.
235. Cembran, A., et al., *NMR mapping of protein conformational landscapes using coordinated behavior of chemical shifts upon ligand binding.* Phys Chem Chem Phys, 2014. **16**(14): p. 6508-18.
236. McClendon, C.L., et al., *Quantifying Correlations Between Allosteric Sites in Thermodynamic Ensembles.* Journal of Chemical Theory and Computation, 2009. **5**(9): p. 2486-2502.
237. Bruystens, J.G.H., et al., *PKA RIα homodimer structure reveals an intermolecular interface with implications for cooperative cAMP binding and Carney complex disease.* Structure (London, England : 1993), 2014. **22**(1): p. 59-69.
238. Kannan, N. and A.F. Neuwald, *Evolutionary constraints associated with functional specificity of the CMGC protein kinases MAPK, CDK, GSK, SRPK, DYRK, and CK2α.* Protein Science, 2004. **13**(8): p. 2059-2077.

239. Aoto, P.C., B.T. Martin, and P.E. Wright, *NMR Characterization of Information Flow and Allosteric Communities in the MAP Kinase p38gamma.* Sci Rep, 2016. **6**: p. 28655.
240. Bonn, S., et al., *Structural Analysis of Protein Kinase A Mutants with Rho-kinase Inhibitor Specificity*.* Journal of Biological Chemistry, 2006. **281**(34): p. 24818-24830.
241. Wu, J., et al., *PKA Type IIα Holoenzyme Reveals a Combinatorial Strategy for Isoform Diversity.* Science, 2007. **318**(5848): p. 274-279.
242. Wiseman, T., et al., *Rapid measurement of binding constants and heats of binding using a new titration calorimeter.* Analytical Biochemistry, 1989. **179**(1): p. 131-137.
243. Delaglio, F., et al., *NMRPipe: A multidimensional spectral processing system based on UNIX pipes.* Journal of Biomolecular NMR, 1995. **6**(3): p. 277-293.
244. Lee, W., M. Tonelli, and J.L. Markley, *NMRFAM-SPARKY: enhanced software for biomolecular NMR spectroscopy.* Bioinformatics, 2015. **31**(8): p. 1325-1327.
245. Jorgensen, W.L., et al., *Comparison of simple potential functions for simulating liquid water.* The Journal of Chemical Physics, 1983. **79**(2): p. 926-935.
246. Hess, B., et al., *LINCS: A linear constraint solver for molecular simulations.* Journal of Computational Chemistry, 1997. **18**: p. 1463-1472.
247. Darden, T., D. York, and L. Pedersen, *Particle mesh Ewald: An N·log(N) method for Ewald sums in large systems.* The Journal of Chemical Physics, 1993. **98**: p. 10089.
248. Hess, B., et al., *GROMACS 4: Algorithms for Highly Efficient, Load-Balanced, and Scalable Molecular Simulation.* Journal of Chemical Theory and Computation, 2008. **4**: p. 435-447.
249. Best, R.B., et al., *Optimization of the additive CHARMM all-atom protein force field targeting improved sampling of the backbone φ, ψ and side-chain χ(1) and χ(2) dihedral angles.* Journal of chemical theory and computation, 2012. **8**: p. 3257-3273.
250. Parrinello, M. and A. Rahman, *Crystal Structure and Pair Potentials: A Molecular-Dynamics Study.* Physical Review Letters, 1980. **45**: p. 1196-1199.
251. Alam, S.L., et al., *Structural basis for ubiquitin recognition by the human ESCRT-II EAP45 GLUE domain.* Nature Structural &Amp; Molecular Biology, 2006. **13**: p. 1029.
252. Dominguez, C., R. Boelens, and A.M.J.J. Bonvin, *HADDOCK: A Protein−Protein Docking Approach Based on Biochemical or Biophysical Information.* Journal of the American Chemical Society, 2003. **125**(7): p. 1731-1737.
253. Pasi, M., et al., *xPyder: a PyMOL plugin to analyze coupled residues and their networks in protein structures.* Journal of chemical information and modeling, 2012. **52**: p. 1865-74.
254. Liu, S., et al., *Fibrolamellar hepatocellular carcinoma.* Am J Gastroenterol, 2009. **104**(10): p. 2617-24; quiz 2625.
255. Weeda, V.B., et al., *Fibrolamellar variant of hepatocellular carcinoma does not have a better survival than conventional hepatocellular carcinoma--results and treatment recommendations from the Childhood Liver Tumour Strategy Group (SIOPEL) experience.* European journal of cancer (Oxford, England : 1990), 2013. **49**: p. 2698-704.
256. Katzenstein, H.M., et al., *Fibrolamellar hepatocellular carcinoma in children and adolescents.* Cancer, 2003. **97**(8): p. 2006-12.

257. Mavros, M.N., et al., *A systematic review: treatment and prognosis of patients with fibrolamellar hepatocellular carcinoma.* Journal of the American College of Surgeons, 2012. **215**: p. 820-30.
258. El-Serag, H.B. and J.A. Davila, *Is fibrolamellar carcinoma different from hepatocellular carcinoma? A US population-based study.* Hepatology (Baltimore, Md.), 2004. **39**: p. 798-803.
259. Simon, E.P., et al., *Transcriptomic characterization of fibrolamellar hepatocellular carcinoma.* Proc Natl Acad Sci U S A, 2015. **112**(44): p. E5916-25.
260. Xu, L., et al., *Genomic analysis of fibrolamellar hepatocellular carcinoma.* Human Molecular Genetics, 2014. **24**(1): p. 50-63.
261. Jedrzejewski, P.T., et al., *A conserved deamidation site at asn 2 in the catalytic subunit of mammalian cAMP-dependent protein kinase detected by capillary LC-MS and tandem mass spectrometry.* Protein Science, 1998. **7**(2): p. 457-469.
262. Riggle, K.M., et al., *Enhanced cAMP-stimulated protein kinase A activity in human fibrolamellar hepatocellular carcinoma.* Pediatric research, 2016. **80**(1): p. 110-118.
263. Cao, B., et al., *Structures of the PKA RIα Holoenzyme with the FLHCC Driver J-PKAcα or Wild-Type PKAcα.* Structure, 2019. **27**(5): p. 816-828.e4.
264. Averill, A.M., et al., *Inhibition of the chimeric DnaJ-PKAc enzyme by endogenous inhibitor proteins.* Journal of Cellular Biochemistry, 2019. **120**(8): p. 13783-13791.
265. Williamson, J.R., *Cooperativity in macromolecular assembly.* Nature Chemical Biology, 2008. **4**(8): p. 458-465.
266. Kay, L.E., D.A. Torchia, and A. Bax, *Backbone dynamics of proteins as studied by nitrogen-15 inverse detected heteronuclear NMR spectroscopy: application to staphylococcal nuclease.* Biochemistry, 1989. **28**(23): p. 8972-8979.
267. Stark, J.L., et al., *Structure and function of human DnaJ homologue subfamily a member 1 (DNAJA1) and its relationship to pancreatic cancer.* Biochemistry, 2014. **53**(8): p. 1360-72.
268. Srivastava, Atul K., et al., *Synchronous Opening and Closing Motions Are Essential for cAMP-Dependent Protein Kinase A Signaling.* Structure, 2014. **22**: p. 1735-1743.
269. Kim, J., et al., *Dysfunctional conformational dynamics of protein kinase A induced by a lethal mutant of phospholamban hinder phosphorylation.* Proceedings of the National Academy of Sciences, 2015: p. 201502299-201502299.
270. Vyas, M., et al., *DNAJB1-PRKACA fusions occur in oncocytic pancreatic and biliary neoplasms and are not specific for fibrolamellar hepatocellular carcinoma.* Modern Pathology, 2019.
271. Singhi, A.D., et al., *Recurrent Rearrangements in PRKACA and PRKACB in Intraductal Oncocytic Papillary Neoplasms of the Pancreas and Bile Duct.* Gastroenterology, 2020. **158**(3): p. 573-582.e2.
272. Riggle, K.M., et al., *Fibrolamellar Hepatocellular Carcinoma: Mechanistic Distinction From Adult Hepatocellular Carcinoma.* Pediatr Blood Cancer, 2016.
273. Graham, R.P., et al., *Fibrolamellar carcinoma in the Carney complex: PRKAR1A loss instead of the classic DNAJB1-PRKACA fusion.* Hepatology, 2018. **68**(4): p. 1441-1447.
274. Zhang, P., et al., *An Isoform-Specific Myristylation Switch Targets Type II PKA Holoenzymes to Membranes.* Structure (London, England : 1993), 2015. **23**(9): p. 1563-1572.

275. Tillo, S.E., et al., *Liberated PKA Catalytic Subunits Associate with the Membrane via Myristoylation to Preferentially Phosphorylate Membrane Substrates.* Cell reports, 2017. **19**(3): p. 617-629.
276. Williamson, J.R., *Cooperativity in macromolecular assembly.* Nat Chem Biol, 2008. **4**(8): p. 458-65.
277. Whitty, A., *Cooperativity and biological complexity.* Nat Chem Biol, 2008. **4**(8): p. 435-9.
278. Tong, M., et al., *Survey of solution dynamics in Src kinase reveals allosteric cross talk between the ligand binding and regulatory sites.* Nature Communications, 2017. **8**(1): p. 2160.
279. Lu, S., et al., *The Mechanism of ATP-Dependent Allosteric Protection of Akt Kinase Phosphorylation.* Structure, 2015. **23**(9): p. 1725-1734.
280. Ni, D., et al., *Molecular Dynamics Simulations and Dynamic Network Analysis Reveal the Allosteric Unbinding of Monobody to H-Ras Triggered by R135K Mutation.* International journal of molecular sciences, 2017. **18**(11): p. 2249.
281. Rivalta, I., et al., *Allosteric Communication Disrupted by a Small Molecule Binding to the Imidazole Glycerol Phosphate Synthase Protein–Protein Interface.* Biochemistry, 2016. **55**(47): p. 6484-6494.
282. Marsiglia, W.M., et al., *A Conserved Allosteric Pathway in Tyrosine Kinase Regulation.* Structure, 2019. **27**(8): p. 1308-1315.e3.
283. Shibata, T., Y. Arai, and Y. Totoki, *Molecular genomic landscapes of hepatobiliary cancer.* Cancer Science, 2018. **109**(5): p. 1282-1291.
284. Schneidman-Duhovny, D., M. Hammel, and A. Sali, *FoXS: a web server for rapid computation and fitting of SAXS profiles.* Nucleic Acids Research, 2010. **38**(suppl_2): p. W540-W544.
285. Hess, B., et al., *GROMACS 4: Algorithms for Highly Efficient, Load-Balanced, and Scalable Molecular Simulation.* J Chem Theory Comput, 2008. **4**(3): p. 435-47.
286. Best, R.B., et al., *Optimization of the Additive CHARMM All-Atom Protein Force Field Targeting Improved Sampling of the Backbone ϕ, ψ and Side-Chain χ1 and χ2 Dihedral Angles.* Journal of Chemical Theory and Computation, 2012. **8**(9): p. 3257-3273.
287. Hess, B., et al., *LINCS: A linear constraint solver for molecular simulations.* Journal of Computational Chemistry, 1997. **18**(12): p. 1463-1472.
288. Darden, T., D. York, and L. Pedersen, *Particle mesh Ewald: An N·log(N) method for Ewald sums in large systems.* The Journal of Chemical Physics, 1993. **98**(12): p. 10089-10092.
289. Parrinello, M. and A. Rahman, *Crystal Structure and Pair Potentials: A Molecular-Dynamics Study.* Physical Review Letters, 1980. **45**(14): p. 1196-1199.
290. Thiel, A., et al., *PRKACA mutations in cortisol-producing adenomas and adrenal hyperplasia: a single-center study of 60 cases.* Eur J Endocrinol, 2015. **172**(6): p. 677-85.
291. Nakajima, Y., et al., *Somatic mutations of the catalytic subunit of cyclic AMP-dependent protein kinase (PRKACA) gene in Japanese patients with several adrenal adenomas secreting cortisol [Rapid Communication].* Endocr J, 2014. **61**(8): p. 825-32.
292. Thompson, E.E., et al., *Comparative surface geometry of the protein kinase family.* Protein Sci, 2009. **18**(10): p. 2016-26.

293. Gapsys, V., et al., *pmx: Automated protein structure and topology generation for alchemical perturbations.* Journal of Computational Chemistry, 2015. **36**(5): p. 348-354.
294. Stratakis, C.A., *Cyclic AMP-dependent protein kinase catalytic subunit A (PRKACA): the expected, the unexpected, and what might be next.* J Pathol, 2018. **244**(3): p. 257-259.
295. Hernández, C.X. and V.S. Pande, *MDEntropy: Information-Theoretic Analyses for Molecular Dynamics.* The Journal of Open Source Software, 2017. **2**(19): p. 427.
296. Pasi, M., et al., *xPyder: A PyMOL Plugin To Analyze Coupled Residues and Their Networks in Protein Structures.* Journal of Chemical Information and Modeling, 2012. **52**(7): p. 1865-1874.